Biochemical characterization of the MMB-Hippo crosstalk and its physiological relevance for heart development

Biochemische Charakterisierung des MMB-Hippo Signalweges und dessen physiologische Rolle in der Herzentwicklung

Doctoral thesis for a doctoral degree
at the Graduate School of Life Sciences,
Julius-Maximilians-Universität Würzburg,
Section Biomedicine

submitted by

Marco Gründl

from

Sennfeld, Germany

Würzburg, 2020

Submitted on: ……..……..

Office stamp

Members of the Thesis Committee

Chairperson: Prof. Dr. Alexander Buchberger

Primary Supervisor: Prof. Dr. Stefan Gaubatz

Supervisor (Second): Prof. Dr. Manfred Gessler

Supervisor (Third): Prof. Dr. Eva Klopocki

Date of Public Defence: ……..……

Date of Receipt of Certificates: ……...……

Substantial parts of this thesis were published in the following articles:

Pattschull G., Walz S., **Gründl M**., Schwab M., Rühl E., Baluapuri A., Cindric-Vranesic A., Kneitz S., Wolf E., Ade CP., Rosenwald A., von Eyss B., Gaubatz S. (2019): **The Myb-MuvB complex is required for YAP-dependent transcription of mitotic genes.** Cell Reports 27:12, 3533-3546. https://doi.org/10.1016/j.celrep.2019.05.071

Gründl M., Walz S., Hauf L., Schwab M., Werner KM., Spahr S., Schulte C., Maric HM., Ade CP., Gaubatz S. (2020): **Interaction of YAP with the Myb-MuvB (MMB) complex defines a transcriptional program to promote the proliferation of cardiomyocytes.** PLOS Genetics 16(5): e1008818. https://doi.org/10.1371/journal.pgen.1008818

Summary

The Myb-MuvB (MMB) complex plays an essential role in the time-dependent transcriptional activation of mitotic genes. Recently, our laboratory identified a novel crosstalk between the MMB-complex and YAP, the transcriptional coactivator of the Hippo pathway, to coregulate a subset of mitotic genes (Pattschull et al., 2019). Several genetic studies have shown that the Hippo-YAP pathway is essential to drive cardiomyocyte proliferation during cardiac development (von Gise et al., 2012; Heallen et al., 2011; Xin et al., 2011). However, the exact mechanisms of how YAP activates proliferation of cardiomyocytes is not known. This doctoral thesis addresses the physiological role of the MMB-Hippo crosstalk within the heart and characterizes the YAP-B-MYB interaction with the overall aim to identify a potent inhibitor of YAP.

The results reported in this thesis indicate that complete loss of the MMB scaffold protein LIN9 in heart progenitor cells results in thinning of ventricular walls, reduced cardiomyocyte proliferation and early embryonic lethality. Moreover, genetic experiments using mice deficient in SAV1, a core component of the Hippo pathway, and LIN9-deficient mice revealed that the correct function of the MMB complex is critical for proliferation of cardiomyocytes due to Hippo-deficiency. Whole genome transcriptome profiling as well as genome wide binding studies identified a subset of Hippo-regulated cell cycle genes as direct targets of MMB. By proximity ligation assay (PLA), YAP and B-MYB were discovered to interact in embryonal cardiomyocytes. Biochemical approaches, such as co-immunoprecipitation assays, GST-pulldown assays, and μSPOT-based peptide arrays were employed to characterize the YAP-B-MYB interaction. Here, a PY motif within the N-terminus of B-MYB was found to directly interact with the YAP WW-domains. Consequently, the YAP WW-domains were important for the ability of YAP to drive proliferation in cardiomyocytes and to activate MMB target genes in differentiated C2C12 cells. The biochemical information obtained from the interaction studies was utilized to develop a novel competitive inhibitor of YAP called MY-COMP (Myb-YAP competition). In MY-COMP, the protein fragment of B-MYB containing the YAP binding domain is fused to a nuclear localization signal. Co-immunoprecipitation studies as well as PLA revealed that the YAP-B-MYB interaction is robustly blocked by expression of MY-COMP. Adenoviral overexpression of MY-COMP in embryonal cardiomyocytes suppressed entry into mitosis and blocked the pro-proliferative function of YAP. Strikingly, characterization of the cellular phenotype showed that ectopic expression of MY-COMP led to growth defects, nuclear abnormalities and polyploidization in HeLa cells.

Taken together, the results of this thesis reveal the mechanism of the crosstalk between the Hippo signaling pathway and the MMB complex in the heart and form the basis for interference with the oncogenic activity of the Hippo coactivator YAP.

Zusammenfassung

Der Myb-MuvB Komplex spielt eine essenzielle Rolle in der transkriptionellen Aktivierung von Zellzyklusgenen. Unser Labor hat kürzlich einen bis dahin unbekannten Mechanismus zwischen dem MMB-Komplex und Hippo-YAP Signalweg, der zur Aktivierung von Mitosegenen beiträgt, identifiziert. Der Hippo-YAP Signalweg ist beteiligt an der Gewebehomöostase und am Wachstum von Organen. So reguliert der Hippo-YAP Signalweg zum Beispiel während der Herzentwicklung die Proliferation von Herzmuskelzellen. Der exakte Mechanismus wie YAP die Zellteilung von Kardiomyozyten aktiviert, ist jedoch bisher nicht bekannt. In der vorliegenden Doktorarbeit wird das Zusammenspiel zwischen dem Hippo-Signalweg und dem MMB-Komplex im Herzen untersucht. Außerdem wird die Interaktion zwischen YAP und B-MYB biochemisch charakterisiert, um einen Inhibitor zu entwickeln, der die Aktivität von YAP vermindert.

Die Ergebnisse dieser Doktorarbeit zeigen, dass der Verlust der zentralen Untereinheit des MMB-Komplexes, LIN9, in Vorläuferzellen der Kardiomyozyten zu einer Reduktion der Herzwand sowie zu einer niedrigeren Proliferationsrate von Herzmuskelzellen und einer erhöhten Embryonalsterblichkeit führt. Außerdem wurde in genetischen Experimenten mit Hippo- und LIN9-defizienten Mäusen gezeigt, dass der MMB-Komplex wichtig für die Aktivierung der Proliferation in Hippo-defizienten Kardiomyozyten ist. Eine globale Analyse der Transkription und Chromatinbindung von YAP und LIN9 im Herzen zeigte, dass eine Untergruppe von Zellzyklusgenen, die nach Inaktivierung des Hippo-Signalwegs vermehrt exprimiert werden, gleichzeitig den MMB-Komplex am Promoter gebunden haben. Durch Interaktionsstudien konnte gezeigt werden, dass YAP und B-MYB in embryonalen Kardiomyozyten miteinander interagieren. Die Bindung der beiden Transkriptionsfaktoren wurde durch Co-Immunpräzipitation, GST-Pulldown-Analysen und Peptid-Arrays biochemisch untersucht. Dabei wurde gezeigt, dass ein PY-Motiv im N-terminus von B-MYB direkt an die WW-Domänen von YAP bindet. Im Umkehrschluss wurde festgestellt, dass die WW-Domänen von YAP essenziell sind, um sowohl die Proliferation in Herzmuskelzellen als auch die Expression von Mitosegenen in differenzierten C2C12 Zellen zu aktivieren. Letztendlich wurden die Ergebnisse der Interaktionsstudie genutzt, um einen neuartigen kompetitiven Inhibitor von YAP zu entwickeln. Für MY-COMP (Myb-YAP Competition) wurde der Proteinabschnitt von B-MYB, der die YAP Bindedomäne enthält, mit einer Kernlokalisierungssequenz fusioniert. Bindestudien zeigten, dass MY-COMP die Interaktion zwischen YAP und B-MYB effektiv blockiert. Eine durch Adenoviren vermittelte Überexpression von MY-COMP in embryonalen Herzmuskelzellen resultierte in einer verminderten Anzahl von mitotischen Zellen. Somit wird durch Expression von MY-COMP, die proliferative Fähigkeit von YAP vermindert. Interessanterweise wurden in HeLa Zellen, die mit MY-COMP behandelt wurden, vermehrt Abnormalitäten der Zellkerne, polyploide Zellen sowie ein Wachstumsdefizit beobachtet.

Zusammengefasst verdeutlichen die Ergebnisse dieser Doktorarbeit die Bedeutung des Zusammenspiels zwischen dem MMB-Komplex und dem Hippo-YAP-Signalweg für die Herzentwicklung und bilden die Grundlage, für die effektive Inhibierung der onkogenen Eigenschaften des Hippo-Coaktivators YAP.

Table of Contents

1. Introduction

1.1 Control of the mammalian cell cycle

1.1.1 Overview of the cell cycle

"The process of reproduction is a central property of life and this is seen in its simplest form with the reproduction of cells." Sir Paul Nurse - awarded in 2001 with the Nobel prize in physiology and medicine for the discovery of key regulators of the cell cycle.
The cell cycle is a coordinated process all cells pass through during division into two identical daughter cells. Two major events occur during cell division. Genomic DNA is replicated during S phase. Followed by separation of the identical genomes into two nuclei, which is achieved during mitosis (M phase). In eukaryotes, S phase and mitosis are separated by two gap phases. Within the first gap phase (G1) the cell decides to either undergo the next round of DNA replication or to exit from the cell cycle and rest in a quiescent state called G0. In the second gap phase (G2), between S phase and M phase, cells prepare for the next division (**Figure 1**). Together, G1, S and G2 phases are summarized as interphase. Mitosis is further subdivided into four phases: prophase, metaphase, anaphase, and telophase. In prophase, the nuclear envelope breaks down and replicated DNA condensates into chromosomes. Each chromosome consists of two identical chromatids (sister chromatids), which are attached to the mitotic spindle and align around the equator of a cell in metaphase. In anaphase, sister chromatids are separated and pulled to the opposite poles of the spindle apparatus. During telophase, nuclear division is completed and genomic DNA is packed into separate nuclei. Cellular division culminates in separation of the cytoplasm, a process known as cytokinesis. (Alberts et al., 2015; Malumbres and Barbacid, 2001; Weinberg, 2014)
The precise program of the cell cycle requires control points and checkpoints to monitor cell cycle progression. Three major cell cycle checkpoints are known: The first checkpoint is the restriction point (R-point) at the end of G1. Here, a cell decides to proceed into S phase or to exit the cell cycle into G0. The R-point marks the point of no return in the cell cycle. Up to this point a cell senses whether conditions in the internal and external environment are suitable for cellular division. Once the decision is made to replicate the genome, the program of S, G2 and M phase is autonomously completed (**Figure 1**) (Alberts et al., 2015; Blagosklonny and Pardee, 2002; Weinberg, 2014). The second checkpoint between G2 and M phase controls whether replication of the DNA is completed (Bartek et al., 2004). The third checkpoint is known as the spindle assembly checkpoint (SAC), which controls metaphase to anaphase transition. The SAC ensures that all chromosomes are properly attached to the mitotic spindle and thereby prevents premature segregation of chromosomes in anaphase (Morgan, 2016; Musacchio, 2015; Weinberg, 2014).

1.1.2 Regulation of cell cycle control

The molecular mechanisms of cell cycle progression are mainly controlled by cyclin dependent kinases (CDKs). CDKs are serine/threonine kinases, which are activated by a regulatory subunit called cyclins. Whereas CDKs are stably expressed throughout the cell cycle, cyclin levels are specific for unique cell cycle phases. Cyclin/CDK-complexes phosphorylate a set of downstream targets guiding the cell through its distinct phases. (Alberts et al., 2015; Morgan, 1997; Weinberg, 2014)

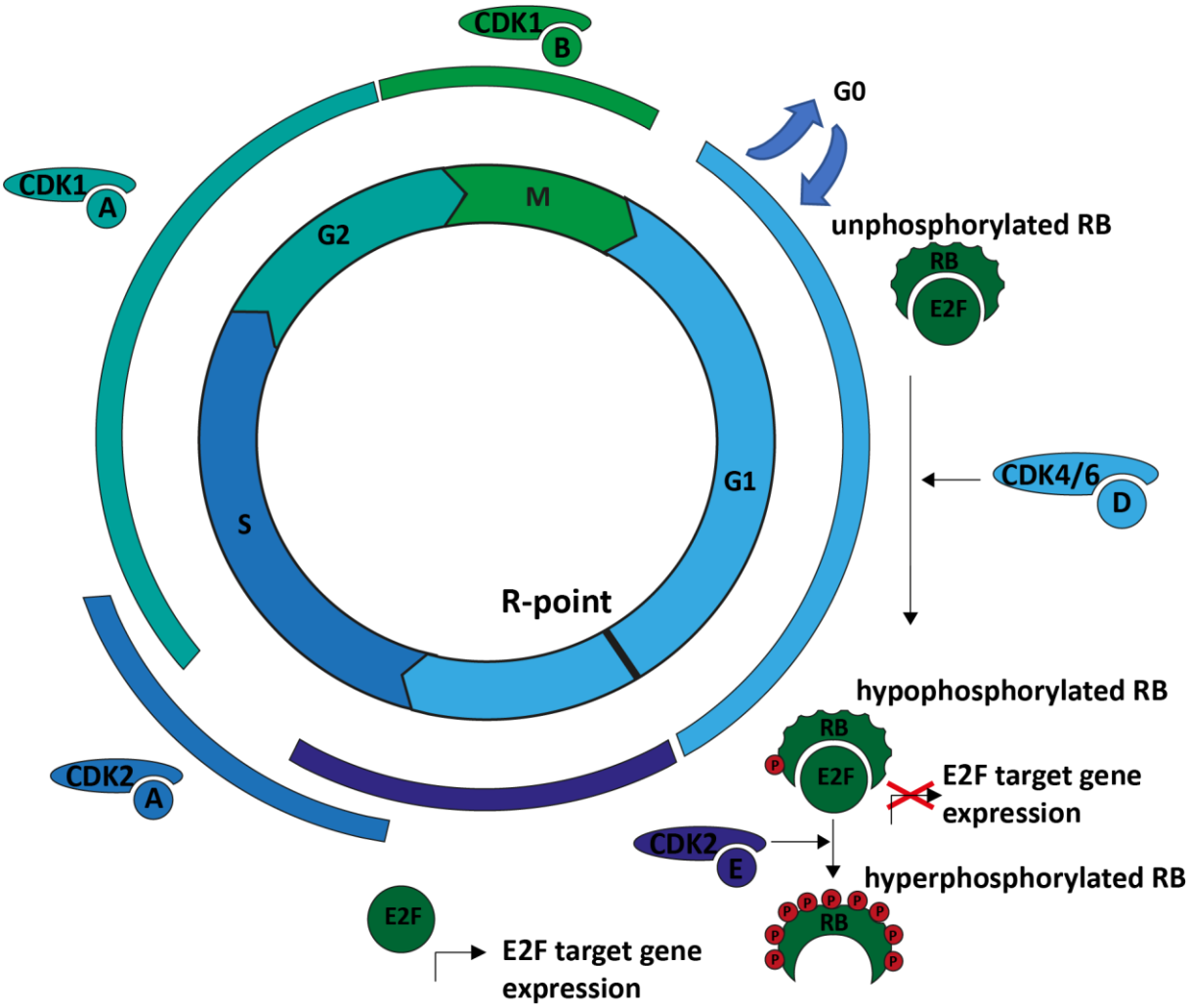

Figure 1: Regulation of the mammalian cell cycle
The mammalian cell cycle is divided into four phases. In **G1**, cells decide to enter the cell cycle or to stay in a quiescent state in **G0**. Replication of the genomic DNA is achieved in **S** phase. In **G2**, the cell prepares for mitosis (**M** phase). Phase-dependent expression of cyclins (Cyclin D, E, A, B), which activate their associate cyclin-dependent kinase (CDK), are the major driver of the cell cycle. In early G1 phase, **E2F** activity is suppressed by the retinoblastoma protein (**RB**). Due to mitogenic signals, a complex of CDK4/6 and cyclin D hypophosphorylates the RB protein at the restriction point (**R-point**). Enhanced expression of Cyclin E at the end of G1 results in hyperphosphorylation of the RB protein and the release of E2F transcription factors. E2F gene expression guides G1 to S phase transition of the cell. Adapted from (Weinberg, 2014).

In early G1 phase a set of D-type cyclins (D1, D2 and D3) binds to CDK4/6. After stimulation by mitogenic signals, the complex of Cyclin D/CDK4/6 phosphorylates substrates resulting in the expression of Cyclin E (Malumbres and Barbacid, 2001; Morgan, 1997). Cyclin E in turn binds to CDK2 and elevates levels of Cyclin A at the end of G1 phase. Cyclin A/CDK2 promotes gene expression required for replication. During S-phase until the end of G2 Cyclin A binds to CDK1. Complexes of CDK1 and Cyclin B initiate expression of genes required for mitosis (Morgan, 1997, 2014, 2016). (**Figure 1**). Beside the phase-dependent expression of Cyclins, CDK activity is also regulated by a set of CDK inhibitors (CKIs). Basically, there are two classes of CKIs. One group, the INK4 proteins, specifically inhibit Cyclin D/CDK4/6-complexes. Among these proteins are $p16^{INK4A}$, $p15^{INK4B}$, $p18^{INK4C}$ and $p19^{INK4D}$ (Sherr and Roberts, 1999; Weinberg, 2014). The second group of CKIs are $p21^{Cip1}$, $p27^{Kip1}$ and $p57^{Kip2}$, which block the activity of Cyclin/CDK2 and Cyclin/CDK1 complexes (Sherr and Roberts, 1999; Weinberg, 2014).

Another set of proteins that regulate cell cycle progression are the so-called pocket proteins, which include the retinoblastoma (RB) protein and the related p130 and p107 proteins. This class of proteins was originally identified, because of their binding to viral oncogenes, such as adenoviral E1A (Henley and Dick, 2012). Beside this, all pocket proteins have in common that they bind to E2F transcription factors. E2Fs are classical DNA-binding transcription factors, which regulate a large set of cell cycle related genes. The E2F transcription factor family has eight members, E2F1 to E2F8, which can be subdivided into three groups (Bertoli et al., 2013; Kent and Leone, 2019). The first group are activators of E2F target gene expression, which are represented by E2F1, E2F2 and E2F3a (Bertoli et al., 2013; Kent and Leone, 2019). The second group are canonical repressors of E2F target genes and includes E2F4, E2F5, E2F6, and E2F3b. The third group is represented by the atypical E2Fs, E2F7 and E2F8 (Bertoli et al., 2013; Kent and Leone, 2019). For DNA binding and fulfilling their function, E2F1-E2F6, require binding to dimerization partner 1 or 2 protein (DP1/2). In contrast, atypical E2Fs, E2F7 and E2F8, contain two DNA binding domains and can repress E2F target genes independent of DP1/2 (Christensen et al., 2005; Kent and Leone, 2019; Maiti et al., 2005; Di Stefano et al., 2003). Once bound to DP1/2, E2F1, E2F2 and E2F3a act as transcriptional activators by recruiting histone acetylases to the promoters of genes required in G1/S phase transition. In early to mid G1 phase un- or hypophosphorylated pRB binds to the activating E2Fs (E2F1, E2F2 and E2F3a) and thereby suppresses gene expression. Unlike the activator E2Fs, E2F3b, E2F4 and E2F5 mainly act as transcriptional repressors. Heterodimers of E2F3b/4/5 and DP1/2 bind to the pocket proteins p130 and p107 and repress E2F target gene expression (Bertoli et al., 2013; Weinberg, 2014). E2F6, E2F7 and E2F8 do not interact with the pocket proteins and act solely as transcriptional repressors (Di Stefano et al., 2003). Thereby, E2F6 builds heterodimers with DP1/2 and inhibits E2F gene expression (Dimova and Dyson, 2005; Gaubatz et al., 1998).

1.1.3 E2F-RB-complexes regulate gene expression at the R-point

One of the first mechanisms that were identified to regulate transition from G1 into S phase is the E2F-RB network. Regulation of S phase genes by E2F-RB-complexes is controlled in two ways. First, E2F target gene expression is suppressed by binding of unphosphorylated or hypophosphorylated RB protein to the activating E2Fs (E2F1, E2F2 and E2F3a) during early G1 phase (Bertoli et al., 2013; Henley and Dick, 2012). In a second stage of regulation, repressive E2F4/5 interact with p130/p107 to repress gene expression at the promoters of E2F target genes (Bertoli et al., 2013; Henley and Dick, 2012). Continuous mitogenic stimulation during G1 phase results in expression of D-type cyclins. In a first set of events Cyclin D/CDK4/6-complexes phosphorylate the p130/107 pocket proteins, thus leading to dissociation of repressive E2Fs from the promoters of E2F target genes (Bertoli et al., 2013; Henley and Dick, 2012). Moreover, Cyclin D/CDK4/6-complexes hypophosphorylate the RB protein, which promotes elevated expression of Cyclin E. Prior to the R-point, Cyclin E/CDK2 activity is directly blocked by $p21^{Cip1}$ and $p27^{Kip1}$, whereas Cyclin D/CDK4/6 activity is not suppressed by $p21^{Cip1}$ and $p27^{Kip1}$. Therefore, increasing levels of Cyclin D/CDK4/6 titrate the free pool of CKIs ($p21^{Cip1}$/$p27^{Kip1}$) and sequester CKIs away from Cyclin E/CDK2-complexes, resulting in rising activity of Cyclin E/CDK2-complexes (Sherr and Roberts, 1999; Weinberg, 2014). Elevated activity of Cyclin E/CDK2 results in hyperphosphorylation of the RB protein, which in turn releases E2F transcription factors (E2F1, E2F2, E2F3a). The activator E2Fs then promote expression of S phase genes (**Figure 1**). Therefore, this mechanism creates a positive feedback loop, which results in the commitment of cells to enter the cell cycle. (Weinberg, 2014)

1.2 DREAM and MMB complexes

1.2.1 MuvB protein complexes

Beside the regulation of genes required for G1/S transition by E2F-RB, a second set of genes, linked to G2/M phase, must be differentially regulated. In *Caenorhabditis elegans* three classes of genes were identified, which control vulva development and are linked to cell proliferation. These clusters were termed as the synthetic multi-vulva (synMuv) genes and are categorized into the synMuv A, B and, C family of genes (Fay and Han, 2000; Ferguson et al., 1987). Interestingly, class B of the synMuv genes contains homologues of RB, E2F and DP (Ceol and Horvitz, 2001). Protein complexes that include the Multi-vulva class B genes (MuvB) were first identified in fly (Beall et al., 2002; Korenjak et al., 2004). Together with the later purified complexes from worm, human and plant, they share a conserved protein core built by orthologues from the synMuv class B family (Fischer and Müller, 2017; Sadasivam and DeCaprio, 2013).

The human MuvB complex consists of five core proteins: LIN9, LIN54, LIN37, LIN52 and RBBP4. Depending on the cell cycle phase MuvB forms either a repressive complex named dimerization partner (DP), retinoblastoma-like (RB), E2F and MuvB (DREAM) or an activator complex called Myb-MuvB (MMB) (Fischer and Müller, 2017; Sadasivam and DeCaprio, 2013). When cells are in G0, MuvB interacts with p130, E2F4 and DP1/2, which leads to the formation of the DREAM-complex. In S and G2 phase, MuvB binds to B-MYB and later FOXM1 transcription factors resulting in the formation of the MMB-complexes (Fischer and Müller, 2017; Sadasivam and DeCaprio, 2013).

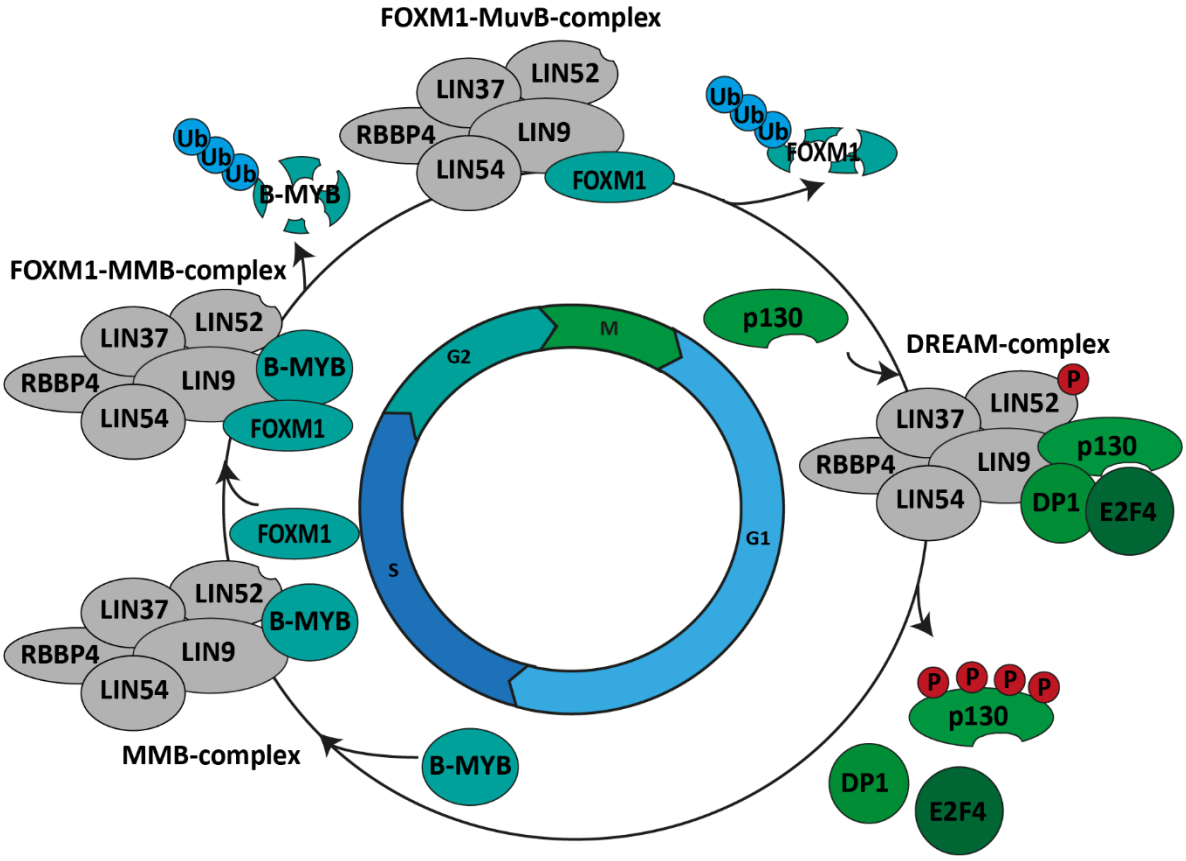

Figure 2: Regulation of gene expression by DREAM and MMB complexes during the cell cycle
MuvB core consists of five subunits: LIN9, LIN54, LIN37, LIN52 and RBBP4 (grey). Together with p130, E2F4 and DP1/2 (green), MuvB proteins form the DREAM complex, which represses E2F target gene expression and mediates a quiescent state. Upon hyperphosphorylation, p130 dissociates from the DREAM-complex and B-MYB binds to the MuvB core to form the Myb-MuvB (MMB) complex in the early S phase. At the beginning of G2, FOXM1 interacts with the MMB complex to activate G2/M target gene expression. In mid G2, B-MYB dissociates from the MuvB core and is degraded, whereas FOXM1 stays with the MuvB core until mitosis to activate some late mitotic genes. Later on, FOXM1 also dissociates from the MuvB core and is degraded by the APC/C. Adapted from (Fischer and Müller, 2017; Sadasivam and DeCaprio, 2013).

Several studies show that LIN9 is the central component of the MuvB core. The C-terminus of LIN9 binds to LIN52 (Schmit et al., 2007), whereas the N-terminus binds to the pocket protein p130 in the repressor DREAM complex (Sandoval et al., 2009). In parallel, LIN9 also binds to B-MYB and FOXM1 transcription factors in the activator complexes (Esterlechner et al., 2013; Guiley et al., 2018; Osterloh et al., 2007; Schmit et al., 2007; Wiseman et al., 2015). Moreover, LIN9 is known to bind to RBBP4 (Schmit et al., 2007). Knockdown of LIN9 decreases levels of

G2/M genes and results in defects during mitosis (Esterlechner et al., 2013; Knight et al., 2009; Osterloh et al., 2007; Reichert et al., 2010; Schmit et al., 2007). Two subunits of the MuvB core, LIN54 and RBBP4, can bind to chromatin and DNA. RBBP4 interacts with chromatin via the tails of the histones H3 and H4 and recruits repressor complexes, such as histone deacetylases (HDAC) (Murzina et al., 2008; Nicolas et al., 2001; Saade et al., 2009; Zhang et al., 2013). In contrast, the DNA binding domain of LIN54 directly interacts with the DNA and binds a consensus DNA sequence (TTYRAA), the so-called cell cycle gene homology region (CHR). CHR elements are enriched in the promoter of G2/M genes bound by MuvB (Marceau et al., 2016; Matsuo et al., 2012; Müller and Engeland, 2010; Müller et al., 2014; Schmit et al., 2009). Deletion of LIN54 or mutation within the DNA-binding domain result in reduced levels of mitotic genes and in defects during mitosis indicating that DNA binding is essential for the correct function of MuvB-complexes (Matsuo et al., 2012; Schmit et al., 2009). Recent data from knockout mouse embryonic fibroblasts indicate that LIN37 is dispensable for the activating functions of MuvB-complexes, but essential for the repressive functions of MuvB (Mages et al., 2017; Uxa et al., 2019). In contrast, LIN52 is involved in repressive as well as activator functions of MuvB-complexes. Together with LIN9, LIN52 binds to the B-MYB transcription factor (Guiley et al., 2018).

1.2.2 The repressive DREAM complex mediates a quiescent state

After a cell completes mitosis, it decides to undergo the next round of cell division or to stay in a quiescent state in G0. Therefore, the expression of cell cycle genes needs to be silenced. In addition to the E2F-RB pathway, formation of the DREAM complex by interaction of the MuvB core with p130/p107, E2F4, and DP1/2 suppresses G1/S as well as G2/M gene expression in early G1 phase. After cellular division, two major steps are known to be essential for DREAM assembly. First, p130/p107 are dephosphorylated by PP2A phosphatase to allow re-binding to the MuvB core (Naetar et al., 2014). Second, the MuvB core subunit LIN52 is phosphorylated at serine 28 by the dual specificity tyrosine-phosphorylation-regulated kinase 1A (DYRK1A) (Litovchick et al., 2011). DYRK1A kinase activity is activated by phosphorylation of the Hippo signaling kinase LATS1/2 (Tschöp et al., 2011). Phosphorylation of LIN52 at serine 28 allows p130 to bind to the MuvB core. Structural analysis of the DREAM-complex revealed that LIN52 binds through a LxSxExL sequence together with the phosphate group of serine 28 to the LxCxE cleft of the pocket proteins (Guiley et al., 2015) (**Figure 2**). When E2F4 and DP1/2 bind to complete DREAM function, the complex suppresses expression of G1/S and G2/M genes by binding to two distinct DNA sequences in the promoter of those genes (Litovchick et al., 2007; Schmit et al., 2007). Chromatin binding studies showed that the DREAM subunits E2F4 and DP1/2 bind to so-called cell cycle dependent elements (CDEs). Moreover, the MuvB core subunit LIN54 directly interacts with CHR elements (Müller and Engeland, 2010; Müller et al., 2012). Thus, the DREAM complex suppresses cell cycle dependent gene expression in early G1 phase and in quiescent cells (Litovchick et al., 2007; Schmit et al., 2007). Since, p130 is the most abundant pocket protein compared to the expression of RB and p107 in resting cells in G0, the repression of cell cycle gene expression by DREAM is most relevant in G0 (Litovchick et al., 2007; Schmit et al., 2007).

1.2.3 Activator MMB-complexes regulate G2/M gene expression

As mentioned before mitogenic stimulation exits cells from the quiescent G0 state and allows cells to re-enter the cell cycle. This process requires perturbation of the DREAM complex to activate expression of the early G1/S cell cycle genes. As noted above, cyclin D/CDK4/6 complexes hyperphosphorylate pocket proteins, which leads to the disassembly of DREAM and RB-E2F-complexes. In a first wave of gene expression, activator E2Fs regulate G1/S associated genes. Among these genes is the transcription factor B-MYB, which contains a DNA-binding domain (DBD). B-MYB binds to the MuvB core by interacting with LIN52 and LIN9 (Guiley et al., 2018; Osterloh et al., 2007). Structural analysis revealed that the C-terminal part of B-MYB (amino acids M677 and Q674) is necessary for binding to the MuvB core (Guiley et al., 2018). When B-MYB is bound to the MuvB core, it forms the Myb-MuvB (MMB) complex (**Figure 2**). Later during the cell cycle FOXM1 is recruited to MMB, which is required for activation of late mitotic genes (Sadasivam et al., 2012). At the mid of G2, B-MYB is degraded by a Cullin1 (Cul1) dependent E3 ubiquitin ligase (Charrasse et al., 2000). FOXM1 remains in the complex and is degraded by the anaphase promoting complex or cyclosome (APC/C) at the end of mitosis (Park et al., 2008) (**Figure 2**). The interplay between B-MYB, FOXM1 and MuvB core is responsible for the activation of a second wave of cell cycle genes during G2/M phase. DNA binding motifs of B-MYB, FOXM1 and MuvB are found in several promoters of G2/M genes (Sadasivam et al., 2012). Correct functions of the individual MMB components (B-MYB, FOXM1 and MuvB) are critical for gene activation. For example, loss of B-MYB results in decreased levels of G2/M genes and leads to defects during mitosis (Mannefeld et al., 2009; Sadasivam et al., 2012). Similar phenotypes are observed in cells lacking FOXM1 or MuvB (Laoukili et al., 2005; Matsuo et al., 2012; Osterloh et al., 2007; Reichert et al., 2010; Schmit et al., 2009).

1.2.4 The physiological role of MMB

Given the role in regulation of G2/M genes, several studies addressed the question which phenotype is associated with the loss of MMB. In summary, deletion of different MMB components results in a similar cellular phenotype indicating errors during mitosis. For example, RNAi mediated knockdown of B-MYB, FOXM1, LIN9 or LIN54 showed a downregulation of *CCNB1* gene expression (Sadasivam et al., 2012).
However, there are some unique characteristics according to the loss of distinct MMB components. For example, conditional knockout of LIN37 leads to upregulation of late cell cycle genes in quiescent NIH3T3 cells. In the absence of LIN37, the remaining components of the DREAM complex still assemble at the promoters of cell cycle genes indicating that LIN37 is specifically required for repressive functions of the DREAM complex (Mages et al., 2017).
Among the MYB family members, B-MYB is the only protein expressed in embryonic stem cells. Knockout of B-MYB in mice results in early embryonic lethality between E4.5 and E6.5. In B-MYB knockout mice the inner cell mass fails to grow (Tanaka et al., 1999). Like the B-MYB phenotype, knockout of LIN9 in mice causes early embryonic lethality. After loss of LIN9 in

mouse embryonic fibroblasts, growth deficits due to defects during mitosis are observed (Reichert et al., 2010). Loss of LIN9 in adult mice results in rapid death within seven days due to proliferation defects in the intestine epithelium (Reichert et al., 2010). Compared to knockout of LIN9 and B-MYB, FOXM1 knockout mice survive longer during development, but die during E13.5 and E18.5 (Krupczak-Hollis et al., 2004). FOXM1 knockout mice show polyploidization of hepatocytes due to mitotic defects (Krupczak-Hollis et al., 2004). Interestingly, knockout of FOXM1 in early heart progenitor cells causes a severe phenotype (Bolte et al., 2012). Taken together these studies implicate that MMB is critical for early embryogenesis as well as organ formation and tissue homeostasis.

1.3 The Hippo pathway

1.3.1 The Hippo signaling cascade

The Hippo signaling pathway was first identified in *drosophila melanogaster*. Genetic screens identified several serine/threonine kinases, which restrict tissue growth. Mutations of the *salvador* (*sav*), *warts* (*wts*), *Hippo* (*hpo*) and *mats* (*mats*) kinases result in tissue overgrowth caused by increased cell proliferation and reduced apoptosis (Harvey et al., 2003; Justice et al., 1995; Lai et al., 2005; Tapon et al., 2002). Genetic interactions between the kinases suggested a common mechanism of regulation. The Hippo pathway is named after the *hpo* kinase (Ma et al., 2019; Meng et al., 2016).

In mammals, homologues of the drosophila kinases were identified: mammalian Ste20-like kinase 1/2 (MST1/2, homolog of *hpo*), Salvador Family WW-Domain Containing Protein 1 (SAV1, homolog of *sav*), Mps One Binder Kinase Activator 1 (MOB1, homolog of *mats*) and Large Tumor Suppressor 1/2 (LATS1/2, homolog of *wts*). Together these kinases form the core signaling cascade of the Hippo pathway. When Hippo signaling is active (ON), MST1/2 kinases form a complex with SAV1, which subsequently phosphorylates SAV1, MOB1 and LATS1/2. Phosphorylation of LATS1/2 by MST1/2 results in autophosphorylation of the kinases (Chan et al., 2005). Active LATS1/2 kinases in turn phosphorylate Yes associated protein (YAP) and WW-domain containing transcription regulator protein 1 (TAZ). Specifically, YAP is phosphorylated by LATS1/2 at five HxRxxS motifs, which leads to the cytoplasmic retention of YAP by binding to the 14-3-3 protein. Phosphorylation of YAP at serine 127 has been identified to be most relevant for YAP inhibition by LATS1/2, since a mutation into alanine reduces the mobility shift of YAP after LATS1/2 phosphorylation (Zhao et al., 2007). In parallel, TAZ is phosphorylated by LATS1/2 at four HxRxxS motifs, which results in cytoplasmic retention mediated by the 14-3-3 protein (Lei et al., 2008). Subsequent phosphorylation of YAP/TAZ at a phosphodegron by casein kinase 1 δ/ε (CK1) results in the proteasomal degradation of YAP/TAZ mediated by the $SCF^{\beta\text{-}TRCP}$ E3 ubiquitin ligase (Liu et al., 2010; Zhao et al., 2010). Thereby, phosphorylation by LATS1/2 at serine residue 381 of YAP and serine 311 of TAZ primes YAP/TAZ for degradation (Liu et al., 2010; Zhao et al., 2010). When Hippo signaling is inactive (OFF), YAP/TAZ are unphosphorylated and translocate to the nucleus. YAP/TAZ are transcriptional coactivators that do not contain a DNA-binding domain. They activate transcription of genes important for

cell proliferation and survival by binding to Transcriptional Enhanced Associate Domain family member 1-4 (TEAD1-4). Therefore, interaction of YAP/TAZ with TEAD1-4 mediates the main transcriptional output of the Hippo pathway (Zhao et al., 2008). In contrast, when Hippo signaling is active it prevents YAP/TAZ from translocation to the nucleus. In the absence of YAP/TAZ, vestigial-like protein 4 (VGLL4) binds to TEADs and represses target gene expression (Jiao et al., 2017; Zhang et al., 2014a) (**Figure 3**).

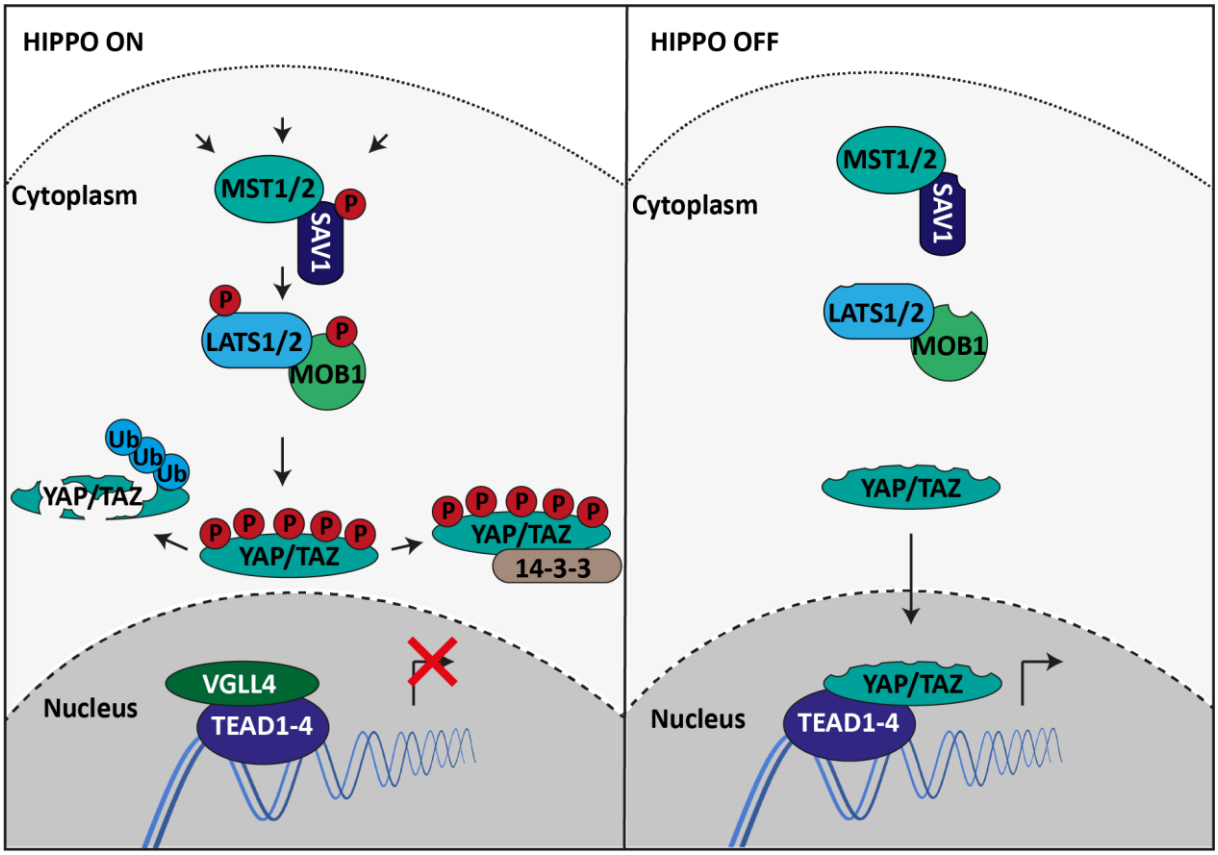

Figure 3: The Hippo signaling cascade
When Hippo signaling is active (**left side**), MST1/2 together with SAV1 phosphorylate the LATS1/2-MOB1 complex. Activated LATS1/2 in turn phosphorylates the transcriptional coactivators YAP/TAZ. Phosphorylated YAP/TAZ are inactivated by either cytoplasmic retention through the 14-3-3 protein or by proteasomal degradation. When Hippo signaling is off (**right side**), unphosphorylated YAP/TAZ translocate to the nucleus, bind to TEAD1-4 transcription factor, and in turn activate genes responsible for cell proliferation and survival. In the absence of YAP/TAZ, VGLL4 interacts with TEAD proteins to repress target gene expression. Adapted from (Meng et al., 2016).

1.3.2 Regulation of Hippo signaling

Beside the aforementioned core kinase cascade, several other upstream signals control the activity of YAP/TAZ. An overview of well-known examples that regulate YAP/TAZ activity upstream from the core cassette are described below. In general, activation of the core kinases inhibits YAP/TAZ, while sequestration of the core kinases prevents repression of YAP/TAZ.

Other kinases than MST1/2 are also able to phosphorylate and activate LATS1/2. Genetic deletions of the MAP4K kinase family, TAO kinases and MST1/2 suggest that all kinases individually contribute to the activation of LATS1/2 (Meng et al., 2015; Plouffe et al., 2016). In a similar manner neurofibromatosis type II (NF2) acts on the activation of LATS1/2 by recruiting LATS1/2 to the plasma membrane where it is activated by MST1/2 (Yin et al., 2013). Moreover, NF2 interacts with Kidney and Brain Expressed Protein (KIBRA), which promotes MST1/2 activity (Genevet et al., 2010; Yu et al., 2010). Several biomechanical forces, such as cell-cell contact, cell tension, cell stretching and interaction with the extra cellular matrix (ECM) are known to regulate the activity of the Hippo cascade (Ma et al., 2019). For instance, there are two mechanisms how the Hippo regulating protein angiomotin (AMOT) controls cascade activity in response to cell density. First, binding of AMOT to the NF2 complex increases the activity of LATS1/2 in confluent cells (Dai et al., 2015). Second, AMOT directly interacts with YAP in a phosphorylation independent manner and therefore inhibits YAP activity by sequestering YAP from the nucleus (Li et al., 2015). AMOT as well as LATS1/2 and NF2 are target genes of YAP/TAZ, which creates a negative feedback loop that reduces cell proliferation in dense cell cultures (Dai et al., 2015; Moroishi et al., 2015). Beside biomechanical forces, soluble factors such as growth factors or hormones, influence the activity of YAP/TAZ. For example, the lysophosphatidic acid (LPA), a diffusible hormone, blocks LATS activity by binding to G protein-coupled receptors (GPCRs) $G\alpha_{12/13}$ and thereby activating YAP/TAZ (Yu et al., 2012). In some cancer subtypes GPCRs are mutated resulting in activation of YAP/TAZ. For example, in uveal melanoma a mutation in the $G\alpha_{q/11}$ drives YAP-dependent tumor growth (Li et al., 2019; Yu et al., 2014).

1.3.3 YAP/TAZ, the transcriptional coactivators of the Hippo pathway

1.3.3.1 Protein domain structure of YAP and TAZ

The transcriptional coactivators of the Hippo pathway, YAP and TAZ, possess a modular protein structure. In the N-terminus of both proteins a TEAD-binding domain (TBD) is located followed by WW-domain, a SH3-binding domain, and a transactivation domain. Overall YAP and TAZ share a very similar domain architecture. There are two major isoforms of YAP containing either one WW-domain (YAP1) or a tandem WW-domain (YAP2). Similar to YAP1, TAZ contains only one WW-domain, but lacks the SH3-binding domain (**Figure 4**).

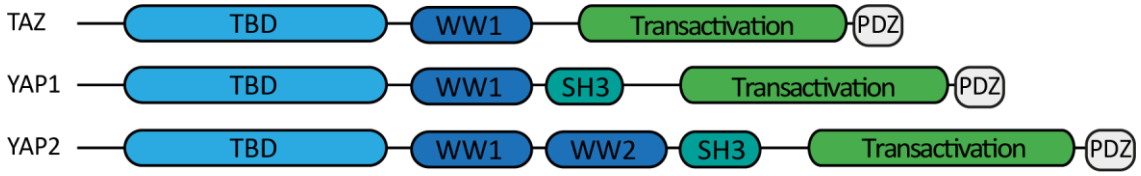

Figure 4: Domain architectures of YAP and TAZ
YAP and TAZ show a very similar protein domain structure including a TEAD-binding domain (**TBD**) followed by a WW-domain (tandem **WW**-domain, YAP2), **SH3**-binding domain (only YAP1 and YAP2), a transactivation domain and a **PDZ**-binding motif.

1.3.3.2 Interaction with TEAD

Structural analysis of the YAP-TEAD interaction revealed that the N-terminal TBD domain in YAP interacts with the C-terminal YAP-binding domain (YBD) in TEAD. YAP-TEAD interaction is mediated by binding at three different interfaces. The YBD of TEAD forms a globulin-like structure, which is in contact with two helices (α_1 and α_2) of YAP that are connected by a hydrophobic loop containing a PxxϕP motif (Chen et al., 2010; Li et al., 2010). YAP and TEAD form heterodimers. Crystal structures of TAZ-TEAD interaction showed that the main difference to YAP-TEAD is the interaction at the hydrophobic loop. In contrast to YAP, TAZ is lacking the PxxϕP motif within the loop suggesting a heterotetrametric structure, in which two TAZ molecules bind to two TEAD molecules (Kaan et al., 2017).

1.3.3.3 The WW-domain of YAP

The WW-domain is a small protein domain containing approximately 35 to 40 amino acids. The core of the protein domain is built by an anti-parallel triple-stranded β-sheet. Two tryptophan residues that are 20-21 amino acids apart from each other form a binding pocket for proline-rich interaction partners (Chen and Sudol, 1995; Sudol et al., 2012). Two known motifs can interact with the WW-domain. The first class of proteins contains a proline-tyrosine motif (PPXY) (Sudol et al., 2012). The second class of proteins contains serine-proline clusters (SP), which are phosphorylated by serine/threonine kinases. Moreover, phosphorylation of SP-sites can either result in enhanced binding to the WW-domain (activating SP-site) or in decreased binding to the WW-domain (repressive SP-site) (Aragón et al., 2012). Structural analysis of the YAP WW-domains revealed that the first WW-domain can bind both types of ligands, whereas the second WW-domain preferentially binds PPXY containing ligands (Aragón et al., 2012). Interestingly, beside YAP and TAZ also other proteins of the Hippo pathway contain WW-domains, such as SAV1 and KIBRA. Furthermore, several Hippo regulating proteins contain PPXY motifs, such as AMOTL, LATS1/2, TP53BP2 and PTPN14. Recent studies implicate that there is a high specificity between WW-domains and their corresponding PPXY-binding partners (Lin et al., 2019; Vargas et al., 2019). Different modes in binding of tandem WW-domains to PPXY-ligands is one reason for WW specificity (Lin et al., 2019). Moreover, the amino acid sequence of WW-domains contributes to its specificity, since the Hippo WW-domain containing proteins share a unique amino acid sequence (Vargas et al., 2019).

1.3.3.4 Transcriptional regulation mediated by YAP and TAZ

The transcriptional output of the Hippo signaling is mainly regulated by YAP/TAZ. Several studies show that YAP/TAZ control a transcriptional program involved in proliferation including genes necessary for G1/S phase transition, DNA replication and mitosis (Cordenonsi et al., 2011; Liu et al., 2016; Zanconato et al., 2015). As mentioned before, YAP/TAZ bind to TEAD transcription factors. Genome wide binding studies revealed that YAP/TAZ bind to the

DNA via TEAD at the so-called MCAT consensus motif (5'-g/a CATTCCa/t-3') (Farrance et al., 1992; Galli et al., 2015; Stein et al., 2015; Zanconato et al., 2015). Several examples are known were YAP cooperates with other transcription factors to regulate gene expression. YAP together with the activator protein 1 (AP-1) promotes expression of genes required for S phase and mitosis and drives tumor growth in mice (Koo et al., 2020; Liu et al., 2016; Zanconato et al., 2015). In parallel, YAP and the transcription factor Myc coordinatively regulate expression of genes required for cell proliferation (Croci et al., 2017). Although there is a number of genes where YAP is directly located at the promoter, the majority of YAP binding sites is located at distal enhancers or super-enhancers (Galli et al., 2015; Pattschull et al., 2019; Stein et al., 2015; Zanconato et al., 2015). Enhancer or super-enhancers are distinct genomic regions that contain sequence-specific binding sites for transcription factors. Enhancers can be located at any region within the genome and regulate the transcription of a target gene by cohesion mediated loop formation with the promoter (Shlyueva et al., 2014). Super-enhancers contain clusters of enhancers with a high number of transcription factors bound to the genome (Jia et al., 2019). The current model how YAP regulates gene expression from distal enhancers suggests that there are promoter-enhancer loops bridging YAP-bound enhancers with the promoters of the associated genes (Galli et al., 2015; Zanconato et al., 2015). The fact that YAP interacts with a subunit of the mediator complex supports this model (Galli et al., 2015). In line with this, YAP and the MMB-complex interact via the B-MYB subunit at promoter-enhancer loops of late cell cycle genes (Pattschull et al., 2019).

1.3.4 The physiological role of the Hippo pathway

The Hippo pathway was identified in *drosophila melanogaster* by genetic screens to regulate cell proliferation and organ size. Mutations in Hippo core kinases result in overgrowth of organs such as eyes, wings and limbs (Bunney et al., 2017; Halder and Johnson, 2011; Pan, 2010). Similar to the phenotype in *drosophila*, mutations in Hippo signaling as well as transgenic overexpression of YAP/TAZ in mice lead to overgrowth in several organs, such as liver, heart, intestine and skin (Camargo et al., 2007; Dong et al., 2007; Heallen et al., 2011; Lee et al., 2008). For instance, liver-specific transgenic expression of YAP in mice results in a reversible overgrowth (Camargo et al., 2007; Dong et al., 2007). Moreover, knockout of SAV1, MST1/2 and NF2 in the liver of mice also results in liver enlargement (Yin et al., 2013; Zhang et al., 2010; Zhou et al., 2009). Complete loss of YAP in mice leads to embryonic lethality and YAP knockout mice die at E8.5 (Morin-Kensicki et al., 2006). In contrast, TAZ knockout mice are viable suggesting different roles of YAP and TAZ in development (Tian et al., 2007). Elevated expression and activity of YAP/TAZ are involved in many types of cancer including liver, breast, lung and colon (Bunney et al., 2017). Long-term activation of YAP drives cell transformation and tumor growth (Dong et al., 2007). Conversely, the Hippo pathway acts as a tumor suppressor and perturbation of the pathway is linked to cancer. For instance, mutations in the *Nf2* gene causes neurofibromatosis type II lesions (Xiao et al., 2003). Due to its pro-proliferative function YAP/TAZ are also involved in tissue homeostasis, wound healing, and regenerative repair of organs. One well-characterized example is the heart. Heart-specific knockout of SAV1, MST1/2 and LATS2 in mice results in enlarged hearts due to increased

cardiomyocyte proliferation (Heallen et al., 2011). In contrast, heart-specific deletion of YAP leads to thinning of the myocardium and results in prenatal lethality (von Gise et al., 2012; Xin et al., 2011). Moreover, expression of activated YAP phenocopied Hippo-deficient hearts suggesting that YAP activation is the driving mechanism in Hippo mutant hearts (von Gise et al., 2012; Monroe et al., 2019; Xin et al., 2013). Taken together, the Hippo pathway with its coactivators YAP/TAZ plays a major role in organ growth, tissue homeostasis, tumorigenesis, and heart development.

1.4 Murine heart development

1.4.1 Overview of the heart development in mice

1.4.1.1 Embryonal heart development

Murine heart development starts between E6.5 and E7.5. Genetic tracing studies identified two lineages of progenitor cells marked by the expression of transcription factor mesoderm posterior protein 1 (MESP1) (Lescroart et al., 2014). MESP1 positive cells migrate laterally towards the head folds to form the first heart field (FHF) in the cardiac crescent and the second heart field (SHF) in the pharyngeal mesoderm (Meilhac and Buckingham, 2018). Thereby, canonical WNT-β-catenin signaling is critical to direct progenitor cells towards the cardiac crescent (Yue et al., 2008). Cardiac progenitor cells express cardiac transcription factors, such as GATA binding protein 4 (GATA4), T-box transcription factor 5 (TBX5), NK2 Homeobox 5 (NKX2.5), Myocyte specific enhancer factor 2C (MEF2C) and Insulin gene enhancer protein 1 (ISL1). Together with the inhibitory WNT signaling expression of these transcription factors is critical to maintain the cardiac fate of the progenitor cells at the cardiac crescent (Wang et al., 2018). Cardiac progenitor cells of the FHF later form the future left ventricle (Zaffran et al., 2004). In contrast, progenitor cells of the SHF build the future right ventricle and interventricular myocardium (Ai et al., 2007; Zaffran et al., 2004). At E8.5 the heart tube starts to form, which is composed of an inner layer of endocardium and an outer layer of myocardium. As the heart tube elongates, chamber formation begins and the future right atrium (RA), right ventricle (RV), left atrium (LA), left ventricle (LV) and the outflow tract become visible at E10.5. The interventricular septum (IVS) separates the cardiac chambers. Between E14.5 and E16.5 outflow tract of the heart and blood circulation complete heart development. During embryogenesis, hyperplastic growth through proliferation of cardiac progenitor cells and division of preexisting cardiomyocytes drives heart growth (Wang et al., 2018) (**Figure 5**).

1.4.1.2 Postnatal heart development

In contrast to embryogenesis where heart growth is primarily achieved by hyperplasia, the proliferative capacity of cardiomyocytes decreases shortly after birth. Thus, heart growth switches from hyperplastic to hypertrophic growth (Foglia and Poss, 2016; Uygur and Lee, 2016). In mice, within the first two weeks after birth cardiomyocytes undergo DNA replication and karyokinesis without cytokinesis leading to binucleated cardiomyocytes (Li et al., 1996; Soonpaa et al., 1996). Consequently, cardiomyocytes increase in size (**Figure 5**). This process starts around day four after birth and results in 85% to 90% of binucleated cells by day 21 (Soonpaa et al., 1996). Comparable studies in humans show that only 25% of cardiomyocytes are binucleated (Olivetti et al., 1996). Adult human cardiomyocytes renew the pool of existing cardiomyocytes with a replacement rate between 1% and 0.45% per year confirming that there is a remaining low-rate of cardiomyocyte turnover (Bergmann et al., 2009, 2015; Mollova et al., 2013). Genetic fate mapping studies in mice support the idea that division of preexisting cardiomyocytes contributes to renewal of the cardiomyocyte pool (Ali et al., 2014; Senyo et al., 2013). Taken together, murine cardiomyocytes exit the cell cycle soon after birth and become binucleated, but a low fraction of adult cardiomyocytes can renew the pool of existing cardiomyocytes.

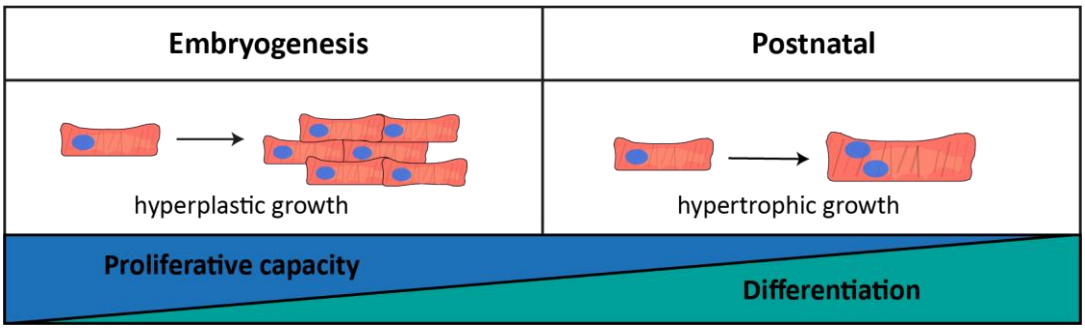

Figure 5: Cardiomyocyte growth during heart development
During embryogenesis, cardiomyocytes rapidly divide by hyperplastic growth. Shortly after birth, cardiomyocytes start to differentiate and the proliferative capacity starts to decrease. Postnatal cardiomyocytes become binucleated by uncoupling DNA synthesis and karyokinesis from cytokinesis. Cardiomyocytes increase in size and the heart grows by hypertrophy. Adapted from (Ahuja et al., 2007; Tzahor and Poss, 2017; Wang et al., 2018).

1.4.2 Cell cycle regulation in cardiomyocytes

Cell cycle exit of murine cardiomyocytes after birth is accompanied by decreased expression of G1/S and G2/M cyclins and their associated CDKs (Flink et al., 1998). In contrast, the expression of cell cycle inhibitors, such as p21, p27 and p57 is increased in cardiomyocytes after birth (Poolman and Brooks, 1998). Manipulation of the cell cycle regulatory network impacts cardiomyocyte proliferation. For example, heart-specific deletion of RB or p130 results in re-entry of adult cardiomyocytes to the cell cycle (Sdek et al., 2011). Moreover, overexpression of D-type cyclins in cardiomyocytes leads to increased levels of DNA synthesis (Pasumarthi et al., 2005). In contrast, premature binucleation of cardiomyocytes is observed

after knockout of the MMB target gene GAS2L3 in mice, causing a severe cardiac phenotype (Stopp et al., 2017). Beside the classical cell cycle regulators, other pathways, such as neuregulin 1/ErbB2, Meis1 transcription factor and the Hippo pathway regulate proliferation of cardiomyocytes (D'Uva et al., 2015; Heallen et al., 2011; Mahmoud et al., 2013). As mentioned before, deletion of Hippo pathway components (SAV1, LATS2 and MST1/2) in cardiac progenitor cells increases proliferation in embryonal cardiomyocytes, whereas deletion of Hippo coactivator YAP1 results in embryonic lethality accompanied by decreased cardiomyocyte proliferation (von Gise et al., 2012; Heallen et al., 2011; Xin et al., 2011). However, cardiac-specific expression of an activated YAP mutant leads to enhanced proliferation of cardiomyocytes and partially reprograms adult cardiomyocytes to a more fetal like state (von Gise et al., 2012; Monroe et al., 2019; Xin et al., 2013). Moreover, the function of TEAD is essential for correct formation of the heart (Chen et al., 1994; Tsika et al., 2010). Mechanisms that reverse the shift from hyperplastic to hypertrophic growth in the heart are potential targets for heart regeneration since those factors can stimulate cardiomyocyte proliferation.

1.4.3 Heart regeneration

Approximately 38 million patients worldwide suffer from heart failure due to injuries, such as infarction (Tzahor and Poss, 2017). Therefore, regeneration of the heart is studied in several injury models, such as apical resection, myocardial infarction (MI), cryoinjury or genetic ablation of cardiomyocytes. Hearts from distinctive species show a different regenerative potential (Uygur and Lee, 2016). For example, teleost fish can effectively regenerate parts of their heart. After apical resection of adult zebrafish hearts, lost cardiomyocyte tissue is replaced within 60 days post resection resulting in hearts with normal contractile functions (Poss et al., 2002). In contrast, the regenerative capacity of the heart in rodents rapidly decreases after birth and postnatal or adult hearts show only limited regeneration after injury (Tzahor and Poss, 2017; Uygur and Lee, 2016). For instance, the embryonic murine heart can compensate and restore up to 50% of the lost material by proliferation of cardiomyocytes (Drenckhahn et al., 2008). Similarly, 1-day-old neonatal mice regenerate their hearts after surgical resection with minimal scar formation (Porrello et al., 2011). However, in mice this ability is already lost 7 days after birth (Porrello et al., 2011). Likewise, adult murine hearts insufficiently replace the lost tissue after MI, which leads to extensive scar formation limiting the function of the heart. Immune response from infiltrating macrophages or monocytes, neoangiogenesis, deposition of extracellular matrix and regenerative responses due to nerves influence proliferation of cardiomyocytes after an injury (Tzahor and Poss, 2017; Uygur and Lee, 2016). It is well established that the Hippo pathway influences heart regeneration. For instance, in adult murine hearts genetic deletion of Hippo pathway components, such as SAV1 and LATS1/2, promotes efficient repair after surgical resection or MI due to elevated cardiomyocyte proliferation (Heallen et al., 2013). Moreover, in neonate murine hearts YAP is essential for recovery after MI and expression of an constitutively active YAP mutant improves function of adult hearts after MI (Del Re et al., 2013; Xin et al., 2013). Mice that suffer from an infarction, benefit from treatment with an adeno-associated virus (AAV) expressing an

activated YAP mutant or from the deletion of SAV1 (Leach et al., 2017; Lin et al., 2014). In conclusion, the Hippo pathway with its transcriptional coactivator YAP could serve as a potential therapeutic target in cardiac regeneration.

1.5 Aim of the project

Shifting cardiomyocyte proliferation from hypertrophy to hyperplasia is one key aspect in cardiac regeneration. Several genetic studies have shown that the Hippo pathway with its transcriptional coactivator YAP is essential to drive cardiomyocyte proliferation during heart development (von Gise et al., 2012; Heallen et al., 2011; Xin et al., 2011). However, the exact mechanism how YAP activates proliferation of cardiomyocytes is not known. Recently, the MMB-complex and its transcription factor B-MYB were identified to physically interact with YAP. Moreover, a YAP-driven mechanism was reported that explains activation of G2/M target genes (Pattschull et al., 2019). This raises the question whether YAP and the MMB complex cooperate to orchestrate YAP driven proliferation of cardiomyocytes.

The first major aim of this thesis was to explore the crosstalk between the Hippo pathway and the MMB complex in cardiomyocytes *in vivo* and to test whether the linkage between Hippo signaling and MMB pathway is of biological relevance for the proliferation of cardiomyocytes. The second aim of this thesis was to characterize the YAP-B-MYB interaction using biochemical approaches, such as co-immunoprecipitation, GST-pulldown, and µSPOT-based peptide arrays to develop a peptide based competitive inhibitor. The final part of the thesis analyzes the biological phenotype caused by the inhibition of the YAP-B-MYB interaction.

2. Material and Methods

2.1 Material

2.1.1 Chemical stocks and reagents

Unless otherwise noted, all chemicals were purchased from AppliChem, Roth, Invitrogen, Merck or Sigma Aldrich.

Table 1: Chemical stocks and reagents

Chemical	Stock concentration
4-Hydroxytamoxifen (4-OHT)	25 µM in ethanol
Acetic acid	N/A
Agarose	N/A
Ammonium persulfate (APS)	10% (w/v) in ddH_2O
AMPure XP beads (Beckman Coulter)	N/A
β-Glycerol phosphate	1 M in ddH_2O
Bovine serum albumin (BSA)	N/A
Bromophenol blue	N/A
Coomassie brilliant blue R250	N/A
Diethyl pyrocarbonate (DEPC)	ready-to-use
Dimethyl sulfoxide (DMSO)	ready-to-use
Dithiothreitol (DTT)	1 M in ddH_2O
dNTPs (dATP, dTTP, dCTP, dGTP)	2 mM in ddH_2O
Eosin Y solution 0.5% (w/v) in water (Roth)	0.1% (v/v) in ddH_2O, add 2 drops acetic acid
Ethanol	N/A
Ethidium bromide	10 mg/ml
Glycine	1 M in ddH_2O
Glycogen (Roche)	20 mg/ml
Hemalum solution acid according to Meyer (Roth)	ready-to-use
Hoechst 33258	10 mg/ml in ddH_2O
ImmuMount (ThermoFisher)	ready-to-use
Isopropanol	N/A
Isopropyl-β-D-1-thiogalactopyranoside (IPTG)	1 M in ddH_2O
Luminol	250 mM in DMSO
NP-40	ready-to-use
p-Coumaric acid	90 mM in DMSO
peqGOLD TriFast (Trizol; Peqlab)	ready-to-use
Phenylmethylsulphonyl fluoride (PMSF)	100 mM in isopropanol
Ponceau S solution	0.1% Ponceau S in 5% acetic acid

Chemical	Stock concentration
Paraffine	ready-to-use
Protease inhibitor cocktail (PIC; Sigma)	ready-to-use
Proteinase K	10 mg/ml in 50 mM Tris pH 8.0, 1 mM $CaCl_2$
ProtoGel (30% Acrylamide; National Diagnostics)	ready-to-use
Random Primer (Roche)	500 µg/ml in ddH_2O
RNase A	10 mg/ml in 10 mM Tris pH 7.4, 150 mM NaCl
Sodium dodecyl sulfate (SDS)	20% in ddH_2O
SYBER Green (Sigma)	1:10 in DMSO
TEMED	ready-to-use
Triton-X-100	ready-to-use
Tween-20	ready-to-use
Xylene	ready-to-use

2.1.2 Enzymes

Table 2: Enzymes

Enzymes	Company
His-Taq16 DNA Polymerase (5 U/µl)	provided by AG Prof. Dr. Gessler
Phusion High-Fidelity DNA Polymerase (2 U/µl)	Thermo Fisher
Restriction endonucleases (10 U/µl)	Thermo Fisher & New England Biolabs
RevertAid Reverse Transcriptase (200 U/µl)	Thermo Fisher
RiboLock RNase Inhibitor (40 U/µl)	Thermo Fisher
T4 DNA Ligase (400 U/µl)	New England Biolabs

2.1.3 Antibiotics

Table 3: Antibiotics used for selection of bacterial and mammalian cells

Antibiotic	Stock concentration	Final concentration	Application
Ampicillin	100 mg/ml	100 µg/ml	Selection of DH5α bacteria
Ampicillin	100 mg/ml	50 µg/ml	Selection of BL21 (DE3) bacteria
Chloramphenicol	40 mg/ml	35 µg/ml	Selection of BL21 (DE3) bacteria
Doxycycline	1 mg/ml	0.5 µg/ml	Induction of protein expression in HeLa cells
Kanamycin	50 mg/ml	50 µg/ml	Selection of DH5α bacteria
Neomycin	200 mg/ml	1 mg/ml	Selection of HeLa cells

2.1.4 Kits

Table 4: Kits used for molecular and cellular biology

Kit	Company
(DNF-471) Fragment Analyzer RNA Kit	Agilent
(DNF-474) HS NGS Fragment Kit (1-6000bp)	Agilent
Duolink® In Situ Detection Reagents Red (DUO92008)	Sigma Aldrich
GeneJET Gel Extraction Kit	Thermo Fisher
NEBNext® Multiplex Oligos for Illumina® (Dual Index Primers Set 1)	New England Biolabs
NEBNext® Poly(A) mRNA Magnetic Isolation Module	New England Biolabs
NEBNext® Ultra™ II DNA Library Prep Kit for Illumina®	New England Biolabs
NEBNext® Ultra™ II RNA Library Prep Kit for Illumina®	New England Biolabs
Pierce™ Primary Cardiomyocyte Isolation Kit	Thermo Fisher
PureLink™ HiPure Plasmid Midiprep or Maxiprep Kit	Thermo Fisher
QIAquick PCR Purification Kit	Qiagen
Quant-iT™ Picogreen™ dsDNA Assay Kit	Thermo Fisher
RNase-Free DNase Set	Qiagen
RNeasy Mini Kit	Qiagen

2.1.5 Beads and Protein/DNA markers

Table 5: Beads

Beads	Company
Glutathione sepharose 4B	GE healthcare
Ni-NTA Agarose	Thermo Fisher
Pierce™ Anti-HA Magnetic Beads	Thermo Fisher
Protein G Dynabeads	Thermo Fisher

Table 6: Protein and DNA marker

Marker	Company
100 bp DNA ladder	Thermo Fisher
GeneRuler 1 kb DNA ladder	Thermo Fisher
PageRuler™ Prestained Protein Ladder, 10 to 180 kDa	Thermo Fisher

2.1.6 Buffers and Solutions

2.1.6.1 General buffers

Table 7: General buffers

Buffer	Ingredients
Phosphate buffered saline (1xPBS)	137 mM NaCl 2.68 mM KCl 10.14 mM Na_2HPO_4 1.75 mM KH_2PO_4 pH is adjusted to 7.4 with HCl
Tris buffered saline (1xTBS)	50 mM Tris/HCl, pH 7.5 150 mM NaCl pH is adjusted to 7.4 with NaOH
Tris buffer (1xTE)	10 mM Tris/HCl, pH 8.0 1 mM EDTA (pH 8.0)

2.1.6.2 Cell biological buffers

Table 8: Cell biological buffers

Buffer	Ingredients
10% Acetic acid	10% (v/v) Acetic acid in ddH_2O
2.5 M $CaCl_2$	2.5 M $CaCl_2$, sterile filtered
0.1% Crystal Violet	0.1% (w/v) Crystal Violet in 20% (v/v) Ethanol
2xHBS (pH 7.05)	280 mM NaCl 50 mM HEPES 1.5 mM Na_2HPO_4 pH is adjusted to 7.05 with NaOH sterile filtered
PBS-T (for Immunofluorescence)	0.1% Triton X-100 in PBS
PSP (for Immunofluorescence)	3% (w/v) Paraformaldehyde, 2% (w/v) Sucrose solved at 60°C in PBS

2.1.6.3 Molecular biological buffers

Table 9: Molecular biological buffers

Buffer	Ingredients
5x DNA loading buffer	15% (v/v) Ficoll 0.05% (w/v) Bromophenol blue 0.05% (w/v) Xylene cyanol 0.05 M EDTA in 1xTAE buffer
10x ReproFast buffer	100 mM $(NH_4)_2SO_4$ 100 mM KCl 20 mM $MgSO_4$ 200 mM Tris/HCl, pH 8.8 1% (w/v) BSA 1% (v/v) Triton X-100
Base buffer	25 mM NaOH 0.2 mM EDTA adjust to pH 12 with NaOH
DEPC-ddH_2O	0.1% (v/v) DEPC is stirred overnight and then autoclaved
LB Medium	40 g/l LB powder, autoclaved
Neutralization buffer	40 mM Tris/HCl, pH 5.0
S1 buffer	25 mM Tris/HCl, pH 8.0 10 mM EDTA
S2 buffer	200 mM NaOH 1% SDS
S3 buffer	0.6 M KCH_3COO 20% (v/v) acetic acid
1xTAE buffer	40 mM Tris/HCl 5 mM acetic acid 10 mM EDTA (pH 8.0)

2.1.6.4 Buffers for protein biochemistry

Table 10: Buffers for whole cell lysates

Buffers	Ingredients
Bradford solution	50 mg Comassie Brilliant Blue G250 23.75 ml Ethanol 50 ml 85% (v/v) phosphoric acid ad 500 ml ddH_2O / filter twice
TNN lysis buffer	50 mM Tris/HCl, pH 7.5 120 mM NaCl 5 mM EDTA, pH 8.0 0.5% NP-40 10 mM $Na_4P_2O_7$ 2 mM Na_3VO_4 100 mM NaF adjust pH with HCl to 7.5 Protease Inhibitor Cocktail (PIC) 1:1000 (freshly added) 1 mM DTT (freshly added) 1 mM PMSF (freshly added) 10 mM β-glycerophosphate (freshly added)

Table 11: Buffers for SDS-PAGE and immunoblotting

Buffer	Ingredients
Blocking solution	5% (w/v) milk in TBS-T
Blotting buffer	125 mM Tris 75 mM Glycine 15% (v/v) Methanol
Chemiluminescence solution	100 mM Tris/HCl, pH 8.5 1.25 mM luminol 0.2 mM coumaric acid 0.009% (v/v) H_2O_2
3x ESB buffer	300 mM Tris/HCl, pH 6.8 15 mM EDTA 150 mM DTT 12% (w/v) SDS 0.03% (w/v) Bromophenol blue
Ponceau S solution	0.1% (w/v) Ponceau S 5% (v/v) acetic acid
1x SDS running buffer	192 mM Glycine 25 mM Tris 3.5 mM SDS
Separation gel buffer	1.5 M Tris/HCl, pH 8.8
Stacking gel buffer	0.5 M Tris/HCl, pH 6.8
TBS-T	50 mM Tris/HCl, pH 7.4 150 mM NaCl 0.1% (v/v) Tween-20

Table 12: Buffers for recombinant protein purification

Buffer	Ingredients
GST lysis buffer	50 mM Tris/HCl, pH 7.5 150 mM NaCl 1 mM PMSF (freshly added) 1:1000 Protease Inhibitor Cocktail (freshly added) 1 mM DTT
GST washing buffer	50 mM Tris/HCl, pH 7.5 150 mM NaCl 1% NP-40 1 mM PMSF (freshly added) 1:1000 Protease Inhibitor Cocktail (freshly added) 1 mM DTT
GST elution buffer	50 mM Tris/HCl, pH 8.5 150 mM NaCl 1% NP-40 20mM Glutathione (reduced)
His-tag lysis buffer	20 mM Na_2HPO_4 300 mM NaCl 10 mM Imidazole ($C_3H_4N_2$) Adjust pH to 7.4 with HCl
His-tag washing buffer	20 mM Na_2HPO_4 300 mM NaCl 25 mM Imidazole ($C_3H_4N_2$) Adjust pH to 7.4 with HCl
His-tag elution buffer	20 mM Na_2HPO_4 300 mM NaCl 250 mM Imidazole ($C_3H_4N_2$) Adjust pH to 7.4 with HCl
Pulldown buffer	50 mM Tris/HCl, pH 7.4 150 mM NaCl 0.1% NP-40 Adjust pH to 7.4 with HCl
Coomassie Blue Staining Solution	1 g Coomassie Brilliant Blue R 250 25% (v/v) Isopropanol 10% Acetic acid
Coomassie Destaining Solution	25% (v/v) Isopropanol 10% Acetic acid

Table 13: Buffers for Proximity ligation assay (PLA)

Buffer	Ingredients
Wash buffer A	10 mM Tris/HCl, pH 7.4 150 mM NaCl 0.05% Tween
Wash buffer B	200 mM Tris/HCl, pH 7.5 100 mM NaCl

Table 14: Buffers for Chromatin immunoprecipitation (ChIP)

Buffer	Ingredients
ChIP Lysis Buffer	50 mM Tris/HCl, pH 8.0 10 mM EDTA, pH 8.0 1% SDS
ChIP Dilution Buffer	50 mM Tris/HCl, pH 8.0 167 mM NaCl 1.1% Triton X-100 0.11% Sodium deoxycholate
RIPA-150	50 mM Tris/HCl pH 8.0 150 mM NaCl 1 mM EDTA, pH 8.0 0.1% SDS 1% Triton X-100 0.1% Sodium deoxycholate
RIPA-500	50 mM Tris/HCl pH 8.0 0.5 M NaCl 1 mM EDTA, pH 8.0 0.1% SDS 1% Triton X-100 0.1% Sodium deoxycholate
RIPA-LiCl	50 mM Tris/HCl pH 8.0 0.5 M $LiCl_2$ 1 mM EDTA, pH 8.0 1% NP-40 0.7% Sodium deoxycholate
Direct Elution Buffer	10 mM Tris/HCl, pH 8.0 300 mM NaCl 5 mM EDTA, pH 8.0 0.5% SDS

2.1.6.5 Buffers for histology

Table 15: Buffers used for histology and immunohistology

Buffer	Ingredients
Bouin's Fixative	10 % (v/v) Formaldehyde 5 % (v/v) Glacial acetic acid 85 % (v/v) picric acid (saturated)
Blocking solution (for immunohistology)	5 % BSA in PBS-T
PBS-T (for immunohistology)	PBS with 0.1 % Tween-20

2.1.7 Antibodies

Table 16: Primary antibodies

Name	Origin	Internal number	Company	Application	Catalog number
B-MYB (LX015.1)	mouse	#149	gift from Watson lab (Hybridoma)	WB 1:5	Tavner et al., 2007
LIN9	rabbit	#292	Bethyl laboratories	ChIP-Seq	A300-BL2981
α-Tubulin (B-5-1-2)	mouse	#295	Santa Cruz	IF 1:150 WB 1:1000	sc-23948
β-Actin (C4)	mouse	#196	Santa Cruz	WB 1:5000	sc-47778
YAP (63.7)	mouse	#297	Santa Cruz	WB 1:1000	sc-10199
YAP1	rabbit	#302	Novus Biological	ChIP-Seq	NB110-58358
flag (M2)	mouse	#93	Sigma Aldrich	WB 1:5000 IP 1:500	F-3165
HA.11	mouse	#92	Covance	WB 1:1000	MMA-101P
Phospho Histone H3 (Ser10)	rabbit	#290	Santa Cruz	IF 1:200 IHC 1:100	sc-8656
Troponin T (CT3)	mouse	#277	Developmental studies hybridoma bank (DSHB)	IHC 1:50	N/A
Ki-67 (SP6)	rabbit	#185	Thermo Fisher Scientific	IHC 1:200 IF 1:200	RM-9106
IgG	rabbit	#104	Sigma Aldrich	N/A	I5006
Phospho YAP (Ser127)	rabbit	#317	Cell Signaling Technologies	WB 1:1000	4911

Table 17: Secondary antibodies

Name	Origin	Company	Application	Catalog number
anti-mouse IgG (H+L) HRP conjugated	goat	GE healthcare	WB 1:5000	NXA931
anti-mouse IgG (H+L) Alexa Fluor 488	goat	Thermo Fisher	IF 1:500	A11029
anti-mouse IgG2a (H+L) Alexa Fluor 488	goat	Thermo Fisher	IF 1:500	A21131
anti-mouse IgG (H+L) Alexa Fluor 594	goat	Thermo Fisher	IF 1:500	A11032
anti-mouse IgG (H+L) Alexa Fluor 700	goat	Thermo Fisher	IF 1:500	A21036
anti-rabbit IgG (H+L) Alexa 488	goat	Thermo Fisher	IF 1:500	A21206
anti-rabbit IgG (H+L) Alexa 594	goat	Thermo Fisher	IF 1:500	A11037

Name	Origin	Company	Application	Catalog number
HRP Protein A	N/A	BD Biosciences	WB 1:5000	610438
Duolink In Situ PLA Probe Anti-Mouse PLUS	donkey	Sigma Aldrich	PLA 1:5	DUO92001
Duolink In Situ PLA Probe Anti-Rabbit MINUS	donkey	Sigma Aldrich	PLA 1:5	DUO92005

2.1.8 Plasmids

Table 18: Plasmids used for transient transfection

Name	Internal number	Description
pBABE_H2B-GFP	746	GFP expression vector, which was used to determine transfection efficiency
pCMV-2xflag-YAP	1504	transient expression of flag-tagged full-length YAP, which was used in Co-immunoprecipitation studies
pcDNA4/TO-HA-B-MYB	1159	transient expression of HA-tagged full-length B-MYB, which was used in Co-immunoprecipitation studies or pulldown experiments
pcDNA4/TO	587	empty vector control, which was used to transfect equal amounts of plasmid DNA
pCDNA3-flag	374	empty vector control, which was used to transfect equal amounts of plasmid DNA
pCMV-2xflag-YAP_2-499	1605	transient expression of flag-tagged YAP (aa 2-499; TEAD-Transactivation domain), which was used in Co-immunoprecipitation studies
pCMV-2xflag-YAP_2-287	1606	transient expression of flag-tagged YAP (aa 2-287; TEAD-SH3 dom ain), which was used in Co-immunoprecipitation studies
pCMV-2xflag-YAP_2-263	1607	transient expression of flag-tagged YAP (aa 2-263; TEAD-WW1/2 domain), which was used in Co-immunoprecipitation studies
pCMV-2xflag-YAP_2-154	1608	transient expression of flag-tagged YAP (aa 2-154; TEAD domain), which was used in Co-immunoprecipitation studies
pCMV-2xflag-YAP_155-504	1609	transient expression of flag-tagged YAP (aa 155-504; WW1/2-PDZ domain), which was used in Co-immunoprecipitation studies
pCMV-2xflag-YAP_264-504	1610	transient expression of flag-tagged YAP (aa 264-504; SH3-PDZ domain), which was used in Co-immunoprecipitation studies

Name	Internal number	Description
pCMV-2xflag-YAP_288-504	1611	transient expression of flag-tagged YAP (aa 288-504; Transactivation-PDZ domain), which was used in Co-immunoprecipitation studies
pCMV-2xflag-YAPΔWW1/2	1624	transient expression of flag-tagged YAP ΔWW1/2 (lacking aa 154-263), which was used in Co-immunoprecipitation studies
pcDNA4/TO-HA-B-MYB_2-410	1646	transient expression of HA-tagged B-MYB (aa 2-410), which was used in pulldown experiments
pcDNA4/TO-HA-B-MYB_411-700	1645	transient expression of HA-tagged B-MYB (aa 411-700), which was used in pulldown experiments
pcDNA4/TO-HA-B-MYB_2-331	1665	transient expression of HA-tagged B-MYB (aa 2-331), which was used in pulldown experiments
pcDNA4/TO-HA-B-MYB_80-331	1666	transient expression of HA-tagged B-MYB (aa 80-331), which was used in pulldown experiments
pcDNA4/TO-HA-B-MYB_80-410	1667	transient expression of HA-tagged B-MYB (aa 80-410), which was used in pulldown experiments
pcDNA4/TO-HA-B-MYB_2-241	1668	transient expression of HA-tagged B-MYB (aa 2-241), which was used in pulldown experiments
pcDNA4/TO-HA-B-MYB_2-79	1669	transient expression of HA-tagged B-MYB (aa 2-79), which was used in pulldown experiments
pcDNA4/TO-HA-B-MYB_241-410	1670	transient expression of HA-tagged B-MYB (aa 241-410), which was used in pulldown experiments
pcDNA4/TO-HA-B-MYBΔPPXY	1615	transient expression of HA-tagged B-MYBΔPPXY (lacking aa 198-201), which was used in Co-immunoprecipitation studies and pulldown experiments
pcDNA4/TO-MY-COMP	1705	transient expression of HA-tagged NLS-B-MYB (aa 2-241)
pcDNA4/TO-MY-COMP_2-79	1706	transient expression of HA-tagged NLS-B-MYB (aa 2-79)
pcDNA4/TO-MY-COMP_ΔPPXY	1707	transient expression of HA-tagged NLS-B-MYBΔPPXY (aa 2-241; lacking aa 198-201)
pcDNA4/TO-MY-COMP_ΔDNA	1708	transient expression of HA-tagged NLS-B-MYBΔDNA (aa 2-241; N174A)

Table 19: Plasmids used for expression of recombinant proteins in bacteria

Name	Internal number	Description
pGEX-4T2-YAP_2-263	1619	expression of recombinant GST-tagged YAP (aa 2-263, TEAD-WW1/2 domain), which was used in pulldown experiments
pGEX-4T2-YAP_155-263	1620	expression of recombinant GST-tagged YAP (aa 155-263, WW1/2 domain), which was used in pulldown experiments
pGEX-4T2-YAP_168-204	1658	expression of recombinant GST-tagged YAP (aa 168-204, WW1 domain), which was used in pulldown experiments
pGEX-4T2-YAP_231-263	1659	expression of recombinant GST-tagged YAP (aa 231-263, WW2 domain), which was used in pulldown experiments
pRSETA-6xHis-B-MYB_2-241	1674	expression of recombinant 6xHis-tagged B-MYB (aa 2-241), which was used in pulldown experiments
pRSETA-6xHis-B-MYB_2-241ΔPPXY	1701	expression of recombinant 6xHis-tagged B-MYB (aa 2-241Δ198-201, ΔPPXY), which was used in pulldown experiments

Table 20: Plasmids used for lentiviral and adenoviral infection of mammalian cells

Name	Internal number	Description
pAd/CMV/LacZ	1577	β-Galactosidase expressing adenoviral construct for infection of murine cardiomyocytes
pAd/CMV/2xflag-YAPS127A	1598	flag-tagged YAPS127A expressing adenoviral construct for infection of murine cardiomyocytes
pAd/CMV/2xflag-YAPS94A/S127A	1648	flag-tagged YAPS94A/S127A expressing adenoviral construct for infection of murine cardiomyocytes
pAd/CMV/2xflag-YAPS127A/ΔWW1/2	1649	flag-tagged YAPS127A/ΔWW1/2 expressing adenoviral construct for infection of murine cardiomyocytes
pAd/CMV/GFP	1732	GFP expressing adenoviral construct for infection of murine cardiomyocytes
pAd/CMV/MY-COMP-T2A-GFP	1733	adenoviral construct, which expresses MY-COMP (HA-NLS-B-MYB_2-241) fused to GFP by a 2A self-cleavage peptide
pAd/CMV/MY-COMP_2-79-T2A-GFP	1734	adenoviral construct, which expresses MY-COMP_2-79 (HA-NLS-B-MYB_2-79) fused to GFP by a 2A self-cleavage peptide

Name	Internal number	Description
pAd/CMV/MY-COMP_ΔDNA-T2A-GFP	1735	adenoviral construct, which expresses MY-COMP_ΔDNA (HA-NLS-B-MYB_2-241; N174A) fused to GFP by a 2A self-cleavage peptide
pAd/CMV/MY-COMP_ΔPPXY-T2A-GFP	1736	adenoviral construct, which expresses MY-COMP_ΔPPXY (HA-NLS-B-MYB_2-241; lacking aa 198-201) fused to GFP by a 2A self-cleavage peptide
pInd20/GFP	1727	lentiviral construct, which doxycycline inducible expresses GFP
pInd20/MY-COMP-T2A-GFP	1728	lentiviral construct with doxycycline inducible expression of MY-COMP (HA-NLS-B-MYB_2-241) fused to GFP by a 2A self-cleavage peptide
pInd20/MY-COMP_2-79-T2A-GFP	1729	lentiviral construct with doxycycline inducible expression of MY-COMP_2-79 (HA-NLS-B-MYB_2-79) fused to GFP by a 2A self-cleavage peptide
pInd20/MY-COMP_ΔDNA-T2A-GFP	1730	lentiviral construct with doxycycline inducible expression of MY-COMP_ΔDNA (HA-NLS-B-MYB_2-241; N174A) fused to GFP by a 2A self-cleavage peptide
pInd20/MY-COMP_ΔPPXY-T2A-GFP	1731	lentiviral construct with doxycycline inducible expression of MY-COMP_ΔPPXY (HA-NLS-B-MYB_2-241; lacking aa 198-201) fused to GFP by a 2A self-cleavage peptide

2.1.9 Primers

All Primers for genotyping, qPCR or cloning were purchased from Eurofins Genomics. Unless otherwise stated primers were dissolved in 1xTE to a stock concentration of 100 µM and stored at -20°C. For final use, primers were diluted in ddH_2O to a final concentration of 10 µM.

Table 21: Primers used for genotyping of mice and murine cells

Gene	Internal number	Sequence (5' to 3')	Directionality
CreER	1113	TGGGATACAGAAGACCAATGC	forward
	1114	ACGGACAGAAGCATTTTCCA	forward
	1115	GTCTCTGCCTCCAGAGTGCT	reverse
Lin9	722	GCAAAAGCTGCAAGTCCTCT	reverse
	893	CCTGGCTGCCTAGCATTTAC	forward
α-MHC-Cre	1114	ACGGACAGAAGCATTTTCCA	forward
	1936	ATGACAGACAGATCCCTCCTATCTCC	reverse

Gene	Internal number	Sequence (5' to 3')	Directionality
Nkx2.5-Cre	2157	TTACGGCGCTAAGGATGACT	forward
	2158	GAGCCTGGTAGGGAAAGAGC	forward
	2159	GTGTGGAATCCGTCGAAAGT	reverse
Sav1	2358	AGGGGATTCTGACATTTCAGTCAGTT	forward
	2359	AGTCACATGCTGACCACAAGCAGAA	forward
	2360	TGCCATTAAGTGTAATCACTGG	reverse

Table 22: Primers used for quantitative real-time PCR (qPCR) of murine cDNA

Gene	Internal number	Sequence (5' to 3')	Directionality
Amotl2	2917	TGACTGTACCTAAGCCGAACC	forward
	2918	GCACACACCTGCCTAGACAAT	reverse
Anln	2314	ACAATCCAAGGACAAACTTGC	forward
	2315	GCGTTCCAGGAAAGGCTTA	reverse
Aspm	1026	GATGGAGGCCGAGAGAGG	forward
	1027	CAGCTTCCACTTTGGATAAGTATTTC	reverse
Birc5	961	CCCGATGACAACCCGATA	forward
	962	CATCTGCTTCTTGACAGTGAGG	reverse
Cenpf	1038	AGCAAGTCAAGCATTTGCAC	forward
	1039	GCTGCTTCACTGATGTGACC	reverse
Ctgf	2165	TGACCTGGAGGAAAACATTAAGA	forward
	2166	AGCCCTGTATGTCTTCACACTG	reverse
Cyr61	2395	CAGCACCTCGAGAGAAGGAC	forward
	2396	GGTCAAGTGGAGAAGGGTGA	reverse
Ect2	2195	TGCTCTGCTTCACTGGATTC	forward
	2196	ATGATGAACCAACGTCACCA	reverse
Gas2l3	1034	GCAGCCTGCAATCCAAGT	forward
	1035	AGGGGACACCTGGGACTTA	reverse
Lin9	785	TTGGGACTCACACCATTCCT	forward
	786	GAAGGCCGCTGTTTTTGTC	reverse
Mybl2	820	TTAAATGGACCCACGAGGAG	forward
	821	TTCCAGTCTTGCTGTCCAAA	reverse
Nusap1	1030	TCTAAACTTGGGAACAATAAAAGGA	forward
	1031	TGGATTCCATTTTCTTAAAACGA	reverse
Sav1	25152	TCACACCAATAAAAGGGCTCA	forward
	2516	CTTTCAGTTTGTTGTGGCTGA	reverse
Top2a	2193	CAAAAGAGTCATCCCCCAAG	forward
	2194	GGGGTACCCTCAACGTTTTC	reverse

2.1.10 siRNAs

All siRNAs were purchased from Eurofins Genomics or Dharmacon and were dissolved in the appropriate buffer to a stock concentration of 75 µM.

Table 23: siRNAs

Target Gene	Name	Species	Internal number	Sequence (5' to 3')	Supplier
Lin9	siLIN9	mouse	S3	GCUACUUACAGAGUAACUUUC	Dharmacon
Mybl2	siB-MYB	mouse	S1	GCCCAUAAAGUCCUGGGUAAC	Dharmacon
Non-targeting control	sicontrl	N/A	S52	UGGUUUACAUGUCGACUAA	Dharmacon
Wwtr1	siTAZ	mouse	S69	CAGCCGAAUCUCGCAAUGA	Eurofins
Yap	siYAP#1	mouse	S67	CGGUUGAAACAACAGGAAU	Eurofins
Yap	siYAP#2	mouse	S68	GAAGCGCUGAGUUCCGAAA	Eurofins

2.1.11 Cell lines

Table 24: Mammalian cell lines

Cell line	Organism	Description	Reference
HEK293A	*homo sapiens*	human embryonic kidney cell line with constitutive expression of the SV40 large T antigen; cell line was used for production of adenovirus	Invitrogen™: R70507
HEK293T	*homo sapiens*	human embryonic kidney cell line with constitutive expression of the SV40 large T antigen; cell line was used for production of lentivirus	SBI Cat.-no.: LV900A-1
HeLa	*homo sapiens*	epithelial cervical adenocarcinoma cell line; used for protein-protein interaction studies	ATCC® CCL-2™
C2C12	*mus musculus*	murine myoblast cell line, which can be differentiate to myotubes; cell line was used for adenoviral infection	ATCC® CRL-1772™

2.1.12 Cell culture reagents, media, and transfection reagents

Table 25: Cell culture reagents and additives

Reagents	Supplier
1xPBS	see 2.1.6.1, Table 7
4-Hydroxytamoxifen (4-OHT)	Sigma Aldrich
DMEM (1x) + GlutaMAX	Thermo Fisher
Doxycycline	Sigma Aldrich
Fetal bovine serum (FBS) FBS	Thermo Fisher
Horse Serum (Donor herd)	Thermo Fisher/Sigma Aldrich
Penicillin-Streptomycin (10,000 U/ml)	Thermo Fisher
Typsin-EDTA (0.05%), phenol red	Thermo Fisher

Table 26: Composition of cell culture medium

Media	Cell line	Composition
DMEM complete	HEK293A, HEK293T, HeLa, C2C12	DMEM 10% FBS 1% pen-strep
DMEM differentiation	Myogenic differentiation of C2C12	DMEM 2% horse serum 1% pen-strep
Cardiomyocyte complete media	Primary mouse cardiomyocytes	DMEM for Primary Cell Isolation 5% horse serum 1% pen-strep 1:1000 cardiomyocyte growth supplement
Cardiomyocyte infection media	Primary mouse cardiomyocytes	DMEM for Primary Cell Isolation 1% pen-strep

Table 27: Transfections reagents

Transfection reagents	Supplier
2.5 M $CaCl_2$	see **2.1.6.2**, **Table 8**
2x HBS pH 7.05	see **2.1.6.2**, **Table 8**
Lipofectamine 3000	Thermo Fisher
RNAiMax	Thermo Fisher
Opti-MEM (1x) + GlutaMAX	Thermo Fisher

2.1.13 Bacterial strains

Table 28: Bacterial strains

Bacterial strain	Genotype	Application
BL21 (DE3)	F-ompT hsdSB (rB-, mB-) galdcmrne131 (DE3)	expression of recombinant protein
ccdB survival	F-mcrA Δ(mrr-hsdRMS-mcrBC) Φ80lacZΔM15 ΔlacX74 recA1 araΔ139 Δ(ara-leu)7697 galU galK rpsL (StrR) endA1 nupG fhuA::IS2	cloning of pENTR3C entry vector
DH5α	F– Φ80lacZΔM15 Δ(lacZYA-argF) U169 recA1 endA1 hsdR17 (rK–, mK+) phoA supE44 λ– thi-1 gyrA96 relA1	cloning

2.1.14 Mouse strains

Table 29: Mouse strains

Mouse strain	Genotype	Description	Reference
$Sav1^{fl}$	$Sav1^{tm1.1Dupa}$/J	Exon 3 of the Sav1 gene is flanked by loxP sites	(Cai et al., 2010)
$mTmG^{fl}$	B6.129(Cg)-$Gt(ROSA)26Sor^{tm4(ACTB-tdTomato,-EGFP)Luo}$/J	Tomato allele next to a stop cassette is flanked by loxP sites, which are followed by the EGFP allele	(Muzumdar et al., 2007)
$Lin9^{fl}$	N/A	Exon 7 of the Lin9 gene is flanked by loxP sites	(Reichert et al., 2010)
Nkx-Cre	N/A	Cre activation in cardiomyocyte progenitor cells	(Stanley et al., 2002)
α-MHC-Cre	N/A	Postnatal cardiomyocyte-specific Cre activation	(Agah et al., 1997)

2.1.15 Devices

Table 30: Devices

Devices	Supplier
Agarose gel electrophoresis system	Peqlab
Cytomics FC 500 flow cytometer	Beckman Coulter
Fragment Analyzer Automated CE System	Advanced Analytical
Leica DFC350 FX digital camera	Leica Microsystems
Leica DMI 6000B inverted microscope	Leica Microsystems
Microm EC 350 modular paraffin embedding center	Thermo Fisher
Min-PROTEAN 3 Cell System	Bio-Rad Laboratories

Devices	Supplier
Mini Trans-Blot Cell System	Bio-Rad Laboratories
Mx3000P qPCR System	Stratagene
NanoDrop 2000 spectral photometer	Peqlab
NextSeq 500	Illumina
Sonifier W-250 D	Branson
T1 Thermocycler	Biometra

2.1.16 Software

Table 31: Software used for data analysis

Software	Reference
Adobe Illustrator CC 2017	Adobe Inc.
Adobe Photoshop CC 2019	Adobe Inc.
BEDTools v2.26.0	(Quinlan and Hall, 2010)
Bowtie v2.3.2	(Langmead and Salzberg, 2012)
CXP Acquisition and Analysis (Cytomics FC 500)	Beckman Coulter
FASTQ Generation Software v1.0.0	Illumina
GSEA (Broad Institute)	(Subramanian et al., 2005)
Integrated Genome Browser	(Freese et al., 2016)
Leica Application Suite (LAS) 3.7	Leica Microsystems
MACS v.2.1.1	(Zhang et al., 2008)
Prism 5.0	GraphPad Software, Inc.
TopHat v2.1.0	(Kim et al., 2013)

2.2 Methods

2.2.1 Mammalian cell culture

2.2.1.1 Passaging and seeding cells

All cell lines used in this thesis were cultivated in a cell culture incubator at 37°C and 5% carbon dioxide (CO_2). All cells were maintained in GIBCO® Dulbecco's Modified Eagle Medium (DMEM) supplemented with 10% (v/v) fetal bovine serum (FBS) and 1% penicillin-streptomycin. Cells were passaged every three to four days. Therefore, old medium was aspirated, cells were washed once with 1xPBS and incubated for 5 minutes with 0.05% Trypsin/EDTA at 37°C. Detached cells were resuspended in medium and seeded onto a new cell culture dish according to demand.

2.2.1.2 Freezing cells

For freezing, cells were detached from cell culture plates as described in **2.2.1.1.** Cells were centrifuged for 5 minutes at 300xg. The resulting cell pellet was resuspended in freezing medium, containing 50% DMEM, 40% FBS and 10% Dimethyl sulfoxide (DMSO). Aliquots of 1 ml were transferred to precooled cryotubes and stored at -80°C. For long-term storage, cells were shifted to liquid nitrogen.

2.2.1.3 Thawing cells

Cryotubes were thawed in a 37°C water bath. Cells were immediately transferred to a 50 ml falcon containing 30 ml of prewarmed medium and cells were centrifuged for 5 minutes at 300xg. The supernatant was discarded, and the cell pellet was resuspended in fresh medium. Cells were then seeded onto a new cell culture plate.

2.2.1.4 Counting of cells

For counting cells, a Neubauer chamber was used. Cells were detached from cell culture plates as described in **2.2.1.1**. 10 µl of the cell suspension was loaded into the chamber. Cells were counted under a light microscope. The cell number per milliliter was calculated by multiplying the average number of four quadrants of the Neubauer chamber with the factor 10^4.

2.2.1.5 Myogenic differentiation of C2C12 cells

To differentiate C2C12 myoblast cells into myotubes, cells were seeded confluent to their desired cell culture dishes according to **Table 32**. The next day, the medium was changed to differentiation medium (DMEM supplemented with 2% (v/v) horse serum and 1% (v/v) penicillin-streptomycin). The cells were cultivated for 48 hours in differentiation medium and then used for further experiments.

Table 32: C2C12 seeding density in differentiated and undifferentiated cultures

cell culture dish	C2C12 cell number	
	undifferentiated C2C12 cells	differentiated C2C12 cells
6-well	10,000	130,000
6 cm	25,000	400,000
10 cm	75,000	1,200,000

2.2.1.6 Isolation of primary cardiomyocytes

Isolation of primary cardiomyocytes from murine hearts was performed with the Pierce™ Primary Cardiomyocyte Isolation Kit according to the manufacturer's instructions. In brief, dissected neonatal hearts were minced in a petri dish and transferred to a 1.5 ml Eppendorf tube. Dissected embryonal hearts were not minced, but directly transferred to a 1.5 ml Eppendorf tube. Then, hearts were washed two times with ice cold HBSS solution. According to **Table 33** the enzymes, thermolysin and papain, were incubated with the hearts for 35 minutes at 37°C. Afterwards 500 µl ice-cold HBSS solution was added to each heart. The mixture was not resuspended, but carefully vortexed. The heart-HBSS solution was centrifuged for 5 minutes at 3,000 rpm in a benchtop centrifuge and the supernatant was discarded. This washing step was repeated two times. After the last washing step, the supernatant was removed completely, and the digested heart tissue was resuspended in 500 µl cardiomyocyte complete medium (DMEM for Primary Cell Isolation, 5% (v/v) horse serum, 1% (v/v) penicillin-streptomycin and 1:1000 cardiomyocyte growth supplement) by pipetting up and down twenty times. The recovered cardiomyocytes were seeded on fibronectin covered 24-well plates (30 minutes incubated with 0.025 mg/ml fibronectin at 37°C). After 24 hours the medium was replaced by cardiomyocyte complete medium and the cells were then used for further experiments.

Table 33: Volume of thermolysin and papain used for digestion of hearts

Age	Volume of enzyme	
	Thermolysin	Papain
E14.5	2.5 µl	50 µl
P1-P4	5 µl	100 µl

2.2.1.7 Plasmid transfection using Lipofectamine 3000

For production of adenoviruses, $5*10^5$ HEK293A cell were seeded in a 6-well plate. 24 hours later, the medium was replaced with 1.5 ml DMEM medium without antibiotics. 1 µg of PacI digested adenoviral genome was transfected with Lipofectamine 3000 reagent according to **Table 34**. The diluted DNA mixture was added to the lipofectamine mixture and vortexed thoroughly. The solution was incubated for 15 minutes at RT and then added dropwise to the cells. The plate was mixed gently by rocking the plate back and forth. The next day, the cells were fed with fresh complete DMEM medium. Two days after transfection, the cells were trypsinized and transferred to a new 10 cm cell culture dish. The cells were further processed as described below in **2.2.1.10**.

Table 34: Transfection of adenoviral genome using Lipofectamine 3000 reagent

Mix	Reagents			
	Lipofectamine	**P3000**	**DNA**	**Opti-MEM**
Lipofectamine Mix	4 µl	-	-	247 µl
DNA/P3000 Mix	-	10 µl	1 µg	add 250 µl

2.2.1.8 Plasmid transfection using calcium phosphate

For calcium phosphate transfection cells were seeded on a 10 cm cell culture dish at a confluency of 75%. The next day, up to 18 µg of plasmid DNA was mixed with 50 µl 2.5 M $CaCl_2$ and filled up with autoclaved ddH_2O to a volume of 500 µl. In a 15 ml falcon 500 µl 2xHBS buffer was bubbled using a pipette aid and a Pasteur pipette. While continuously bubbling, the DNA-$CaCl_2$ mixture was added dropwise to the HBS solution. The mixture was incubated 20 minutes at room temperature and then added dropwise to the cells covering the whole cell culture dish evenly. After 24 hours incubation, cells were fed with fresh medium.

2.2.1.9 siRNA transfection using Lipofectamine RNAiMAX

As a control for the Proximity Ligation Assay (PLA), primary cardiomyocytes (E14.5) were treated with siRNAs against LIN9, B-MYB and YAP/TAZ. Therefore, Lipofectamine RNAiMAX reagent was used according to manufacturer's instructions. In brief, embryonal cardiomyocytes were cultivated with 25 µl complete cardiomyocyte medium for 24 hours on a 18-well ibidi slide. Lipofectamine mixture and siRNA mixture were prepared according to **Table 35**. After incubation for 5 minutes, the lipofectamine solution was added to the siRNA solution and thoroughly mixed by pipetting up and down. Subsequently, the Lipofectamine/siRNA mixture was incubated for 20 minutes at room temperature and finally 7.5 µl were added to the cells. The next day, cells were fed with fresh medium. Two days after transfection cardiomyocytes were fixed for PLA assay and further processed as described in **2.2.3.4**.

Table 35: siRNA transfection in embryonal cardiomyocytes using RNAiMAX reagent

Solution for 5 wells	siRNA	
	sicontrl/siLIN9/siB-MYB	**siYAP/TAZ**
Lipofectamine solution	21.825 µl Opti-MEM + 0.675 µl RNAiMAX	21.825 µl Opti-MEM + 0.675 µl RNAiMAX
siRNA solution	20.34 µl Opti-MEM + 2.16 µl siCtrl (S52)/ siLIN9 (S3) /siB-MYB (S1) (pre-diluted 1:10)	20.34 µl Opti-MEM + 2.16 µl siYap/Taz-Mix (S67-69) (each pre-diluted 1:30)

siRNAs were prediluted with nuclease free water as follows:

1 µl siCtrl (S52) / siLin9 (S3) / siB-MYB (S1) + 9 µl ddH_2O

1 µl siYAP#1 (S67) + 1 µl siYAP#2 (S68) + 1 µl siTAZ (S69) + 27 µl ddH_2O

2.2.1.10 Adenovirus production using HEK293A cells

For production of adenoviruses, the ViraPower™ Adenoviral Expression System was used according to the manufacturer's instructions. In brief, 7.5 µg of the adenoviral vector was digested for 90 minutes with PacI enzyme (NEB). As a control, 20% of the digested vector was loaded on a 1% agarose gel. Then, the digested vector was purified using phenol-chloroform extraction (**2.2.2.16**). 1 µg of the PacI digested adenoviral genome was transfected with lipofectamine 3000 as described in **2.2.1.7**. Two days after transfection the cells were trypsinized and placed into a 10 cm cell culture dish. The medium was replaced every three days, until visible regions of cytopathic effects (CPE) were observed. Usually this happened 7 to 10 days after transfection. When 80% of cells show CPEs, adenovirus containing cells were harvested by squirting cells off the culture dish. Subsequently, cells and medium were transferred to a 15 ml falcon. Crude viral lysates were produced by repeating a freeze-thaw cycle two times. In detail, adenovirus containing cells and medium was frozen for 30 minutes at -80°C. Then, the falcon was thawed for 15 minutes in a 37°C water bath. Finally, the viral lysates were centrifuged at 3,000 rpm for 15 minutes at room temperature. The virus containing supernatant was aliquoted in 1 ml and stored in cryotubes at -80°C. This stock of virus was named crude viral stock. To obtain highest viral titers and optimal transduction efficacy, it was necessary to amplify the crude viral stock. Therefore, $3.0*10^6$ HEK293A cells were plated onto 10 cm dishes. The next day, HEK293A cells were infected with 100 to 200 µl of the crude viral stock. Typically, two days after infection, 90% to 100% of cells show CPE. Subsequently, the adenovirus containing cells were harvested and processed as described before and this viral lysate was named amplified viral stock. Finally, the amplified viral stock was titrated (**2.2.1.11**) and used for further experiments.

2.2.1.11 Titration of adenoviral stocks

Adenoviral stocks were titrated using the Adeno-X™ RapidTiter Kit from Takara according to the manufacturer's instructions. In brief, $2.5*10^5$ HEK293A cells were cultivated for 24 hours on a 24-well plate. On the day of infection, the viral stock was diluted in series from 10^{-2} to 10^{-6} using medium as a diluent. The cells were infected in duplicates with 50 µl of each dilution. Two days after infection, cells were fixed with methanol. Positive infected cells were visualized by 3,3'-Diaminobenzidin (DAB) staining with an anti-Hexon antibody. Usually 10 to 20 positive infected cells per field was an optimal dilution for calculation of the infectious units. A minimum of 10 fields (pictures) from each well were imaged using a light microscope. The mean of positive infected cells was calculated out of these pictures. The infectious units (IFU) per milliliter were calculated as followed: [(infected cells/field)*(fields/well)]/[(volume virus (ml))*(dilution factor)]

2.2.1.12 Lentivirus production using HEK293T cells

For production of lentiviral vectors $5,0*10^6$ HEK293T cells were seeded onto a 10 cm cell culture dish. The next day, HEK293T cells were transfected using calcium phosphate (**2.2.1.8**) with the following amount of plasmid: 9 µg lentiviral vector, 6 µg psPAX2 and 3 µg pCMV-VSV-G. The next morning, old medium was discarded and cells were fed with 8 ml of fresh DMEM medium. 48 hours after transfection, the medium containing lentiviruses was collected in a 15 ml falcon and stored at 4°C. HEK293T cells were supplemented with 8 ml fresh DMEM medium for additional 20 hours. Then, virus supernatant was collected for a second time and mixed with the first supernatant. Finally, the lentiviral supernatant was filtered using a 0.45 µm pyrogen filter and either directly used for infection or aliquoted in 1 ml and stored at -80°C.

2.2.1.13 Generation of stable cell lines using lentiviruses

For generation of stable cell lines $1*10^5$ HeLa cells were seeded on a 6-well plate. The next day medium was aspirated, and cells were supplemented with a mixture of lentiviral supernatant and complete DMEM medium in a 1:1 ratio. Polybrene was added to a final concentration of 8 µg/ml and cells were incubated with the lentiviral supernatant overnight. Then, medium was changed and selection with the appropriate concentration of antibiotics was started (HeLa, neomycin: 1000 µg/ml). Cells were kept under selection for 7 to 10 days until control cells were dead. HeLa pInducer20 cell lines were further cultured with reduced levels of neomycin (200 µg/ml).

2.2.1.14 Flow cytometric analysis of cell cycle with propidium iodide DNA staining

For cell cycle analysis $8*10^4$ stable pInducer-MY-COMP HeLa cells were cultivated on 6 cm plates and treated with or without doxycycline. After four days cells were harvested by trypsinization and transferred into 15 ml polystyrol falcons. Cells were then pelleted by centrifugation at 1,200 rpm at 4°C and washed once with ice-cold 1xPBS. Afterwards cells were fixated with 1% paraformaldehyde in 1xPBS for 10 minutes on ice. Subsequently, cells were washed with 1xPBS and fixated by dropwise adding 80% ice-cold ethanol under constant vortexing. Afterwards, cells were washed with 1xPBS, centrifuged and the resulting cell pellet was resuspended in 500 µl ice-cold 38 mM natrium citrate buffer. RNA was digested by adding 25 µl RNAse A (10 mg/ml) followed by incubation for 30 minutes at 37°C. Finally, DNA was stained by adding 15 µl propidium iodide (1 mg/ml). Flow cytometric analysis was performed using an FC 500 flow cytometer from Beckman Coulter.

2.2.1.15 Cell proliferation assay using crystal violet staining

For measurement of cell growth stable pInducer20 HeLa cells were seeded at low cell density (185 cells/24-well) on a 24-well plate. Per condition cells were seeded in triplicates. Cells were cultivated for 10 days with constant replacement of medium supplemented with fresh antibiotics every second day (neomycin: 400 µg/ml). 6 hours after seeding, a reference time point was taken, and cells were fixated with 10% formalin for 10 minutes at room temperature. Every second day further time points were taken. Fixed cells were washed twice with tap water and were then air dried. Cells were stained with 0.1% crystal violet in 20% ethanol for 30 minutes rocking at room temperature. After washing the plates twice with tap water, cells were air dried and pictures were taken. For quantification, crystal violet was extracted by adding 500 µl 10% acetic acid for 30 minutes rocking at room temperature. Absorbance at 595 nm of 100 µl extracted dye was measured in a 96-well plate using the Multiscan Ascent microtiter plate reader (Labsystems). Samples with an absorbance above 1 were diluted 1:10. Per condition three replicates were measured and relative growth was calculated in relation to the reference time point.

2.2.1.16 Immunofluorescence

For immunofluorescence, cells were seeded in 6-wells or 24-wells on glass coverslips. The following steps were carried out at room temperature. On the day of harvest, cells were first washed once with 1xPBS and then fixed using PSP (3% paraformaldehyde/2%succrose in 1xPBS) for 10 minutes. Cells were then rinsed two times with 1xPBS and washed once with 1xPBS for 5 minutes. For permeabilization, cells were incubated in 1xPBS with 0.2% Triton-X100 for 5 minutes. Afterwards, cells were rinsed twice and washed once for 5 minutes in 1xPBS with 0.1% Triton-X100 (PBS-T). Unspecific binding sites were reduced by incubation with 3% BSA in PBS-T for 30 minutes. Then, cells were washed three times for three minutes

in PBS-T. The primary antibody was diluted at the desired ratio in blocking solution. Cells on coverslips were incubated with the antibody in a humidified chamber for 1 hour. Then, cells were washed three times for three minutes in PBS-T. The desired secondary antibody was diluted 1:500 in blocking solution. Cells on coverslips were incubated with the secondary antibody in a humidified chamber for 30 minutes. Next, cells were washed three times for three minutes with PBS-T. After the last washing step, coverslips were mounted on glass slides using ImmuMount, dried and finally sailed with nail polish. Coverslips were stored at 4°C in the dark until they were analyzed using an inverted Leica DMI 6000B microscope equipped with a Prior Lumen 200 fluorescence light source and a Leica DFC350 FX digital camera. Leica Application Suite (LAS) 3.7 was used for the analysis.

2.2.2 Molecular biology

2.2.2.1 Transformation of chemically competent bacteria with plasmid DNA

For transformation of plasmid DNA, chemically competent DH5α or BL21 (DE3) were thawed on ice and 1 µg (for standard cloning: 10 µl ligation reaction) plasmid DNA was added to 50 µl (re-transformation of plasmid DNA) or 100 µl (standard cloning or BL21 (DE3)) of bacteria. The reaction was mixed by flicking the tube. Then, the plasmid-bacteria mixture was incubated for 30 minutes on ice. Heat shock transformation of plasmid DNA was achieved by incubating the tubes for 60 seconds (DH5α) / 45 seconds (BL21 (DE3)) in a 42°C water bath. Directly after the heat shock, tubes were transferred onto ice and incubated for 15 seconds. Subsequently, 250 µl of pre-warmed LB-medium was added and bacteria were incubated at a 37°C thermocycler for 30-60 minutes shaking at 600 rpm. Afterwards, bacteria were pelleted using a bench top centrifuge for 1 minute at maximum speed and resuspended in 100 µl fresh LB-medium. Finally, bacteria were plated on LB agar with the appropriate antibiotics, dried and incubated overnight upside down at 37°C.

2.2.2.2 Mini preparation of plasmid DNA from bacteria

Mini preparation of plasmid DNA was used for standard cloning procedure to verify positive clones. After transformation (**2.2.2.1**) a single bacterial colony was inoculated in 3 ml LB-medium with the appropriate antibiotics at 37°C overnight shaking at 160 rpm. On the next day, 1.5 ml of the overnight culture was transferred to a 1.5 ml Eppendorf tube and centrifuged for 1 minute at 16,000 rpm using a bench top centrifuge. Next, the supernatant was aspirated and the bacterial pellet was resuspended in 250 µl S1 buffer supplemented with RNAse A. Bacterial lysis was achieved by adding 250 µl S2 buffer and inverting the tube several times. After 5 minutes incubation at room temperature, the lysis was stopped by adding 250 µl of S3 buffer and inverting the tube several times. The reaction was cleared by centrifugation for 15 minutes at 14,000 rpm and 4°C. The supernatant containing the plasmid DNA was transferred to a new tube. To precipitate the plasmid DNA, isopropanol was added in a 1:1

ratio and the reaction was mixed by vortexing. Subsequently, plasmid DNA was pelleted by centrifugation for 15 minutes at 14,000 rpm and 4°C. The resulting pellet was washed once with 70% ethanol and air dried for approximately 5 minutes. Finally, the plasmid DNA was resuspended in 50 µl TE buffer and used for analytical restriction digestion.

2.2.2.3 Midi and Maxi preparation of plasmid DNA from bacteria

For Midi and Maxi preparation of plasmid DNA, the PureLink™ HiPure Plasmid Midi/MaxiPrep Kit (Thermo Fisher) was used according to the manufacturer's instructions. Therefore, a single bacterial colony was inoculated in 3 ml LB-medium with appropriate antibiotics for 6-8 hours at 37°C and 160 rpm. This clone was further grown overnight in 100 ml (Midi) or 250 ml (Maxi) LB-medium with appropriate antibiotics at 37°C and 160 rpm. The next day, the bacterial culture was further processed using the PureLink™ HiPure Plasmid Midi/MaxiPrep Kit. The final plasmid DNA was set up to a concentration of 1 µg/µl and stored at -20°C.

2.2.2.4 Polymerase chain reaction (PCR) for standard cloning

For polymerase chain reaction (PCR), the Phusion™ High-Fidelity DNA Polymerase (Thermo Fisher) was used according to **Table 36** and **37**. Annealing temperature for primers were calculated with the T_m calculator of Thermo Fisher.

Table 36: PCR pipetting scheme for standard cloning

Reagents	Volume [µl]
DNA template [25ng/µl]	1 µl
5xHF buffer	10 µl
dNTPs [2 mM]	5 µl
Primer fwd [10 µM]	2.5 µl
Primer rev [10 µM]	2.5 µl
DMSO (final 10%)	5 µl
Phusion	1 µl
ddH_2O	23 µl
total volume	50 µl

Table 37: PCR temperature profile for standard cloning

Temperature	Time	Cycles
98°C	30 s	1
98°C	10 s	35
X°C	30 s	
72°C	30 s/kb	
72°C	300 s	1
4°C	∞	1

2.2.2.5 Agarose gel electrophoresis

DNA fragments were separated according to their size using the agarose gel electrophoresis system from Peqlab Biotechnologie GmbH. Therefore, the appropriate amount of agarose was weighted and boiled in 50 ml (small gel tray) or 100 ml (large gel tray) of 1xTAE using a microwave oven. Once the agarose solution was cooled down, ethidium bromide was added to a final concentration of 0.4 µg/ml and the mixture was poured to a gel tray with inserted well comb. Next, DNA samples were prepared by adding the appropriate amount of 5xDNA loading buffer. 1 kb or 100 bp DNA ladder from Thermo Fisher served as a size marker. Agarose gel electrophoresis was performed for 1 hour at 100 V in 1xTAE running buffer. DNA was visualized and photographed using a UV transilluminator. For quantitative DNA agarose electrophoresis, DNA was sliced out and saved in a 1.5 ml Eppendorf tube.

2.2.2.6 Extraction of DNA fragments from agarose gels

After agarose gel electrophoresis (**2.2.2.5**), DNA fragments (PCR and digested vector backbone) were extracted using the GeneJet PCR Purification kit from Thermo Fisher according to the manufacturer's protocol.

2.2.2.7 Restriction digestion using DNA endonucleases

To specifically cut vector backbones or PCR products, DNA endonucleases from Thermo Fisher and New England Biolabs were used according to the manufacturer's instructions. In brief, for standard cloning procedure 1 µg of the plasmid DNA and half of the extracted PCR product was used in a reaction volume of 50 µl. Double digestion using two enzymes in parallel was performed according to the DoubleDigest Calculator from Thermo Fisher. Quantitative agarose gel electrophoresis was performed to verify the correct digestion of plasmid DNA and to purify the digested vector backbone (**2.2.2.5**, **2.2.2.6**).

2.2.2.8 Ligation

Ligation reaction of digested PCR product and plasmid DNA was performed using the T4 DNA Ligase from New England Biolabs according to the manufacturer's instructions. In brief, digested vector backbone and PCR product were set up to a ratio 1:2 (vector : PCR) in a total volume of 10 µl and were incubated for 30 minutes at room temperature. Next, the whole ligation reaction was transformed to DH5α *E.coli*, as described in **2.2.2.1**. As a negative control served a reaction without digested PCR product.

2.2.2.9 Standard cloning procedure

For molecular cloning of a DNA insert into an appropriate vector, the first step was the amplification of the insert DNA by PCR described in **2.2.2.4**. To verify the correct size of the insert and to purify the DNA insert from the PCR reaction, quantitative agarose gel electrophoresis and DNA extraction was performed (**2.2.2.5**, **2.2.2.6**). Next, PCR product and vector DNA were digested with DNA endonucleases (**2.2.2.7**) and separated by quantitative agarose gel electrophoresis (**2.2.2.5**). Digested DNA insert and vector backbone were then purified (**2.2.2.6**) and ligated (**2.2.2.8**). After transformation of the ligation reaction in *E.coli* (**2.2.2.1**), plasmid DNA was prepared from single bacterial clones (**2.2.2.2**) and checked by restriction digestion.

2.2.2.10 Site directed mutagenesis and site directed deletion

To introduce one mutation at a distinct site of a gene, site directed mutagenesis by PCR was used. Primers were designed according to the QuickChange™ Site-Directed Mutagenesis Kit from Stratagene. PCR was performed according to **Table 38** and **39**. As a quality control, 10% of the PCR were checked on an agarose gel. To eliminate the vector template, a DpnI restriction digestion with 10 Units of enzyme was performed directly in the HF buffer of the Phusion polymerase for 1 hour at 37°C. Next, 5 µl of the reaction were transformed in *E.coli* using super competent TOP10 cells from Thermo Fisher. Single bacterial clones were tested by sequencing.

Table 38: PCR pipetting scheme for site directed mutagenesis

Reagents	Volume [µl]
DNA template [25ng/µl]	1 µl
5xHF buffer	10 µl
dNTPs [2 mM]	5 µl
Primer fwd [10 µM]	1 µl
Primer rev [10 µM]	1 µl
DMSO (final 10%)	5 µl
Phusion	1 µl
ddH_2O	26 µl
total volume	50 µl

Table 39: PCR temperature profile for site-directed mutagenesis

Temperature	Time	Cycles
98°C	30 s	1
98°C	10 s	18
55°C	30 s	
72°C	30 s/kb	
72°C	300 s	1
4°C	∞	1

For site directed deletion at a distinct site of a gene, PCR was used. Primers were designed according to the Q5-Site Directed Mutagenesis Kit from New England Biolabs. PCR was performed according to **Table 40** and **41**. Annealing temperature for primers were calculated with the T_m calculator of Thermo Fisher. As a quality control, 10% of the PCR product were verified on an agarose gel. To eliminate the vector template, a DpnI restriction digestion with 10 Units of enzyme was performed directly in the HF buffer of the Phusion polymerase for 1 hour at 37°C. After DpnI digestion, the reaction was purified by quantitative gel extraction (**2.2.2.6**) and solved in 30 µl of ddH_2O. To label the 5'-end of the amplified DNA with a phosphate group, a T4-PNK reaction was set up in a total volume of 30 µl for 30 minutes at 37°C using the T4-ligation buffer. To this reaction fresh T4-ligase buffer and T4-ligase was added to a total volume of 10 µl and incubated for additional 30 minutes at room temperature. Finally, the ligation reaction was transformed in DH5α (**2.2.2.1**). Single bacterial clones were tested by sequencing.

Table 40: PCR pipetting scheme for site directed deletion

Reagents	Volume [µl]
DNA template [25ng/µl]	1 µl
5xHF buffer	10 µl
dNTPs [2 mM]	5 µl
Primer fwd [10 µM]	2.5 µl
Primer rev [10 µM]	2.5 µl
DMSO (final 10%)	5 µl
Phusion	1 µl
ddH_2O	23 µl
total volume	50 µl

Table 41: PCR temperature profile for site directed deletion

Temperature	Time	Cycles
98°C	30 s	1
98°C	15 s	25
X°C	30 s	
72°C	30 s/kb	
72°C	300 s	1
4°C	∞	1

2.2.2.11 Extraction of genomic DNA from tissue or cells

For extraction of genomic DNA from mouse tissue or cells, murine ear biopsy, embryonal mouse tails or cell pellets were resuspended in 75 µl of base buffer and boiled for 30 minutes at 95°C. After cooling the samples for 5 minutes at 4°C, 75 µl of neutralization buffer was added. Samples were stored at 4°C.

2.2.2.12 PCR of genomic DNA

For genotyping of cells or mice isolated genomic DNA was used (**2.2.2.11**). PCR reactions amplifying specific genomic loci of *Lin9*, *Sav1*, *mTmG*, *Nkx-Cre* and *α-MHC-Cre* were performed according to **Table 42**, **43**, **44**, **45** and **46**. PCR products were analyzed on 1% (Lin9, MHC-Cre and Nkx-Cre) and 2% (Sav1 and mTmG) agarose gels (**2.2.2.5**).

Table 42: PCR conditions for *Lin9* allele

Reagents	Volume [µl]	Temperature	Time	Cycles
genomic DNA template	1 µl	94°C	120 s	1
10x ReproFast buffer	2.5 µl	94°C	30 s	
dNTPs [2 mM]	2.5 µl	58°C	60 s	31
Primer SG722 [10 µM]	1 µl	72°C	60 s	
Primer SG893 [10 µM]	1 µl	72°C	240 s	1
HisTaq 16 (5 U/µl)	0.2 µl	4°C	∞	1
ddH_2O	16.8 µl			
total volume	25 µl			

Table 43: PCR conditions for *Sav1* allele

Reagents	Volume [µl]	Temperature	Time	Cycles
genomic DNA template	1 µl	94°C	120 s	1
10x ReproFast buffer	2.5 µl	94°C	30 s	
dNTPs [2 mM]	2.5 µl	53°C	30 s	35
Primer SG2358 [10 µM]	1 µl	72°C	60 s	
Primer SG2359 [10 µM]	1 µl	72°C	240 s	1
Primer SG2360 [10 µM]	1 µl	4°C	∞	1
HisTaq 16 (5 U/µl)	0.2 µl			
ddH_2O	15.8 µl			
total volume	25 µl			

Table 44: PCR conditions for *mTmG* allele

Reagents	Volume [µl]	Temperature	Time	Cycles
genomic DNA template	3 µl	94°C	120 s	1
10x ReproFast buffer	2.5 µl	94°C	30 s	
dNTPs [2 mM]	2.5 µl	58°C	60 s	35
Primer SG2361 [10 µM]	1 µl	72°C	60 s	
Primer SG2362 [10 µM]	1 µl	72°C	240 s	1
Primer SG2363 [10 µM]	1 µl	4°C	∞	1
HisTaq 16 (5 U/µl)	0.2 µl			
ddH_2O	13.8 µl			
total volume	25 µl			

Table 45: PCR conditions for *Nkx-Cre* allele

Reagents	Volume [µl]	Temperature	Time	Cycles
genomic DNA template	3 µl	94°C	120 s	1
10x ReproFast buffer	2.5 µl	94°C	30 s	
dNTPs [2 mM]	2.5 µl	57°C	30 s	35
Primer SG2157 [10 µM]	1 µl	72°C	60 s	
Primer SG2158 [10 µM]	1 µl	72°C	240 s	1
Primer SG2159 [10 µM]	1 µl	4°C	∞	1
HisTaq 16 (5 U/µl)	0.05 µl			
ddH_2O	13.95 µl			
total volume	25 µl			

Table 46: PCR conditions for *MHC-Cre* allele

Reagents	Volume [µl]	Temperature	Time	Cycles
genomic DNA template	1 µl	94°C	120 s	1
10x ReproFast buffer	2.5 µl	94°C	30 s	
dNTPs [2 mM]	2.5 µl	60°C	30 s	35
Primer SG1114 [10 µM]	1 µl	72°C	60 s	
Primer SG1936 [10 µM]	1 µl	72°C	240 s	1
HisTaq 16 (5 U/µl)	0.05 µl	4°C	∞	1
ddH_2O	16.95 µl			
total volume	25 µl			

2.2.2.13 RNA extraction from tissue or cells

Total RNA from heart ventricular tissue or cells was isolated using peqGOLD TriFast (Peqlab) according to the manufacturer's instructions. The following steps were performed on ice or at 4°C. To isolated RNA from heart ventricle, the tissue was minced in 1 ml TriFast solution in a 2 ml reaction tube two times for 30 seconds using an Ultra-turrax. For cultured cells, medium was discarded, cells were lysed in 1 ml TriFast solution and transferred to a 2 ml reaction tube. Next, 200 µl chloroform was added, samples were vortexed thoroughly for 15 seconds and then incubated for 3 minutes on ice. To separate between DNA, RNA and proteins, samples were centrifuged for 10 minutes at 12,000xg and 4°C. The upper aqueous phase containing RNA was transferred into a fresh 1.5 ml tube. To precipitate the RNA, 500 µl ice-cold isopropanol was added, the mixture was vortexed and incubated for 10 minutes on ice. Subsequently, the RNA was pelleted by centrifugation for 10 minutes at 12,000xg and 4°C. The resulting RNA pellet was washed two times with 1 ml ice-cold 70% ethanol and centrifuged at each washing step for 5 minutes at 7,000xg and 4°C. After the last washing step, ethanol was removed completely, the pellet was air dried for 5 minutes at room temperature and finally resuspended in 25 µl RNase-free ddH_2O. The RNA was stored at -80°C.

2.2.2.14 Reverse transcription of RNA into cDNA

For reverse transcription (RT) of isolated RNA into cDNA, the RevertAid Reverse Transcriptase (Thermo Fisher) and RiboLock RNase Inhibitor was used. First, 2.5 µg of total RNA and 0.5 µl of random hexamer primers (0.5 µg/µl) were filled up with RNase-free water to a total volume of 10 µl and incubated for 5 minutes at 70°C. After the reaction was cooled down to 4°C, 15 µl of the RT master mix was added, which contains 6,25 µl dNTPs (2 mM), 5 µl 5xRT buffer, 0.5 µl RevertAid enzyme (200 U/µl), 0.5 µl RiboLock enzyme (40 U/µl) and 2.75 ml RNase-free water. The reaction was mixed by pipetting up and down and incubated for 1 hour at 37°C. Then, the reaction was inactivated at 70°C for 15 minutes and cooled down to 4°C. To prepare cDNA for RT-qPCR, the reaction was diluted in a 1:16 ratio and stored at -20°C.

2.2.2.15 Quantitative real-time PCR (qPCR)

Quantitative real-time PCR (qPCR) was used to calculate the relative mRNA expression of a specific gene normalized to the expression of a housekeeping gene. To do so, qPCR was performed according to **Table 47** and **48**. Therefore cDNA transcribed from RNA was used (**2.2.2.14**). As a non-targeted control (NTC), water was used instead of cDNA. The qPCR was run on a Stratagene Mx3000P qPCR machine. Primers amplifying specific loci of a mRNA were created with the help of either the ProbeFinder web-based software (Roche) or the Primer3Input web-based software.

Table 47: qPCR conditions and temperature profile

Reagents	Volume [µl]	Temperature	Time	Cycles
cDNA (1:16)	5 µl	95°C	120 s	1
Master Mix	18.2µl	95°C	15 s	
Primer fwd [10 µM]	0.75 µl	60°C	30 s	40
Primer rev [10 µM]	0.75 µl	72°C	30 s	
HisTaq 16 [5 U/µl]	0.3 µl	95°C	15 s	
total Volume	25 µl	60°C	30 s	1
		72°C	30 s	

Table 48: qPCR master mix

Reagents	Volume [µl]
dNTPs [2 mM]	3.5 µl
10x ReproFast	2.5µl
SYBER Green [1:2000 in DMSO]	0.75 µl
ddH_2O	11.45 µl
total volume	18.2 µl

The relative expression of a gene in the sample of interest relative to the gene expression in a reference sample was calculated using the following formula:

$$2^{-\Delta\Delta Ct}$$

with ΔCt = Ct (gene of interest) – Ct (housekeeping gene)

and ΔΔCt = ΔCt (sample) – ΔCt (reference)

The standard deviation of ΔΔCt was calculated by using:

$$s=\sqrt{s_1^2 + s_2^2}$$

with s_1 = standard deviation of gene of interest

and s_2 = standard deviation of housekeeping gene

The margin of error for $2^{(-\Delta\Delta Ct)}$ was calculated by using:

$$2^{(-\Delta\Delta Ct \pm s)}$$

The error used for the error bars was calculated by using:

$$2^{(-\Delta\Delta Ct \pm s)} - 2^{(-\Delta\Delta Ct)}$$

2.2.2.16 Phenol/Chloroform extraction of DNA

Phenol/Choroform extraction was used to either purify PacI digested adenoviral genome for transfection (**2.2.1.10**, **2.2.1.7**) or to purify fragmented chromatin for size-control (**2.2.3.8**). Therefore, samples were transferred to a 2 ml reaction tube and filled up with 1xTE buffer to a volume of 500µl. Then, 500µl phenol was added, vortexed and the mixture was incubated for 10 minutes on a rotating wheel. Subsequently, 500 µl chloroform/isoamyl alcohol (24:1) was incubated with the mixture for 10 minutes on a rotating wheel. To separate DNA from proteins, samples were centrifuged for 5 minutes at 16,000 xg and 4°C. The aqueous phase was transferred to a fresh 1.5 ml tube and DNA was precipitated by adding 2 volumes ice-cold 100% ethanol, 0.1 volumes 3 M Na-acetate and 1 µl glycogen (Roche). The mixture was incubated for 60 minutes at -80°C and then DNA was pelleted for 30 minutes at 16,000 xg and 4°C. The resulting DNA pellet was washed twice with 70% ethanol. DNA was air dried and solved in 20 µl 1xTE buffer and further used for transfection (adenovirus, **2.2.1.7**) or loaded on a agarose gel (ChIP, **2.2.2.5**).

2.2.3 Protein biochemistry

2.2.3.1 Whole cell lysates

For whole cell lysates cells were transferred on ice, old medium was discarded, and the cells were washed once with 10 ml ice-cold 1xPBS. Next, cells were scraped off the plate in 10 ml 1xPBS and transferred to a 15 ml falcon. Cells were pelleted for 5 minutes at 1,200 rpm and 4°C. For cell lysis, the pellet was resuspended in an appropriate amount of TNN lysis buffer by pipetting up and down at least twenty times and then transferred to a 1.5 Eppendorf tube. After 20 minutes incubation on ice, cell debris was pelleted by centrifugation for 10 minutes at 14,000 rpm and 4°C. The supernatant was transferred to a fresh tube and protein concentration was measured using Bradford assay (**2.2.3.2**). The cell lysate was either directly used for further assays or supplemented with 3x electrophoresis sample buffer (ESB) and boiled for 5 minutes at 95°C. Finally, samples were used for SDS-PAGE (**2.2.3.5**) or stored at -20°C.

2.2.3.2 Determination of protein concentration according to Bradford

To determine the protein concentration of either cell lysates (**2.2.3.1**) or purified recombinant proteins, Bradford assay was performed. In brief, 1µl of cell lysate or recombinant protein were mixed with 1 ml Bradford solution in a semi-micro cuvette. Using a spectrophotometer, absorbance at 595 nm was measured. All measurements were performed in duplicates. Protein concentration was calculated by using a standard curve of a serial dilution of a BSA reference.

2.2.3.3 Immunoprecipitation

To study protein-protein interaction between ectotopic expressed flag-YAP constructs and HA-B-MYB constructs, flag immunoprecipitation was performed. Therefore, $2.4*10^6$ HeLa cell were seeded onto a 10 cm cell culture dish and were transfected the next day with 18 µg of plasmid DNA (9 µg flag-YAP, 9 µg HA-B-MYB) as described in **2.2.1.8**. One day after transfection, cells were moved onto a 15 cm cell culture dish. 48 hours after transfection cells were harvested and whole cell lysis was performed (**2.2.3.1**).

For flag immunoprecipitation 30 µl of Protein G Dynabeads (Thermo Fisher) were blocked two times with 5 mg/ml BSA in 1xPBS for 10 minutes. A magnetic rack was used to change buffers during each step. Then, 1 µg flag antibody was coupled to the beads in a total volume of 500 µl TNN lysis buffer on a rotating wheel for at least 1 hour in the cold room. After the antibody was coupled to the beads, 1-2.5 mg of whole protein lysate was diluted in a total volume of 500 µl with TNN lysis buffer and incubated for 2-3 hours with the antibody coupled beads on a rotating wheel at 4°C. In parallel, 3% of the cell lysate was kept as input material.

Subsequently, the beads were washed five times with 1 ml TNN lysis buffer rotating on a wheel for 5 minutes at 4°C. After the last washing step, tubes were shortly spun down and TNN buffer was thoroughly removed. Finally, proteins were eluted from the beads by boiling them in 30 µl 3xESB buffer for 5 minutes at 95°C. Samples were transferred to fresh tubes and stored at -20°C until they were analyzed by western blot.

2.2.3.4 Proximity Ligation Assay (PLA)

To study protein-protein interaction between endogenous proteins, proximity ligation assay (PLA) was performed using the Duolink™ PLA Technology (Sigma Aldrich). For PLA of embryonal cardiomyocytes (E14.5), cells were seeded on fibronectin coated 18-well ibidi slides, cultured initially for one day and then transfected with siRNA against the interaction partners (**2.2.1.9**). For PLA of HeLa cells, 10,000 cells were seeded on 18-well ibidi slides and cultivated 24 hours. Cells were washed once with 1xPBS and then fixed in PSP for 10 minutes. After fixation, cells were rinsed two times and washed once for 3 minutes with 1xPBS. For permeabilization, cells were incubated for 5 minutes in 1xPBS containing 0.2% Triton-X100. Next, cells were rinsed twice in 1xPBS. Unspecific binding sites were blocked by incubation with 3% goat serum in 1xPBS with 0.2% Tween-20 for 20 minutes at room temperature. After removal of the blocking solution, cells were incubated with the desired primary antibody diluted in blocking solution overnight at 4°C. The next day, primary antibody solution was removed, and cells were washed twice for 5 minutes in a 10 cm cell culture dish filled with PBS while shaking. Then, cells were incubated with the secondary PLA probe diluted 1:5 in antibody diluent for 1 hour at 37°C in a humidified chamber. After washing the slides two times for 5 minutes with buffer A, cells were incubated with the ligation solution for 30 minutes at 37°C in a humidified chamber. Subsequently, slides were washed twice with buffer A for 5 minutes and were then incubated with the amplification solution for 120 minutes at 37°C in a humidified chamber. Nuclei of cells were stained with Hoechst 33258 1:1000 for 5 minutes. Then, slides were washed once with buffer B for 10 minutes and once with 0.01x buffer B for 1 minute. After the last washing step, buffer was removed carefully using a P20 pipette and cells were prepared for microscopy using one drop of ImmuMount. Slides were immediately imaged using an inverted Leica DMI 6000B microscope equipped with a Prior Lumen 200 fluorescence light source and a Leica DFC350 FX digital camera.

To visualize embryonal cardiomyocytes, a second immunostaining with a cardiomyocyte marker was performed. Therefore, the amplification reaction was discarded, slides were washed twice with buffer B for 10 minutes and once with buffer A for 1 minute. Then, cells were incubated with cardiac Troponin (cTnT) primary antibody diluted 1:50 in blocking solution for 40 minutes. Slides were washed two times with buffer A for 2 minutes, before slides were incubated with the secondary antibody (α-mouse IgG2a conjugated to Alexa 488) diluted 1:500 and Hoechst 33258 1:1000 in blocking solution for 20 minutes. Slides were then washed two times with buffer A for 2 minutes and once in buffer B for 1 minute. Finally, slides were prepared for microscopy as described above.

2.2.3.5 Sodium dodecyl sulfate polyacrylamide gel electrophoresis (SDS-PAGE)

Sodium dodecyl sulfate polyacrylamide gel electrophoresis (SDS-PAGE) was carried out using the Mini-Protean® III system from Biorad. First a separation gel (8% - 12.5%) was prepared as stated in **Table 49**. After polymerization of the separation gel, a stacking gel (5%) (**Table 49**) was poured on top and 10- or 15-well comb was inserted. Gels were run with constant amperage (35 mA/gel) in 1x SDS running buffer for approximately 1.5 hours.

Table 49: SDS-PAGE separation and stacking gels

Reagents	Acrylamide concentration			
	5% (Stacking)	**8%**	**10%**	**12.5%**
ddH_2O	3.0 ml	4.6 ml	3.8 ml	3.2 ml
1.5 M Tris pH 8.8	-	2.6 ml	2.6 ml	2.6 ml
0.5 M Tris pH 6.8	1.25 ml	-	-	-
30% Acrylamide/ProtoGel	0.67 ml	2.6 ml	3.4 ml	4.0 ml
20% (w/v) SDS	25 µl	50 µl	50 µl	50 µl
10% (w/v) APS	25 µl	50 µl	50 µl	50 µl
TEMED	2.5 µl	5 µl	5 µl	5 µl
3xESB	25 µl	-	-	-

2.2.3.6 Coomassie brilliant blue staining

For visualization of protein bands, polyacrylamide gels were stained with Coomassie brilliant blue solution for 15-30 minutes under constant shaking. Afterwards, the gel was incubated in Coomassie destaining solution until protein bands become visible. To accelerate this process, Coomassie destaining solution was exchanged regularly.

2.2.3.7 Immunoblotting

For protein transfer from polyacrylamide gels to polyvinylidene fluoride (PVDF) membranes, the Mini Trans-Blot® system from Biorad was used according to the manufacturer's instructions. In brief, the PVDF membrane was first activated in methanol for 1 minute. Then, blotting pads, whatman papers and PVDF membrane were soaked in cold blotting buffer. The blotting stack was assembled in the gel holder cassette. Starting on the black side of the cassette, pre-wetted blotting pad, two whatman paper, PVDF membrane, polyacrylamide gel, two whatman paper and a blotting pad were assembled. Next, the gel holder cassette was placed into the electrode module with the black side of the cassette towards the black side of the module. A frozen cooling unit was put in the blotting tank. Transfer was achieved in cold blotting buffer under constant amperage (250 mA/module) for 90 minutes. Ponceau S staining was used to control successful transfer of the proteins to the PVDF membrane. Unspecific binding of proteins to the membrane was blocked by incubating the membrane with 5% milk powder or BSA in TBS with 0.1% Tween-20 (TBS-T) for 1 hour while constantly shaking. Then,

the desired primary antibody diluted in blocking solution was incubated with the membrane overnight in the cold room. The next day, the primary antibody was removed, and membrane was washed once with TBS-T for 10 minutes and twice with TBS-T for 5 minutes at room temperature. Subsequently, the membrane was incubated with the secondary antibody diluted in blocking solution 1:5000 for 1 hour at room temperature. Three washing steps with TBS-T were performed, one for 10 minutes and two for 5 minutes. Finally, the membrane was incubated in freshly prepared enhanced chemiluminescence (ECL) solution for 1 minute, before it was wrapped in plastic foil and exposed to X-ray films in the dark room.

2.2.3.8 Chromatin-immunoprecipitation (ChIP)

For Chromatin-immunoprecipitation (ChIP), Chromatin was isolated from ventricular heart tissue of E16.5 or P10 hearts. In brief, minced tissue was crosslinked with 1% formaldehyde for 20 minutes at room temperature on a rotating wheel. The reaction was stopped by adding 125 mM glycine for additional 5 minutes. Tissue was incubated in lysis buffer (50 mM Tris-HCl pH 8, 10 mM EDTA, 1% SDS) for 1 hour at 4°C on a rotating wheel. Samples were sonicated using Branson sonifier 250 for 1 minute (sonication time) at 25% amplitude (10s ON / 30s OFF) at 4°C, insoluble material was removed by centrifugation and chromatin was fragmented to an approximate size of 150 to 300bp by additional sonication for 10 minutes (sonication time) at 25% amplitude (10 seconds On/ 30 seconds OFF) at 4°C. To determine concentration and size of the fragmented chromatin, 100 µl of chromatin was incubated with RNAse A (final concentration 10 µg/ml) and crosslink was reversed overnight at 65°C. The next day, proteins were digested by Proteinase K digestion (final concentration 200 µg/ml) at 55°C for 2 hours. Then, DNA was purified using phenol-chloroform extraction (**2.2.2.16**). Concentration of the isolated DNA was measured, and size was controlled by agarose gel electrophoresis (**2.2.2.5**). Afterwards chromatin was diluted ten times in ChIP dilution buffer (50 mM Tris-HCl pH 8, 0.167 M NaCl, 1.1% Triton X-100, 0.11% sodium deoxycholate). For immunoprecipitation, 9µg of the desired antibody was coupled to 90 µl of protein G dynabeads (Thermo Fisher) in a total volume of 500 µl of ChIP dilution buffer for 6 hours at 4°C on a rotating wheel. Then, antibody coupled beads were incubated with 240 µg fragmented chromatin over night at 4°C. Beads were washed in total twelve times (three times per buffer) with 800 µl RIPA-150 (50 mM Tris-HCl pH 8, 0.15 M NaCl, 1 mM EDTA, 0.1% SDS, 1% Triton X-100, 0.1% sodium deoxycholate), RIPA-500 (50 mM Tris-HCl pH 8, 0.5 M NaCl, 1 mM EDTA, 0.1% SDS, 1% Triton X-100, 0.1% sodium deoxycholate), RIPA-LiCl (50 mM Tris-HCl pH 8, 0.5 M $LiCl_2$, 1 mM EDTA, 1% nonident P-40, 0.7% sodium deoxycholate) and 1xTE (10 mM Tris-HCl pH 8, 1 mM EDTA). 1mM PMSF and protease inhibitor cocktail were added freshly to all buffers. After all washing steps were completed, chromatin was eluted in 200 µl direct elution buffer (10 mM Tris-HCl pH 8, 0.3 M NaCl, 5 mM EDTA, 0.5% SDS, 10 µg/ml RNAse A) and crosslink was reversed at 65°C overnight. Proteins were digested by adding 200 µg/ml proteinase K at 55°C for 2 hours. DNA was purified using the QIAquick PCR Purification Kit (QIAGEN) and eluted in 50 µl EB buffer. Samples were stored at -20°C.

2.2.3.9 Overexpression of recombinant proteins in bacteria

For overexpression of recombinant proteins in bacteria, plasmid DNA was transformed into BL21 (DE3) as described in **2.2.2.1**. The next day, bacterial clones were detached from LB agar plate by resuspending them in 10 ml LB medium. The bacterial suspension was transferred in a 2 l flask containing 500 ml LB medium supplemented with the appropriate antibiotics. The culture was incubated at 37°C while shaking at 140 rpm. To determine the optical density of the bacterial culture, absorbance at 600 nm was measured using a spectrophotometer. Bacterial culture was grown at 37°C until a density of 0.5-0.6 was reached. Then, the culture was shifted to 18°C and incubated for additional 10 minutes shaking at 200 rpm. 500 µl of the bacterial culture was kept as pre-induction sample. Therefore, bacteria were centrifuged for 1 minute at maximal speed using a bench top centrifuge. The resulting pellet was resuspended in 20 µl 3x ESB buffer and boiled for 5 minutes at 95°C and saved at -20°C. For expression of recombinant proteins, the culture was induced by adding 1 mM isopropyl-β-D-thiogalactopyranosid (IPTG). Subsequently, the culture was incubated overnight at 18°C shaking at 200 rpm. The next day, 250 µl of the bacterial culture was used as post-induction sample and prepared as described above. Finally, the bacterial culture was pelleted by centrifugation for 10 minutes at 4,000xg and 4°C. The bacterial pellet was transferred to a 50 ml falcon and saved at -20°C. To verify successful overexpression of recombinant proteins, pre- and post-induction samples were analyzed by SDS-PAGE (**2.2.3.5**) and stained with Coomassie (**2.2.3.6**).

2.2.3.10 Purification of recombinant GST fusion proteins

After overexpression of recombinant GST fusion proteins (**2.2.3.9**), cell pellets were thawed on ice and resuspended in 30 ml GST lysis buffer freshly supplemented with protease inhibitor cocktail 1:1000, 1 mM PMSF and 1 mM DTT. For bacterial lysis, the suspension was sonicated using a Branson sonicator 250 for 80 s (sonication time) at 40% amplitude (10 s ON/45 s OFF). Bacterial lysates were then transferred to Corex glass tubes and centrifuged for 30 minutes at 12,000xg and 4°C. The cleared supernatant was transferred to a fresh 50 ml falcon and incubated with 500 µl pre-washed Glutathione sepharose beads (GE healthcare) for 2 hours on a rotating wheel in the cold room. Next, beads were centrifuged for 5 minutes at 1,200 rpm and 4°C. The supernatant was discarded, and beads were washed six times with 40 ml GST wash buffer. At every washing step the resin was incubated for 5 minutes on a rotating wheel at 4°C, followed by centrifugation for 5 minutes at 1,200 rpm and 4°C. For the first and the last washing step, GST washing buffer was freshly supplemented with protease inhibitor cocktail (PIC) 1:1000, 1 mM PMSF and 1 mM DTT. Beads with bound proteins were stored in GST lysis buffer with protease inhibitor cocktail (PIC) 1:1000, 1 mM PMSF at 4°C and directly used for pulldown assays (**2.2.3.12**). To control the success of the purification, 20 µl samples were taken from each step, run on a SDS-PAGE (**2.2.3.5**) and stained with Coomassie (**2.2.3.6**).

2.2.3.11 Purification of recombinant 6xHis fusion proteins

For purification of recombinant 6xHis fusion proteins, bacterial pellets obtained according to **2.2.3.9** were thawed on ice. Once thawed, pellets were resuspended in 30 ml His-tag lysis buffer freshly supplemented with protease inhibitor cocktail (PIC) 1:1000 and 1 mM PMSF and transferred to a 50 ml falcon. For bacterial lysis, the suspension was sonicated using a Branson sonicator 250 for 80 s (sonication time) at 40% amplitude (10 s ON/45 s OFF). Bacterial lysates were then transferred to Corex glass tubes and centrifuged for 30 minutes at 12,000xg and 4°C. The cleared supernatant was transferred to a fresh 50 ml falcon and incubated with 500 µl pre-washed Ni-NTA agarose (Thermo Fisher) for 2 hours on a rotating wheel at 4°C. Next, the resin was centrifuged for 5 minutes at 700 rpm and 4°C. The supernatant was discarded, and agarose was washed six times with 40 ml His-tag washing buffer. At every washing step resin was incubated for 5 minutes on a rotating wheel at 4°C, followed by centrifugation for 5 minutes at 700 rpm and 4°C. For the first and the last washing step, His-tag washing buffer was freshly supplemented with protease inhibitor cocktail (PIC) 1:1000 and 1 mM PMSF. To elute the His-tagged protein, beads were transferred onto a gravity column and eluted in 8x1.5 ml aliquots with His-tag elution buffer by gravity flow. 20 µl of the elution fractions were run on SDS-PAGE (**2.2.3.5**) and stained by Coomassie staining (**2.2.3.6**). Protein concentration of elution fractions were calculated using the Bradford assay (**2.2.3.2**). Purity and amount of protein were used as criteria to pool elution fractions. Pooled fractions were then dialyzed against cold TBS supplemented with 1 mM DTT overnight at 4°C. Finally, purified His tagged proteins were aliquoted and snap frozen in liquid nitrogen and stored at -80°C.

2.2.3.12 GST pulldown assay

To study protein-protein interaction between recombinant proteins, GST pulldown assays were performed. Therefore, GST tagged YAP constructs were either incubated with HA tagged B-MYB constructs expressed in HeLa cells or with purified recombinant His tagged B-MYB constructs.

2.2.3.12.1 GST pulldown assay using HA tagged B-MYB expressed in HeLa cells

To analyze the interaction of truncated HA tagged B-MYB constructs with GST tagged YAP constructs, HA tagged B-MYB constructs were expressed in HeLa cells. Therefore, 18 µg of HA-B-MYB constructs were transfected in HeLa cells as described in **2.2.1.8**. Two days after transfection, cells were harvested and whole cell lysates were performed (**2.2.3.1**). HeLa whole cell lysate containing 1 to 2 mg of total protein was incubated with 5 µg of purified GST tagged YAP constructs immobilized on Glutathione sepharose beads in a total volume of 500 µl TNN lysis buffer for 3 hours on a rotating wheel at 4°C. In this reaction Glutathione sepharose beads containing GST tagged YAP constructs was filled up with pre-washed empty beads to a total volume of 30 µl. In parallel, 3% of the cell lysate was kept as input material. Beads were washed six times with 1 ml TNN lysis buffer for 5 minutes on a rotating wheel at 4°C, followed

by centrifugation for 5 minutes at 1,200xg and 4°C. After the last washing step, supernatant was removed completely using a Hamilton syringe. Proteins were eluted in 30 µl 3xESB buffer and boiled for 5 minutes at 95°C. Samples were stored at -20°C until they were analyzed by immunoblot (**2.2.3.7**).

2.2.3.12.2 GST pulldown assay using recombinant His tagged B-MYB

To analyze direct interaction between YAP and B-MYB, purified recombinant proteins were used in a pulldown assay. Therefore, 380 µg His-tagged B-MYB was thawed on ice and incubated with approximately 5 µg of purified GST tagged YAP constructs immobilized on Glutathione sepharose beads in a total volume of 500 µl recombinant pulldown buffer for 3 hours on a rotating wheel at 4°C. Beads were washed three times with 1 ml recombinant pulldown buffer and were then further processed as described in **2.2.3.12.1**.

2.2.4 Next-generation sequencing (NGS)

2.2.4.1 RNA-sequencing (RNA-Seq)

For whole transcriptome analysis, total RNA was isolated in biological triplicates from ventricular heart tissue with the desired genotype as described in **2.2.2.13**. As an additional step for RNA-Seq, the Trizol obtained RNA was further purified using the RNeasy Mini Kit (Qiagen) with on-column DNase I digest according to the manufacturer's instructions. RNA quality and concentration were measured using the Fragment Analyzer™ Automated CE System (Advanced Analytical) with the (DNF-471) Fragment Analyzer RNA Kit (Agilent). cDNA libraries were generated using 1µg RNA as starting material with the NEBNext® Poly (A) mRNA Magnetic Isolation Module (New England Biolabs) together with NEBNext® Ultra II RNA Library Prep Kit for Illumina (New England Biolabs). Size selection (150 bp) and purification steps within the protocol were performed using the Agencourt AMPure XP Beads (Beckman Coulter). Adaptor ligation and amplification of the cDNA library with i5/i7 index primers were performed using the NEBNext® Multiplex Oligos for Illumina® (Dual Index Primers Set 1). Finally, cDNA library was amplified using 7 PCR cycles and quality was analyzed using the Fragment Analyzer™ Automated CE System (Advanced Analytical) with the (DNF-474) HS NGS Fragment Kit (1-6000bp) (Agilent). Libraries were pooled at an equimolar ratio and sequenced on the NextSeq 500 platform (Illumina).

2.2.4.2 Chromatin immunoprecipitation-sequencing (ChIP-Seq)

Chromatin immunoprecipitation for ChIP-Seq was performed as described in **2.2.3.8**. Purified ChIP-DNA was quantified using the Quant-iT PicoGreen dsDNA Assay Kit (Thermo Fisher). Therefore, each sample was measured in duplicates using a black 96-well plate with F-bottom (Greiner). Fluorescence intensity of the samples was quantified using a Tecan Infinite M200 plate reader. DNA concentration of the sample was calculated using a standard curve.

cDNA libraries were generated using 10 ng purified ChIP-DNA and the NEBNext® Ultra II DNA Library Prep Kit for Illumina® (New England Biolabs) according to the manufacturer's instructions. Agencourt AMPure XP Beads (Beckman Coulter) were used for size selection (150 bp) and purification steps within the library preparation. DNA library was amplified by 12-15 PCR cycles using i5/i7 index primers from the NEBNext® Multiplex Oligos for Illumina® (Dual Index Primers Set 1) kit (New England Biolabs). Quality and concentration were analyzed using the Fragment Analyzer™ Automated CE System (Advanced Analytical) with the (DNF-474) HS NGS Fragment Kit (1-6000bp) (Agilent). Libraries were pooled at an equimolar ratio and sequenced on the NextSeq 500 platform (Illumina).

2.2.5 Animal experiments

All animal studies were carried out in accordance with national and institutional guidelines and were approved by the regional state administration agency for Würzburg (approval number 55.2-2532-2-293). Euthanasia was achieved by cervical dislocation of adults and decapitation of embryos. Mice were maintained in a C57BL/6 background. Sav1$^{tm1.1Dupa}$/J, short *Sav1$^{fl/fl}$*, mice were obtained from Jackson laboratories, in which exon 3 of the *Sav1* gene is flanked by loxP sites (Cai et al., 2010). B6.129(Cg)-Gt(ROSA)26Sor$^{tm4(ACTB-tdTomato,-EGFP)Luo}$/J, short *mTmG$^{fl/fl}$*, mice were obtained from Jackson laboratories. *mTmG$^{fl/fl}$* is a cell membrane tagged, double fluorescence Cre-Reporter mouse line (Muzumdar et al., 2007). In these mice, the Tomato allele next to a stop cassette is flanked by loxP sites, which are followed by the EGFP allele. Thus, under normal conditions membrane localized Tomato (mT) is expressed in these mice. After Cre activation, the Tomato allele is deleted and membrane localized EGFP (mG) is expressed (**Figure 9**). In *Lin9$^{fl/fl}$* mice exon 7 of the *Lin9* gene is flanked by loxP sites (Reichert et al., 2010). Cardiomyocyte-specific deletion of Sav1 and Lin9 was achieved by crossing mice to Nkx2.5-Cre mice (Stanley et al., 2002). Postnatal cardiomyocyte-specific deletion of Sav1 and Lin9 was achieved by crossing mice to α-MHC-Cre mice (Agah et al., 1997). To obtain *Lin9$^{fl/fl}$; CreER^{T2}*, *Lin9$^{fl/fl}$* mice were crossed with a mouse line ubiquitously expressing CreER^{T2} transgene (Hameyer et al., 2007).

2.2.5.1 Preparation of heart tissue sections

Postnatal hearts and embryos were dissected at distinct time points and fixated in Bouin's solution overnight at 4°C. The next day, hearts or embryos were washed twice with 1xPBS and once with 0.9% NaCl solution for 1 hour at room temperature on a rotating wheel. Then, tissue was dehydrated and embedded into paraffine according to **Table 50**. Paraffine embedded tissues were cut in 5 µm section using a Hyrax M 40 rotary microtome. Sections were shortly dried at a 42°C heating plate and stored at 4°C until they were further processed.

Table 50: Dehydration of heart tissue

Reagents	Time
50% ethanol	1 h (RT)
70% ethanol	1 h (RT); storage for several weeks at 4°C; 70% ethanol is changed regularly, since picric acid is washed out
80% ethanol	1 h (RT)
90% ethanol	1 h (RT)
95% ethanol	1 h (RT)
100% ethanol	two times 1 h (RT)
100% ethanol/xylene (1:1)	1 h (RT)
Xylene	two times 1 h (RT)
Xylene/paraffine (1:1)	1 h (60°C)
Paraffine	changed 2-3 times

2.2.5.2 Hematoxylin and eosin staining (HE-staining)

Hematoxylin and eosin staining (HE-staining) was used to stain cell nuclei (Hematoxylin) and cell plasma (eosin). As a result, different tissue structures and morphological changes of the analyzed hearts were determined. For HE-staining, paraffin-embedded sections were pre-selected for comparable contour using a binocular light microscope. Sections were pre-warmed for 10 minutes at room temperature. First, sections were deparaffinized according to **Table 51**. Second, sections were stained as described in **Table 51**. Finally, sections were dehydrated again (**Table 51**) and mounted with Roti-Histokitt (Roth). HE-stained sections were imaged under a light microscope and stored at 4°C.

Table 51: Deparaffinization and HE-staining of heart sections

Step	Reagents	Time
Deparaffinization	Xylene	two times 10 minutes
	100% ethanol	3 minutes
	95% ethanol	3 minutes
	90% ethanol	3 minutes
	80% ethanol	3 minutes
	70% ethanol	3 minutes
	50% ethanol	3 minutes
	VE-H_2O	5 minutes
HE-staining	Hemalum solution according to Meyer (Roth)	10 minutes
	tap water	rinse for 15 minutes
	ddH_2O	2 minutes
	0.1% Eosin Y solution (Roth)	5 minutes
	tap water	rinse for 5 minutes
Dehydration	95% ethanol	3 minutes
	100 % ethanol	3 minutes
	Xylene	two times 10 minutes

2.2.5.3 Immunohistochemistry (IHC)

To visualize specific proteins, such as cell cycle marker or cardiac marker proteins, on paraffine-embedded sections, immunohistochemistry was performed. Therefore, sections were deparaffinized as described in **2.2.5.2**. For antigen retrieval, sections were boiled for 10 minutes in 10 mM Na-citrate pH 6 using a coplin jar in a microwave oven. In detail, samples were boiled for 1 minute at 1000 W until buffer spills over. Then, samples were boiled for additional 9 minutes at 300 W. During this period buffer level in the coplin jar was refilled approximately after 7 minutes. After 30 minutes of cool down, sections were washed three times with 1xPBS for 3 minutes. To reduce the level of antibody, which is necessary to cover the tissue, section was surrounded with an ImmEdge™ Hydrophobic Barrier Pen (Vector Laboratories Inc.). Unspecific binding sites were blocked by incubation with 5% BSA in 1xPBS with 0.1% Tween-20 (PBS-T) for 2 hours. Sections were washed three times with PBS-T for 3 minutes and incubated with the desired primary antibody diluted in blocking solution overnight in a humidified chamber at 4°C. The next day, samples were washed three times for 3 minutes with PBS-T and then incubated with the secondary antibody (1:200) and Hoechst 33258 (1:500) diluted in blocking solution for 2 hours in a humidified chamber at room temperature. Next, sections were washed three times for 3 minutes and air dried carefully. Finally, sections were mounted using ImmuMount and sealed with nail polish. Sections were stored at 4°C in the dark until they were imaged using an inverted Leica DMI 6000B microscope equipped with a Prior Lumen 200 fluorescence light source and a Leica DFC350 FX digital camera. Leica Application Suite (LAS) 3.7 was used for the analysis.

2.2.6 Data acquisition and statistical analysis

2.2.6.1 RNA-Seq analysis

Data acquisition and statistical analysis of RNA-Seq data was performed by Susanne Walz (Comprehensive Cancer Center Mainfranken, Core Unit Bioinformatics, Biocenter, University of Würzburg, Würzburg, Germany). After sequencing, bases were called using Illuminas GenerateFASTQ v1.1.0.64 software and sequencing quality was controlled with the FastQC script. For RNA-seq, reads were mapped with TopHat v2.1.0 (Kim et al., 2013) and BOWTIE2 (Langmead and Salzberg, 2012) with default parameters to the murine genome (mm10). Samples were normalized to the sample with the smallest number of mappable reads and a read count matrix for each Ensembl gene (GRCm38.p6) was generated with the summarizeOverlaps function in the R package {GenomicFeatures}. Before differential gene expression analysis, non- or weakly expressed genes were removed using the threshold: mean read count per gene over all samples >1. Differentially expressed genes were called with EdgeR and p-values were adjusted for multiple-testing with the Benjamini-Höchberg procedure (FDR: false discovery rate). Gene set enrichment analyses (Broad institute) was performed as described before (Subramanian et al., 2005) with signal2noise metric, 1000 permutations and a combined gene set database comprising Hallmark and C2 gene sets. The C2 gene set from MSigDB was spiked with “LIN9 targets” (Reichert et al., 2010) and “Direct LIN9 targets” (Pattschull et al., 2019).

2.2.6.2 ChIP-Seq analysis

Analysis of ChIP-Seq data was performed by Susanne Walz. For ChIP-seq, sequenced reads were mapped to the Mus musculus genome mm10 with BOWTIE v1.2 (Langmead and Salzberg, 2012) and default parameters. Subsequently, reads were normalized to the sample with the smallest number of sequenced reads. Peaks were called with MACS14 (Zhang et al., 2008) with maximal 3 duplicates, a p-value cut-off of $1e^{-5}$ and the input sample as control. Resulting peaks were annotated to the next transcriptional start of Ensembl genes with the closestBed function from the bedtools suite v2.26.0 (Quinlan and Hall, 2010). Overlapping peaks were identified with bedtools intersect and a minimal overlap of 1bp. LIN9 occupancy was calculated in a window of +/-1kb around TSSs with bedtools coverage function. Density matrices were generated with deeptools v2.3.5 computeMatrix function at a resolution of 1bp and subsequently used for plotting heat maps with plotHeatmap (Ramírez et al., 2014). Promoters, enhancers and super-enhancers were defined as follows: Enhancer were defined by having an enrichment for H3K4me1 overlapping with H3K27ac without H3K4me3 enrichment and being at least 1 kb away from annotated transcriptional start sites (TSS) of Ensembl genes (mouse: GRCm38.p6). Open and active promoters were defined by having an enrichment for H3K4me3 overlapping with H3K27ac without H3K4me1 enrichment and being in a region of ± 1 kb around annotated transcriptional start sites of Ensembl genes. H3K27ac enrichments and read density were used to identify super-enhancers with the ROSE software

(Lovén et al., 2013; Whyte et al., 2013). The overlap of Lin9 and Yap binding sites or Lin9 binding sites at E16.5 and P10 was calculated with bedTools intersectBed with at least 1bp overlap and the proportional Venn diagram was drawn with the Galaxy open source web-based software (Afgan et al., 2018).

2.2.6.3 Data availability

ChIP- and RNA-sequencing datasets are available at the NCBI's Gene Expression Omnibus under the accession number GEO: GSE137132 (Edgar et al., 2002). Mapped ChIP-seq data for histone marks were taken from the ENCODE portal (Sloan et al., 2016) (https://www.encodeproject.org/) with the following identifiers: ENCFF056JGV, ENCFF295HNV, ENCFF642EEK, ENCFF687BWU.

2.2.6.4 Statistical analysis

Unless stated otherwise, data in bar charts are presented as mean +/- standard error of the mean (SEM). For statistical analysis, Prism 5.0 (GraphPad) was used. Statistical tests to determine statistical significance were indicated in the corresponding figure legend. For comparison of two groups, two-tailed Student's t-test was used. For analysis of RNA expression data to a hypothetical pre-defined value, one-sample t-test was used with the hypothetical value set to 1. P-values ≤ 0.05 were considered to be statistically significant and marked by asterisk: * $P \leq 0.05$; ** $P \leq 0.01$; *** $P \leq 0.001$; **** $P \leq 0.0001$. P-values > 0.05 are labeled as not significant (ns). In box plots, the central line reflects the median, the borders of the boxes indicate the first and third quartile and whiskers extend to 1.5 of the interquartile range. Outliers are shown as dots. P-values were calculated with a two-tailed Wilcoxon rank sum test (unpaired samples) or Wilcoxon's signed-rank test (paired samples).

3. Results

3.1 Myb-MuvB (MMB) target genes are downregulated during heart development

Recently, our laboratory was able to show that deletion of GAS2L3 in mice results in heart failure after birth (Stopp et al., 2017). GAS2L3 is a cytosceleton crosslinking protein, which interacts with both actin and tubulin filaments (Wolter et al., 2012). Moreover, GAS2L3 is a member of the chromosomal passenger complex (CPC) and is essential for correct timing of cytokinesis and abscission in mammalian cells (Fackler et al., 2014; Wolter et al., 2012). Initially, GAS2L3 was identified in a micorarray study as a target gene of the mammalian Myb-MuvB complex (MMB) (Reichert et al., 2010). In this study, GAS2L3 was strongly downregulated in LIN9 knockout mouse embryonic fibroblasts (MEFs). In cultured cells, knockdown or depletion of GAS2L3 resulted in defects during mitosis and cytokinesis, which led to bi- or multinucleated cells (Reichert et al., 2010; Stopp et al., 2017; Wolter et al., 2012). *In vivo* in mice, the deletion of GAS2L3 results in premature binucleation of cardiomyocytes (Stopp et al., 2017). During murine heart development, the process of cardiomyocyte binucleation starts shortly after birth and ends between 10 to 14 days after birth. Around 80% of murine cardiomyocytes become binucleated (Uygur and Lee, 2016). The mechanism behind this process is poorly understood. In Stopp et al., 2017, we showed that the expression of GAS2L3 was strongly reduced in wildtype hearts shortly after birth. In this thesis we addressed the question whether other MMB target genes exhibit a similar expression pattern and how the MMB complex regulates gene expression of cell cycle genes in the heart.

In the first set of experiments, gene expression of the MMB complex as well as of MMB targets was analyzed by RT-qPCR and western blotting in wildtype hearts during the time period around birth when cardiomyocytes get binucleated. Therefore, hearts of E16.5 (embryonic day 16), P1 (postnatal day 1) and P10 (postnatal day 10) mice were collected and RNA or proteins were isolated. Then, the expression of the MMB-complex and several MMB target genes was analyzed by RT-qPCR or immunoblotting. mRNA expression of the MuvB core proteins, *Lin9* and *Lin54,* was downregulated at P1 and further downregulated at P10, compared to the embryonal time point (**Figure 6A**, (1)). Expression of *Lin37* peaked at P1 and dropped later at P10, whereas the expression of *Lin52* did not change over time (**Figure 6A**, (1)). The transcription factors of the repressive DREAM-complex, *p130* and *E2F4*, showed a peak in expression at P1. However, expression of *p107* was reduced at P1 and further downregulated at P10 (**Figure 6A**). Transcription factors of the Myb-MuvB complex, *Mybl2* and *FoxM1*, were strongly downregulated at P1 and further downregulated at P10 (**Figure 6A**, (1)). On protein level the expression pattern of P130, B-MYB, FOXM1 and LIN9 were validated by immunoblotting (**Figure 6B**). In **Figure 6C**, expression of well-known MMB target genes was analyzed by RT-qPCR. At P1 and P10 the analyzed genes, like *Ect2* or *Top2a*, were robustly downregulated compared to the embryonal time point (1). For TOP2A, NUSAP1 and CENPF the expression pattern was confirmed on protein level analyzed by immunoblotting (**Figure 6D**, (1)).

Together these results suggest that the MMB complex as well as MMB target genes are strongly downregulated after birth and are important in the heart during embryogenesis.

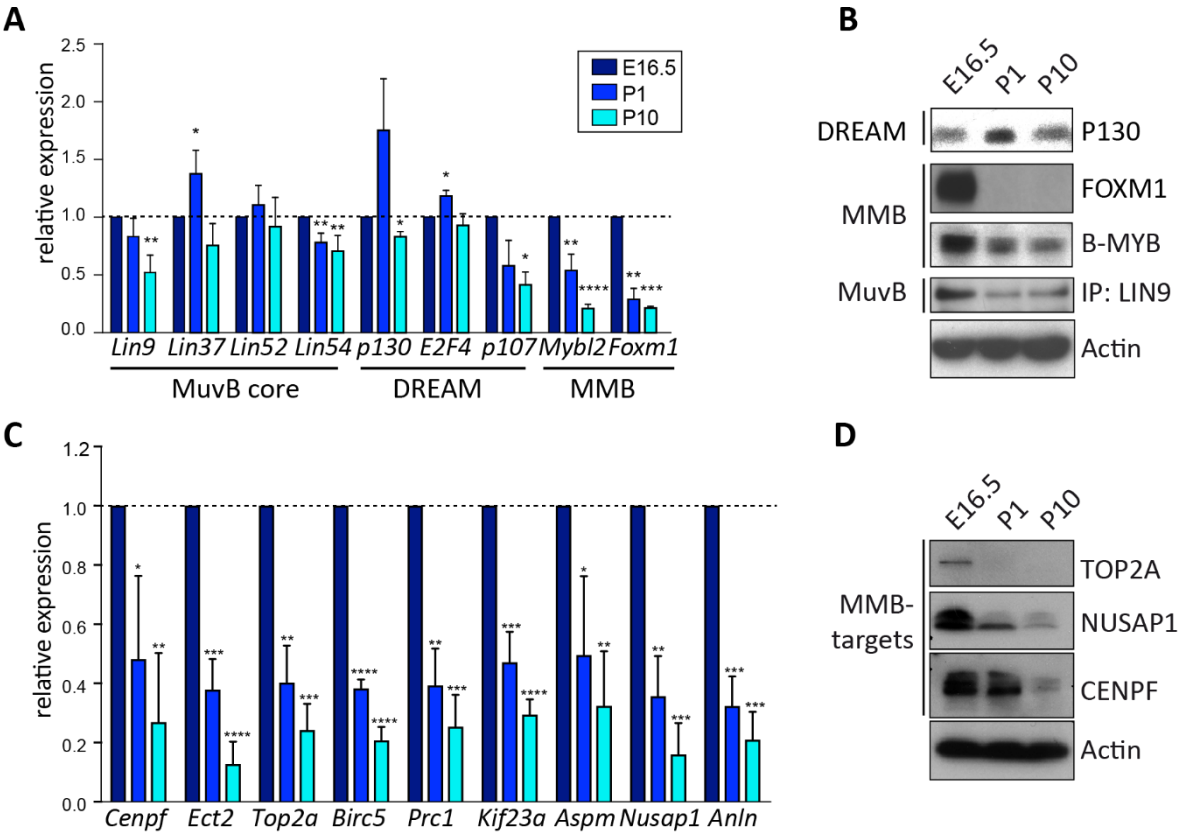

Figure 6: Regulation of the MMB complex and MMB target genes during heart development
(**A**-**D**) RNA (**A** and **C**) or protein (**B** and **D**) was isolated from hearts of the depicted time points (E16.5, P1 or P10). (**A**) mRNA expression of genes of the MuvB core, DREAM or MMB complex was analyzed by RT-qPCR in P1 and P10 hearts relative to E16.5 hearts. (**B**) Protein lysates of the depicted time points were separated by SDS-PAGE and subsequently analyzed by immunoblotting using specific antibodies against P130, FOXM1, B-MYB and LIN9. Actin served as a loading control. (**C**) mRNA expression of MMB target genes was analyzed by RT-qPCR in P1 and P10 hearts relative to E16.5 hearts. (**D**) Protein lysates of the depicted time points were separated by SDS-PAGE and then analyzed by immunoblotting using specific antibodies against TOP2A, NUSAP1 and CENPF. Actin served as a loading control. (**A**, **C**) *Actin* and *Hprt* were used for normalization. Means of three biological replicates, each measured in technical triplicates, are depicted. Error bars represent standard error of the mean (SEM). Statistical significance was tested using the one sample Student's t-test, two-tailed. *P≤0.05, ** P≤0.01, ***P≤0.001, ****P≤0.0001, ns, not significant, P≥0.05. (**A**, **C**, **D**) Parts of the experiment were performed by Laura Hauf (B.Sc. student) (1).

3.2 Loss of MuvB core subunit LIN9 in heart progenitor cells results in early embryonal lethality

Given the regulation of MMB target genes in the heart, we wanted to know whether the MMB complex is important for correct heart development. To answer this question, *Lin9*, the central subunit of the MuvB core, was deleted in heart progenitor cells by Nkx2.5-Cre. In this system

the Cre-recombinase is driven by a Nkx2.5 promoter, which is active in early heart development (Lints et al., 1993; Stanley et al., 2002). To analyze the survival of *Nkx-Cre; Lin9$^{fl/fl}$* mice, mice were bred according to the scheme in **Figure 7A**. Until embryonic day 13 (E13.5), *Nkx-Cre; Lin9$^{fl/fl}$* and heterozygous *Nkx-Cre; Lin9$^{fl/+}$* control animals were identified in the expected mendelian ratios. After that time point no *Nkx-Cre; Lin9$^{fl/fl}$* animals could be detected. Hence, *Nkx-Cre; Lin9$^{fl/fl}$* mice died between E13.5 and E18.5 (**Figure 7A**). Complete deletion of Lin9 in the heart was confirmed by genomic *Lin9* PCR of embryos (tails) and their corresponding hearts (**Figure 7B**). To further characterize the phenotype of *Nkx-Cre; Lin9$^{fl/fl}$* mice, E13.5 sections were stained with hematoxylin and eosin (H&E). **Figure 7C** shows representative images from heart sections of *Nkx-Cre; Lin9$^{fl/fl}$* and *Nkx-Cre; Lin9$^{fl/+}$* with a high magnification demonstrating pleiromorphic and enlarged nuclei.

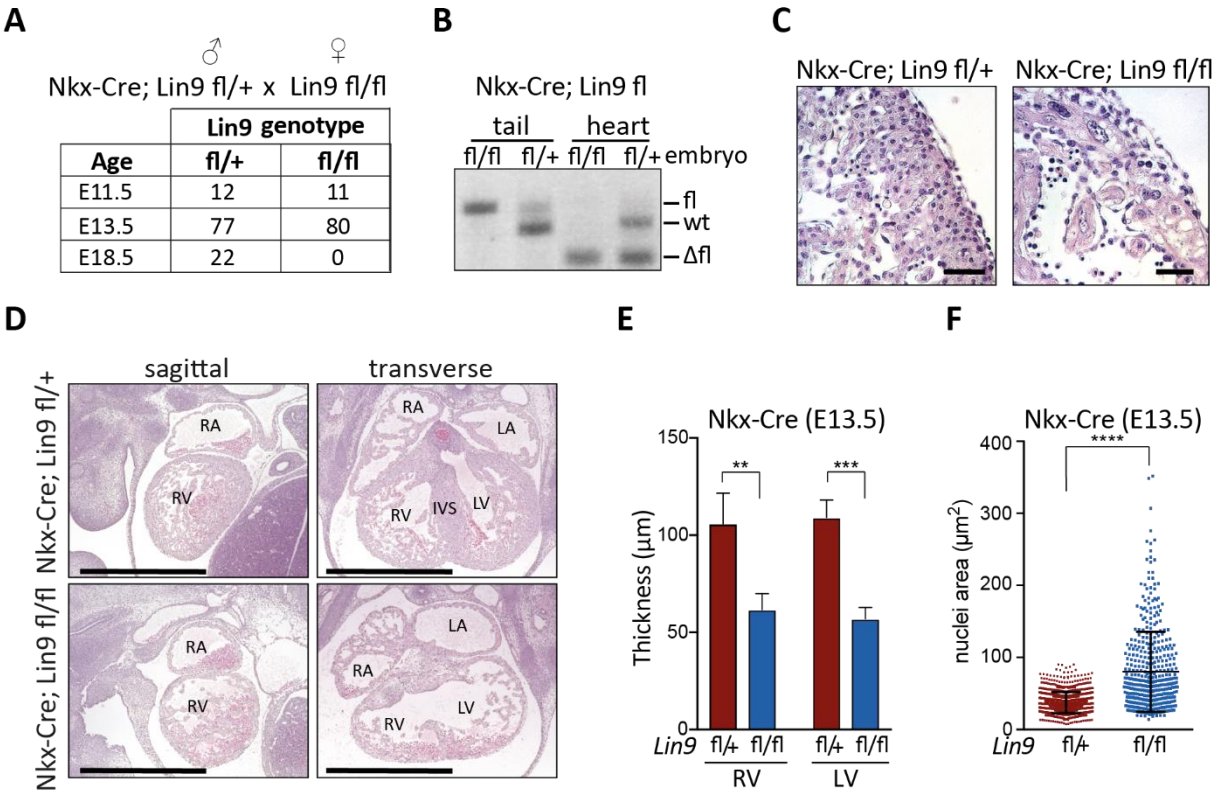

Figure 7: Loss of LIN9 in heart progenitor cells results in embryonic lethality and thinning of ventricular walls

(**A**) Breeding scheme and resulting genotypes at the depicted time points of *Nkx-Cre; Lin9* mice. (**B**) Genomic PCR to determine *Lin9* allele status in embryos (tail) or hearts at E13.5: wt: wildtype *Lin9* allele; fl: non-recombined *Lin9* allele; Δfl: recombined *Lin9* allele. (**C**) High magnification images of hematoxylin and eosin (H&E) stained section of *Nkx-Cre; Lin9* mice with the indicated genotypes at E13.5. Scale bar: 25µm. (**D**) Representative images of H&E stained sagittal and transverse sections of *Nkx-Cre; Lin9* mice with the depicted genotypes at E13.5. RA: right atrium; LA: left atrium; RV: right ventricle; LV: left ventricle; IVS: interventricular septum. Scale bar: 1 mm. (**E**) Quantification of ventricular wall thickness. n=3 *Nkx-Cre; Lin9$^{fl/fl}$* and n=5 *Nkx-Cre; Lin9$^{fl/+}$*. (**F**) Quantification of nuclear area in the myocardium of *Nkx-Cre; Lin9* mice with the indicated genotypes at E13.5. Per genotype, 500 cells were measured. (**E**, **F**) Error bars indicate standard deviation (SD). Statistical significance was tested using the Student's t-test, two-tailed. *P≤0.05, ** P≤0.01, ***P≤0.001, ****P≤0.0001, ns, not significant, P≥0.05. (**E**, **F**) Quantification was done by Laura Hauf (B.Sc. student) (1).

Overview images from sagittal and transverse section are shown in **Figure 7D**. Transverse sections were used to measure ventricular wall thickness. Thickness of the right ventricle (RV) and left ventricle (LV) were significantly reduced after loss of *Lin9* (**Figure 7E,** (1)). In contrast to that, the nuclear area of cardiomyocytes from *Nkx-Cre; Lin9$^{fl/fl}$* mice was robustly increased compared to heterozygous *Nkx-Cre; Lin9$^{fl/+}$* animals (**Figure 7F**, (1)).
To further characterize the phenotype of *Nkx-Cre; Lin9* mice, immunohistochemical analysis of sections of E13.5 embryos was performed. To assess the proliferation rate of cardiomyocytes, sections were stained for cell cycle marker Ki67 and phosphorylated histone H3 (pH3). Ki67 is expressed in the nucleus of cells at all active phases of the cell cycle (G_1, G_2, S and M phase) and is absent in quiescent cells (G_0). Therefore, Ki67 is a general marker for proliferating cells. On the contrary, pH3 is only expressed in the nucleus of cells during mitosis. Hence, pH3 is a marker for mitotic cells. To specifically identify dividing cardiomyocytes, cell cycle markers were co-stained with cardiac Troponin T (cTnT), a sarcomere-associated protein, which serves as a marker for cardiomyocytes. **Figure 8A** shows representative images of the immunohistochemical analysis. Quantification of these images revealed that loss of *Lin9* strongly reduces the percentage of mitotic cardiomyocytes from 1.2% in *Nkx-Cre; Lin9$^{fl/+}$* (control) sections to 0.1% in *Nkx-Cre; Lin9$^{fl/fl}$* (Lin9KO) animals (**Figure 8B**, (1)). Consistently, the fraction of Ki67 positive cardiomyocytes decreases from over 80% in control sections to almost 20% in Lin9KO sections (**Figure 8C**, (1)). In summary, deletion of *Lin9* results in decreased levels of mitotic as well as proliferating cardiomyocytes.

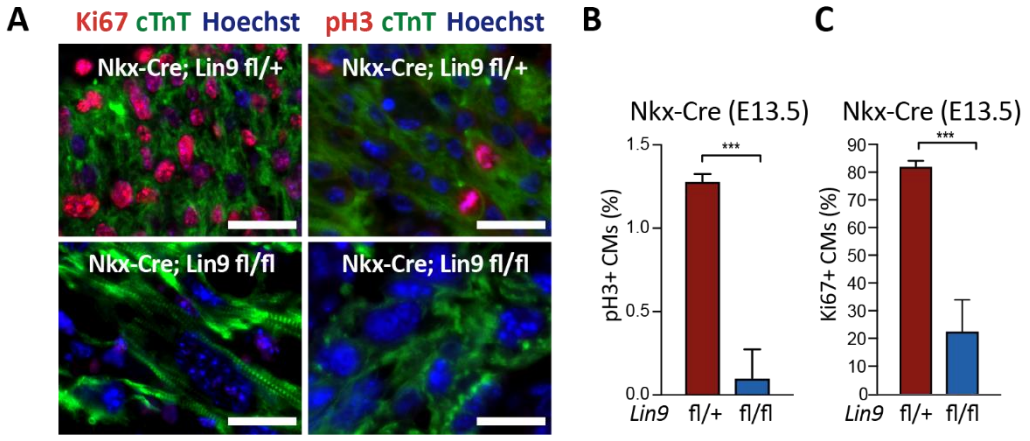

Figure 8: Deletion of *Lin9* leads to reduced proliferation
(**A**) Representative images of immunohistochemical analysis of *Nkx-Cre; Lin9* sections with the indicated genotype at E13.5. Left panel is stained for Ki67 (red) and cardiac Troponin T (cTnT, green). Nuclei were counterstained with Hoechst (blue). Right panel is stained for phosphorylated histone H3 (pH3, red), cTnT (green) and Hoechst (blue). Scale bar: 25 µm. (**B**, **C**) Quantification of (**A**). n=3 *Nkx-Cre; Lin9$^{fl/+}$* and n=3 *Nkx-Cre; Lin9$^{fl/fl}$*. Error bars indicate standard deviation (SD). Statistical significance was tested using the Student's t-test, two-tailed. ***P≤0.001. Per genotype, 500 cells were counted. (**B**, **C**) Quantification was done by Laura Hauf (B.Sc. student) (1).

Next, we wanted to determine whether there is a selection disadvantage for proliferation of cardiomyocytes following loss of *Lin9*. For that reason, we crossed *Nkx-Cre; Lin9* mice with a double fluorescent reporter strain (*mT/mG*). In this strain, membrane bound Tomato (mT) is ubiquitously expressed under a ROSA26 promoter. Upon Cre mediated deletion of the mT allele, membrane bound GFP (mG) is expressed and cells switch from red to green fluorescence (**Figure 9A**) (Muzumdar et al., 2007).

This change in fluorescence was measured by flow cytometry analysis (FACS). As a control, no fluorescent signal was detected in cardiomyocytes that do not harbor the *mT/mG* allele. In cardiomyocytes that do not express Cre recombinase, but harbor the *mT/mG* allele, 95% of cells show red fluorescence (**Figure 9A**, **B**). After combining the *Nkx-Cre; Lin9*$^{fl/+}$ with the *mT/*mG allele 95% of cardiomyocytes exhibit green fluorescence, indicating complete recombination. In contrast, in *Nkx-Cre; Lin9*$^{fl/fl}$*; ROSA26*$^{mTmG/+}$ cardiomyocytes almost 50% of the analyzed cells remained red (**Figure 9B**, **C**). This result indicates that the loss of *Lin9* is detrimental for growth of cardiomyocytes. To sum up this part, loss of the MuvB subunit LIN9 in heart progenitor cells causes a severe embryonal lethal phenotype. Reduced proliferation and disadvantage in growth of cardiomyocytes after loss of *Lin9* culminate in malformation of the heart.

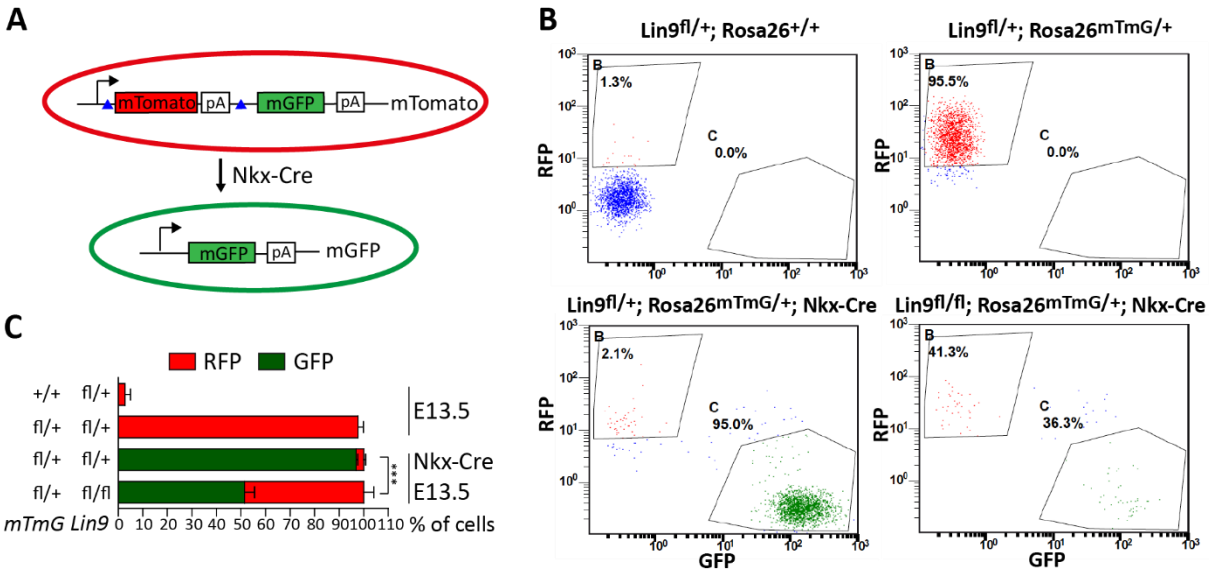

Figure 9: Loss of LIN9 results in a selection disadvantage for growth of cardiomyocytes
(**A**) Scheme of the mT/mG double fluorescent reporter system. Upon Cre-recombination, red fluorescent mTomato (mT) is deleted and green fluorescent mGFP (mG) is expressed. (**B**) Representative FACS profiles with the indicated genotypes. Gates were determined for mT positive cells (B, top left) and mG positive cells (C, bottom right). 10,000 cells were analyzed for each genotype. (**C**) Quantification of (**B**). n=3-4 biological replicates. Error bars indicate standard error of the mean (SEM). Statistical significance was tested using the Student's t-test, two-tailed. ***P≤0.001.

3.3 LIN9-dependent genes overlap with signatures of mitotic as well as respiratory genes

To identify the reason for the *Nkx-Cre; Lin9* phenotype at the transcriptional level and to analyze LIN9-dependent genes in cardiomyocytes, whole transcriptome analysis was performed. Thus, RNA was isolated from ventricular heart tissue of *Nkx-Cre; Lin9*$^{fl/fl}$ (Lin9KO) and *Nkx-Cre; Lin9*$^{fl/+}$ (control) mice at E13.5. Subsequently, RNA was subscribed in cDNA libraries and sequenced by next-generation sequencing (RNA-Seq). For the analysis of the *Nkx-Cre; Lin9* transcriptome, RNA-Seq was performed in two biological replicates, each done in triplicates of control and Lin9KO hearts. Next, gene set enrichment analysis was performed to

identify classes of genes enriched or depleted by the loss of *Lin9* in the heart. To identify clusters of genes, which are significantly regulated by *Lin9* in each replicate, the normalized enrichment score (NES) of each gene set was plotted in **Figure 10A**. Gene sets located at the diagonal dotted line are equally regulated in each replicate after deletion of *Lin9*. Gene sets in the top right quadrant have a positive NES and are upregulated in both replicates by loss of *Lin9*. Gene sets in the bottom left quadrant have a negative NES and are downregulated in both replicates by loss of *Lin9*. This method allows to identify several significant Lin9-dependent gene signatures (grey). For example, hematopoietic gene signatures (ochre) are upregulated after loss of *Lin9* in the heart indicating incipient inflammatory reactions (**Figure 10A**). On the other hand, respiratory gene signatures such as respiratory electron transport (**Figure 10D**) as well as citric acid cycle (**Figure 10E**) were significantly downregulated after loss of *Lin9* in the heart indicating reduced metabolic activity of cardiomyocytes. Subsequently, several mitotic gene signatures, such as Reichert: LIN9 targets (Reichert et al., 2010) or Pattschull: direct LIN9 (Pattschull et al., 2019) were downregulated after deletion of *Lin9* in the heart (**Figure 10B**, **C**). In line with the characterization by H&E and immunohistochemical staining, transcriptional analysis of the *Nkx-Cre; Lin9* phenotype revealed a strong downregulation of mitotic gene signatures including several well-known MMB-target genes. In addition, hematopoietic gene signatures associated with inflammatory reactions are upregulated and respiratory genes are downregulated.

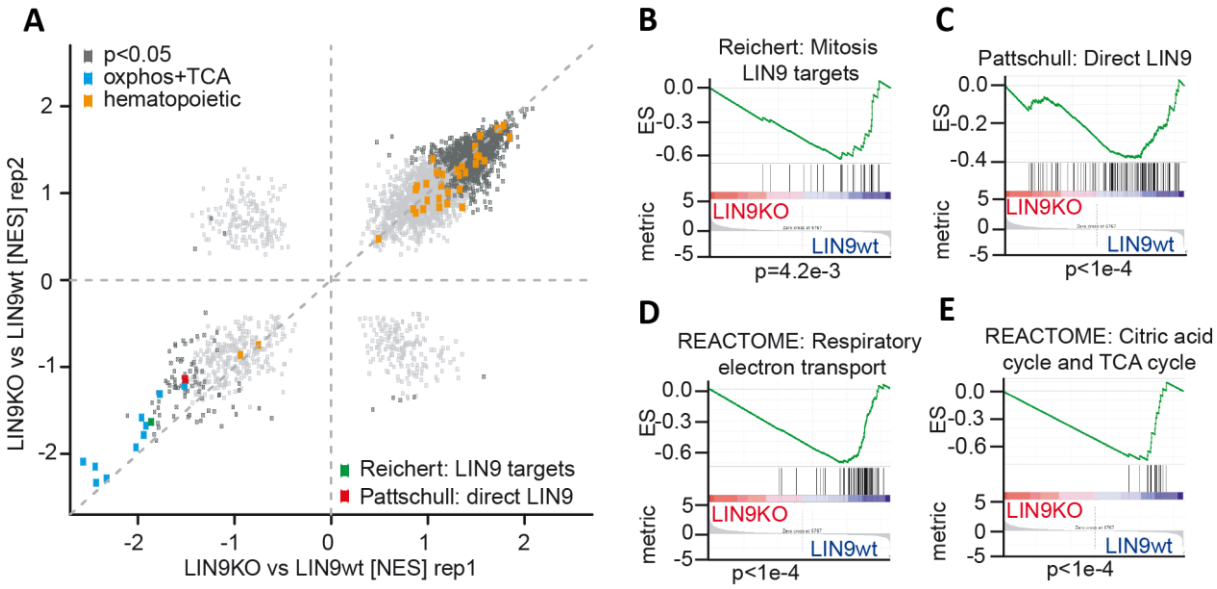

Figure 10: Signatures of mitotic as well as respiratory genes are downregulated after loss of *Lin9*
(**A**) Gene set enrichment analysis (GSEA) comparing expression differences in *Nkx2.5-Cre; Lin9$^{fl/fl}$* (LIN9 KO) and *Nkx2.5-Cre; Lin9$^{fl/+}$* (LIN9 wt) heart ventricles from E13.5 mice in two biological replicates (each done in triplicates). The C2 MSigDB was spiked with the Hallmark gene sets and a set of LIN9 direct targets genes from (Pattschull et al., 2019) (red). The mitotic LIN9 target gene set from (Reichert et al., 2010) is highlighted in green. Gene sets related to respiration/TCA cycle ("oxphos") and hematopoietic cells are highlighted in blue and ochre, respectively. Gene sets significantly regulated in both replicates are depicted in grey ($p \leq 0.05$). NES: normalized enrichment score. (**B**-**E**) Representative gene sets from the analysis in (**A**). p-values were calculated using a permutation test with 1000 permutations. „Signal2Noise" was used as a metric to rank genes. ES: enrichment score.

3.4 Proliferation of embryonal Hippo-deficient cardiomyocytes depends on LIN9

As described above, the transcriptomic analysis showed that expression of mitotic genes in the heart is strongly dependent on *Lin9*. Recently, we could demonstrate that late cell cycle genes are co-regulated by the MMB-complex and the transcriptional coactivator of the Hippo pathway, YAP1, in a lung tumor cell line (Pattschull et al., 2019). Interestingly, there is strong evidence that the Hippo-YAP pathway regulates expression of mitotic genes in the heart (von Gise et al., 2012; Heallen et al., 2011; Xin et al., 2013). This led to the hypothesis that there might be a crosstalk between the MMB complex and the Hippo-YAP pathway in the heart.
To address this hypothesis, we designed a genetic mouse model where we deleted *Lin9*, the core component of the MMB-complex, and *Sav1*, a scaffold protein required for Hippo kinase activity. Deletion of the conditional (floxed) alleles of *Lin9* and *Sav1* in cardiac progenitor cells was achieved by using *Nkx-Cre*. Hence, we could specifically delete *Lin9* alone (*Nkx-Cre; Lin9$^{fl/fl}$; Sav1$^{+/+}$*), *Sav1* alone (*Nkx-Cre; Lin9$^{fl/+}$; Sav1$^{fl/fl}$*) or *Lin9* and *Sav1* together (*Nkx-Cre; Lin9$^{fl/fl}$; Sav1$^{fl/fl}$*). Mice heterozygous for *Lin9* (*Nkx-Cre; Lin9$^{fl/+}$; Sav1$^{+/+}$*) served as a control.
In a first set of experiments, immunohistochemical analysis was performed to assess whether proliferation of Hippo-deficient cardiomyocytes was dependent on *Lin9*. Therefore, E13.5 heart sections of *Nkx-Cre; Lin9; Sav1* mice with the indicated genotypes were stained for cell cycle marker Ki67. To identify cardiomyocytes, sections were co-stained with cardiac Troponin T (cTnT). Compared to *Sav1* wildtype hearts, the fraction of Ki67 positive cardiomyocytes increased from 65% to 82% after deletion of *Sav1*, indicating enhanced proliferation in Hippo-deficient hearts as reported previously (Heallen et al., 2011) (**Figure 11A**, **B**). As demonstrated before, deletion of *Lin9* strongly reduced the number of Ki67 positive cardiomyocytes to almost 15%. Interestingly, the fraction of Ki67 positive cardiomyocytes remained low after deletion of *Sav1* and *Lin9*, indicating that proliferation in Hippo-deficient cardiomyocytes is dependent on *Lin9* (**Figure 11A**, **B**).
This result was verified by an immunohistochemical analysis of E13.5 heart sections stained for pH3, a marker for mitosis. Again, cTnT was used to identify cardiomyocytes. After deletion of *Sav1*, the fraction of mitotic cardiomyocytes increased from 2% to more than 5% compared to *Sav1* wildtype hearts (**Figure 11C**, **D**). In contrast, deletion of *Lin9* reduced the fraction of mitotic cardiomyocytes to 0.2%. After deletion of *Sav1* and *Lin9*, the fraction of mitotic cardiomyocytes remained low.
These results suggest that the pro-proliferative phenotype after inactivation of the Hippo signaling cascade is dependent on the MMB subunit LIN9.

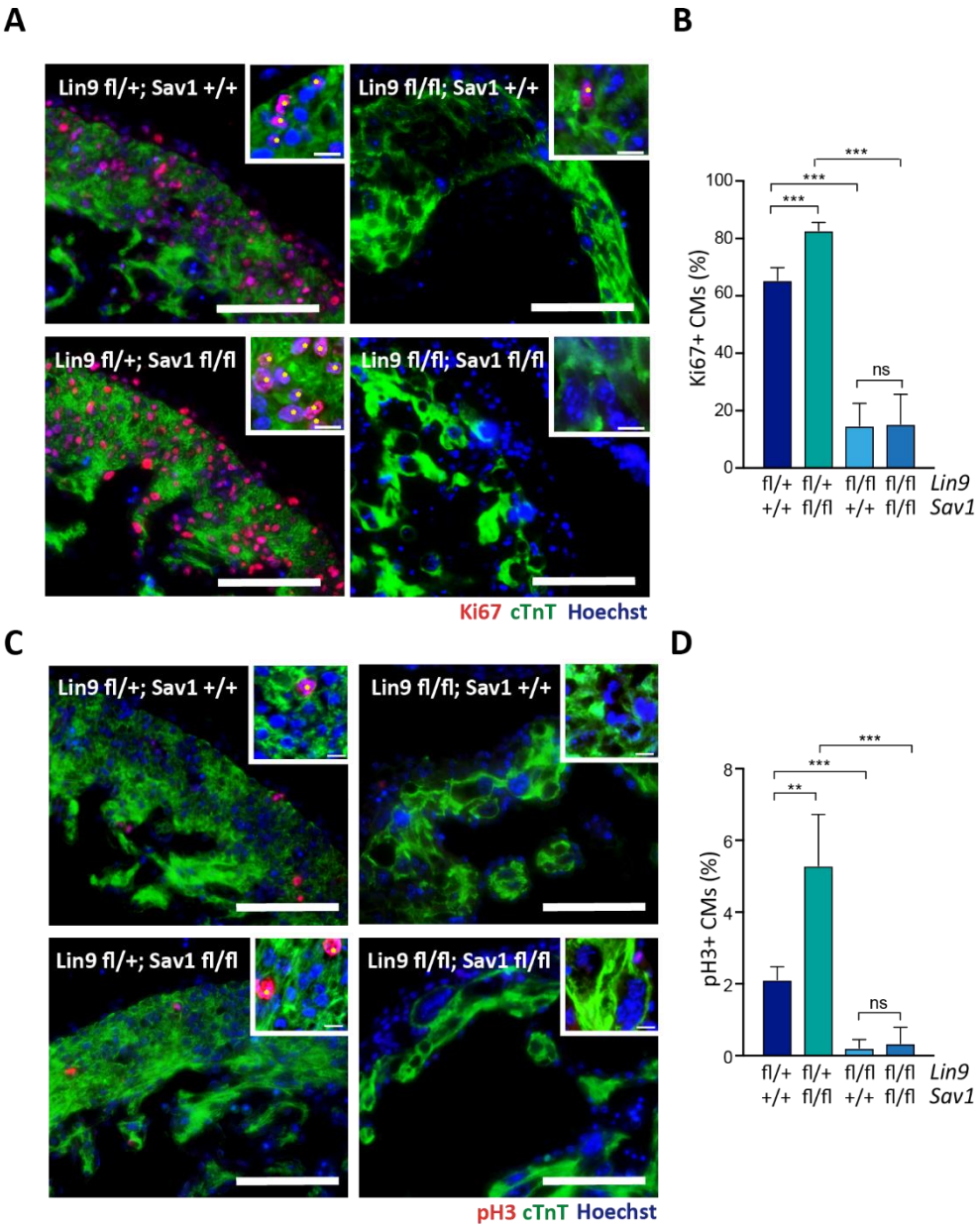

Figure 11: Proliferation of embryonal Hippo-deficient cardiomyocytes is LIN9 dependent
(**A**) Representative images of immunohistochemical analysis of *Nkx-Cre; Lin9; Sav1* sections with the indicated genotypes at E13.5. Sections were stained for Ki67 (red), cTnT (green) and Hoechst (blue). Scale bar: 200 µm. Magnification images (x63) are shown in the top right corner. Asterisk mark Ki67 positive cardiomyocytes. (**B**) Quantification of (**A**). (**C**) Representative images of immunohistochemical analysis of *Nkx-Cre; Lin9; Sav1* E13.5 heart sections with the indicated genotypes. Sections were stained for pH3 (red), cTnT (green) and Hoechst (blue). Scale bar: 200 µm. Magnification images (x63) are shown in the top right corner. Asterisk mark pH3 positive cardiomyocytes. (**D**) Quantification of (**C**). n=5 *Nkx-Cre; Lin9$^{fl/+}$; Sav1$^{+/+}$*; n=4 *Nkx-Cre; Lin9$^{fl/+}$; Sav1$^{fl/fl}$*; n=6 *Nkx-Cre; Lin9$^{fl/fl}$; Sav1$^{+/+}$;* n=6 *Nkx-Cre; Lin9$^{fl/fl}$; Sav1$^{fl/fl}$*. (**B**, **D**) Error bars indicate standard error of the mean (SEM). Statistical significance was tested using the Student's t-test, two-tailed. ** P≤0.01, ***P≤0.001, ns, not significant, P≥0.05.

3.5 Enrichment of mitotic gene signatures in Hippo-deficient cardiomyocytes is LIN9 dependent

To identify genes responsible for the proliferative phenotype of Hippo-deficient cardiomyocytes and to analyze the impact of *Lin9* deletion on these genes, we performed RNA-sequencing. To do so, we isolated RNA from ventricular heart tissue of *Lin9* deleted, *Sav1* deleted and *Lin9* and *Sav1* double mutant mice. By gene set enrichment analysis (GSEA) we compared *Sav1* deleted and *Sav1* wildtype hearts in a *Lin9* wildtype background (x-axis) or *Lin9* knockout background (y-axis). Gene sets were plotted according to their normalized enrichment score (NES) in **Figure 12A**.

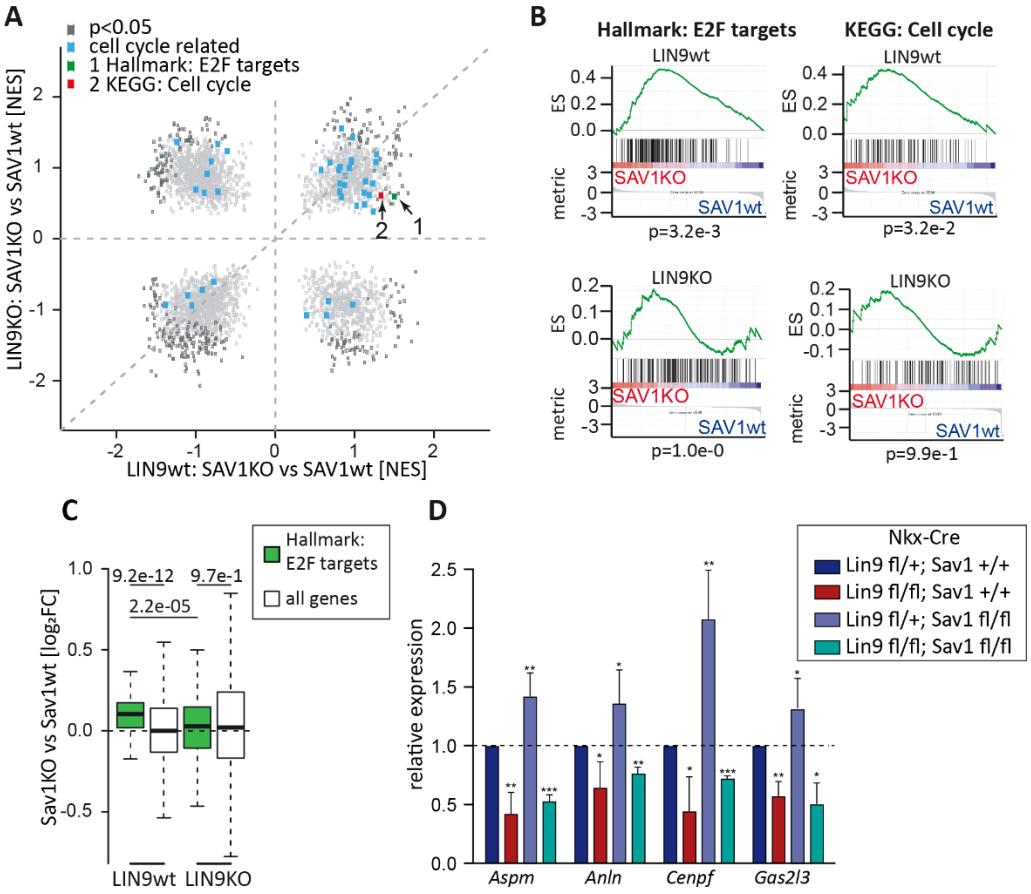

Figure 12: The Hippo pathway and MuvB regulate an overlapping set of cell cycle genes
(**A**) GSEA comparing the effect of deletion of *Sav1* in Nkx-Cre LIN9 wt and LIN9 KO heart ventricles at E13.5. The C2 MSigDB was spiked with the Hallmark gene set: E2F targets (green) and the KEGG pathway: Cell cycle (red). Gene sets related to cell cycle are highlighted in blue. Gene sets significantly regulated are indicated in dark grey (p≤0.05). NES: normalized enrichment score. (**B**) Representative gene sets from the analysis in (**A**). p-values were calculated using a permutation test with 1000 permutations. „Signal2Noise" was used as a metric to rank genes. ES: enrichment score. (**C**) Boxplot comparing differences in E2F target gene expression between *Nkx2.5-Cre; Sav1$^{fl/fl}$* (Sav1 KO) and *Nkx2.5-Cre; Sav1$^{+/+}$* (Sav1 wt) heart ventricles in *Lin9$^{fl/fl}$* (LIN9 KO) or *Lin9$^{fl/+}$* (LIN9 wt) background. (**D**) Expression of the indicated genes analyzed by RT-qPCR in heart ventricles of embryos at E13.5 with the indicated genotypes. Expression is relative to *Actin* and *Hprt*. n=6 biological replicates. Error bars indicate standard error of the mean (SEM). Statistical significance was tested using the one-sample Student's t-test, two-tailed. * P≤0.05, ** P≤0.01, ***P≤0.001, ns, not significant, P≥0.05.

This allowed us to identify genes which are upregulated by deletion of *Sav1* in the heart. Most of the cell cycle related gene signatures (blue) are enriched in *Sav1* knockout hearts. On the other hand, genes whose activation due to *Sav1* deletion is suppressed by simultaneous deletion of *Lin9* could be identified. For example, gene signatures of Hallmark: E2F targets (green) or KEGG: Cell Cycle (red), are significantly enriched after Hippo inactivation, whereas this activation is prevented by co-deletion of *Lin9* with *Sav1* (**Figure 12B**, **C**). To verify the results obtained from the RNA-seq experiment, RNA was isolated from hearts with the depicted genotypes and independent qPCR experiments were performed. The expression of the cell cycle related genes *Aspm*, *Anln*, *Cenpf* and *Gas2l3* was upregulated after deletion of *Sav1*, downregulated after *Lin9* deletion and expression levels remained low after deletion of both *Sav1* and *Lin9* (**Figure 12D**). Together these results suggest that there is a set of cell cycle genes, in which the elevated expression after Hippo inactivation is dependent on the function of the MMB complex.

3.6 Cell cycle genes induced by Hippo-inactivation are direct targets of LIN9

To further investigate whether the cell cycle genes upregulated in Hippo-deficient hearts are direct targets of the MMB complex, genome-wide binding studies were performed. First, high confident LIN9 binding sites were identified by chromatin immunoprecipitation of LIN9 followed by next-generation sequencing (ChIP-Seq) at two time points during heart development (E16.5 and P10). At E16.5 we could identify 3,357 LIN9 binding sites, compared to 2,672 LIN9 binding sites at P10 (**Figure 13A**).

By using previously reported genome wide data on histone modifications from ENCODE (H3K27ac, H3K4me3 and H3K4me1), we could assign LIN9 binding sites to active or inactive promoter sites, enhancers or super-enhancers in the genome. At E16.5 and P10, most LIN9 binding sites are located at active promoters, whereas only less than 5% are located at enhancers or super-enhancers (**Figure 13B**). By comparing LIN9 binding sites from E16.5 with those from P10, we could identify 1,758 overlapping sites with 1,458 of those sites located at promoters of genes. At E16.5, 1,599 unique LIN9 binding sites were identified (812 at promoters). At P10, there are 914 unique LIN9 binding sites (491 of those sites located at promoters) (**Figure 13C**, **E**). In more than 80% of the overlapping LIN9 promoter binding sites, the distance of the center of the peak between E16.5 and P10 is under 250 bp, indicating that the identified binding sites reflect high confident LIN9 bound promoters (**Figure 13D**).

Next, we asked whether the transcriptional coactivator of the Hippo signaling cascade, YAP1, and LIN9 have overlapping binding sites in the embryonal heart. To answer this question, ChIP-Seq with a YAP-specific antibody was performed using chromatin from E16.5 heart ventricles. 1,920 YAP binding sites were identified at E16.5 (**Figure 13A**).

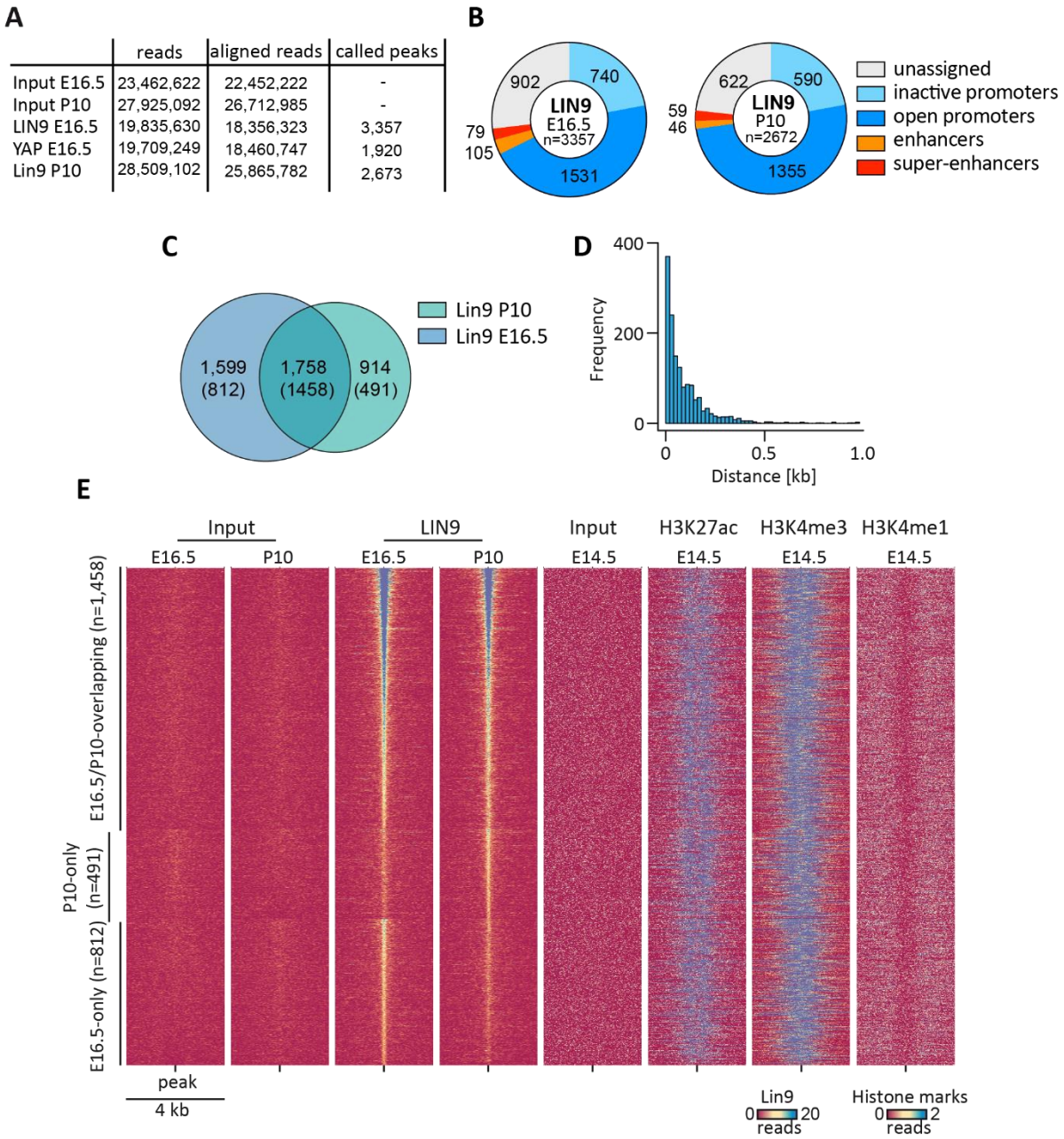

Figure 13: High confident chromatin binding sites of LIN9 at E16.5 and P10

(**A**) E16.5 and P10 heart ventricles were used for ChIP-Seq to identify genome wide LIN9 or YAP binding sites. Table shows the number of reads, reads aligned to the genome and called peaks. (**B**) Pie chart showing the genomic localization of LIN9 binding sites in E16.5 and P10 heart ventricles. Active or inactive promoters, enhancers or super-enhancers were assigned based on ChIP-Seq data from histone modifications (ENCODE). (**C**) VENN diagram showing the overlap between LIN9 peaks at E16.5 and P10. Numbers indicate overall binding sites. Numbers in brackets indicate promoter peaks. (**D**) Histogram showing the absolute distance between overlapping LIN9 peaks called in E16.5 and P10 heart ventricles located at promoters (n=1,458) with a resolution of 20 bp. (**E**) Heat map showing overlapping promoter peaks in E16.5 and P10 heart ventricles (n=1,458), promoter peaks only called in P10 ventricles (n=491) and promoter peaks only called in E16.5 ventricles (n=812). Read density is plotted in a window of +/- 2kb around the center of the peak with a resolution of 20bp (LIN9) or 2bp (histone). Data for histone modifications are taken from ENCODE (GSE31039).

In order to assign YAP peaks to active or inactive promoters, enhancers or super-enhancers, ChIP-Seq data of histone modifications from ENCODE were used. In contrast to LIN9, YAP was predominantly bound to enhancers (450 peaks) and super-enhancers (212 peaks) and only a minor fraction of peaks were located at active promoter sites (192 peaks) (**Figure 14A**). This is consistent with recently published ChIP-Seq data from YAP in human cell lines and in Hippo-deficient murine hearts (Galli et al., 2015; Morikawa et al., 2015; Pattschull et al., 2019; Zanconato et al., 2015). As a consequence, there is only little overlap between LIN9 and YAP binding sites at promoters, enhancer or super-enhancers in E16.5 hearts (**Figure 14B**). For a more detailed view, heatmaps were generated showing the read density of LIN9, YAP and histone modifications from ENCODE at LIN9 bound promoters, YAP bound enhancers and super-enhancers (**Figure 14C**). Overall LIN9 was enriched at promoter sites, whereas almost no YAP signal could be detected at the same sites. In contrast, YAP was strongly enriched at enhancer or super-enhancers sites, while no LIN9 signal could be detected at these regions (**Figure 14C**).

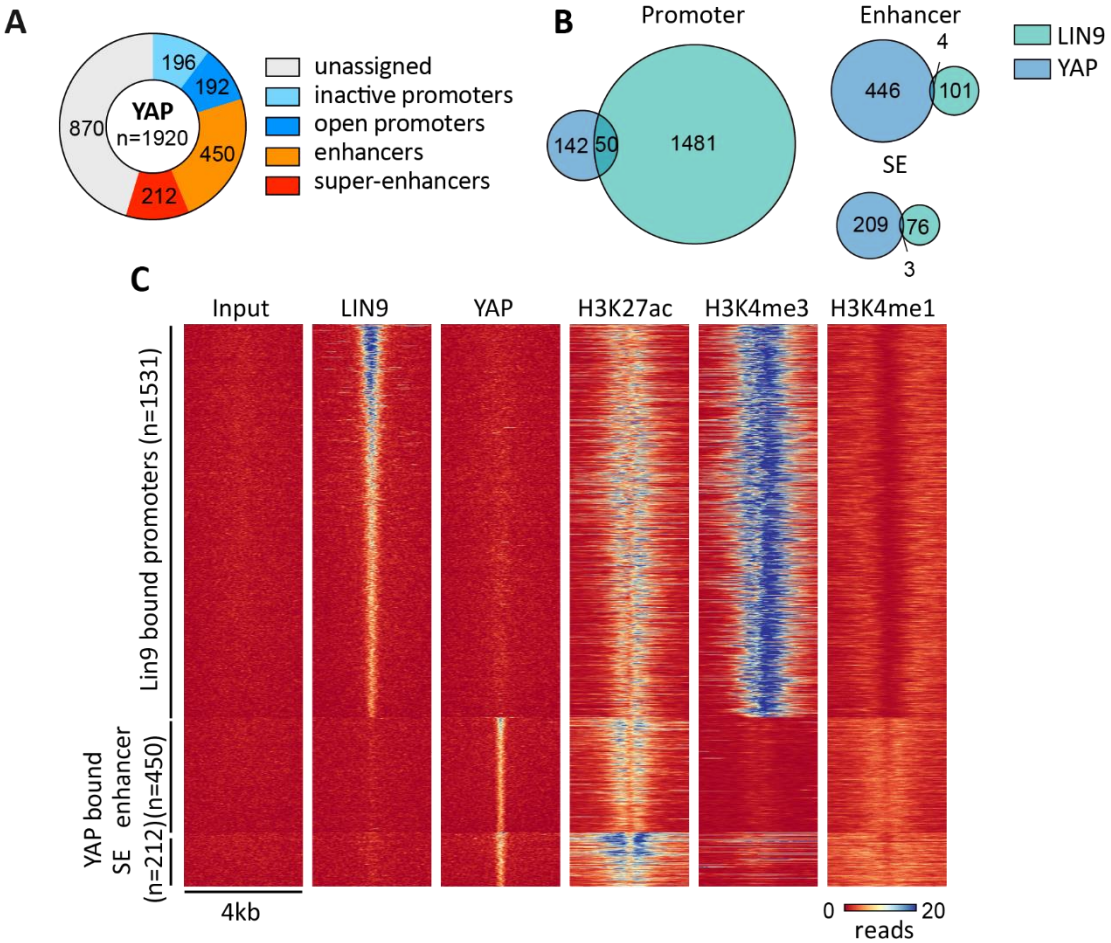

Figure 14: Little overlap between YAP and LIN9 chromatin binding sites in embryonal hearts
(**A**) Pie chart showing the genomic localization of YAP binding sites in E16.5 heart ventricles. Active or inactive promoters, enhancers or super-enhancers were assigned based on ChIP-Seq data from histone modifications (ENCODE). (**B**) VENN diagram showing the overlap between LIN9 and YAP peaks at promoters, enhancers and super-enhancers (SE) in E16.5 heart ventricles. Numbers indicate overall binding sites. (**C**) Heat map showing LIN9, YAP, H3K27ac, H3K4me3, and H3K4me1 read density at LIN9 bound promoters in E16.5 (n=1,531), YAP bound enhancer (n=450), and YAP bound super-enhancers (n=212). Read density is plotted in a window of +/-2kb around the center of the peak with a resolution of 20bp. Data for histone modifications are taken from ENCODE (GSE31039).

Genome browser tracks of well-known MMB target genes (*Aspm* and *Anln*) as well as direct target genes of YAP (*Amotl2* and *Ctgf*) and YAP bound enhancers visualize the ChIP-Seq results (**Figure 15A**, **B** and **Figure 37A**-**C**).

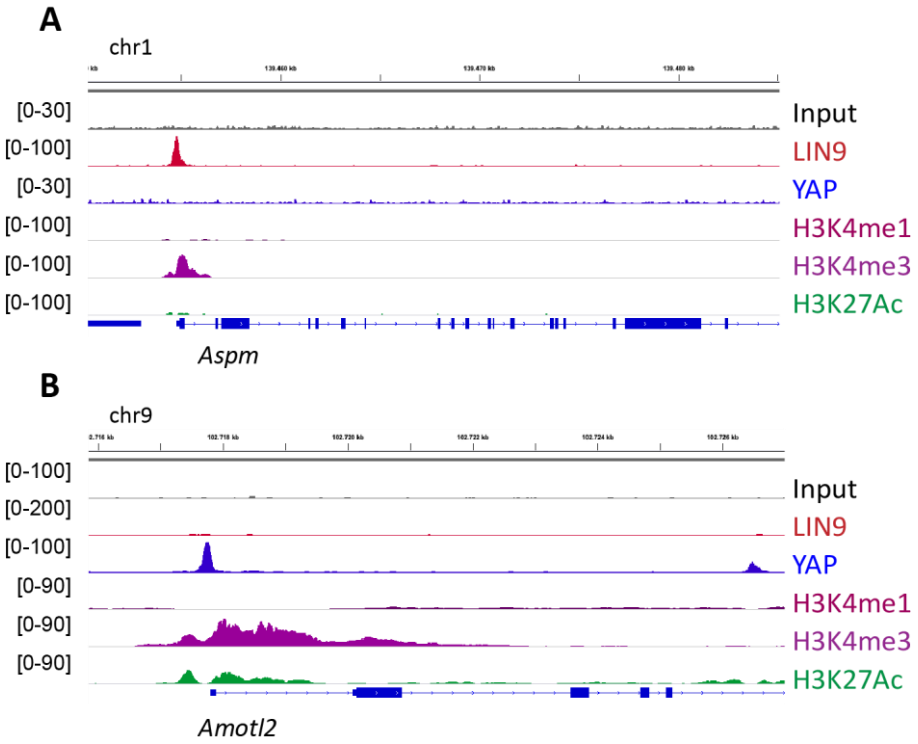

Figure 15: Genome browser tracks of the *Aspm* and *Amotl2* genomic loci
(**A**) Genome browser tracks illustrating the binding of LIN9 to the promoter of *Aspm*. (**B**) Genome browser tracks illustrating the binding of YAP to the promoter of *Amotl2*. ChIP-Seq data of LIN9 and YAP are from E16.5 heart ventricles and histone modifications H3K4me1, H3K4me3 and H3K27Ac in E14.5 heart ventricles are from ENCODE (GSE31039).

To determine classes of genes with a LIN9 or YAP bound promoter, bioinformatic analysis with Database for annotation, visualization and integrated discovery (DAVID) was performed, a tool to categorize genes into biological GO-terms and to identify enriched GO-terms according to p-values. DAVID analysis of genes with a LIN9 bound promoter showed that LIN9 is primarily bound to promoters of cell cycle and mitotic genes (**Figure 16A**). On the contrary, YAP binds to promoters of genes involved in muscle or heart development indicating that LIN9 and YAP bind to promoters of different genes at E16.5 (**Figure 16B**).

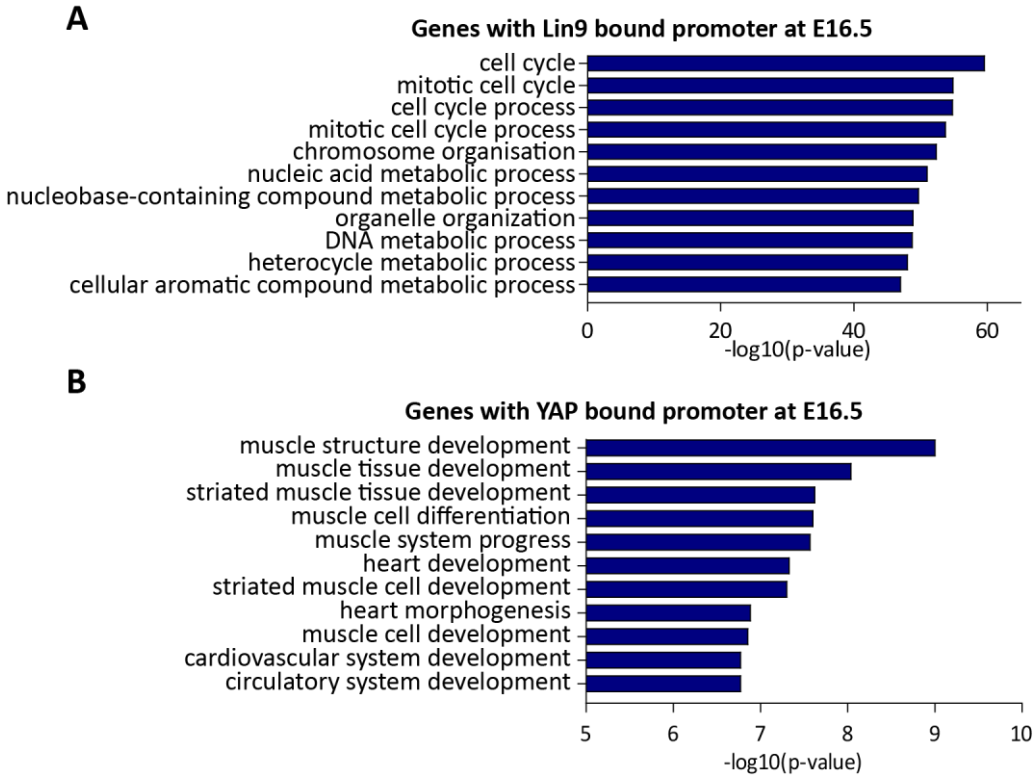

Figure 16: YAP and LIN9 are bound to different gene set at E16.5
Database for annotation, visualization and integrated discovery (DAVID) analysis: Functional annotation of LIN9 (**A**) and YAP (**B**) bound promoter genes in E16.5 heart ventricles. Top 11 classifications are shown ranked according to the negative decardian logarithm of their p-value. LIN9 binds to promoters of cell cycle related genes at E16.5. On the contrary, YAP binds to promoters of genes involved in heart or muscle development at E16.5.

To identify direct targets of LIN9 in the heart, we compared RNA-Seq and ChIP-Seq data. Therefore, we plotted changes in the expression upon deletion of *Lin9* against LIN9 occupancy at the promoter of those genes. Density of LIN9 at the promoter of genes negatively correlates with the changes in expression upon deletion of *Lin9*. In other words, LIN9 was enriched at promoters of genes, which were downregulated after loss of *Lin9* in the heart (**Figure 17A**). Interestingly, we observed a positive correlation between LIN9 enrichment at the promoters of genes that change expression upon *Sav1* deletion in the heart. This result indicates that LIN9 binds to genes that are upregulated after Hippo-inactivation (**Figure 17B**). Specifically, LIN9 strongly binds to the promoters of cell cycle regulated genes (**Figure 17C**) that were also identified to be regulated by the Hippo pathway and the MMB-complex (**Figure 12A**, **B**, **10B**, **C**).

In contrast, LIN9 only weakly binds to promoters of genes related to metabolism, oxidative phosphorylation and mitochondrial function (**Figure 17C**), although these genes were also strongly downregulated after deletion of *Lin9* (**Figure 12A**, **10D**, **E**). The downregulation of these genes is likely an indirect consequence of the deletion of *Lin9* in the heart. Consistent with recently published data, our ChIP-Seq and RNA-Seq analysis point to a model where YAP activates the expression of cell cycle genes from distal enhancers (Morikawa et al., 2015; Pattschull et al., 2019; Zanconato et al., 2015).
Taken together, Hippo inactivation by deletion of *Sav1* leads to YAP mediated upregulation of LIN9-bound cell cycle genes.

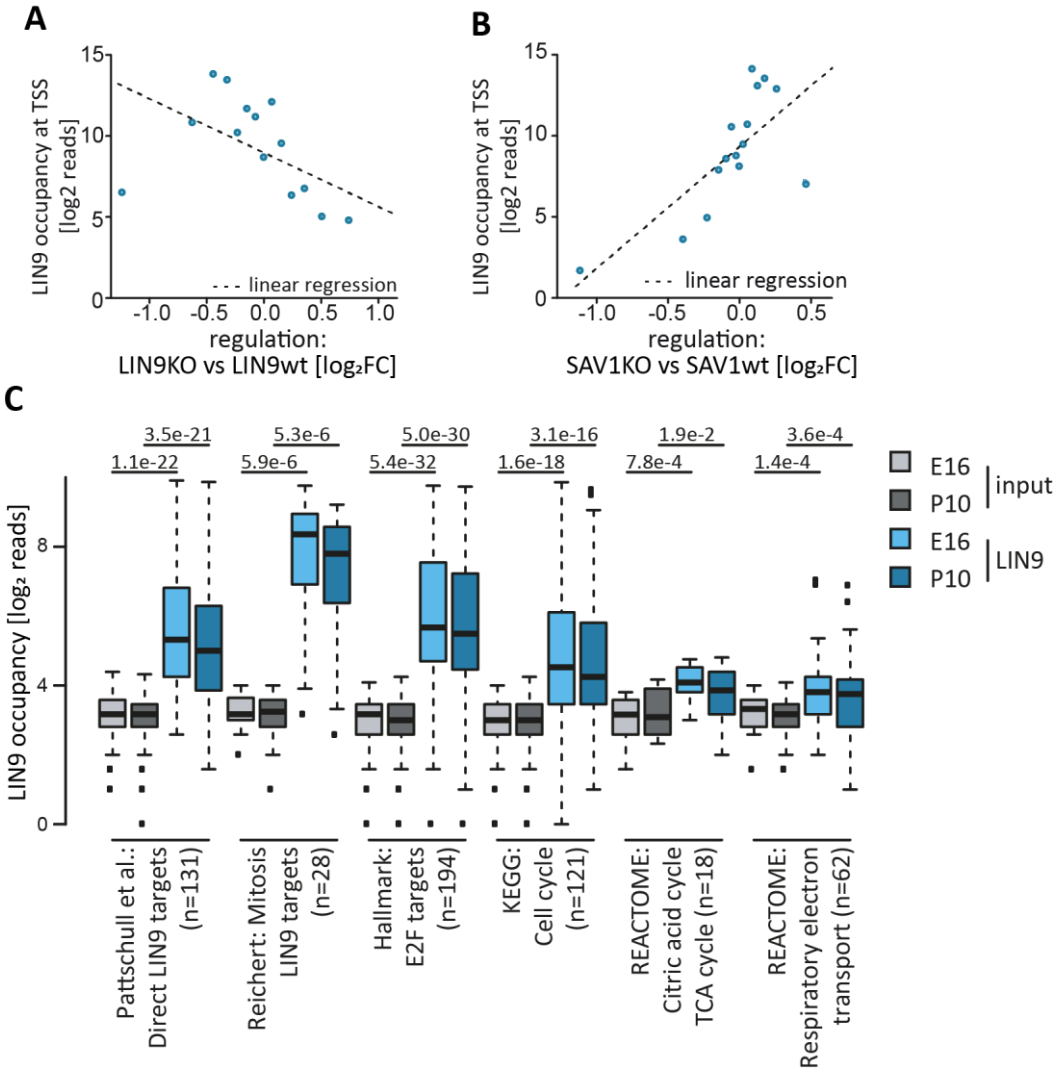

Figure 17: Mitosis and cell cycle related genes induced by Hippo-inactivation are direct LIN9 targets
(**A**) Bin plot correlating changes in gene expression in Nkx-Cre; Lin9$^{fl/fl}$ E13.5 heart ventricles with binding of LIN9 to the promoters at E16.5. Analyzed was a region 1kb upstream the transcription start site (TSS) and input signals were subtracted. 15,642 expressed genes were grouped into 15 bins and the mean of each bin is plotted. Dashed line: Regression based on a linear model. (**B**) Bin plot correlating changes in gene expression in *Nkx-Cre; Sav1*$^{fl/fl}$ in E13.5 heart ventricles with binding of LIN9 to the promoters at E16.5. Analysis was performed as in (**A**). (**C**) Boxplot representing LIN9 binding to genes from the gene sets shown in Figure 10 and 12. Analyzed was a region of +/-250bp around the TSS.

3.7 Increased proliferation and expression of MMB target genes in Hippo-deficient neonatal hearts

So far, we evaluated the impact of Hippo inactivation in embryonal hearts. After birth, cardiomyocytes switch from hyperplastic to hypertrophic growth and proliferation decreases (Van Amerongen and Engel, 2008; Li et al., 1996). As described above, direct target genes of LIN9 are downregulated in the heart within this time period (**Figure 6C**, **D**). To test whether Hippo inactivation reverses this effect and results in increased proliferation of cardiomyocytes and increased expression of MMB target genes, we investigated neonatal *Nkx-Cre; Sav1* mice. Immunohistochemical analysis of neonatal *Nkx-Cre; Sav1* heart sections with the cell cycle marker Ki67 and pH3 showed increased proliferation in Hippo-deficient mice (**Figure 18A-C**), which is consistent with previous studies (Heallen et al., 2011, 2013; Morikawa et al., 2015).

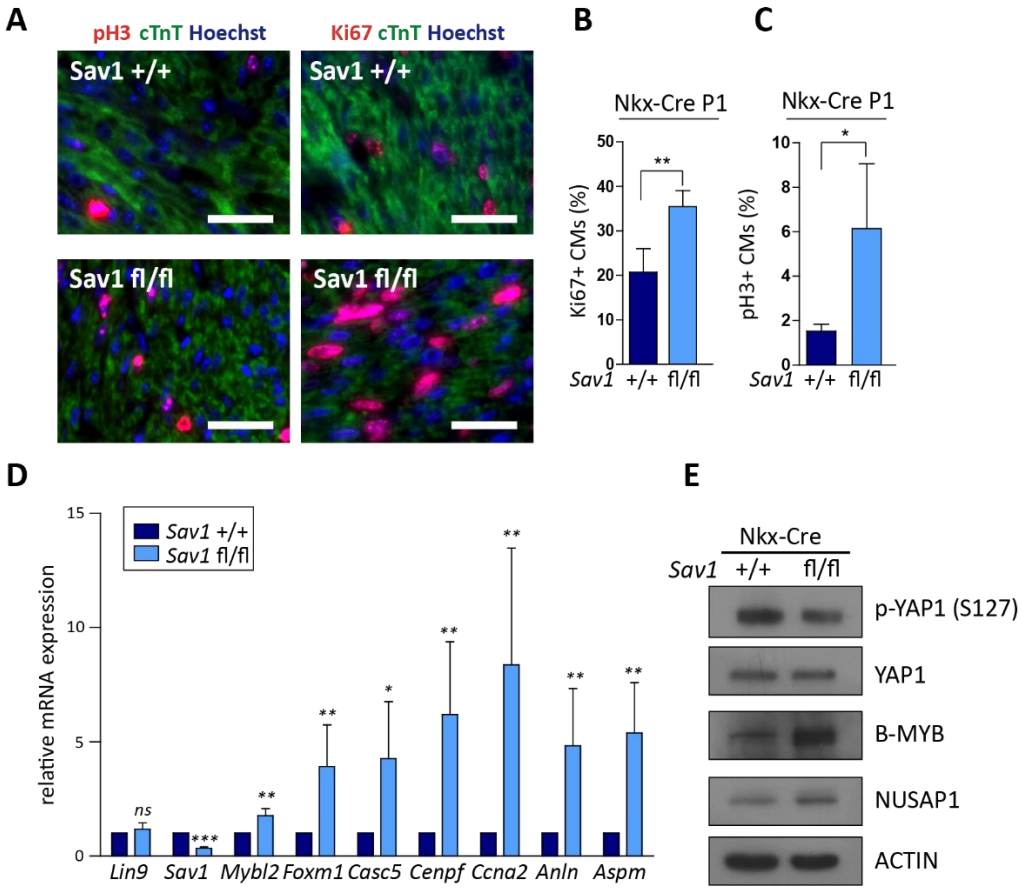

Figure 18: Hippo deficient cardiomyocytes show increased proliferation and expression of MMB target genes

(**A**) Representative images of immunohistochemical analysis of neonatal *Nkx-Cre; Sav1* heart section (P1) with the indicated genotypes. Sections were stained for pH3 (left panel, red), Ki67 (right panel, red) cTnT (green) and Hoechst (blue). (**B**, **C**) Quantification of (**A**). n=3 *Nkx-Cre; Sav1*$^{+/+}$ and n=4 *Nkx-Cre; Sav1*$^{fl/fl}$. (**D**) mRNA expression of the indicated genes in neonatal *Nkx-Cre; Sav1*$^{fl/fl}$ P1 heart ventricles was analyzed by RT-qPCR. *Nkx-Cre; Sav1*$^{+/+}$ served as a control. *Actin* and *Hprt* were used for normalization. n=4 *Nkx-Cre; Sav1*$^{+/+}$ and n=7 *Nkx-Cre; Sav1*$^{fl/fl}$. (**E**) Immunoblotting of protein lysates from *Nkx-Cre; Sav1* P1 heart ventricles with the indicated antibodies. Actin served as a loading control. (**B**-**D**) Error bars indicate standard deviation (SD). Statistical significance was tested using the Student's t-test, two-tailed. *P≤0.05, **P≤0.01, ***≤0.001; ns, not significant, P≥0.05. Per genotype, 1000 cells were counted. (**E**) Part of the experiment was performed by Melissa Schwab (M.Sc. student) (2).

To analyze the expression of MMB target genes in *Nkx-Cre; Sav1* hearts, RNA and protein was isolated from neonatal heart ventricles. First, deletion of *Sav1* was confirmed by qPCR experiments in *Nkx-Cre; Sav1$^{fl/fl}$* (Sav1KO) compared to *Nkx-Cre; Sav1$^{+/+}$* (Sav1WT) neonatal hearts (**Figure 18D**). Second, immunoblotting verified decreased levels of phosphorylated YAP in SavKO hearts indicating the impact of Hippo-inactivation (**Figure 18E**). Next, qPCR experiments indicate that *Mybl2* and *Foxm1* expression levels are significantly upregulated in Sav1KO hearts compared to wildtype controls. In parallel, expression of MMB target genes, *Casc5*, *Cenpf*, *Ccna2*, *Anln* and *Aspm*, was increased after Hippo-inactivation. However, *Lin9* was not regulated by deletion of *Sav1* (**Figure 18D**). For B-MYB and NUSAP1 these results were validated by immunoblotting (**Figure 18E**, (2)).
In summary, this data indicates that Hippo inactivation by deletion of *Sav1* results in increased expression of MMB target genes in neonatal hearts.

3.8 Proliferation of postmitotic cardiomyocytes due to Hippo-deficiency depends on LIN9

To analyze the impact of LIN9 deletion on Hippo-deficiency in neonatal or postnatal hearts, we had to by-pass the embryonic lethality of *Nkx-Cre; Lin9* mice (**Figure 7A**). Therefore, we used another transgenic mouse line, in which the *Cre* recombinase is under control of the α-MHC promoter, which is activated later during heart development (Agah et al., 1997). First, we tested the impact of the loss of *Lin9* in the postnatal heart. Surprisingly, *MHC-Cre; Lin9$^{fl/fl}$* mice survived into adult hood and were detected in the expected mendelian ratios at P10 and P21-25 (**Figure 19A**).
To validate the complete loss of *Lin9* in P10 hearts, *MHC-Cre; Lin9* mice and heart ventricles were genotyped by genomic PCR of the *Lin9* allele. *MHC-Cre; Lin9$^{fl/fl}$* mice showed complete deletion of *Lin9* in P10 heart ventricles compared to heterozygous controls (**Figure 19B**). This result was confirmed on protein level by immunoblotting. Immunoprecipitated LIN9 was completely lost in heart ventricles of *MHC-Cre; Lin9$^{fl/fl}$* mice (**Figure 19C**). Although the phenotype of *MHC-Cre; Lin9* mice was carefully analyzed by staining P10 heart sections with H&E, no obvious morphological changes were observed after loss of *Lin9* compared to heterozygous control mice (**Figure 19D**).
The ratio of heart to body weight is one criterion often used to identify abnormalities in development of murine hearts. Compared to heterozygous control animals, *MHC-Cre; Lin9$^{fl/fl}$* mice did not show any differences in their heart to body rate (**Figure 19E**).

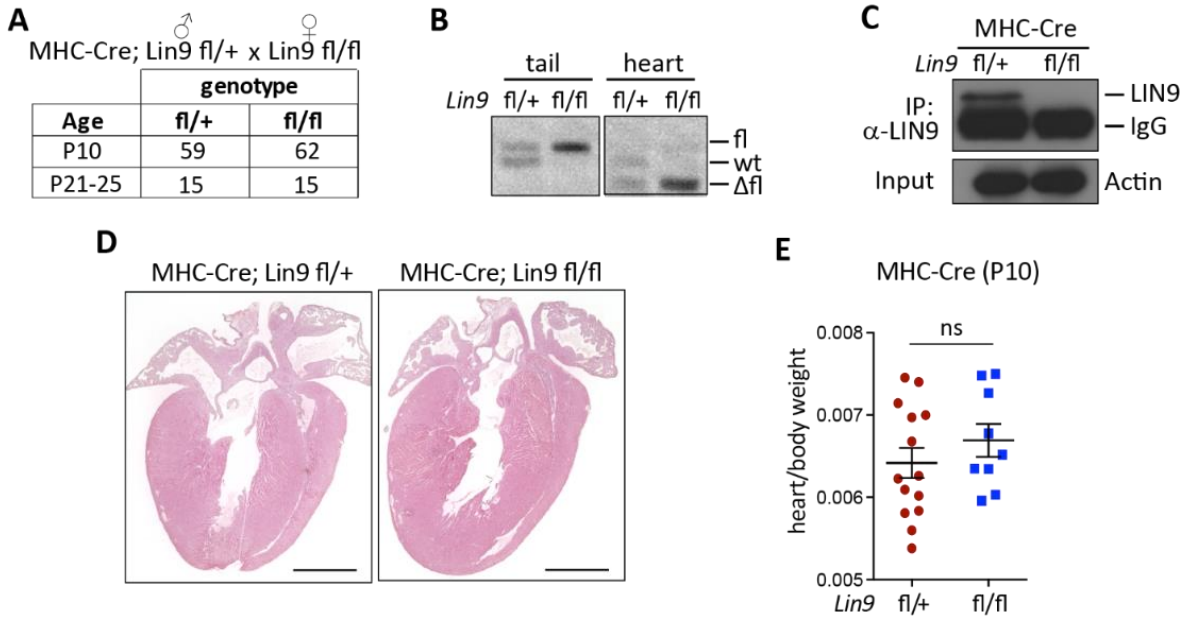

Figure 19: Loss of *LIN9* in postmitotic hearts displays no obvious phenotype
(**A**) Breeding scheme and resulting genotypes at the indicated time points of *MHC-Cre; Lin9* mice. (**B**) Genomic PCR to determine *Lin9* allele status of mice (tail) and corresponding hearts at P10: wt: wildtype *Lin9* allele; fl: non-recombined *Lin9* allele; Δfl: recombined *Lin9* allele. (**C**) To verify loss of *Lin9* at protein level, heart lysates with the indicated genotypes were immunoprecipitated with LIN9 - specific antibody and analyzed by immunoblotting. 3% of the protein lysates used for IP served as a loading control and were analyzed by immunoblotting with an antibody specific for Actin. IgG reflects the heavy chain of the antibody used for IP. (**D**) Representative images of H&E stained P10 heart sections of *MHC-Cre; Lin9* with the depicted genotypes. Scale bar: 1 mm. (**E**) Analysis of the heart to body weight of *MHC-Cre; Lin9* mice with the indicated genotypes. n= 14 *MHC-Cre; Lin9$^{fl/+}$* and n=9 *MHC-Cre; Lin9$^{fl/fl}$* mice. Error bars indicate SDs. To determine statistical significance the Student's t-test, two-tailed was used. ns= not significant.

To analyze the efficiency of Cre mediated deletion in *MHC-Cre; Lin9* mice at different time points during heart development, the *mT/mG* reporter system was used. In FACS analysis between 30-40% of E13.5 cardiomyocytes showed a green fluorescence, whereas 60-70% showed a red fluorescence indicating incomplete recombination of *mT/mG* allele at E13.5 (**Figure 20A**, **B**). On the contrary, almost 100% of P10 cardiomyocytes showed green fluorescence indicating complete recombination of the *mT/mG* allele in *MHC-Cre; Lin9* mice at P10 (**Figure 20A**, **B**). While the percentage of E13.5 cardiomyocytes showing green fluorescence was reduced from almost 40% to around 30% after the loss of *Lin9* compared to heterozygous control mice, recombination at P10 was not affected by loss of Lin9.
Taken together, this data indicates that recombination in *MHC-Cre; Lin9* is incomplete at the embryonal time point and activated later compared to *Nkx-Cre; Lin9.* Moreover, the impact of *Lin9* deletion on the recombination rate is smaller in *MHC-Cre; Lin9* compared to *Nkx-Cre; Lin9* at E13.5 indicating that loss of *Lin9* is less detrimental in *MHC-Cre; Lin9* mice compared to *Nkx-Cre; Lin9* mice (**Figure 9** and **Figure 20**).
To sum up this part, *MHC-Cre; Lin9$^{fl/fl}$* mice survived into adult hood and showed no obvious heart phenotype. The relative low recombination frequency of *MHC-Cre; Lin9* mice in early embryonal hearts could explain the lack of a phenotype compared to the embryonal lethal phenotype of *Nkx-Cre; Lin9* mice.

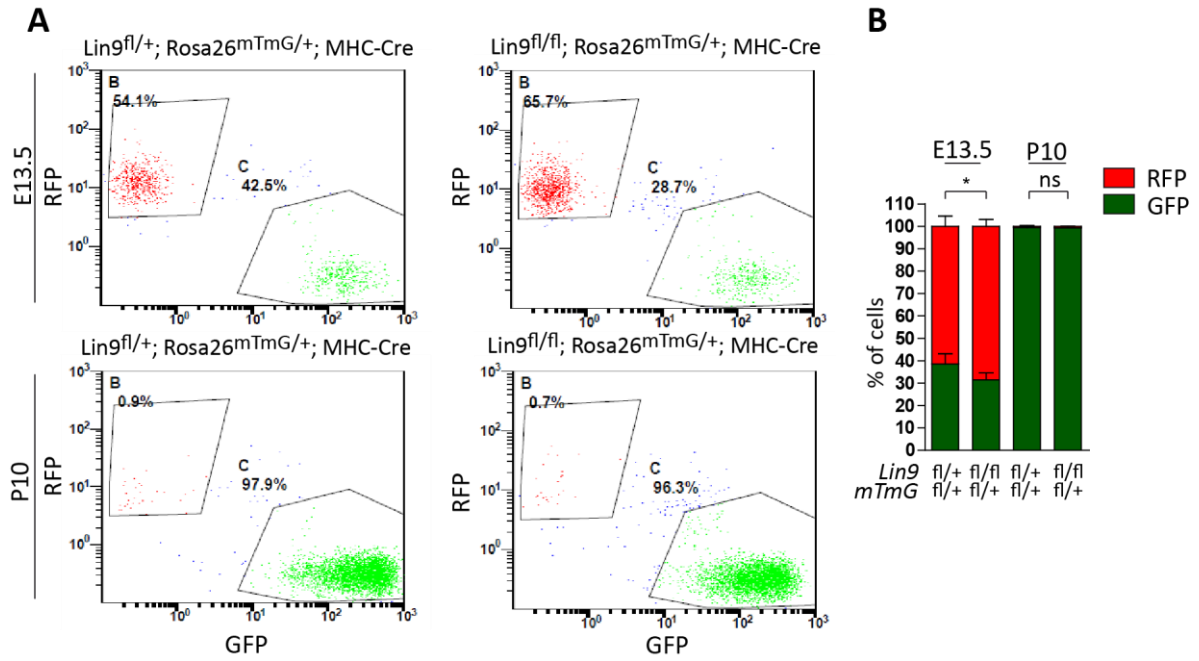

Figure 20: Analysis of recombination using a double fluorescent reporter system
(**A**) Representative FACS profiles of isolated cardiomyocytes with the indicated genotypes. Red fluorescence is plotted on the y-axis. Green fluorescence is plotted on the x-axis. Gates were determined for mT positive cells (B, top left) and mG positive cells (C, bottom right). 10,000 cells were analyzed for each genotype. (**B**) Quantification of (**A**). n=3-4 biological replicates. Error bars indicate standard error of the mean (SEM). Statistical significance was tested using the Student's t-test, two-tailed. *P≤0.05; ns=not significant p>0.05.

By intercrossing *MHC-Cre; Lin9* mice and mice with a conditional (floxed) *Sav1* allele, we generated a genetic model to study the impact of *Lin9* deletion on Hippo-deficiency in postnatal hearts. First, we performed immunohistochemical analysis of P10 heart sections of *MHC-Cre; Lin9; Sav1* mice stained for pH3, a marker of mitotic cells. Cardiomyocytes were identified by co-staining with cTnT (**Figure 21A**). Consistent with previous data (Heallen et al., 2011), quantification of this analysis revealed that Hippo-deficiency robustly induced the fraction of mitotic cardiomyocytes from 1% to 3% in *MHC-Cre; Lin9; Sav1* mice (**Figure 21B**). As expected, the loss of *Lin9* alone does not change the rate of mitotic cardiomyocytes compared to heterozygous control animals. However, the proliferative phenotype of Hippo-deficiency in postnatal cardiomyocytes was suppressed by the loss of *Lin9* and significantly reduced the levels of mitotic cardiomyocytes to 1.8% in *MHC-Cre; Lin9$^{fl/fl}$; Sav1$^{fl/fl}$* double knockout mice (**Figure 21B**).
Taken together, LIN9 seems to be dispensible for the postnatal heart, but is necessary for the induction of proliferation in Hippo-deficient cardiomyocytes.

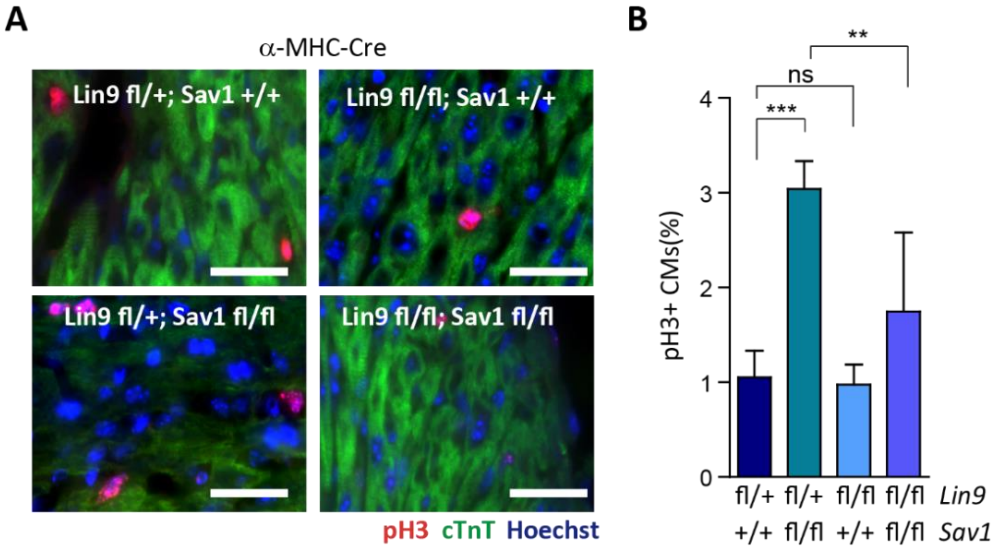

Figure 21: Proliferation of postmitotic Hippo-deficient cardiomyocytes is dependent on LIN9
(**A**) Representative images of immunohistochemical analysis of *MHC-Cre; Lin9; Sav1* P10 heart sections with the depicted genotypes. Sections were stained for pH3 (red), cTnT (green) or Hoechst (blue). Scale bar: 25 µm. (**B**) Quantification of (**A**). n=3 *MHC-Cre; Lin9$^{fl/+}$; Sav1$^{+/+}$*; n=3 *MHC-Cre; Lin9$^{fl/fl}$; Sav1$^{+/+}$*; n=6 *MHC-Cre; Lin9$^{fl/+}$; Sav1$^{fl/fl}$*; n=7 *MHC-Cre; Lin9$^{fl/fl}$; Sav1$^{fl/fl}$*. Error bars indicating standard deviation (SD). Statistical significance was tested using Student's t-test, two tailed. **P≤0.01, ***≤0.001; ns, not significant, P≥0.05. Per genotype, 2000 cells were counted.

3.9 Cardiomyocyte proliferation induced by activated YAP is dependent on LIN9

So far, we could show that the proliferative phenotype of Hippo-deficient hearts is dependent on the function of the MMB-complex. To test whether increased cardiomyocyte proliferation is a direct consequence of YAP activation, we transduced neonatal cardiomyocytes with an activated mutant of YAP, YAPS127A (von Gise et al., 2012). YAP is phosphorylated by LATS1/2 at five serine residues, which marks the protein for proteasomal degradation (Zhao et al., 2010). YAPS127A is more stable compared to wildtype YAP, since serine 127 is mutated to alanine and cannot be phosphorylated by LATS1/2 anymore.
In order to investigate whether increased proliferation following YAP activation is dependent on *Lin9*, we isolated cardiomyocytes from transgenic mice harboring a conditional (floxed) *Lin9^{fl}* allele. In these mice deletion of *Lin9* allele was achieved by a hormone inducible Cre recombinase fused to the mutated ligand binding domain of the human estrogen receptor (CreER^{T2}). Upon 4-hydroxytamoxifen (4-OHT) treatment, CreER^{T2} dissociates from the heat-shock proteins, translocates to the nucleus and recombines exon 7 of *Lin9* (*Lin9$^{\Delta fl}$*) (Feil et al., 1997; Fuhrmann-Benzakein et al., 2000) (**Figure 22A**).

Complete deletion of *Lin9* after treatment of *CreER^{T2}; Lin9$^{fl/fl}$* cardiomyocytes for 96 hours with 100 nM 4-OHT was confirmed by genomic PCR (**Figure 22B**). Cardiomyocytes were transduced with an adenovirus either expressing Flag-tagged YAPS127A or LacZ as a control. 72 hours after virus transduction ectopic expression of YAPS127A was confirmed by immunoblotting with a flag-tag specific antibody (**Figure 22C**).

To determine the rate of proliferation in embryonal cardiomyocytes, immunofluorescence analysis was performed and cells were stained for the mitotic marker pH3. To track cardiomyocytes, cardiac troponin T was co-stained (**Figure 22D**). Quantification revealed no change in the level of mitotic cardiomyocytes in LacZ transduced control cells after deletion of *Lin9*. However, the fraction of mitotic cardiomyocytes dramatically increased from around 3.2% in LacZ control cells to almost 12.5% in cardiomyocytes infected with activated YAP (**Figure 22E**). This is consistent with previous studies using YAPS127A in cardiomyocytes (von Gise et al., 2012). Interestingly, loss of *Lin9* suppresses the YAP mediated increase in proliferation, since only 6.3% of cells were pH3 positive in YAPS127A infected and 4-OHT treated cardiomyocytes (**Figure 22E**).

Similar results were obtained in neonatal P1 cardiomyocytes (**Figure 22F**). Following infection with activated YAP the fraction of pH3-positive cardiomyocytes increased to almost 5% compared to 0.5% LacZ control cells. This effect was repressed by additional deletion of *Lin9*, since only 2.6% of 4-OHT treated YAPS127A cardiomyocytes showed a pH3 signal (**Figure 22G**). Importantly, in control cardiomyocytes isolated from *CreER^{T2}* mice without conditional *Lin9* allele (floxed), OHT treatment had no effect on the ability of YAP to stimulate mitosis (**Figure 22H**).

Taken together, these results confirm the *in vivo* data and indicate that YAP mediated proliferation in cardiomyocytes requires the function of MMB. Furthermore, this validates that the obtained results from Hippo-deficient cardiomyocytes are cell autonomously.

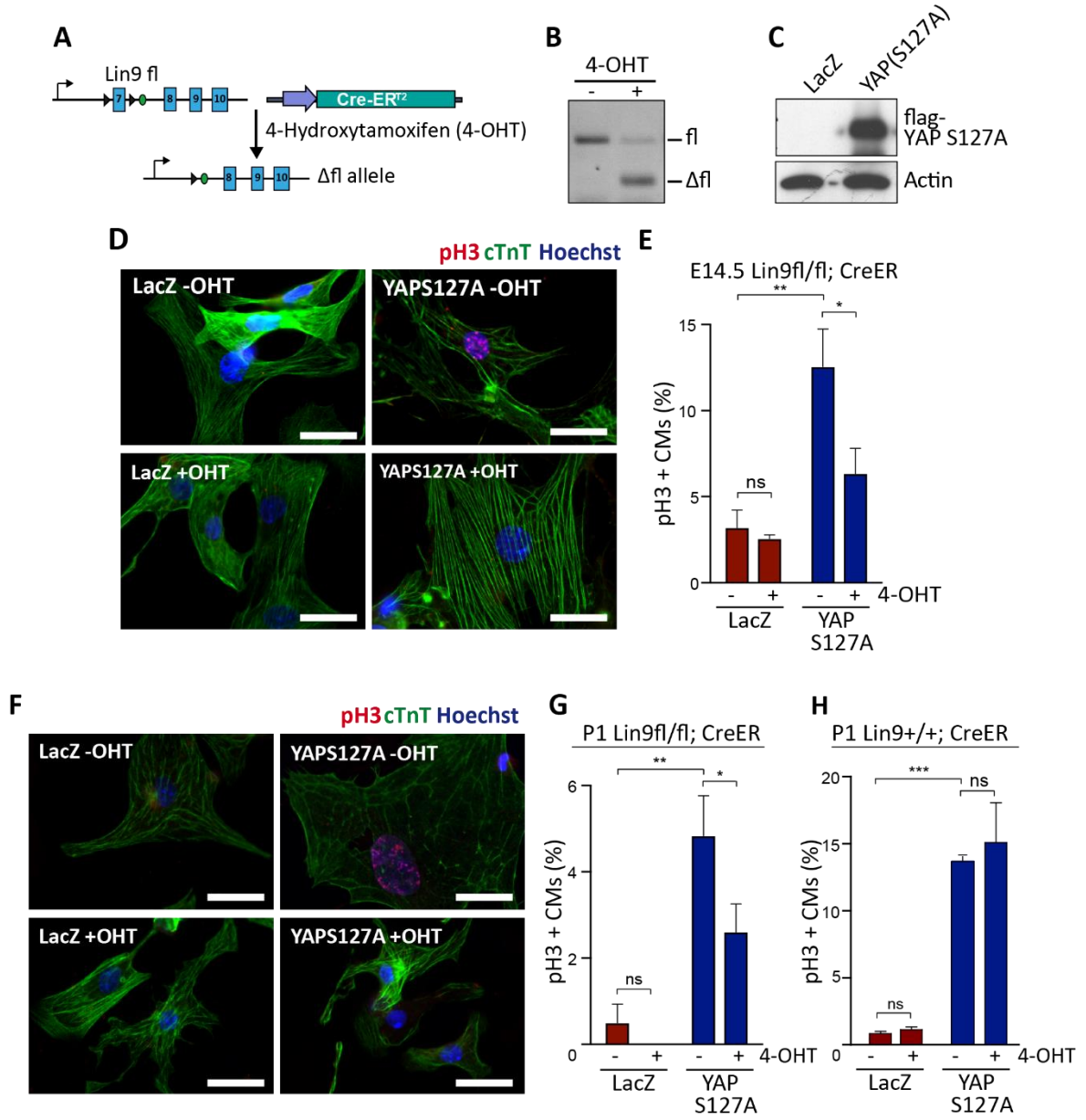

Figure 22: Lin9 is required for YAP induced entry into mitosis

(**A**) Representative scheme of the *CreER^{T2}; Lin9^{fl}* system. Upon 4-hydroxytamoxifen (4-OHT) treatment, the floxed exon 7 of the *Lin9* allele is deleted. (**B**) Genomic PCR to determine the allele status of *Lin9* in cardiomyocytes isolated from *CreER^{T2}; Lin9$^{fl/fl}$* mice, which were treated with and without 100 nM 4-OHT for 96 hours. (**C**) Immunoblotting with a flag-specific antibody to verify the expression of flag tagged YAPS127A in cardiomyocytes. Protein lysates were obtained 72 hours after virus transduction with a LacZ control or a flag-YAPS127A adenoviral construct. Actin served as a loading control. (**D**) Representative images of immunofluorescence analysis from E14.5 embryonal *CreER^{T2}; Lin9$^{fl/fl}$* cardiomyocytes stained for pH3 (red), cTnT (green), Hoechst (blue). Scale bar: 25 µm. Cardiomyocytes were transduced with a LacZ control or flag-YAPS127A adenoviral construct and treated with or without 4-OHT as indicated. (**E**) Quantification of (**D**). n=3 biological replicates. (**F**) Representative images of immunofluorescence analysis from P1 neonatal *CreER^{T2}; Lin9$^{fl/fl}$* cardiomyocytes stained for pH3 (red), cTnT (green), Hoechst (blue). Scale bar: 25 µm. (**G**) Quantification of (**F**). (**H**) Quantification of immunofluorescence analysis from P1 neonatal *CreER^{T2}; Lin9$^{+/+}$* control cardiomyocytes stained for pH3 (red), cTnT (green), Hoechst (blue). (**E**, **G**, **H**) n=3 biological replicates. Error bars indicate standard deviation (SD). Statistical significance was tested using Student's t-test, two tailed. *P≤0.05, **≤0.01, ***≤0.001; ns, not significant, P≥0.05. Per condition, 300-500 cells were counted.

3.10 Interaction of YAP and MMB in developing cardiomyocytes

A recently published study of our lab indicated that YAP and the B-MYB transcription factor of the MMB complex physically interact in tumor cell lines (Pattschull et al., 2019). To test whether YAP and MMB also interact in the heart, we performed proximity ligation assays (PLA) in embryonal cardiomyocytes. The PLA assay is a tool to visualize protein interactions based on immunofluorescence. In an amplification reaction a red fluorescence dye is incorporated when the analyzed proteins are in close proximity to each other. Red foci indicate spots where the interaction takes place. Cardiomyocytes from E13.5 *Nkx-Cre; Lin9* mice were isolated and PLA was performed with specific antibodies against YAP and LIN9 (**Figure 23A**). To quantify the interaction, PLA foci per nucleus were counted (**Figure 23B**). Endogenous YAP was in close proximity to endogenous LIN9 in the nucleus of heterozygous *Nkx-Cre; Lin9* cardiomyocytes indicated by red PLA foci (**Figure 23A**, **B).** The PLA signal seemed to be specific, since the number of foci per nucleus dropped significantly in single antibody treated control cells (**Figure 23A**, **B**). Moreover, the specificity of the interaction was demonstrated by decreased PLA signal in *Lin9* deleted cardiomyocytes compared to heterozygous control cells (**Figure 23A**, **B**).

In another set of experiments, we tested whether YAP also interacts with the B-MYB transcription factor in wildtype E14.5 cardiomyocytes. To show the specificity of the assay, one of the analyzed proteins was deleted using siRNA mediated knockdown. Thus, endogenous YAP was identified to be in close proximity to endogenous B-MYB in sicontrol treated cardiomyocytes indicated by a strong PLA signal (**Figure 23C**, **D**). Reduction of the number of PLA foci after siYAP or siB-MYB treatment validated the specificity of the reaction (**Figure 23C**, **D**). In parallel, the data obtained from *Nkx-Cre; Lin9* cardiomyocytes was confirmed by performing PLA using specific antibodies against LIN9 and YAP after siRNA mediated knockdown in cardiomyocytes (**Figure 23C**, **D**).

Together, PLA showed the interaction of YAP with the MMB complex in embryonal cardiomyocytes.

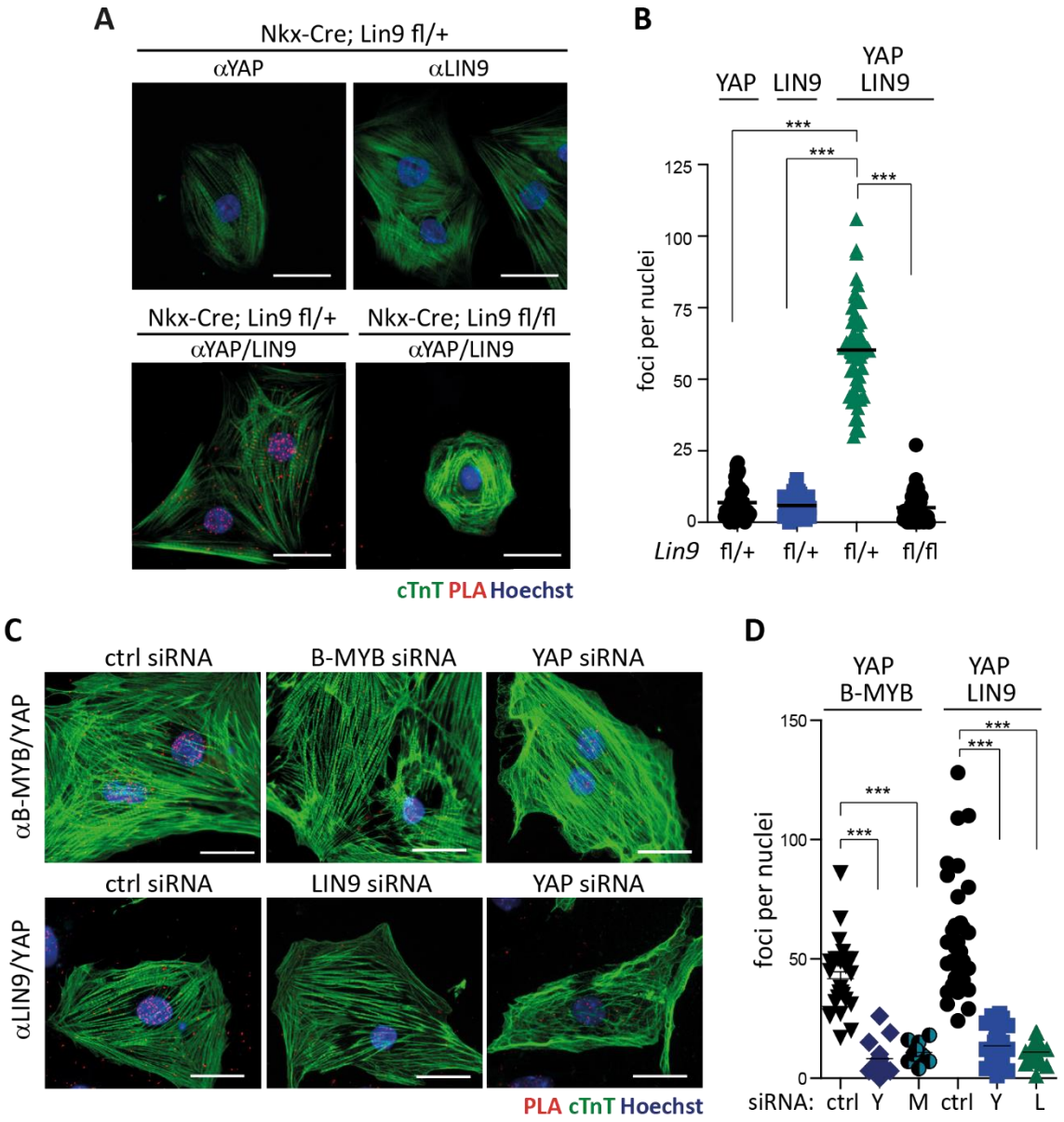

Figure 23: YAP and MMB interact in developing cardiomyocytes

(**A**) Representative images of proximity ligation assay (PLA) performed in isolated *Nkx-Cre; Lin9* E13.5 cardiomyocytes with the indicated genotypes stained for PLA (red), cTnT (green) and Hoechst (blue). Scale bar: 25 µm. PLA assay was performed using specific antibodies against LIN9 and YAP. Single antibody treated cells served as a control. (**B**) Quantification of (**A**). (**C**) Representative images of proximity ligation assay (PLA) performed in isolated E14.5 wildtype cardiomyocytes stained for PLA (red), cTnT (green) and Hoechst (blue). Scale bar: 25 µm. PLA assay was performed using specific antibodies against either B-MYB and YAP or LIN9 and YAP. To test the specificity of the reaction, cardiomyocytes were transfected with siRNAs against LIN9, B-MYB, YAP or a non-targeted control (ctrl). (**D**) Quantification of (**C**). (**B**, **D**) Per condition, foci in the nucleus of 30-50 cells were counted. Error bars indicate standard deviation (SD). Statistical significance was tested using Student's t-test, two tailed. ***≤0.001.

3.11 A PPXY-motif in B-MYB mediates the direct interaction with the WW-domains of YAP

To gain further insights into the interaction between YAP and B-MYB, we wanted to identify the protein domains responsible for this interaction. First, we mapped the protein domain of YAP, interacting with the B-MYB protein. Therefore, the YAP protein was subdivided into seven truncated constructs according to the domain architecture (**Figure 24A**): TEAD-binding domain (white), WW1 and WW2 domain (blue), SH3-binding domain (cyan), transactivation domain (green) and PDZ motif (gray). Flag-tagged YAP constructs 1 to 4 are C-terminal deletions, whereas constructs 5 to 7 are truncated from the N-terminus (**Figure 24A**). Next, we performed co-immunoprecipitation studies of HA-tagged B-MYB with truncated flag-tagged YAP constructs in HeLa cells according to the scheme in **Figure 24B**. Cells transfected with either HA-tagged B-MYB or flag-tagged YAP served as a control. HA-tagged B-MYB interacted only with YAP constructs containing the WW-domains (**Figure 24C**). Densiometric quantification of three individual co-immunoprecipitation experiments using ImageJ visualized the binding of B-MYB to the WW-domains of YAP (**Figure 24E**). To confirm this result, co-immunoprecipitation experiments were performed using HeLa cells transfected with HA-tagged B-MYB and a flag-tagged YAP mutant lacking the WW-domains. Consequently, loss of the WW-domains prevents binding of YAP to B-MYB (**Figure 24D**).
In contrast to YAP, TAZ harbors only one WW-domain. To test whether TAZ interacts with B-MYB, co-immunoprecipitation experiments were performed using HeLa cells transfected with HA-tagged B-MYB and flag-tagged TAZ. Cells transfected with HA-tagged B-MYB and flag-tagged YAP served as a positive control. Cells transfected with one of the constructs as well as cells transfected with HA-tagged B-MYB and a flag-tagged YAP mutant lacking the WW-domains were used as a negative control. In parallel to YAP, TAZ interacts with B-MYB, whereas no interaction was observed with a YAP mutant lacking both WW-domains (**Figure 24F**).

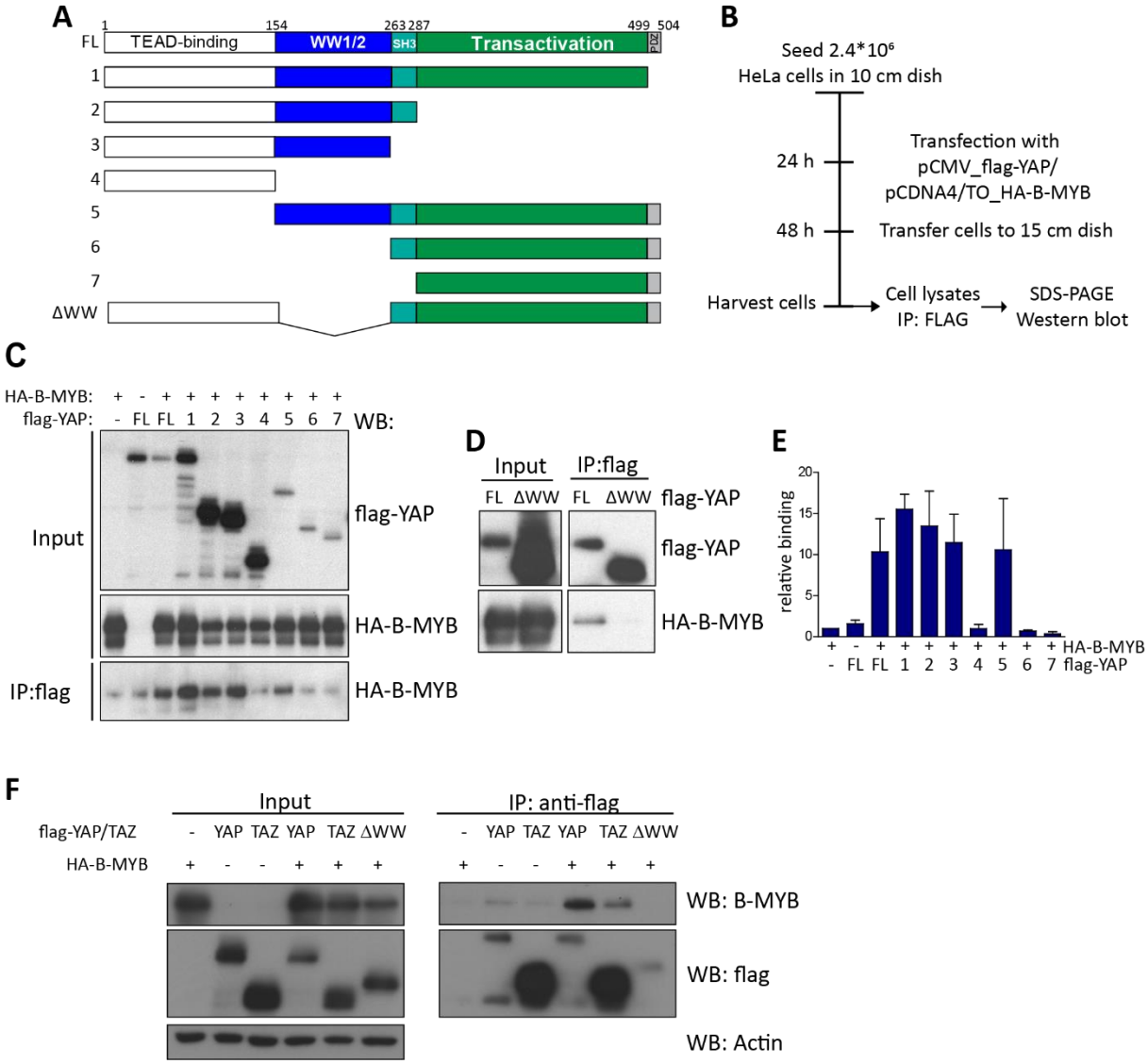

Figure 24: The WW-domains of YAP are necessary for binding to B-MYB

(**A**) Scheme of truncated YAP mutants used in co-immunoprecipitation assays. TEAD-binding domain (aa 1-154), WW1 and WW2 domain (aa 155-263), SH3-binding (aa 264-287), transactivation domain (288-499) and PDZ motif (aa 500-504). (**B**) Flow chart describing the co-immunoprecipitation experiments between HA-tagged B-MYB and flag-tagged YAP constructs. (**C**) Whole cell lysates of HeLa cells expressing HA-tagged B-MYB and truncated flag-tagged YAP mutants (**C**), flag-tagged YAP mutant lacking the WW-domains (YAPΔWW) (**D**) or flag-tagged TAZ (**F**) were immunoprecipitated with flag anti-serum. Subsequently, proteins were separated by SDS-PAGE and detected by immunoblotting using flag-specific and B-MYB-specific antibodies. 3% of the lysates were immunoblotted as an input control. Lysates of HeLa cells transfected either with flag-tagged YAP, flag-tagged TAZ or HA-tagged B-MYB served as a control. (**E**) Densiometric quantification of three individual experiments from (**C**) using ImageJ. Binding is relative to HA-B-MYB control transfected cells.

To validate the results obtained from the co-immunoprecipitation experiments, we performed pulldown experiments with recombinant YAP constructs fused to Glutathione-S-Transferase (GST) and HA-tagged B-MYB expressed in HeLa cells (**Figure 25B**). Therefore, four different GST-YAP fusion constructs were isolated from bacteria: GST-TEAD-WW1/2 containing the TEAD-binding domain and both WW domains (aa 1-263), GST-WW1/2 containing both WW domains (aa 155-263), GST-WW1 containing only the first WW domain (aa 168-204) and GST-

WW2 containing the second WW domain (aa 231-263) (**Figure 25A**). In pulldown assays, HA-tagged B-MYB robustly interacted with GST-TEAD-WW1/2 and GST-WW1/2 containing the WW-domains, but not with GST alone (**Figure 25C**). As a positive control, the assay was performed with HA-tagged TEAD4, which specifically bound to GST-TEAD-WW1/2 containing the TEAD-binding domain (**Figure 25C**). However, no interaction was detected between HA-tagged TEAD4 and GST-WW1/2 or GST alone as expected (**Figure 25C**). HA-tagged EB1, an actin binding protein, served as a negative control and bound to none of the recombinant proteins (**Figure 25C**). To test whether both WW-domains can bind individually to B-MYB, we performed pulldown experiments with GST-WW1/2, GST-WW1 and GST-WW2. Results in **Figure 25D** indicate that both WW-domains bound indiviually to HA-tagged B-MYB and the first WW-domain showed a higher affinity to B-MYB than the second WW-domain (3). However, strongest binding was observed, when both WW-domains were present (**Figure 25D**, (3)). Taken together, co-immunoprecipitation experiments and pulldown assays show, that the WW-domains of YAP bind to B-MYB.

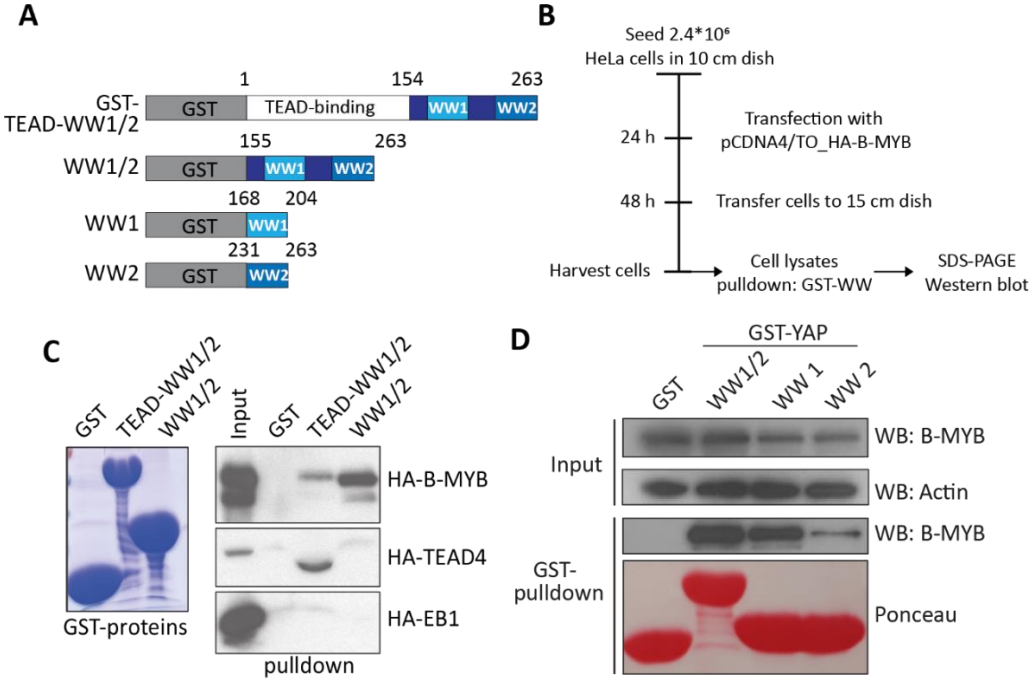

Figure 25: Both WW-domains of YAP can individually bind to B-MYB

(**A**) Scheme of YAP constructs fused to glutathione-S-transferase (GST) used in pulldown assays. TEAD-binding domain (aa 1-154), WW1-domain (aa 168-204) and WW2-domain (aa 231-263). (**B**) Flow chart describing pulldown assays between recombinant GST fusion proteins and HA-tagged B-MYB expressed in HeLa cells. (**C**) Lysates of HeLa cells expressing HA-tagged B-MYB were used in pulldown assays with recombinant GST-TEAD-WW1/2, GST-WW1/2 or GST alone. Lysates of HeLa cells expressing HA-tagged TEAD4 or HA-tagged EB1 served as positive or negative controls. Immunoblotting with HA antiserum indicated the interaction of the WW-domains of YAP with B-MYB and of the TEAD-binding domain with TEAD4. 3% of the lysates used for the pulldown assay was loaded on the gel and served as an input control. 5 µg of the recombinant GST proteins were separated by SDS-PAGE and visualized by Coomassie staining. (**D**) Pulldown experiments of recombinant GST-WW1/2, GST-WW1, GST-WW2, or GST alone with HeLa cell lysates expressing HA-tagged B-MYB. Immunoblotting with a HA-specific antibody confirmed binding of B-MYB to the WW-domains. 3% of the lysates were loaded on the gel as an input control. Actin served as a loading control. Ponceau staining confirmed equal amounts of the recombinant proteins. (**D**) Experiment was performed by Marcela Werner (M.Sc. student) (3).

To identify the corresponding part of the B-MYB protein that interacts with the WW-domains, we mapped the part of B-MYB interacting with YAP-WW-domains. Therefore, the B-MYB protein was subdivided into eight deletion mutants according to its domain stucture: DNA-binding domain (DBD), Transactivation domain (TAD), Negative-regulation domain (NRD) and MuvB-binding domain (MBD) (**Figure 26A**). Pulldown experiments performed with HeLa cells expressing HA-tagged deletion mutants of B-MYB showed that recombinant GST-WW1/2 interacts with the N-terminal part (2-410) of B-MYB as well as with the fulllength protein (**Figure 26B**). In contrast, no binding of the WW-domains to the C-terminal part (411-700) of B-MYB containing the MuvB-binding domain (MBD) was observed (Guiley et al., 2018) (**Figure 26B**). Pulldown assay performed with GST alone showed no interaction with B-MYB, as expected. These results suggest that binding of B-MYB to the WW-domains is independent of the MuvB core.

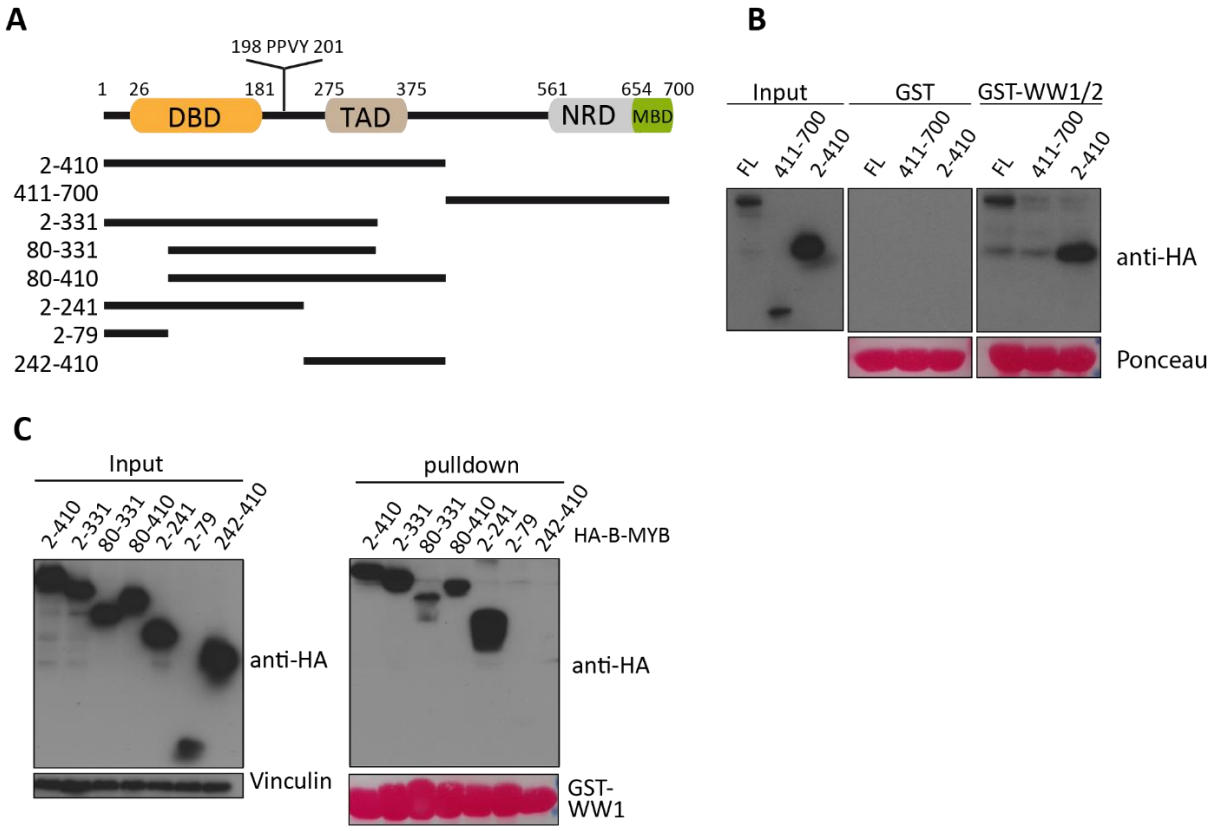

Figure 26: The N-terminal part of B-MYB interacts with YAP via a PPXY motif
(**A**) Scheme of HA-tagged BMYB deletion mutants used in pulldown assays. DNA-binding domain (DBD; aa 26-181), Transactivation domain (TAD; aa 275-375), Negative-regulation domain (NRD; aa 561-653), MuvB-binding domain (MBD; aa 654-700). (**B**) Lysates of HeLa cells expressing the indicated HA-tagged B-MYB mutants were used for pulldown experiments with recombinant GST-WW1/2 YAP protein. Subsequent immunoblotting with HA-specific antibody indicates that the N-terminal part of B-MYB interacts with WW-domains of YAP. 3% of the lysate used in the pulldown assay was loaded on the gel as an input control. Actin served as a loading control. Ponceau staining visualized the amount of recombinant protein used in the pulldown assay. (**C**) Pulldown assays were performed with recombinant GST-WW1 protein and lysates of HeLa cells expressing the indicated HA-tagged B-MYB mutants. Immunoblotting with HA antiserum indicates that the part of B-MYB from amino acid 80 to 241 interacts with WW-domains of YAP. 3% of the lysate used in the pulldown assay was loaded on the gel as an input control. Vinculin served as a loading control. Ponceau staining visualized the amount of recombinant protein used in the pulldown assay.

To map the binding between the N-terminal part of B-MYB and the WW-domains more closely, another set of truncated HA-tagged B-MYB mutants was used in pulldown assays with the WW-domains. Constructs, which contain the part between amino acid 80 and 241, showed robust interaction with the WW-domains (**Figure 26C**). In contrast, constructs, which lacked this part of the protein, such as construct 2-79 and 242-410, showed no interaction (**Figure 26C**). Strongest interaction in pulldown experiments with the WW-domains of YAP was observed with the B-MYB construct containing the first 241 amino acids (**Figure 26C**).

To test whether the interaction between YAP and B-MYB is direct and to exclude that additional cellular proteins are necessary for the binding of B-MYB to the WW-domains, we purified the part of amino acid 2 to 241 of B-MYB interacting most strongly with the WW-domains as a recombinant His-fusion protein. Pulldown experiments performed with the recombinant proteins indicated that his-B-MYB(2-241) directly interacts with the individual WW-domains and highest affinity was observed when both WW-domains were present (**Figure 27A**).

The WW-domain is one of the smallest protein domains in the human proteome that mediates protein-protein interactions. The central part of the protein domain is built by two tryptophan residues, which are 20 to 22 amino acids apart from each other (Chen and Sudol, 1995; Macias et al., 1996). Known interaction motifs of the WW-domain are phosphorylated serine-proline sites (SP-sites) and proline-tyrosine motifs (PPXY-motifs)(Aragón et al., 2012). No SP-sites are found in B-MYB between amino acid 2 to 241. However, an PPXY motif is located at amino acid 198 until 201 (**Figure 26A**).

PPXY motifs are proline-tyrosine rich motifs, which mediate direct interaction with the WW-domain. To test whether this motif in B-MYB is necessary for the interaction with the WW-domains of YAP, we purified recombinant his-B-MYB(2-241)ΔPPXY lacking the PPXY motif and performed pulldown experiments with the WW-domains of YAP. Interestingly, the interaction with GST-WW1/2 was strongly reduced after deletion of the PPXY motif compared to wildtype B-MYB(2-241) (**Figure 27B**). To validate this result, co-immunoprecipitation experiments were performed in HeLa cells expressing flag-tagged YAP and either wildtype HA-tagged B-MYB or mutant HA-tagged B-MYBΔPPXY. Thus, we could confirm that deletion of the PPXY motif in B-MYB results in reduced binding to YAP (**Figure 27C**, **D**).

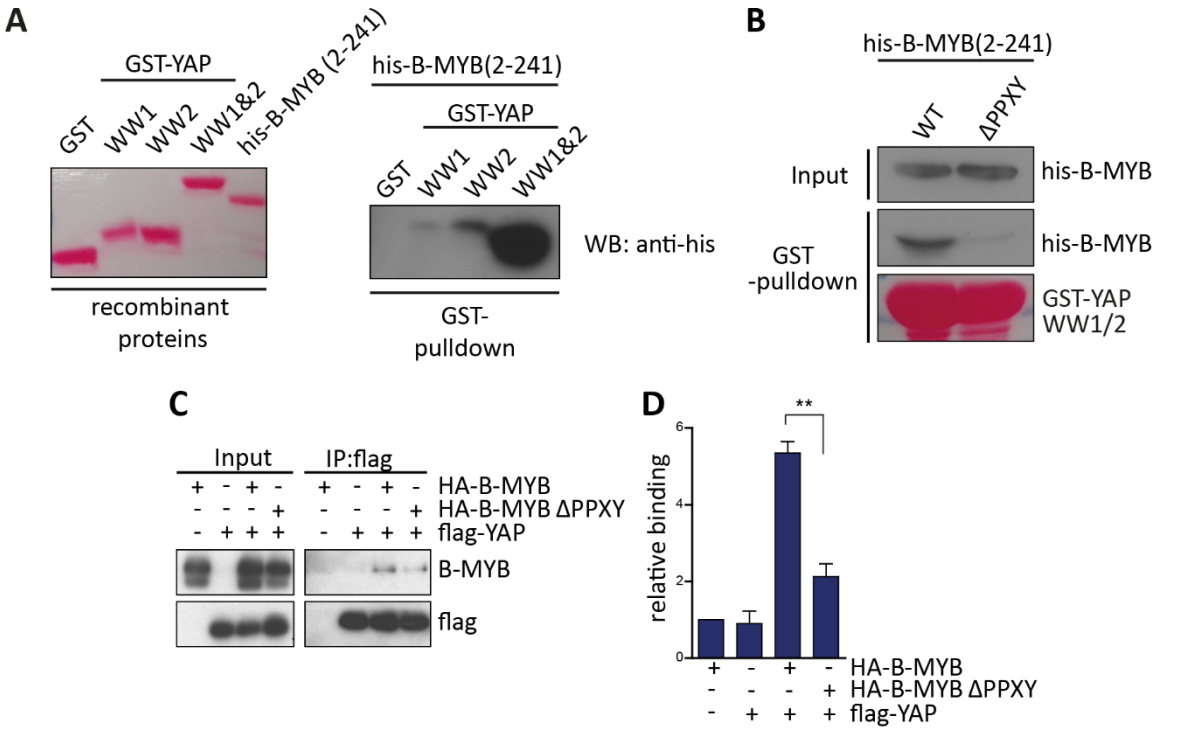

Figure 27: The WW-domains of YAP directly interacts with recombinant his-B-MYB and the interaction is dependent on the PPXY motif of B-MYB

(**A**) Pulldown experiments with the indicated recombinant proteins. Immunoblotting with a 6xhis-specific antibody showed binding of 6xhis tagged B-MYB(2-241) to GST tagged WW proteins. Pulldown only performed with GST alone served as a negative control. 3% of the recombinant proteins used in the pulldown assay were loaded on a gel as an input control and were stained by Ponceau. (**B**) Pulldown assay between GST-WW1/2 and either wildtype his-B-MYB(2-241) or mutant his-B-MYB(2-241)ΔPPXY. Immunoblotting with a 6xhis-specific antibody indicates that binding of B-MYB to WW-domains of YAP is mediated by a PPXY motif. 3% of the recombinant proteins used in the pulldown assay were loaded on a gel as an input control. Recombinant GST-WW1/2 proteins used in the pulldown assay were detected by Ponceau staining. (**C**) Co-immunoprecipitation experiments in HeLa cells expressing flag-tagged YAP and the indicated HA-tagged B-MYB constructs. Flag-YAP was immunoprecipitated using flag antiserum. Deletion of the PPXY motif in B-MYB results in reduced binding to flag-YAP as indicated by immunoblotting with a B-MYB specific antibody. 3% of the lysates used for IP were loaded on a gel as input control. Lysates from HeLa cells transfected with either flag-YAP or HA-B-MYB were used as a control. (**D**) Densiometric quantification of three individual experiments from (**C**) using the ImageJ software. Binding is relative to HA-B-MYB control cells. Error bars indicate standard error of the mean (SEM). Statistical significance was tested using Student's t-test, two tailed. **≤0.01.

To confirm the results obtained from the pulldown assays and to test whether there are additional binding sites in the B-MYB protein contributing to the interaction with the WW-domains of YAP, we performed µSPOT based peptide assays (in collaboration with Hans Maric and Clemens Schulte). Immobilized 15mer peptides were printed on CelluSpot slides and incubated with GST fused WW1/2-domains of YAP or as a control with GST alone. First, we could show that the WW-domains bind to a set of peptides used as a positive control, which contain PY-motifs of known WW-YAP interaction partners, such as p73, LATS1, AMOT, SMAD7, and p53BP2. Among these proteins the PY-peptide of p73 showed the highest affinity to the WW-domains of YAP (**Figure 28A**).

To identify B-MYB binding to the YAP WW-domains, an overlapping 15mer peptide library mapping the whole B-MYB protein with two amino acids offset was used. Interestingly, a peptide sequence containing the PY-motif of B-MYB showed the highest affinity to the YAP WW-domains (**Figure 28B**). Importantly, no binding was observed using GST alone (**Figure 28B**). Taken together, the results obtained from the interaction studies confirmed that a PPXY motif in the N-terminal part of B-MYB directly mediates the binding with the WW-domains of YAP.

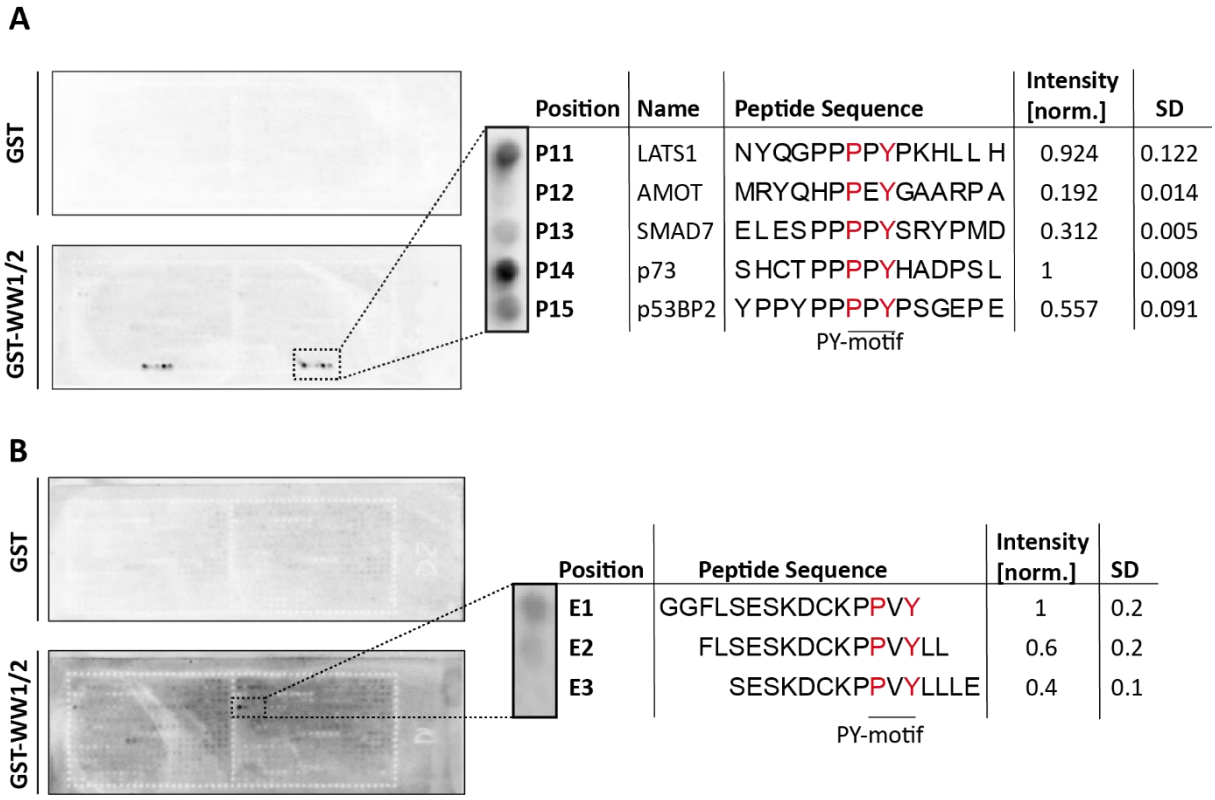

Figure 28: The WW-domains of YAP bind specifically to a 15mer peptide sequence of B-MYB
(**A**) µSPOT based binding of the WW-domains of YAP to well-known interaction partners containing proline-tyrosine (PY)-motifs. 15-mer peptides were probed with either GST-WW1/2 or GST (control) and binding of the recombinant protein was detected by chemiluminescence using a specific GST antibody coupled to HRP. Highest affinity of the YAP WW-domains was observed at position P14 containing a peptide of the p73 protein with the indicated peptide sequence. Relative intensity and standard deviation (SD) were calculated from two individual replicates. (**B**) µSPOT based mapping of the WW-domains of YAP to B-MYB. A peptide library to display the whole B-MYB protein containing 15mer peptides with an offset of two amino acids was probed with either GST-WW1/2 or GST (control). To enhance binding of B-MYB peptides positive control peptides from (**A**) were deleted in this assay. Binding of the recombinant protein was detected by chemiluminescence using a specific GST antibody coupled to HRP. Highest affinity of the YAP WW-domains was observed at position E1 containing a peptide of the B-MYB protein with the indicated peptide sequence. Relative intensity and standard deviation (SD) were calculated from two individual replicates. (In collaboration with Hans Maric and Clemens Schulte)

3.12 Competitive inhibition of the YAP-B-MYB interaction by MY-COMP

To design a tool that disrupts the direct binding of YAP and B-MYB in cells, we next asked the question whether it is possible to interfere with this interaction by competitive inhibition. To answer this question, we used the part of B-MYB, which showed strongest binding in our pulldown assays, B-MYB(2-241), and fused it to a nuclear localization signal (NLS) and an HA-tag. We named this construct, MY-COMP for MYB-YAP competition. We hypothesized that MY-COMP blocks the binding of B-MYB to the WW-domains of YAP in the nucleus of cells due to steric hindrance (**Figure 29A**).

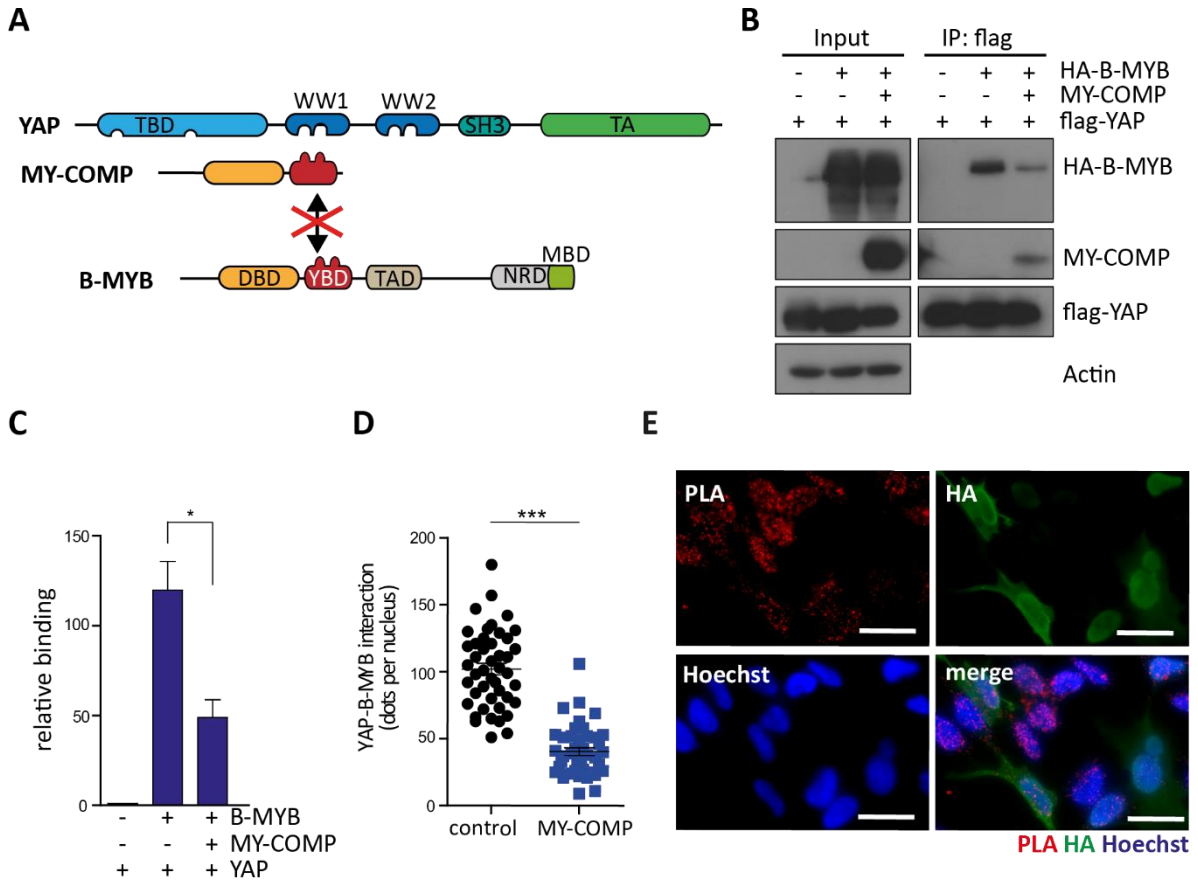

Figure 29: Disruption of the YAP-B-MYB interaction by MY-COMP

(**A**) Scheme of YAP-B-MYB competitive inhibition by MY-COMP. MY-COMP (MYB-YAP competition) is a protein fragment of B-MYB (aa 2-241), which is fused to a nuclear localization signal (NLS) and a HA-tag. MY-COMP blocks the binding of B-MYB to the WW-domains of YAP. (**B**) Lysates of HeLa cells expressing flag-tagged YAP and HA-tagged B-MYB with or without MY-COMP were immunoprecipitated with flag antiserum. Lysates of HeLa cells solely expressing flag-YAP were used as a control. Immunoblotting with HA-specific, flag-specific or B-MYB -specific antibodies revealed that MY-COMP reduces B-MYB binding to YAP and that MY-COMP can bind instead of B-MYB to YAP. 3% of the lysates used for IP were loaded on a gel for an input control. Actin served as a loading control. (**C**) Densiometric quantification of three individual co-immunoprecipitation experiments of (**B**). (**D**) Quantification of PLA assay in (**E**). Dots per nucleus were counted indicating strength of YAP-B-MYB interaction. 75-100 cells were counted per condition. Compared to empty vector transfected cells, MY-COMP transfected cells show reduced binding of B-MYB to YAP. (**E**) Representative images of PLA assay stained for PLA (red), HA (green) and DAPI (blue). (**C**, **D**) Error bars indicate standard error of the mean (SEM). Statistical significance was tested using Student's t-test, two tailed. *≤0.05; ***≤0.001.

To test this hypothesis, we performed co-immunoprecipitation experiments in HeLa cells with ectopic expression of flag-tagged YAP and HA-tagged B-MYB in the absence or presence of MY-COMP. HeLa cells only expressing flag-tagged YAP served as a control. In the absence of MY-COMP, flag-YAP robustly bound to HA-B-MYB. Whereas the expression of MY-COMP significantly reduced the binding of YAP to B-MYB (**Figure 29B**, **C**). Moreover, MY-COMP itself interacted with flag-tagged YAP, replacing HA-B-MYB. This finding indicates that MY-COMP disrupts YAP-B-MYB interaction by competitive inhibition (**Figure 29B**). To determine whether the endogenous interaction between YAP and B-MYB can also be blocked by MY-COMP, PLA assays in HeLa cells expressing MY-COMP were performed. Transfected cells were identified by immunofluorescence staining for HA-tag. Compared to cells transfected with an empty vector, endogenous interaction between YAP and B-MYB was significantly reduced in MY-COMP transfected cells (**Figure 29D**, **E**). Taken together this data indicates that MY-COMP is a tool that interferes with YAP-B-MYB interaction due to competitive inhibition.

3.13 The YAP-B-MYB interaction is required for proliferation and expression of MMB target genes

Next, we assessed the physiological relevance of YAP-B-MYB interaction. Therefore, we asked the question whether deletion of the binding sites or blockage of binding by MY-COMP reduces the ability of YAP to stimulate proliferation or activate the expression of mitotic genes. First, we tested whether interaction of YAP and B-MYB is important for the ability of activated YAP to stimulate proliferation and mitosis in neonatal cardiomyocytes. For this reason, we designed an adenoviral construct of activated YAPS127A lacking the WW-domains that are necessary for the interaction with MMB (**Figure 30A**). In addition, YAPS94A/S127A a mutant, which cannot bind to TEAD proteins, was used as an internal control (**Figure 30A**). β-galactosidase served as a negative control in this experiment. After neonatal cardiomyocytes were transduced with adenoviruses, stable expression of LacZ and YAP mutants was confirmed (**Figure 30B**). Next, we determined the fraction of mitotic cardiomyocytes by immunofluorescence staining against pH3 (**Figure 30C**). As reported previously, transduction of cardiomyocytes with adenoviruses expressing YAPS127A robustly increased the fraction of mitotic cardiomyocytes compared to LacZ control treated cells (von Gise et al., 2012; Xin et al., 2011) (**Figure 30C**, **D**). However, expression of YAPS94A/S127A did not result in an increase of mitotic cardiomyocytes indicating that the proliferative function of YAP is dependent on the binding of YAP to TEAD proteins (**Figure 30C**, **D**). Interestingly, the YAP WW-domains are critical for the proliferative ability of YAP, since the YAPS127A mutant lacking the WW-domains failed to increase the fraction of mitotic cardiomyocytes (**Figure 30C**, **D**). These results were verified by immunofluorescence analysis of neonatal cardiomyocytes transduced with the indicated adenoviral constructs stained for Ki67 as a marker for proliferation (**Figure 30E**, **F**).

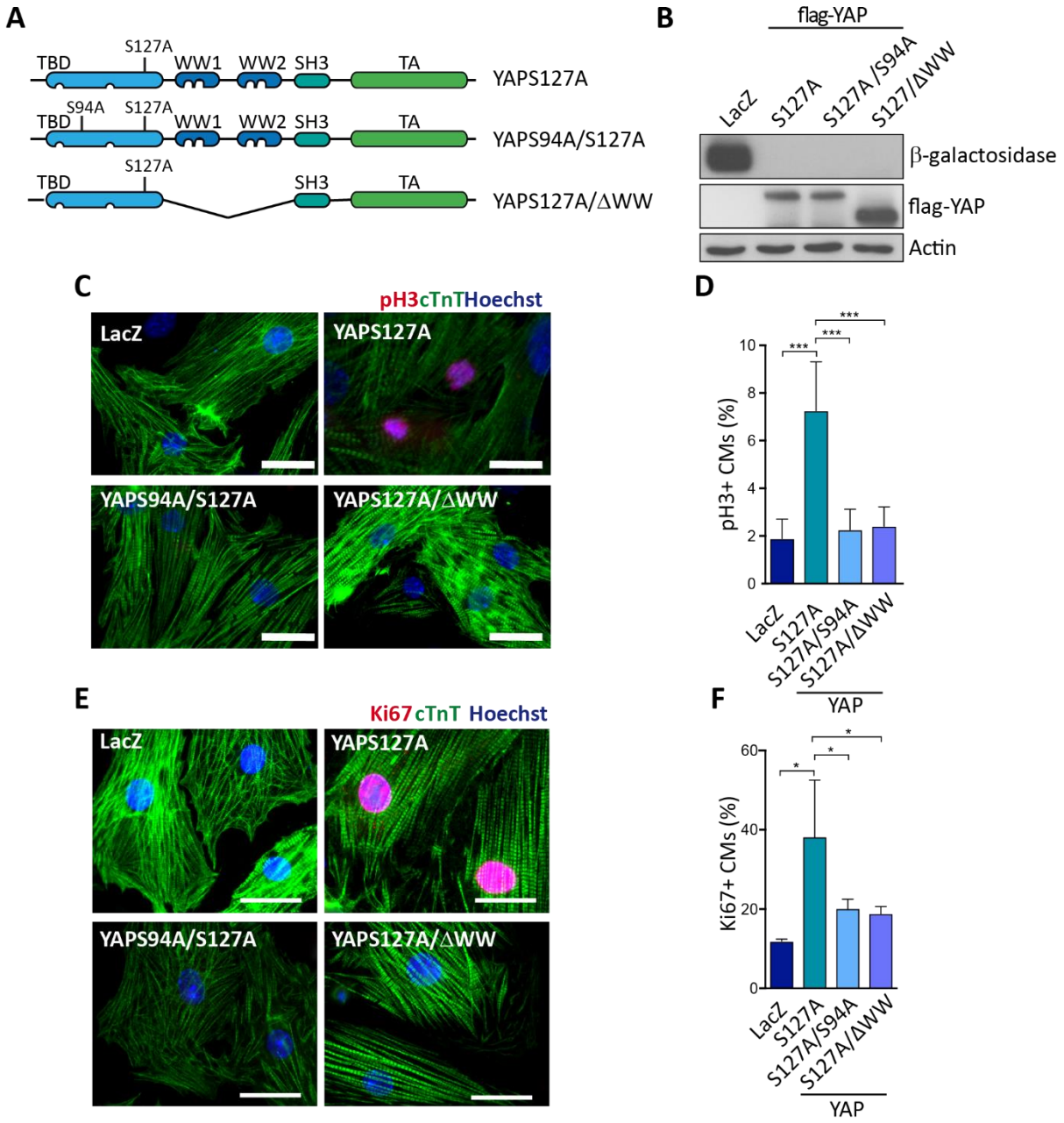

Figure 30: WW-domains of YAP are required to promote proliferation and entry into mitosis of neonatal cardiomyocytes

(**A**) Scheme of adenoviral constructs of flag-tagged YAP mutants, which were used to transduce neonatal P1 cardiomyocytes. (**B**) Lysates of neonatal cardiomyocytes transduced with the depicted adenoviruses are analyzed by immunoblotting with β-Galactosidase-specific or flag-specific antibodies. Actin served as a loading control. (**C**) Representative images of immunofluorescence analysis of neonatal P1 cardiomyocytes transduced with the indicated adenoviral constructs. Mitotic cardiomyocytes were identified by staining for pH3 (red), cTnT (green) and Hoechst (blue). (**D**) Quantification of (**C**). n=6 LacZ; n=8 YAPS127A; n=6 YAPS94A/S127A; n=8 YAPS127AΔWW. (**E**) Representative images of immunofluorescence analysis of neonatal P1 cardiomyocytes transduced with the indicated adenoviral constructs. Proliferating cardiomyocytes were identified by staining for Ki67 (red), cTnT (green) and Hoechst (blue). (**F**) Quantification of (**E**). n=3 LacZ; n=4 YAPS127A; n=4 YAPS94A/S127A; n=4 YAPS127AΔWW. (**D**, **F**) Per condition, 750-1000 cells were counted. Error bars indicate standard deviation (SD). Statistical significance was tested using Student's t-test, two tailed. *≤0.05; ***≤0.001.

Next, we analyzed whether the ability of activated YAP to stimulate mitotic gene expression is dependent on its WW-domains. Therefore, we used C2C12 cells to mimic differentiation of cardiomyocytes during heart development. C2C12 cells are a murine myoblast cell line, which can be differentiated in myotubes. First, we showed in co-immunoprecipitation studies that YAP and B-MYB interacted in C2C12 cells (**Figure 31A**). Second, protein expression of the MMB target genes, TOP2A and CDC20 and B-MYB itself, was strongly downregulated after differentiation of C2C12 cells. Importantly, this effect was partially rescued by transduction of differentiated myotubes with an adenovirus expressing activated YAPS127A (**Figure 31B**, (3)).

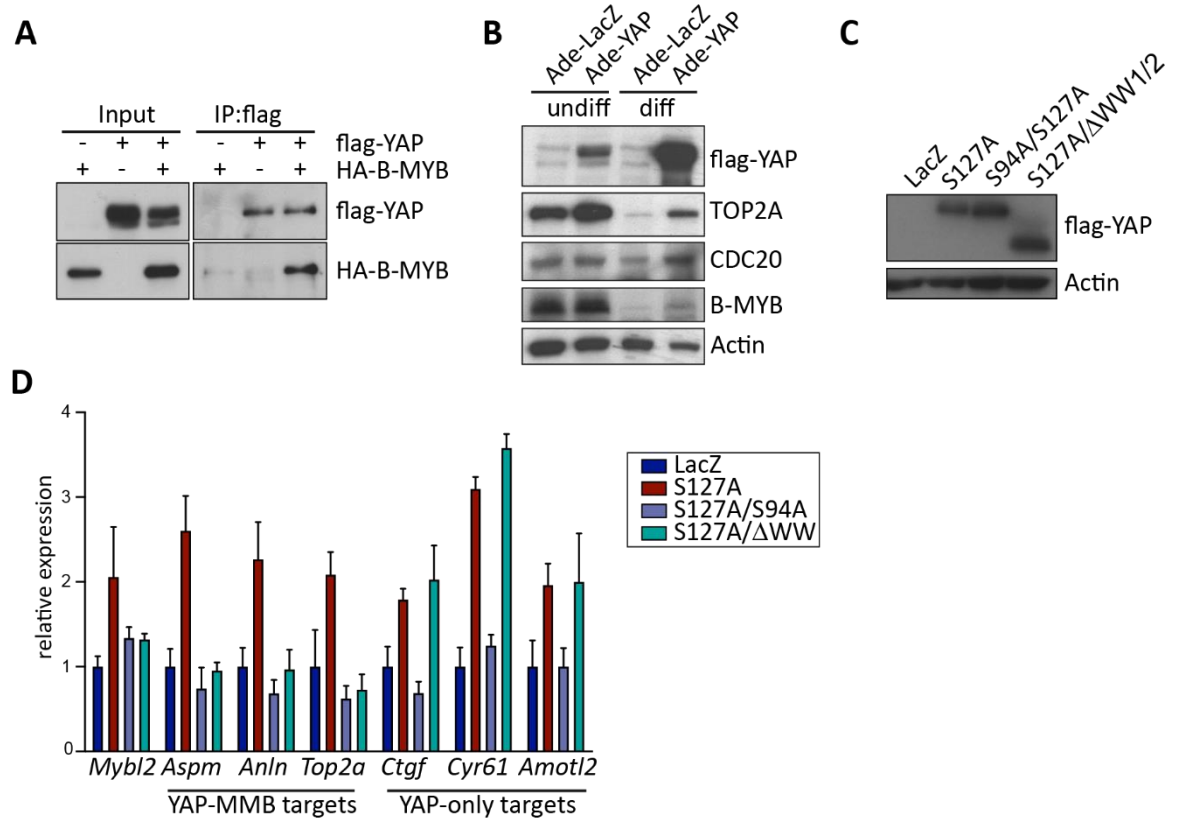

Figure 31: WW-domains of YAP and interaction with TEAD are necessary for YAP-induced expression of MMB target genes in differentiated C2C12 myotubes

(**A**) Lysates of C2C12 cells expressing Flag-YAP and HA-B-MYB were immunoprecipitated using flag antiserum and subsequently immunoblotted using B-MYB-specific and Flag-specific antibodies. Lysates of cells transfected either with Flag-YAP or HA-B-MYB served as a control. 3% of the lysates used for IP were loaded on a gel as an input control. (**B**) Lysates of undifferentiated (undiff) and differentiated (diff) C2C12 cells transduced with adenoviruses expressing β-galactosidase (Ade-LacZ) or YAPS127A (Ade-YAP) were analyzed by immunoblotting using B-MYB-specific, CDC20-specific, TOP2A-specific and flag-specific antibodies. Actin served as a loading control. (**C**) Immunoblotting with flag antiserum of lysates from differentiated C2C12 cells transduced with the indicated adenoviruses showed comparable expression of YAP mutants 72 hours after infection. Actin served as a loading control. (**D**) Relative mRNA expression of *Mybl2*, *Aspm*, *Anln*, *Top2a*, *Ctgf*, *Cyr61* and *Amotl2* in differentiated C2C12 cells transduced with the indicated adenoviruses were analyzed by RT-qPCR using specific primers for each gene. Expression is relative to *Actin* and *Hprt*. n=4 biological replicates. Error bars show standard deviation (SD) of triplicates from one representative experiment. (**B**) Experiment was performed by Marcela Werner (M.Sc. student) (3).

Next, we asked whether the ability of activated YAP to stimulate expression of mitotic genes in differentiated C2C12 cells is dependent on the interaction with the MMB-complex. To answer this question we transduced differentiated C2C12 cells with adenoviral constructs shown in **Figure 30A**. Stable expression of YAP mutants was verified in differentiated C2C12 cells (**Figure 31C**). The expression of the MMB-target genes *Anln*, *Aspm*, and *Top2a* as well as of *Mybl2* was robustly increased by activated YAP compared to LacZ treated control cells (**Figure 31D**). Moreover, the expression of the YAP-target genes *Ctgf*, *Cyr61,* and *Amotl2* was increased upon YAP activation (**Figure 31D**). However, in cells transduced with YAPS94A/S127A, the expression of MMB target genes as well as YAP-target genes was not increased compared to LacZ treated control cells. This indicates that induction of these genes by YAP was dependent on the interaction of YAP with TEAD as expected (**Figure 31D**). Interestingly, the expression of *Mybl2*, *Anln*, *Aspm,* and *Top2a* was not induced in differentiated C2C12 cells transduced with activated YAP lacking the WW-domains, indicating that the induction of MMB-target genes by YAP depends on the interaction with the MMB-complex (**Figure 31D**). In contrast, YAP-only target genes were induced by a YAPS127AΔWW mutant, demonstrating that activation of this subset of genes by YAP is independent of its WW-domains (**Figure 31D**).

Next, we analyzed whether the interaction of YAP and B-MYB is critical for proliferation in embryonal cardiomyocytes. We used MY-COMP as a tool to block binding of B-MYB and YAP. Therefore, adenoviruses expressing MY-COMP fused to a T2A self-cleavage peptide followed by GFP were constructed. In parallel, MY-COMPΔDNA, a mutant of MY-COMP, in which arginine 174 is mutated to alanine, was generated. This mutation in MY-COMP prevents DNA-binding of the construct (Werwein et al., 2012). Similarly, a mutant of MY-COMP, MY-COMPΔPPXY, which shows reduced binding to YAP was established (**Figure 32A**). Infected cardiomyocytes were identified by their GFP signal. In immunofluorescence analysis embryonal cardiomyocytes were stained for pH3 and cTnT to identify mitotic cardiomyocytes (**Figure 32C**). A large fraction of embryonal cardiomyocytes (8%), which were transduced with a GFP expressing control virus, were positive for pH3 (**Figure 32B**). In contrast, mitosis of embryonal cardiomyocytes was reduced to only 1% by the expression of MY-COMP (**Figure 32B**). Expression of MY-COMPΔDNA showed a similar effect on proliferation of cardiomyocytes, suggesting that the effect of MY-COMP is not due to the ability of B-MYB to bind to DNA (**Figure 32B**). Importantly, deletion of the PPXY motif, which is required for interaction with YAP, partially reverses the MY-COMP phenotype. This result indicates that the phenotype of MY-COMP correlates with the ability to disrupt the interaction between YAP and B-MYB (**Figure 32B**).

Taken together, our results indicate that the WW-domains of YAP are necessary for proliferation of neonatal cardiomyocytes and expression of MMB target genes in differentiated C2C12 cells. Moreover, blockage of the YAP-B-MYB interaction by MY-COMP interferes with proliferation of embryonal cardiomyocytes. These results highlight the importance of YAP-B-MYB interaction for proliferation of cardiomyocytes.

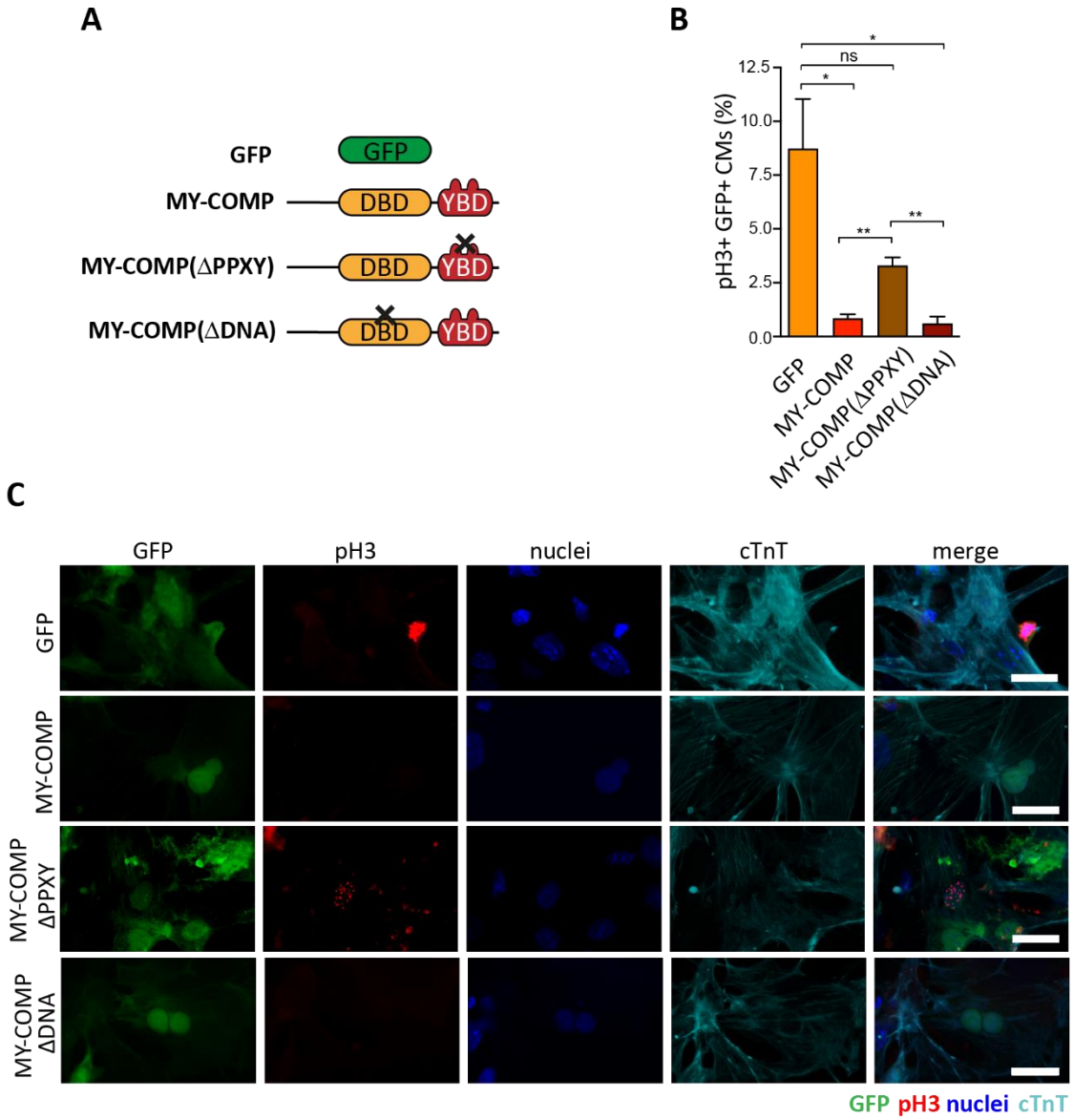

Figure 32: MY-COMP inhibits mitotic entry of embryonal cardiomyocytes

(**A**) Scheme of adenovirus constructs used for infection of embryonal cardiomyocytes. Adenovirus solely expressing GFP was used as a control. MY-COMP constructs were linked by a T2A self-cleavage peptide with GFP. MY-COMPΔPPXY, mutant of MY-COMP, in which PY-motif required for YAP binding is deleted. MY-COMPΔDNA, mutant of MY-COMP, which is incapable in binding to DNA. (**B**) Quantification of (**C**). n=3 biological replicates. 400-600 cells were counted per condition. (**C**) Representative images of immunofluorescence analysis of embryonal cardiomyocytes transduced with the indicated adenoviruses were stained for pH3 (red), cTnT (cyan) and Hoechst (blue). Green fluorescence indicates co-expression of GFP. (**B**) Error bars indicate standard error of the mean (SEM). Statistical significance was tested using the Student's t-test, two-tailed. *P≤0.05, **P≤0.01; ns, not significant, P≥0.05.

3.14 The YAP-B-MYB interaction is important for correct cell cycle progression of HeLa cells

To further characterize the cellular phenotype resulting from the blockage of YAP-B-MYB interaction by MY-COMP, we ectopically expressed MY-COMP mutants in HeLa cells. Immunofluorescence staining of cells with tubulin (green), HA (red) and Hoechst (blue) indicated several nuclear abnormalities in HeLa cells expressing MY-COMP (**Figure 33A**). Specifically, bi- and multinucleation and the presence of micronuclei indicated that errors occur during mitosis in HeLa cells expressing MY-COMP. The cellular phenotype of MY-COMP is not caused by changes in the protein expression of YAP, phosphorylated YAP (p-YAP) or B-MYB (**Figure 33B**). Also, the different MY-COMP mutants are expressed at a comparable levels (**Figure 33B**). In empty vector control transfected HeLa cells, the level of bi- and multinucleated or cells with micronuclei was low. After transfection with MY-COMP these levels increased dramatically. In detail, approximately 9% of control transfected cells were binucleated, 0.5% of cells showed multinucleation and in 2.8% of cells micronuclei were observed (**Figure 33C**). In contrast, more than 25% of MY-COMP transfected cells were binucleated, more than 6% of cells were multinucleated and more than 8% of cells showed micronuclei (**Figure 33C**). This was specific, since expression of a shorter version of MY-COMP(2-79) did not result in this phenotype and behaved like control transfected cells (**Figure 33C**). In addition, the phenotype was not due to interference of MY-COMP with the ability of B-MYB to bind to DNA, since HeLa cells expressing mutant MY-COMPΔDNA showed a similar cellular phenotype as HeLa cells expressing wildtype MY-COMP (**Figure 33C**). Interestingly, deletion of the YAP-binding motif, MY-COMPΔPPXY, weakens the effect of MY-COMP, indicating that the phenotype correlates with the ability of MY-COMP to disrupt the YAP-B-MYB interaction (**Figure 33C**).

Taken together, expression of MY-COMP in HeLa cells results in a cellular phenotype that likely phenocopies the loss of MMB in cells. Upon expression of MY-COMP, HeLa cells start to get bi- or multinucleated and an increased fraction of cells show micronuclei.

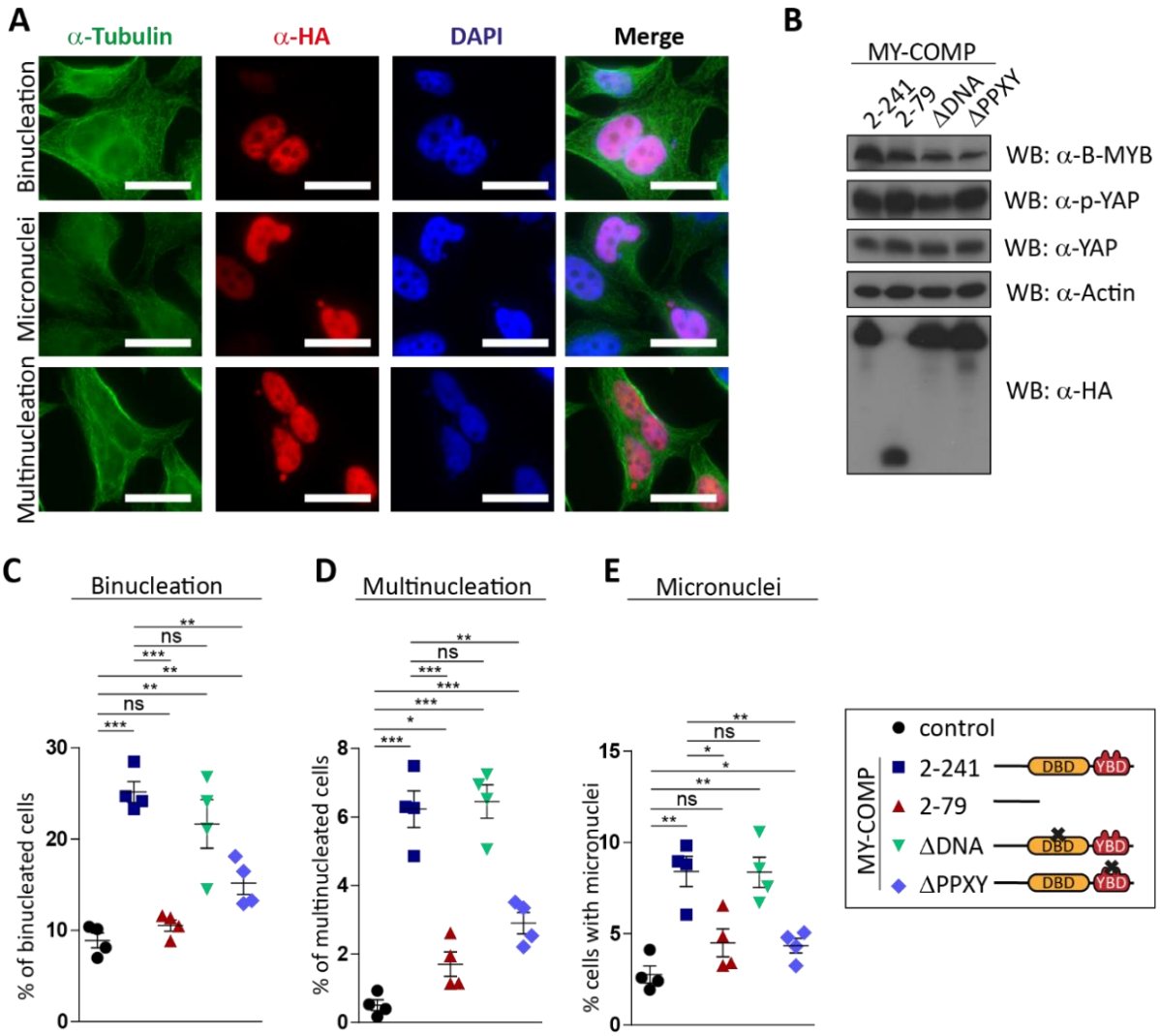

Figure 33: Disruption of YAP-B-MYB binding by MY-COMP results in nuclear abnormalities
(**A**) Representative images of immunofluorescence analysis of HeLa cells expressing MY-COMP stained for tubulin (green), HA (red) and Hoechst (blue). Upon expression of MY-COMP, HeLa cells show several nuclear abnormalities, like bi- or multi-nucleation and micronuclei. (**B**) Lysates of HeLa cells transfected with the indicated MY-COMP constructs for 48 hours were analyzed by immunoblotting with specific antibodies against HA, YAP, B-MYB and phosphorylated YAP (S127). Actin served as a loading control. (**C**) Quantification of (**A**) subdivided in binucleated or multinucleated cells and cells that contain micronuclei. n=4 biological replicates. 1000-2000 cells were counted per condition. Error bars indicate standard error of the mean (SEM). To determine statistical significance, Student's t-test (two-tailed) was used. *P≤0.05, ** P≤0.01, ***P≤0.001; ns, not significant, P≥0.05.

To further analyze the phenotype of MY-COMP expression, we created stable HeLa cells using the pInducer20 system with a neomycin resistance cassette. In this system, doxycycline inducible expression of MY-COMP is linked to GFP expression via a T2A site (**Figure 34A**). HeLa cells harboring pInducer20 constructs exhibit doxycycline dependent expression of MY-COMP or a shorter version of MY-COMP(2-79), which served as a control (**Figure 34B**). To confirm that doxycycline dependent expression of MY-COMP was sufficient to suppress binding of YAP to B-MYB, co-immunoprecipitation experiments were carried out with transiently transfected HeLa cells expressing flag-tagged YAP and HA-tagged B-MYB constructs. HeLa cells expressing HA-tagged B-MYB and a flag-tagged YAP mutant lacking the WW-domains were used as a

positive control. HeLa cells only expressing flag-tagged YAP served as a negative control. HA-tagged B-MYB robustly interacts with flag-tagged YAP (**Figure 34C**). After doxycycline induced expression of MY-COMP, the interaction between flag-tagged YAP and HA-tagged B-MYB is impaired (**Figure 34C**). Deletion of the WW-domains results in complete loss of the YAP-B-MYB interaction, as expected (**Figure 34C**).

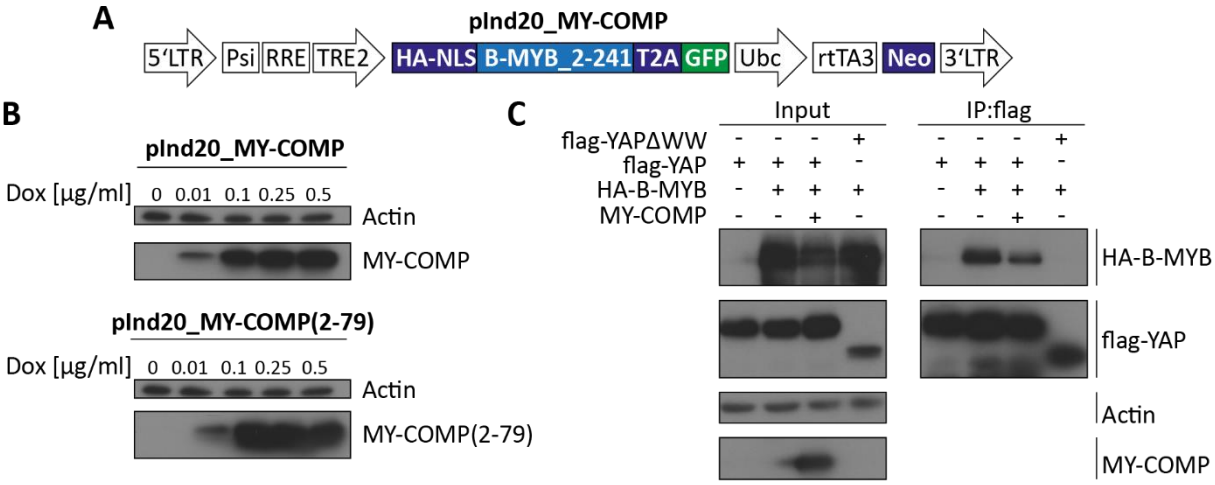

Figure 34: Doxycycline inducible MY-COMP reduces B-MYB-YAP interaction
(**A**) Scheme of lentiviral pInducer20 MY-COMP construct with a neomycin resistance cassette. MY-COMP expression is linked to GFP expression via a T2A self-cleavage peptide. (**B**) Lysates of HeLa cells treated with the indicated doxycycline concentrations for 48 hours were separated by SDS-PAGE. Subsequent immunoblotting with a HA-specific antibody revealed doxycycline induced expression of MY-COMP or MY-COMP(2-79). Actin was used as a loading control. (**C**) Lysates of stable pInducer20_MY-COMP HeLa cells expressing HA-tagged B-MYB or flag-tagged YAP were immunoprecipitated with flag-antiserum. Lysates of HeLa cells expressing a YAP mutant lacking the WW-domains served as a positive control. Lysates of HeLa cells expressing only flag-YAP served as a negative control. Immunoblotting with specific B-MYB and flag-antibodies indicate that doxycycline dependent expression of MY-COMP suppresses the interaction of YAP with B-MYB. 3% of the lysate used for the IP was loaded on a gel as an input control. Actin served as a loading control. Immunoblotting with a HA-specific antibody visualized MY-COMP induction.

To test whether induction of MY-COMP influences the cell cycle of HeLa cells, we performed flow cytometry cell cycle analysis using propidium iodide DNA staining. According to the DNA content of a cell, this method allows to differentiate between G1, S, G2/M phase of the cell cycle or whether cells are polyploid. Green fluorescence was used to identify cells with MY-COMP expression, because in this system MY-COMP expression was dependent on GFP expression. After 4 days of doxycycline treatment, the fraction of polyploid cells increased from 12.5% to more than 47% in HeLa cells expressing MY-COMP, compared to GFP expressing control cells (**Figure 35A**, **C**, **D**). As a consequence, the fraction of cells in G1 phase was decreased after the expression of MY-COMP (**Figure 35A**, **C**, **D**). Importantly, the fraction of polyploid cells was stable in HeLa cells expressing a shorter version of MY-COMP(2-79), indicating the specificity of the MY-COMP construct (**Figure 35B**, **D**). In order to investigate whether the expression of MY-COMP influences the growth of HeLa cells over a longer time period, cells were seeded at low density on 24-well plates and treated with doxycycline for 10 days. Crystal violet staining of viable cells was done every second day. HeLa cells expressing either GFP or a shorter version of MY-COMP(2-79) served as a control (**Figure 35E**).

Quantification revealed that induction of MY-COMP significantly suppressed growth in HeLa cells after six days (**Figure 35G**). Importantly, induction of GFP or MY-COMP(2-79) did not alter growth of HeLa cells (**Figure 35F**, **H**).

Taken together, blockage of YAP-B-MYB interaction by MY-COMP, impairs cell mitosis and cytokinesis, causing polyploidization of the cells. Consequently, cells expressing MY-COMP exhibit a growth deficit.

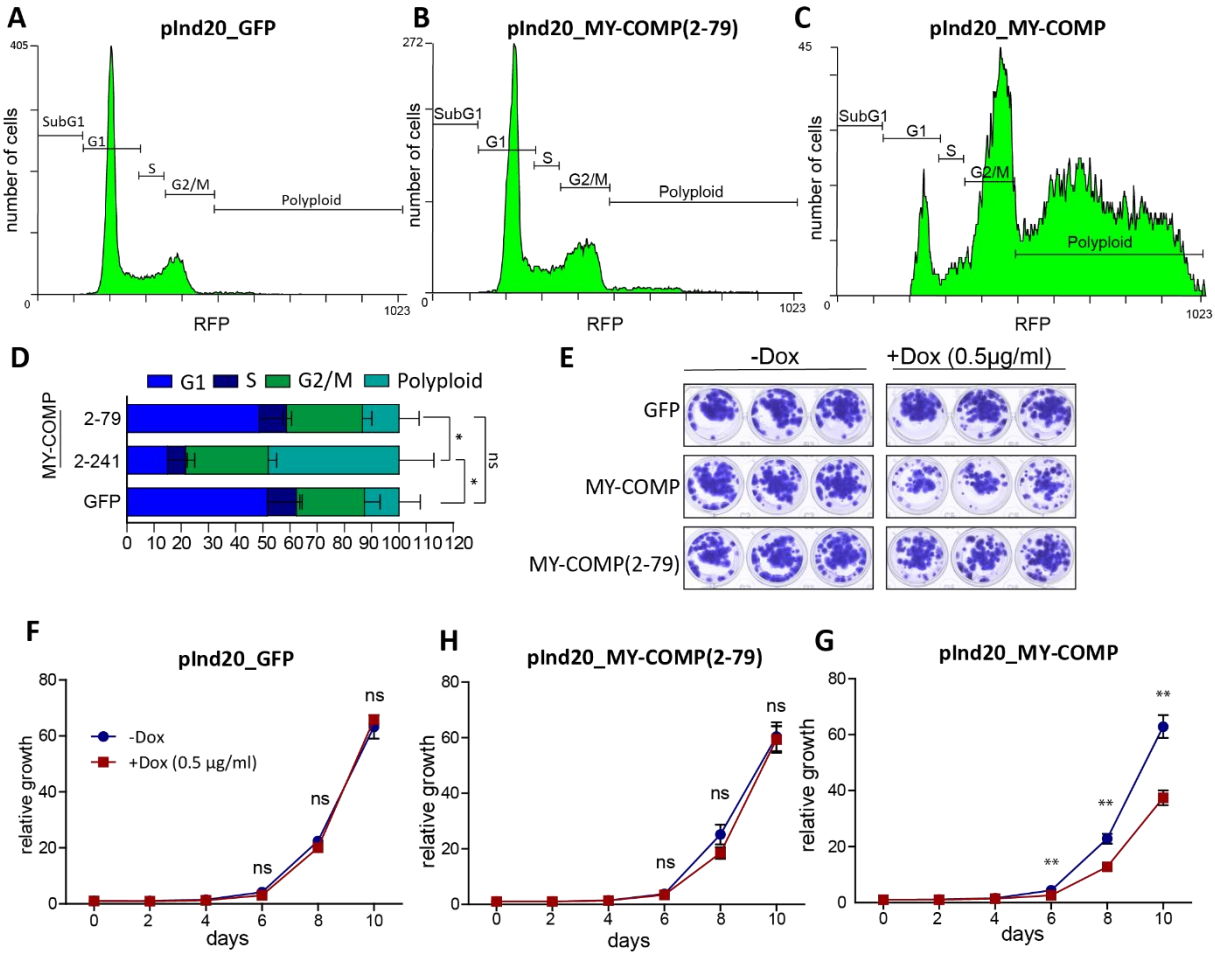

Figure 35: MY-COMP expression results in polyploidization and growth arrest in HeLa cells

After 4 days treatment with 0.5 µg/ml doxycycline, stable pInducer20 HeLa cells expressing either GFP (**A**), MY-COMP(2-79) (**B**) or MY-COMP (**C**) were analyzed by Flow cytometric analysis of cell cycle using propidium iodide DNA staining. According to the amount of DNA, cells were identified to be in subG1, G1, S, G2/M phase of the cell cycle or polyploid. 20,000 GFP positive cells were measured per condition. (**D**) Quantification of the analysis of (**A**, **B**, **C**). n=3 biological replicates. For growth curves, 185 HeLa cells with the indicated pInducer20 constructs were seeded on 24-well plates and treated with 0.5 µg/ml doxycycline for 10 days. HeLa cells were fixed with 10% formalin every two days and subsequently stained with crystal violet. Representative images of crystal violet stained cells with the indicated pInducer20 constructs after eight days of doxycycline treatment (0.5 µg/ml) are shown in (**E**). Quantification of the growth curves of HeLa cells expressing GFP (**F**), MY-COMP(2-79) (**H**) or MY-COMP (**G**) indicate that expression of MY-COMP results in growth deficit. (**F**, **G**, **H**) Error bars show standard error of the mean (SEM) from one representative experiment performed in triplicates. N=2 biological replicates. To determine statistical significance, Student's t-test (two-tailed) was used. *P≤0.05, ** P≤0.01; ns, not significant, P>0.05.

4. Discussion

4.1 The MMB complex is essential for early heart development

The first part of this thesis addressed the role of the MMB complex during heart development. MMB directly regulates a panel of mitotic genes in cardiomyocytes and loss of the MMB subunit LIN9 in heart progenitor cells results in an embryonic lethal phenotype. Recently, our laboratory showed that the MMB target gene GAS2L3 is strongly downregulated in hearts during transition from embryonal to postnatal stages. This developmental period represents the time where murine cardiomyocytes exit from the cell cycle (Stopp et al., 2017). The results of this thesis demonstrated that B-MYB, FOXM1, and several MMB target genes displayed a similar gene expression pattern and were robustly downregulated within the first ten days after birth (**Figure 6**). During this phase, cardiomyocytes exit from the cell cycle and the binucleation process starts. Cell cycle exit of cardiomyocytes is accompanied by increasing levels of cell cycle inhibitors, such as p21 or p27, in the neonatal heart (Tane et al., 2014). Incomplete disassembly of contractile elements, like myofibril structures, are assumed to prohibit cytokinesis and cause binucleation of cardiomyocytes (Ahuja et al., 2004; Engel et al., 2006). However, the exact mechanism how cardiomyocytes exit the cell cycle is still unclear. Results from this thesis revealed that genes associated with the repressive functions of the DREAM complex, such as LIN37, E2F4 and p130, peaked in expression shortly after birth. In contrast, expression of the MuvB core, LIN9, LIN52, and LIN54, did not change at this time point. Together these data reveal the switch from the activator MMB complex to the repressive DREAM complex during transition from the embryonal to the neonate heart. In adult hearts the promoters of cell cycle genes are found in an open chromatin conformation and thereby are accessible for transcription factors (Monroe et al., 2019). Consistent with these data, in this thesis the MuvB subunit LIN9 was still bound to the promoter of MMB target genes at P10 (**Figure 13**). Thus, in cardiomyocytes the DREAM complex may play a dual role in the regulation of cell cycle genes. Firstly, to silence expression of cell cycle genes during the transition from embryonal to postnatal stages. Secondly, DREAM may keep the promoters of cell cycle genes in an open conformation that allows their reactivation.

In another line of evidence knockout of LIN9 in heart progenitor cells leads to early embryonic lethality accompanied by a deficit in cardiomyocyte proliferation. Interestingly, knockout of FOXM1 in heart progenitor cells results in a similar phenotype and cardiomyocytes lacking FOXM1 exhibit reduced proliferation (Bolte et al., 2011). Moreover, several studies showed that expression of LIN9, B-MYB and FOXM1 is essential to sustain cell proliferation and severe phenotypes are accompanied with the loss of MMB. For instance, LIN9 knockout mice die in utero before implantation (Reichert et al., 2010). Taken together, these findings emphasize the role of the MMB complex in maintaining cell proliferation, which is essential for tissue growth and homeostasis. Despite the severe phenotype of *Lin9; Nkx-Cre* mice*,* no obvious phenotype was observed after loss of LIN9 in the adult heart mediated by *α-MHC-Cre* (**Figure 19**). Compared to other organs, such as the hematopoietic system or intestine tissue, where proliferating cells rapidly renew the cell pool, adult cardiomyocytes rarely divide.

During the life period of a human heart only 50% of cardiomyocytes are replaced by division of pre-existing cardiomyocytes (Bergmann et al., 2009). Similar results were found in mice where most of the cardiomyocytes developed before birth and the level of proliferating cardiomyocytes abruptly drops after birth (Wang et al., 2018). However, a small percentage of cardiomyocytes remains within the cell cycle and sustains the pool of pre-existing cardiomyocytes (Ali et al., 2014; Bergmann et al., 2015). All together cardiomyocyte proliferation is very low in the adult heart compared to other tissues, which could explain the loss of a phenotype in *Lin9; MHC-Cre*. In contrast, whole-body deletion of LIN9 in adult *Lin9; CreER^{T2}* mice led to death within seven days due to proliferation defects within the villus epithelium of the small intestine (Reichert et al., 2010). In conclusion, LIN9 is important for maintenance of tissue structures with high cell proliferation, such as the villus epithelium or the embryonal heart, whereas LIN9 is dispensable in postmitotic tissues, such as the postnatal heart.

4.2 MMB is essential for pro-proliferative functions of YAP in cardiomyocytes

Cardiomyocytes switch from hyperplastic to hypertrophic growth shortly after birth. During this phase the regenerative potential of the heart decreases dramatically due to limited capacity of cardiomyocyte proliferation (Porrello et al., 2011). Because the regenerative potential of the adult heart is limited, factors that prolong the hyperplastic growth of cardiomyocytes are of great interest for heart regeneration. The Hippo signaling pathway was first identified in *drosophila melanogaster* to regulate organ growth due to enhanced proliferation and reduction of apoptosis. Similar to other organs, perturbation of the Hippo signaling in the heart results in hyperplastic tissue overgrowth due to enhanced proliferation (Heallen et al., 2011). For example, cardiac-specific knockout of Hippo signaling components, such as SAV1, MST1/2 and LATS1/2, leads to postnatal lethality in mice due to tissue overgrowth (Heallen et al., 2011). In contrast, cardiomyocyte specific deletion of YAP results in embryonic lethality due to reduced levels of cardiomyocyte proliferation (Xin et al., 2011). Thus, Hippo-deficiency or expression of activated YAP results in elevated cardiomyocyte proliferation, which contributes to recovery after myocardial infarction (Heallen et al., 2013; Leach et al., 2017; Xin et al., 2013). YAP-driven proliferation in the neonatal heart is antagonized by the TEAD binding protein VGLL4. VGLL4 negatively regulates YAP-driven proliferation in cardiomyocytes by interacting directly with TEAD proteins and therefore mediating proteasomal degradation of TEAD by cysteine peptidases. Importantly, acetylation of VGLL4 by p300 blocks TEAD binding and thereby enhances YAP-TEAD activity (Lin et al., 2016).

The second part of this thesis provides new insights into YAP-driven proliferation of cardiomyocytes and sheds light on the crosstalk between the Hippo pathway and the MMB complex in the heart. Genetic interaction studies in mice revealed that LIN9, the central component of the MMB complex, is necessary to sustain proliferation in Hippo deficient embryonal hearts (**Figure 11**). Our data implicate that the crosstalk between Hippo signaling and the MMB complex regulates proliferation of cardiomyocytes. As reported previously, cardiac-specific deletion of SAV1 robustly increased proliferation in the embryonic heart

(Heallen et al., 2011). This pro-proliferative phenotype in Hippo-deficient hearts is suppressed completely in SAV1, LIN9 double knockout hearts indicating that LIN9 is essential for proliferation of Hippo-deficient cardiomyocytes. Since proliferation of embryonal cardiomyocytes is strongly affected by the loss of LIN9, it is possible at this stage that there are two independent pathways regulating proliferation of cardiomyocytes. The function of MMB as a regulator of cell cycle dependent gene expression could simply dominate Hippo deficiency and suppresses the pro-proliferative function of the Hippo pathway. However, although LIN9 is dispensable in the postnatal heart, our data indicate that LIN9 is required in postnatal Hippo-deficient hearts to drive proliferation of cardiomyocytes (**Figure 21**). Together these findings support the idea that an interplay between Hippo-YAP and the MMB complex regulates cardiomyocyte proliferation. According to our data it would be interesting to study whether loss of LIN9 is required for heart regeneration after myocardial infarction in postnatal Hippo-deficient hearts. Neonate mice benefit from proliferation of cardiomyocytes, which contributes to better regeneration and limited scarring after myocardial infarction in contrast to adult mice (Porrello et al., 2013). Hippo-deficiency is beneficial for regeneration of the neonatal and postnatal heart after myocardial infarction (Heallen et al., 2013). Despite being dispensable for normal function of the postnatal heart, the utilized *Lin9; α-MHC-Cre* mouse strain is a suitable model to analyze whether LIN9 is important for regeneration in Hippo-deficient hearts. Since LIN9 was necessary for proliferation of embryonal and Hippo-deficient postnatal cardiomyocytes, results of this thesis predict that correct function of MMB is critical for reactivation of cardiomyocyte proliferation after myocardial infarction. Since proliferation of Hippo-deficient cardiomyocytes is suppressed by the loss of LIN9, one would expect that LIN9 highly contributes to the regenerative capacity of the Hippo pathway.
The Hippo-deficient phenotype in the heart is phenocopied after overexpression of activated YAP mutants in cardiomyocytes, indicating that the pro-proliferative function of the Hippo pathway is mainly driven by YAP (von Gise et al., 2012; Monroe et al., 2019; Xin et al., 2013). In line with this, the pro-proliferative function of YAP was directly suppressed by loss of LIN9 in isolated cardiomyocytes transduced with an activated YAP mutant (**Figure 22**). This result validated the data obtained from our genetic model and clearly showed that the effects obtained in the mouse models are cell autonomous.

4.3 Hippo-deficiency facilitates activation of mitotic MMB target genes in the heart

Transcriptomic analysis of Hippo-deficient hearts revealed upregulation of mitotic genes (Heallen et al., 2011; Morikawa et al., 2015). Interestingly, overexpression of activated YAP mutants in cardiomyocytes result in a gene expression pattern similar to Hippo-deficient hearts, suggesting that upregulation of mitotic genes is mainly driven by YAP (von Gise et al., 2012). Therefore, it is of great interest to identify processes contributing to YAP-driven activation of mitotic genes.

The Hippo pathway negatively regulates a set of Wnt target genes in the heart (Heallen et al., 2011). Data from the study by Heallen et al. 2011 point to a model in which YAP and the Wnt transcription factor β-catenin form a complex to regulate gene expression. Genetic interaction studies revealed that heterozygotic loss of β-catenin suppressed tissue overgrowth due to the loss of SAV1 in the heart (Heallen et al., 2011). Thus, β-catenin and YAP together regulate a transcriptional program, which enables cardiomyocyte proliferation.

The findings of this thesis go beyond previously published data, revealing that Hippo-deficient hearts upregulate a set of MMB-bound cell-cycle related genes (**Figure 17**). Chromatin binding studies of the MMB subunit LIN9 revealed a positive correlation between binding of LIN9 and Hippo repressed genes, indicating that MMB binds to promoters of genes, which are upregulated in Hippo-deficient hearts (**Figure 17**). In another line of evidence, upregulation of cell-cycle related genes in Hippo-deficient hearts was suppressed after loss of LIN9 (**Figure 12**). Taken together results of this thesis point to a model were Hippo deficiency activates a transcriptional program to drive mitotic MMB target gene expression.

Several studies in cancer cell lines contribute to the overall understanding of the mechanisms of mitotic gene regulation by YAP. Genome wide binding studies revealed that YAP primarily binds to TEAD sites within the genome. These findings showed that the main transcriptional output of the Hippo signaling cascade is controlled by YAP-TEAD interaction (Zhao et al., 2008). Most of the YAP binding sites are not located at the promoters of YAP activated genes, but YAP primarily binds to distal enhancers of those genes (Galli et al., 2015; Stein et al., 2015; Zanconato et al., 2015). Chromatin conformation capture studies revealed that formation of chromatin loops brings YAP-bound enhancers into close contact with associated promoters. Thus, YAP regulated gene expression is mediated by promoter-enhancer loops (Galli et al., 2015; Zanconato et al., 2015). Recently, our laboratory identified that the MMB complex and YAP regulate an overlapping set of late mitotic genes in lung adenocarcinoma cell lines. On the one hand, YAP directly regulates the expression of the MMB transcription factor B-MYB. On the other hand, YAP recruits B-MYB to the promoter of mitotic genes and activates expression of those MMB target genes (Pattschull et al., 2019). Thus, YAP cooperates with the MMB-complex at promotor-enhancer loops of some late mitotic genes to regulate the expression of these genes (Pattschull et al., 2019).

In line with the findings in tumor cell lines, there is also evidence that YAP drives the expression of mitotic genes, such as *Birc5* and *AurkB*, in Hippo-deficient hearts by binding to the enhancers of the genes (Morikawa et al., 2015). In a similar manner YAP was identified to regulate the expression of *Lin9* in Hippo-deficient hearts (Morikawa et al., 2015). Supporting the literature, this thesis revealed that YAP primarily binds to enhancers or super-enhancers in the fetal heart (**Figure 14**). However, data of this thesis indicate that B-MYB and not LIN9 is elevated in Hippo-deficient hearts (**Figure 18**). Thus, B-MYB appears to be the critical component of the MMB complex, which facilitates gene expression in Hippo deficient hearts. In postnatal hearts, YAP activity is decreased, which is indicated by rising levels of phosphorylated YAP (Heallen et al., 2013). In line with this, B-MYB expression decreases dramatically in postnatal hearts, whereas LIN9 expression is stable (**Figure 6**). Moreover, LIN9 remains associated with the promoters of MMB target genes (**Figure 13**). Taken together, findings provided in this thesis support the idea that B-MYB instead of LIN9 is the critical component of the MMB complex facilitating mitotic gene expression in the heart.

Future work should aim to identify YAP-bound enhancers of MMB target genes in the heart. Therefore, the chromatin architecture could be analyzed by chromatin conformation capture assays. Previous studies suggest that the organization of the chromatin in cardiomyocytes changes during development (Bertero et al., 2019; Rosa-Garrido et al., 2017). However, these studies were focused on the regulation of developmental genes. Therefore, it would be of great interest to test whether conformational changes at genomic regions of cell cycle genes occur during heart development, which affect the expression of those genes.

4.4 Interaction of MMB and YAP is required for proliferation and induction of mitotic genes

The third part of this thesis was to characterize the YAP-B-MYB interaction in detail and to test whether the interaction is responsible for YAP driven gene expression and proliferation. Previous studies from our laboratory showed that YAP and B-MYB physically interacted in lung adeno carcinoma cells. Endogenous interaction between the proteins was confirmed in co-immunoprecipitation studies and by PLA. After growth factor stimulation of serum starved MCF10A cells, YAP-B-MYB interaction is associated with the cell cycle and is detected most abundantly in late S and G2 phase (Pattschull et al., 2019).

Data from this thesis characterizes the YAP-B-MYB interaction in detail revealing that the interaction is necessary for cell cycle progression of cardiomyocytes and further implicating the importance of YAP-driven mitotic gene expression. The biochemical characterization of the interaction revealed that the WW-domains of YAP are necessary for binding to B-MYB (**Figure 24**). The WW-domain is a small protein domain containing between 35-40 amino acids. The core is built by two tryptophan residues, which are embedded within an anti-parallel triple-stranded β-sheet. The structure of the WW-domain facilitates direct protein-protein interaction (Sudol et al., 2012).

Two distinct groups of interaction partners bind to WW-domains. The first cluster of proteins harbors a proline-tyrosine (PY) motif, whereas the second cluster of proteins contains serine-proline (SP) sites. Two WW-domains are found in the YAP protein. Both YAP-WW-domains are known binders of PY motif containing proteins, whereas only the first WW-domain of YAP interacts with SP-sites (Aragón et al., 2012). In pulldown assays, both YAP-WW-domains bind individually to the B-MYB protein, but strongest binding was observed in constructs containing both WW-domains (**Figure 25**). Although B-MYB contains 10 SP sites, which are phosphorylated by CDK1 or CDK2 complexes (Werwein et al., 2019), none of the SP sites are located within the identified N-terminal YAP binding domain of B-MYB. This suggests that B-MYB interacts with YAP-WW-domains via a different motif. Indeed, µSPOT-based peptide mapping identified a 15 amino acid peptide containing a PY motif, which is located within the previously identified YAP binding domain of B-MYB, as the binding motif for the YAP WW-domains (**Figure 28**). Importantly, deletion of the PY motif results in significantly reduced binding of B-MYB to the YAP WW-domains (**Figure 27**). Taken together, our data indicates that the YAP WW-domains interact with a PY motif in the N-terminus of B-MYB.

Like YAP, also the peptidyl-prolyl-cis-trans isomerase NIMA interacting 1 (PIN1) interacts with B-MYB. PIN1 is a WW-domain containing protein that induces conformational changes and facilitates CDK-dependent phosphorylation of B-MYB. In contrast to YAP, PIN1 binding to B-MYB is dependent on 10 SP sites within the B-MYB protein (Werwein et al., 2019). Since SP sites are known binding motifs of WW-domains, it is likely that PIN1 binds to B-MYB in a WW-dependent manner. Therefore, future studies should aim whether WW dependent binding to B-MYB is a general mode of how B-MYB facilitates protein interactions. Consequently, other proteins that share sequence identity to the WW-domains of YAP or PIN1 are possible candidates for B-MYB binding.

Notably, TAZ was also identified to interact with B-MYB in co-immunoprecipitation studies (**Figure 25**). In comparison to YAP, TAZ displays a similar domain architecture but lacks one of the two WW-domains. The first WW-domain of YAP and the WW-domain of TAZ share a very similar amino acid sequence (Vargas et al., 2019). However, there is some individual sequence specificity and it is not clear whether TAZ interacts with B-MYB in a WW-dependent manner. Therefore, future work will be necessary to elucidate the specificity of TAZ-B-MYB interaction.

The human proteasome harbors approximately 100 WW-domains and over 2000 PY motif containing ligands. This variety raises the question about the specificity of the interaction between WW-domains and their corresponding PY ligand. Interestingly, there are four WW-containing proteins and nine PY motif containing proteins within the Hippo pathway. Two recent publications shed light on the specificity of WW-domain interactions. The Hippo WW-domains possess a nine amino acid motif that determines the binding specificity. This motif unifies the Hippo WW-domains compared to other WW-domains. Single point mutation within the nine amino-acid motif abrogated the binding to the PY ligand (Vargas et al., 2019). Often proteins contain more than one WW-domain. The so-called tandem WW-domains display a high affinity to their associated PY containing ligand. The linker of the individual WW-domains plays a critical role in specifying the binding to the ligand (Lin et al., 2019). Taken together, interactions between WW-domains and their PY ligand are specified by the individual structure of the WW-domain and the interplay between tandem WW-domains and their corresponding ligand. Isothermal titration calorimetry (ITC) could be employed to determine the binding specificity of the YAP-B-MYB interaction. Since both YAP WW-domains interact with B-MYB, but only one YAP-binding motif was identified in B-MYB, it raises the question whether two B-MYB molecules interact with the YAP WW-domains or whether even a third interaction partner stabilizes this interaction.

Compared to canonical PY containing motifs, which were used as positive control in the peptide array, the affinity of the B-MYB peptide interacting with the YAP WW-domain was rather low. Moreover, shifting the motif by two amino acids decreased or even abolished the interaction indicating that maybe other amino acid residues contributed to the interaction (**Figure 28**). In line with this result, deletion of the four amino acids in B-MYB that form the PY motif decreased the interaction with YAP but not completely interrupted the interaction (**Figure 27**).

Interaction of YAP with TEAD is critical for YAP to fulfill its transcriptional function. Several studies showed that inhibition of TEAD-YAP interaction by the drug verteporfin abrogate the proliferative phenotype of YAP. A recent study showed that besides the TEAD-binding domain and the transactivation domain, also the WW-domain of YAP is important for correct function of the protein (Kurppa et al., 2020). In line with this, the WW-domain of YAP was found to be important to induce proliferation in neonatal cardiomyocytes (**Figure 30**). Transduction of neonatal cardiomyocytes with activated YAP mutants robustly elevated levels of proliferation. Mutation in either the TEAD-binding domain or deletion of the WW-domains ablated the increase in cardiomyocyte proliferation. As another piece of evidence, the WW-domains as well as binding to TEAD were necessary for YAP mediated induction of MMB target genes in differentiated C2C12 cells. Importantly, TEAD binding but not the WW-domains were required for induction of YAP direct target genes (genes with YAP -bound promoters) (**Figure 31**). This indicates that activation of YAP direct target genes is dependent on YAP-TEAD interaction, while the activation is independent of the WW-domains. In contrast, a different mode of regulation is observed for YAP dependent gene expression of MMB direct target genes. Combination of this information with our ChIP-Seq data implicates that WW dependent interaction of YAP with B-MYB at promoter-enhancer loops of mitotic MMB target genes is critical for activation of these genes.

4.5 MY-COMP - a new tool to suppress the pro-proliferative functions of YAP

As mentioned before, the YAP-TEAD interaction is critical for the pro-proliferative function of YAP. Recently three publications showed that peptide-based inhibitors effectively antagonize YAP activity by blocking the YAP-TEAD interaction. First, a 17-mer cyclic peptide (peptide 17) robustly blocks YAP-TEAD interaction (Zhang et al., 2014b). Second, a peptide that mimics the TDU-domain of VGLL4 is a TEAD super-binder and competes with YAP in binding to TEAD. Super-TDU peptide utilizes that VGLL4 binding to TEAD is stronger than the YAP-TEAD interaction (Jiao et al., 2014). Third, TEADi a construct that combines the TEAD-binding domains of VGLL4, YAP1 and TAZ, inhibits the transcriptional activation of TEAD (Yuan et al., 2020).

Here we inhibit the activity of YAP by blocking the WW-domain of the protein. The information obtained from the characterization of YAP-B-MYB interaction was employed to generate a peptide-based competitive inhibitor that specifically blocks WW function of YAP. Since YAP and B-MYB interact directly, a construct of B-MYB harboring the YAP binding domain was fused to a nuclear localization signal. MY-COMP (Myb-YAP competition) blocks the interaction of B-MYB with the YAP WW-domains by binding to YAP (**Figure 29**). Functionally, adenoviral delivered MY-COMP suppressed mitotic entry of embryonal cardiomyocytes in a PY motif dependent manner (**Figure 32**).

The WW-domain of YAP is known to interact with factors that either promote cell proliferation or suppress YAP activity. For instance, the WW-domain mediates interaction with inhibitors of YAP activity, like AMOTL1 or LATS1/2. This is consistent with the fact that mutation of the WW-domain of YAP promotes the transformation and migration in epithelial MCF10A cells (Zhang et al., 2009). AMOTL1 and LATS1/2 form complexes that sequester YAP in the

cytoplasm and prevent translocation into the nucleus. This contrasts with our findings that MY-COMP blocks proliferation in embryonal cardiomyocytes (**Figure 32**). However, experiments from Zhang and colleagues (2009) showed that the YAP WW-domains are required to drive tissue growth in *Drosophila melanogaster* and to promote cell transformation in NIH-3T3 cells. Therefore, the WW-domain obtains a dual role in regulation of YAP activity that might be cell type-specific (Zhang et al., 2009). Most of the WW-domain mediated interactions that block YAP activity are cytoplasmic, whereas transcription factors, such as B-MYB, exclusively interact with the YAP WW-domain in the nucleus of cells (**Figure 23**). MY-COMP was designed to suppress the nuclear activity of YAP. This was achieved by fusion of a NLS sequence, which renders MY-COMP primarily to the nucleus of cells (**Figure 32**). In conclusion, nuclear blockage of WW-domain activity, as done by MY-COMP, may bypass cytoplasmic inhibitors of YAP and therefore provides a mechanism for antagonizing YAP's pro-proliferative function.

Further characterization of the MY-COMP phenotype in HeLa cells revealed an increase in nuclear abnormalities. After treatment with MY-COMP, cells obtained elevated levels of bi-or multinucleated cells. Moreover, a high number of cells showed micronuclei indicating defects in mitosis or cytokinesis (**Figure 33**). The cellular phenotype caused by MY-COMP is quite similar to the cellular phenotype observed after loss of MMB (Pattschull et al., 2019; Reichert et al., 2010). Beside the cellular phenotype, increase in polypoid cells as well as growth deficit were observed in MY-COMP treated HeLa cells (**Figure 35**). An improved MY-COMP could use a PY-motif with stronger interaction to the YAP WW-domain compared to the B-MYB motif. For instance, the motifs of AMOT or LATS1/2, which were used as a positive control in the peptide array exhibit robust binding to YAP WW-domain. Similar to the TEADi construct that blocks YAP-TEAD binding, several strong YAP WW-binders could be combined to generate a superefficient blockage of YAP WW-domain (Yuan et al., 2020).

A recent study showed that after inactivation of Hippo signaling, cells become addicted to YAP for proliferation. Moreover, high levels of active YAP in certain subtypes of cancer, such as ovarian cancer, liver cancer and breast cancer, renders growth of cancer cell lines dependent on YAP (Han et al., 2018). Therefore, future studies should aim to understand whether MY-COMP can be used as a tool to inhibit tumor growth of YAP-addicted tumor cell lines.

The uveal melanoma, a subtype of melanoma, that occurs in the eye, could be a suitable model to study YAP dependent tumor growth. It is well-known that more than 80% of uveal melanomas harbor mutations in G protein coupled receptor alpha subunits GNAQ and GNA11 that inactivates Hippo signaling. Consequently, activated YAP drives initiation as well as tumor progression in uveal melanomas (Koo et al., 2020; Li et al., 2019; Yu et al., 2014). Uveal melanoma is a very aggressive tumor subtype and efficient treatment strategies are unknown. Therefore, it could be of interest to test whether MY-COMP inhibits proliferation of uveal melanoma cell lines.

4.6 Conclusion

Previous studies identified the Hippo signaling pathway and its transcriptional coactivator YAP to regulate proliferation of cardiomyocytes and to control heart growth during development. Dysregulation of the Hippo core cascade or activating mutations in YAP were shown to increase cardiomyocyte proliferation (von Gise et al., 2012; Heallen et al., 2011, 2013; Leach et al., 2017; Lin et al., 2014; Monroe et al., 2019; Xin et al., 2013).

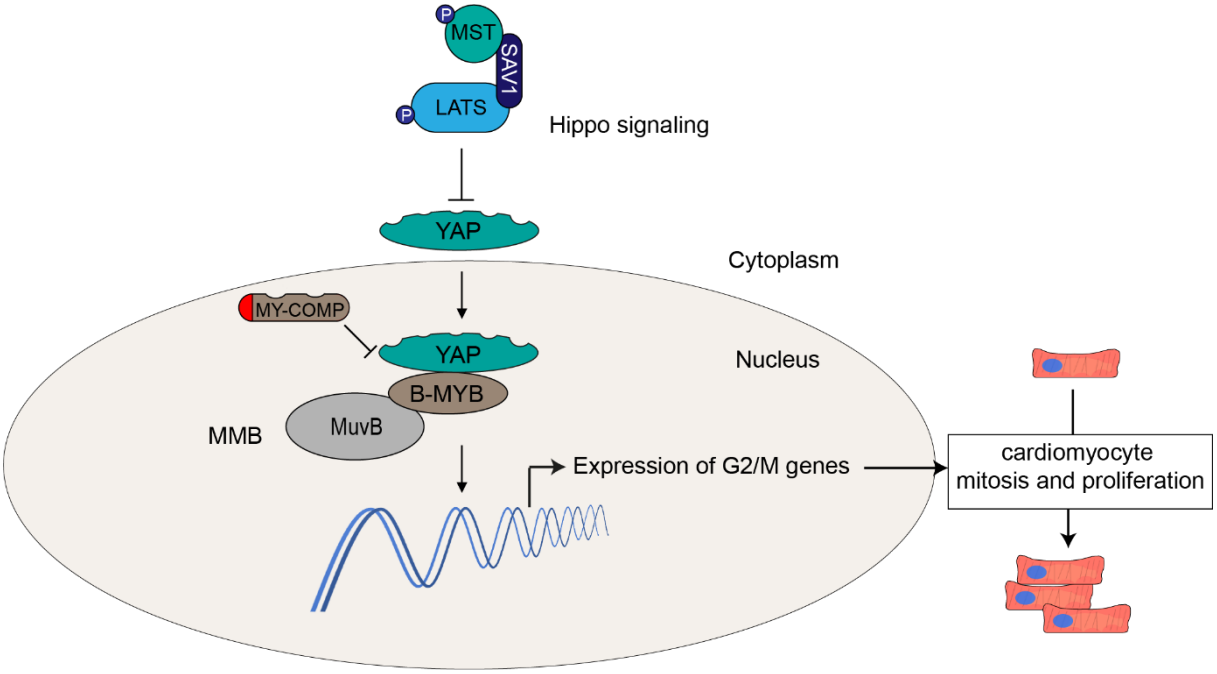

Figure 36: Model of the crosstalk between Hippo signaling and MMB complex in cardiomyocytes
Hippo signaling impedes the pro-proliferative function of YAP in cardiomyocytes. Interaction of YAP and Myb-MuvB complex drives the expression of mitotic genes and thus activates proliferation of cardiomyocytes. Competitive binding of MY-COMP blocks the pro-proliferative phenotype of YAP.

The results reported in this thesis shed light on the molecular mechanisms that control cardiomyocyte proliferation. The Hippo pathway negatively regulates YAP activity and blocks translocation of YAP to the nucleus. The crosstalk between the MMB complex and the Hippo pathway was identified to play a substantial role in cell cycle control of cardiomyocytes. YAP, the coactivator of the Hippo pathway not only interacts with MMB transcription factor B-MYB in developing cardiomyocytes, but YAP and the MMB complex orchestrate the expression of mitotic genes in the embryonal heart. (**Figure 36**). Biochemical characterization showed that YAP WW-domains interact with a PY motif in the N-terminus of B-MYB. This interaction is required to sustain proliferation in the heart. Collectively, the data reported in this thesis provided the basis to design a competitive inhibitor of YAP called MY-COMP. MY-COMP is a peptide-based tool, which is able to suppress the pro-proliferative function of YAP (**Figure 36**). Expression of MY-COMP in HeLa cells is associated with nuclear abnormalities. Thus, blockage of YAP activity by MY-COMP might provide a novel strategy for the treatment of YAP-addicted cancers.

5. References

Afgan, E., Baker, D., Batut, B., Van Den Beek, M., Bouvier, D., Ech, M., Chilton, J., Clements, D., Coraor, N., Grüning, B.A., et al. (2018). The Galaxy platform for accessible, reproducible and collaborative biomedical analyses: 2018 update. Nucleic Acids Research *46*, W537–W544.

Agah, R., Frenkel, P.A., French, B.A., Michael, L.H., Overbeek, P.A., and Schneider, M.D. (1997). Gene recombination in postmitotic cells . Targeted expression of Cre recombinase provokes cardiac-restricted, site-specific rearrangement in adult ventricular muscle in vivo. Journal of Clinical Investigation *100*, 169–179.

Ahuja, P., Perriard, E., Perriard, J.-C., and Ehler, E. (2004). Sequential myofibrillar breakdown accompanies mitotic division of mammalian cardiomyocytes. Journal of Cell Science *117*, 3295–3306.

Ahuja, P., Sdek, P., and Maclellan, W.R. (2007). Cardiac Myocyte Cell Cycle Control in Development , Disease , and Regeneration. Physiol Rev *87*, 521–544.

Ai, D., Fu, X., Wang, J., Lu, M.F., Chen, L., Baldini, A., Klein, W.H., and Martin, J.F. (2007). Canonical Wnt signaling functions in second heart field to promote right ventricular growth. Proceedings of the National Academy of Sciences of the United States of America *104*, 9319–9324.

Alberts, B., Johnson, A., Lewis, J., Morgan, D., Raff, M., Roberts, K., and Walter, P. (2015). Molecular Biology of the Cell (New York: Garland Science, Taylor & Francis Group, LLC).

Ali, S.R., Hippenmeyer, S., Saadat, L. V., Luo, L., Weissman, I.L., and Ardehali, R. (2014). Existing cardiomyocytes generate cardiomyocytes at a low rate after birth in mice. Proceedings of the National Academy of Sciences of the United States of America *111*, 8850–8855.

Van Amerongen, M.J., and Engel, F.B. (2008). Features of cardiomyocyte proliferation and its potential for cardiac regeneration. Journal of Cellular and Molecular Medicine *12*, 2233–2244.

Aragón, E., Goerner, N., Xi, Q., Gomes, T., Gao, S., Massagué, J., and Macías, M.J. (2012). Structural basis for the versatile interactions of Smad7 with regulator WW domains in TGF-β pathways. Structure *20*, 1726–1736.

Bartek, J., Lukas, C., and Lukas, J. (2004). Checking on DNA damage in S phase. Nature Reviews Molecular Cell Biology *5*, 792–804.

Beall, E.L., Manak, J.R., Zhou, S., Bell, M., Lipsick, J.S., and Botchan, M.R. (2002). Role for a Drosophila Myb-containing protein complex in site-specific DNA replication. Nature *420*, 833–837.

Bergmann, O., Bhardwaj, R.D., Bernard, S., Zdunek, S., Barnabé-Heide, F., Walsh, S., Zupicich, J., Alkass, K., Buchholz, B.A., Druid, H., et al. (2009). Evidence for cardiomyocyte renewal in humans. Science *324*, 98–102.

Bergmann, O., Zdunek, S., Felker, A., Salehpour, M., Alkass, K., Bernard, S., Sjostrom, S.L., Szewczykowska, M., Jackowska, T., Dos Remedios, C., et al. (2015). Dynamics of Cell Generation and Turnover in the Human Heart. Cell *161*, 1566–1575.

Bertero, A., Fields, P.A., Ramani, V., Bonora, G., Yardimci, G.G., Reinecke, H., Pabon, L., Noble, W.S., Shendure, J., and Murry, C.E. (2019). Dynamics of genome reorganization during human cardiogenesis reveal an RBM20-dependent splicing factory. Nature Communications *10*, 1538.

Bertoli, C., Skotheim, J.M., and De Bruin, R.A.M. (2013). Control of cell cycle transcription during G1 and S phases. Nature Reviews Molecular Cell Biology *14*, 518–528.

Blagosklonny, M. V., and Pardee, A.B. (2002). The restriction point of the cell cycle. Cell Cycle *1*, 102–109.

Bolte, C., Zhang, Y., Wang, I.C., Kalin, T. V, Molkentin, J.D., and Kalinichenko, V. V. (2011). Expression of Foxm1 transcription factor in cardiomyocytes is required for myocardial development. PLoS ONE *6*, e22217.

Bolte, C., Zhang, Y., York, A., Kalin, T. V., Schultz, J.E.J., Molkentin, J.D., and Kalinichenko, V. V. (2012). Postnatal Ablation of Foxm1 from Cardiomyocytes Causes Late Onset Cardiac Hypertrophy and Fibrosis without Exacerbating Pressure Overload-Induced Cardiac Remodeling. PLoS ONE *7*, e48713.

Bunney, P.E., Zink, A.N., Holm, A.A., Billington, C.J., and Kotz, C.M. (2017). Orexin activation counteracts decreases in nonexercise activity thermogenesis (NEAT) caused by high-fat diet. Physiology & Behavior *176*, 139–148.

Cai, J., Zhang, N., Zheng, Y., De Wilde, R.F., Maitra, A., and Pan, D. (2010). The Hippo signaling pathway restricts the oncogenic potential of an intestinal regeneration program. Genes and Development *24*, 2383–2388.

Camargo, F.D., Gokhale, S., Johnnidis, J.B., Fu, D., Bell, G.W., Jaenisch, R., and Brummelkamp, T.R. (2007). YAP1 Increases Organ Size and Expands Undifferentiated Progenitor Cells. Current Biology *17*, 2054–2060.

Ceol, C.J., and Horvitz, H.R. (2001). dpl-1 DP and efl-1 E2F act with lin-35 Rb to antagonize Ras signaling in C. elegans vulval development. Molecular Cell *7*, 461–473.

Chan, E.H.Y., Nousiainen, M., Chalamalasetty, R.B., Schäfer, A., Nigg, E.A., and Sillje, H.H.W. (2005). The Ste20-like kinase Mst2 activates the human large tumor suppressor kinase Lats1. Oncogene *24*, 2076–2086.

Charrasse, S., Carena, I., Brondani, V., Klempnauer, K.H., and Ferrari, S. (2000). Degradation of B-Myb by ubiquitin-mediated proteolysis: Involvement of the CdC34-SCF(p45Skp2) pathway. Oncogene *19*, 2986–2995.

Chen, H.I., and Sudol, M. (1995). The WW domain of Yes-associated protein binds a proline-rich ligand that differs from the consensus established for Src homology 3-binding modules. Proceedings of the National Academy of Sciences of the United States of America *92*, 7819–7823.

Chen, L., Chan, S.W., Zhang, X.Q., Walsh, M., Lim, C.J., Hong, W., and Song, H. (2010). Structural basis of YAP recognition by TEAD4 in the Hippo pathway. Genes and Development *24*, 290–300.

Chen, Z., Friedrich, G.A., and Soriano, P. (1994). Transcriptional enhancer factor 1 disruption by a retroviral gene trap leads to heart defects and embryonic lethality in mice. Genes and Development *8*, 2293–2301.

Christensen, J., Cloos, P., Toftegaard, U., Klinkenberg, D., Bracken, A.P., Trinh, E., Heeran, M., Di Stefano, L., and Helin, K. (2005). Characterization of E2F8, a novel E2F-like cell-cycle regulated repressor of E2F-activated transcription. Nucleic Acids Research *33*, 5458–5470.

Cordenonsi, M., Zanconato, F., Azzolin, L., Forcato, M., Rosato, A., Frasson, C., Inui, M., Montagner, M., Parenti, A.R., Poletti, A., et al. (2011). The hippo transducer TAZ confers cancer stem cell-related traits on breast cancer cells. Cell *147*, 759–772.

Croci, O., De Fazio, S., Biagioni, F., Donato, E., Caganova, M., Curti, L., Doni, M., Sberna, S., Aldeghi, D., Biancotto, C., et al. (2017). Transcriptional integration of mitogenic and mechanical signals by Myc and YAP. Genes and Development *31*, 2017–2022.

D'Uva, G., Aharonov, A., Lauriola, M., Kain, D., Yahalom-Ronen, Y., Carvalho, S., Weisinger, K., Bassat, E., Rajchman, D., Yifa, O., et al. (2015). ERBB2 triggers mammalian heart regeneration by promoting cardiomyocyte dedifferentiation and proliferation. Nature Cell Biology *17*, 627–638.

Dai, X., Liu, H., Shen, S., Guo, X., Yan, H., Ji, X., Li, L., Huang, J., Feng, X.H., and Zhao, B. (2015). YAP activates the Hippo pathway in a negative feedback loop. Cell Research *25*, 1175–1178.

Dimova, D.K., and Dyson, N.J. (2005). The E2F transcriptional network: Old acquaintances with new faces. Oncogene *24*, 2810–2826.

Dong, J., Feldmann, G., Huang, J., Wu, S., Zhang, N., Comerford, S.A., Gayyed, M.F.F., Anders, R.A., Maitra, A., and Pan, D. (2007). Elucidation of a Universal Size-Control Mechanism in Drosophila and Mammals. Cell *130*, 1120–1133.

Drenckhahn, J.D., Schwarz, Q.P., Gray, S., Laskowski, A., Kiriazis, H., Ming, Z., Harvey, R.P., Du, X.J., Thorburn, D.R., and Cox, T.C. (2008). Compensatory Growth of Healthy Cardiac Cells in the Presence of Diseased Cells Restores Tissue Homeostasis during Heart Development. Developmental Cell *15*, 521–533.

Edgar, R., Domrachev, M., and Lash, A.E. (2002). Gene Expression Omnibus: NCBI gene expression and hybridization array data repository. Nucleic Acids Research *30*, 207–210.

Engel, F.B., Schebesta, M., and Keating, M.T. (2006). Anillin localization defect in cardiomyocyte binucleation. Journal of Molecular and Cellular Cardiology *41*, 601–612.

Esterlechner, J., Reichert, N., Iltzsche, F., Krause, M., Finkernagel, F., and Gaubatz, S. (2013). LIN9, a Subunit of the DREAM Complex, Regulates Mitotic Gene Expression and Proliferation of Embryonic Stem Cells. PLoS ONE *8*, e62882.

Fackler, M., Wolter, P., and Gaubatz, S. (2014). The GAR domain of GAS2L3 mediates binding to the chromosomal passenger complex and is required for localization of GAS2L3 to the constriction zone during abscission. FEBS Journal *281*, 2123–2135.

Farrance, I.K.G., Mar, J.H., and Ordahl, C.P. (1992). M-CAT binding factor is related to the SV40 enhancer binding factor, TEF-1. Journal of Biological Chemistry *267*, 17234–17240.

Fay, D.S., and Han, M. (2000). The synthetic multivulval genes of C. elegans: Functional redundancy, Ras-antagonism, and cell fate determination. Genesis *26*, 279–284.

Feil, R., Wagner, J., Metzger, D., and Chambon, P. (1997). Regulation of Cre recombinase activity by mutated estrogen receptor ligand-binding domains. Biochemical and Biophysical Research Communications *237*, 752–757.

Ferguson, E.L., Sternberg, P.W., and Horvitz, R. (1987). A genetic pathway for the specification of the vulval cell lineages of Caenorhabditis elegans. Nature *327*, 259–267.

Fischer, M., and Müller, G.A. (2017). Cell cycle transcription control: DREAM/MuvB and RB-E2F complexes. Critical Reviews in Biochemistry and Molecular Biology *52*, 638–662.

Flink, I.L., Oana, S., Maitra, N., Bahl, J.J., and Morkin, E. (1998). Changes in E2F complexes containing retinoblastoma protein family members and increased cyclin-dependent kinase inhibitor activities during terminal differentiation of cardiomyocytes. Journal of Molecular and Cellular Cardiology *30*, 563–578.

Foglia, M.J., and Poss, K.D. (2016). Building and re-building the heart by cardiomyocyte proliferation. Development *143*, 729–740.

Freese, N.H., Norris, D.C., and Loraine, A.E. (2016). Integrated genome browser: Visual analytics platform for genomics. Bioinformatics *32*, 2089–2095.

Fuhrmann-Benzakein, E., Garcia-Gabay, I., Pepper, M.S., Vassalli, J.-D., and Herrera, P.L. (2000). Inducible and irreversible control of gene expression using a single transgene. Nucleic Acids Research *28*, e99.

Galli, G.G., Carrara, M., Yuan, W.C., Valdes-Quezada, C., Gurung, B., Pepe-Mooney, B., Zhang, T., Geeven, G., Gray, N.S., de Laat, W., et al. (2015). YAP Drives Growth by Controlling Transcriptional Pause Release from Dynamic Enhancers. Molecular Cell *60*, 328–337.

Gaubatz, S., Wood, J.G., and Livingston, D.M. (1998). Unusual proliferation arrest and transcriptional control properties of a newly discovered E2F family member, E2F-6. Proceedings of the National Academy of Sciences of the United States of America *95*, 9190–9195.

Genevet, A., Wehr, M.C., Brain, R., Thompson, B.J., and Tapon, N. (2010). Kibra Is a Regulator of the Salvador/Warts/Hippo Signaling Network. Developmental Cell *18*, 300–308.

von Gise, A., Lin, Z., Schlegelmilch, K., Honor, L.B., Pan, G.M., Buck, J.N., Ma, Q., Ishiwata, T., Zhou, B., Camargo, F.D., et al. (2012). YAP1, the nuclear target of Hippo signaling, stimulates heart growth through cardiomyocyte proliferation but not hypertrophy. Proceedings of the National Academy of Sciences of the United States of America *109*, 2394–2399.

Guiley, K.Z., Liban, T.J., Felthousen, J.G., Ramanan, P., Litovchick, L., and Rubin, S.M. (2015). Structural mechanisms of DREAM complex assembly and regulation. Genes and Development *29*, 961–974.

Guiley, K.Z., Iness, A.N., Saini, S., Tripathi, S., Lipsick, J.S., Litovchick, L., and Rubin, S.M. (2018). Structural mechanism of Myb-MuvB assembly. Proceedings of the National Academy of Sciences of the United States of America *115*, 10016–10021.

Halder, G., and Johnson, R.L. (2011). Hippo signaling: Growth control and beyond. Development *138*, 9–22.

Hameyer, D., Loonstra, A., Eshkind, L., Schmitt, S., Antunes, C., Groen, A., Bindels, E., Jonkers, J., Krimpenfort, P., Meuwissen, R., et al. (2007). Toxicity of ligand-dependent Cre recombinases and generation of a conditional Cre deleter mouse allowing mosaic recombination in peripheral tissues. Physiological Genomics *31*, 32–41.

Han, H., Yang, B., Nakaoka, H.J., Yang, J., Zhao, Y., Le Nguyen, K., Bishara, A.T., Mandalia, T.K., and Wang, W. (2018). Hippo signaling dysfunction induces cancer cell addiction to YAP. Oncogene *37*, 6414–6424.

Harvey, K.F., Pfleger, C.M., and Hariharan, I.K. (2003). The Drosophila Mst ortholog, hippo, restricts growth and cell proliferation and promotes apoptosis. Cell *114*, 457–467.

Heallen, T., Zhang, M., Wang, J., Bonilla-Claudio, M., Klysik, E., Johnson, R.L., and Martin, J.F. (2011). Hippo pathway inhibits wnt signaling to restrain cardiomyocyte proliferation and heart size. Science *332*, 458–461.

Heallen, T., Morikawa, Y., Leach, J., Tao, G., Willerson, J.T., Johnson, R.L., and Martin, J.F. (2013). Hippo signaling impedes adult heart regeneration. Development *140*, 4683–4690.

Henley, S.A., and Dick, F.A. (2012). The retinoblastoma family of proteins and their regulatory functions in the mammalian cell division cycle. Cell Division *7*, 10.

Jia, Y., Chng, W.J., and Zhou, J. (2019). Super-enhancers: Critical roles and therapeutic targets in hematologic malignancies. Journal of Hematology and Oncology *12*, 1–17.

Jiao, S., Wang, H., Shi, Z., Dong, A., Zhang, W., Song, X., He, F., Wang, Y., Zhang, Z., Wang, W., et al. (2014). A Peptide Mimicking VGLL4 Function Acts as a YAP Antagonist Therapy against Gastric Cancer. Cancer Cell *25*, 166–180.

Jiao, S., Li, C., Hao, Q., Miao, H., Zhang, L., Li, L., and Zhou, Z. (2017). VGLL4 targets a TCF4-TEAD4 complex to coregulate Wnt and Hippo signalling in colorectal cancer. Nature Communications *8*, 14058.

Justice, R.W., Zilian, O., Woods, D.F., Noll, M., and Bryant, P.J. (1995). The Drosophila tumor suppressor gene warts encodes a homolog of human myotonic dystrophy kinase and is required for the control of cell shape and proliferation. Genes & Development *9*, 534–546.

Kaan, H.Y.K., Chan, S.W., Tan, S.K.J., Guo, F., Lim, C.J., Hong, W., and Song, H. (2017). Crystal structure of TAZ-TEAD complex reveals a distinct interaction mode from that of YAP-TEAD complex. Scientific Reports *7*, 2035.

Kent, L.N., and Leone, G. (2019). The broken cycle: E2F dysfunction in cancer. Nature Reviews Cancer *19*, 326–338.

Kim, D., Pertea, G., Trapnell, C., Pimentel, H., Kelley, R., and Salzberg, S.L. (2013). TopHat2: accurate alignment of transcriptomes in the presence of insertions, deletions and gene fusions. Genome Biology *14*, R36.

Knight, A.S., Notaridou, M., and Watson, R.J. (2009). A Lin-9 complex is recruited by B-Myb to activate transcription of G 2 /M genes in undifferentiated embryonal carcinoma cells. Oncogene *28*, 1737–1747.

Koo, J.H., Plouffe, S.W., Meng, Z., Lee, D.-H., Yang, D., Lim, D.-S., Wang, C.-Y., and Guan, K.-L. (2020). Induction of AP-1 by YAP/TAZ contributes to cell proliferation and organ growth. Genes & Development *34*, 72–86.

Korenjak, M., Taylor-Harding, B., Binné, U.K., Satterlee, J.S., Stevaux, O., Aasland, R., White-Cooper, H., Dyson, N., and Brehm, A. (2004). Native E2F/RBF complexes contain Myb-interacting proteins and repress transcription of developmentally controlled E2F target genes. Cell *119*, 181–193.

Krupczak-Hollis, K., Wang, X., Kalinichenko, V. V., Gusarova, G.A., Wang, I.C., Dennewitz, M.B., Yoder, H.M., Kiyokawa, H., Kaestner, K.H., and Costa, R.H. (2004). The mouse Forkhead Box m1 transcription factor is essential for hepatoblast mitosis and development of intrahepatic bile ducts and vessels during liver morphogenesis. Developmental Biology *276*, 74–88.

Kurppa, K.J., Liu, Y., To, C., Zhang, T., Fan, M., Vajdi, A., Knelson, E.H., Xie, Y., Lim, K., Cejas, P., et al. (2020). Treatment-Induced Tumor Dormancy through YAP-Mediated Transcriptional Reprogramming of the Apoptotic Pathway. Cancer Cell *37*, 104–122.

Lai, Z.C., Wei, X., Shimizu, T., Ramos, E., Rohrbaugh, M., Nikolaidis, N., Ho, L.L., and Li, Y. (2005). Control of cell proliferation and apoptosis by mob as tumor suppressor, mats. Cell *120*, 675–685.

Langmead, B., and Salzberg, S.L. (2012). Fast gapped-read alignment with Bowtie 2. Nature Methods *9*, 357–359.

Laoukili, J., Kooistra, M.R.H., Brás, A., Kauw, J., Kerkhoven, R.M., Morrison, A., Clevers, H., and Medema, R.H. (2005). FoxM1 is required for execution of the mitotic programme and chromosome stability. Nature Cell Biology *7*, 126–136.

Leach, J.P., Heallen, T., Zhang, M., Rahmani, M., Morikawa, Y., Hill, M.C., Segura, A., Willerson, J.T., and Martin, J.F. (2017). Hippo pathway deficiency reverses systolic heart failure after infarction. Nature *550*, 260–264.

Lee, J.H., Kim, T.S., Yang, T.H., Koo, B.K., Oh, S.P., Lee, K.P., Oh, H.J., Lee, S.H., Kong, Y.Y., Kim, J.M., et al. (2008). A crucial role of WW45 in developing epithelial tissues in the mouse. EMBO Journal *27*, 1231–1242.

Lei, Q.-Y., Zhang, H., Zhao, B., Zha, Z.-Y., Bai, F., Pei, X.-H., Zhao, S., Xiong, Y., and Guan, K.-L. (2008). TAZ Promotes Cell Proliferation and Epithelial-Mesenchymal Transition and Is Inhibited by the Hippo Pathway. Molecular and Cellular Biology *28*, 2426–2436.

Lescroart, F., Chabab, S., Lin, X., Rulands, S., Paulissen, C., Rodolosse, A., Auer, H., Achouri, Y., Dubois, C., Bondue, A., et al. (2014). Early lineage restriction in temporally distinct populations of Mesp1 progenitors during mammalian heart development. Nature Cell Biology *16*, 829–840.

Li, F., Wang, X., Capasso, J.M., and Gerdes, M.A. (1996). Rapid transition of cardiac myocytes from hyperplasia to hypertrophy during postnatal development. Journal of Molecular and Cellular Cardiology *28*, 1737–1746.

Li, H., Li, Q., Dang, K., Ma, S., Cotton, J.L., Yang, S., Zhu, L.J., Deng, A.C., Ip, Y.T., Johnson, R.L., et al. (2019). YAP/TAZ Activation Drives Uveal Melanoma Initiation and Progression. Cell Reports *29*, 3200–3211.

Li, Y., Zhou, H., Li, F., Chan, S.W., Lin, Z., Wei, Z., Yang, Z., Guo, F., Lim, C.J., Xing, W., et al. (2015). Angiomotin binding-induced activation of Merlin/NF2 in the Hippo pathway. Cell Research *25*, 801–817.

Li, Z., Zhao, B., Wang, P., Chen, F., Dong, Z., Yang, H., Guan, K.L., and Xu, Y. (2010). Structural insights into the YAP and TEAD complex. Genes and Development *24*, 235–240.

Lin, Z., Von Gise, A., Zhou, P., Gu, F., Ma, Q., Jiang, J., Yau, A.L., Buck, J.N., Gouin, K.A., Van Gorp, P.R.R., et al. (2014). Cardiac-specific YAP activation improves cardiac function and survival in an experimental murine MI model. Circulation Research *115*, 354–363.

Lin, Z., Guo, H., Cao, Y., Zohrabian, S., Zhou, P., Ma, Q., VanDusen, N., Guo, Y., Zhang, J., Stevens, S.M., et al. (2016). Acetylation of VGLL4 Regulates Hippo-YAP Signaling and Postnatal Cardiac Growth. Developmental Cell *39*, 466–479.

Lin, Z., Yang, Z., Xie, R., Ji, Z., Guan, K., and Zhang, M. (2019). Decoding WW domain tandem-mediated target recognitions in tissue growth and cell polarity. ELife *8*, e49439.

Lints, T.J., Parsons, L.M., Hartley, L., Lyons, I., and Harvey, R.P. (1993). Nkx-2.5: a novel murine homeobox gene expressed in early heart progenitor cells and their myogenic descendants. Development *119*, 419–431.

Litovchick, L., Sadasivam, S., Florens, L., Zhu, X., Swanson, S.K., Velmurugan, S., Chen, R., Washburn, M.P., Liu, X.S., and DeCaprio, J.A. (2007). Evolutionarily Conserved Multisubunit RBL2/p130 and E2F4 Protein Complex Represses Human Cell Cycle-Dependent Genes in Quiescence. Molecular Cell *26*, 539–551.

Litovchick, L., Florens, L.A., Swanson, S.K., Washburn, M.P., and Decaprio, J.A. (2011). DYRK1A protein kinase promotes quiescence and senescence through DREAM complex assembly. Genes and Development *25*, 801–813.

Liu, C.Y., Zha, Z.Y., Zhou, X., Zhang, H., Huang, W., Zhao, D., Li, T., Chan, S.W., Lim, C.J., Hong, W., et al. (2010). The hippo tumor pathway promotes TAZ degradation by phosphorylating a phosphodegron and recruiting the SCFβ-TrCP E3 ligase. Journal of Biological Chemistry *285*, 37159–37169.

Liu, X., Li, H., Rajurkar, M., Li, Q., Cotton, J.L., Ou, J., Zhu, L.J., Goel, H.L., Mercurio, A.M., Park, J.S., et al. (2016). Tead and AP1 Coordinate Transcription and Motility. Cell Reports *14*, 1169–1180.

Lovén, J., Hoke, H.A., Lin, C.Y., Lau, A., Orlando, D.A., Vakoc, C.R., Bradner, J.E., Lee, T.I., and Young, R.A. (2013). Selective inhibition of tumor oncogenes by disruption of super-enhancers. Cell *153*, 320–334.

Ma, S., Meng, Z., Chen, R., and Guan, K.-L. (2019). The Hippo Pathway: Biology and Pathophysiology. Annual Review of Biochemistry *88*, 577–604.

Macias, M.J., Hyvönen, M., Baraldi, E., Schultz, J., Sudol, M., Saraste, M., and Oschkinat, H. (1996). Structure of the WW domain of a kinase-associated protein complexed with a proline-rich peptide. Nature *382*, 646–649.

Mages, C.F.S., Wintsche, A., Bernhart, S.H., and Müller, G.A. (2017). The DREAM complex through its subunit Lin37 cooperates with Rb to initiate quiescence. ELife *6*, e26876.

Mahmoud, A.I., Kocabas, F., Muralidhar, S.A., Kimura, W., Koura, A.S., Thet, S., Porrello, E.R., and Sadek, H.A. (2013). Meis1 regulates postnatal cardiomyocyte cell cycle arrest. Nature *497*, 249–253.

Maiti, B., Li, J., De Bruin, A., Gordon, F., Timmers, C., Opavsky, R., Patil, K., Tuttle, J., Cleghorn, W., and Leone, G. (2005). Cloning and characterization of mouse E2F8, a novel mammalian E2F family member capable of blocking cellular proliferation. Journal of Biological Chemistry *280*, 18211–18220.

Malumbres, M., and Barbacid, M. (2001). To cycle or not to cycle: A critical decision in cancer. Nature Reviews Cancer *1*, 222–231.

Mannefeld, M., Klassen, E., and Gaubatz, S. (2009). B-MYB is required for recovery from the DNA damage-induced G2 checkpoint in p53 mutant cells. Cancer Research *69*, 4073–4080.

Marceau, A.H., Felthousen, J.G., Goetsch, P.D., Iness, A.N., Lee, H.W., Tripathi, S.M., Strome, S., Litovchick, L., and Rubin, S.M. (2016). Structural basis for LIN54 recognition of CHR elements in cell cycle-regulated promoters. Nature Communications *7*, 12301.

Matsuo, T., Kuramoto, H., Kumazaki, T., Mitsui, Y., and Takahashi, T. (2012). LIN54 harboring a mutation in CHC domain is localized to the cytoplasm and inhibits cell cycle progression. Cell Cycle *11*, 3227–3236.

Meilhac, S.M., and Buckingham, M.E. (2018). The deployment of cell lineages that form the mammalian heart. Nature Reviews Cardiology *15*, 705–724.

Meng, Z., Moroishi, T., Mottier-Pavie, V., Plouffe, S.W., Hansen, C.G., Hong, A.W., Park, H.W., Mo, J.S., Lu, W., Lu, S., et al. (2015). MAP4K family kinases act in parallel to MST1/2 to activate LATS1/2 in the Hippo pathway. Nature Communications *6*, 8357.

Meng, Z., Moroishi, T., and Guan, K.L. (2016). Mechanisms of Hippo pathway regulation. Genes and Development *30*, 1–17.

Mollova, M., Bersell, K., Walsh, S., Savla, J., Das, L.T., Park, S.Y., Silberstein, L.E., Dos Remedios, C.G., Graham, D., Colan, S., et al. (2013). Cardiomyocyte proliferation contributes to heart growth in young humans. Proceedings of the National Academy of Sciences of the United States of America *110*, 1446–1451.

Monroe, T.O., Hill, M.C., Morikawa, Y., Leach, J.P., Heallen, T., Cao, S., Krijger, P.H.L., de Laat, W., Wehrens, X.H.T., Rodney, G.G., et al. (2019). YAP Partially Reprograms Chromatin Accessibility to Directly Induce Adult Cardiogenesis In Vivo. Developmental Cell *48*, 765–779.

Morgan, D.O. (1997). CYCLIN-DEPENDENT KINASES : Engines , Clocks , and Microprocessors. Annual Review of Cell and Developmental Biology *13*, 261–291.

Morgan, D.O. (2014). The Cell Cycle: Prinzipals of Control (Oxford University Press).

Morgan, D.O. (2016). Mitotic regulation comes into focus. Nature *536*, 407–408.

Morikawa, Y., Zhang, M., Heallen, T., Leach, J., Tao, G., Xiao, Y., Bai, Y., Wei, L., Willerson, J.T., and Martin, J.F. (2015). Actin cytoskeletal remodeling with protrusion formation is essential for heart regeneration in Hippo-deficient mice. Science Signaling *8*, 1176–1185.

Morin-Kensicki, E.M., Boone, B.N., Howell, M., Stonebraker, J.R., Teed, J., Alb, J.G., Magnuson, T.R., O'Neal, W., and Milgram, S.L. (2006). Defects in Yolk Sac Vasculogenesis, Chorioallantoic Fusion, and Embryonic Axis Elongation in Mice with Targeted Disruption of Yap65. Molecular and Cellular Biology *26*, 77–87.

Moroishi, T., Park, H.W., Qin, B., Chen, Q., Meng, Z., Plouffe, S.W., Taniguchi, K., Yu, F.X., Karin, M., Pan, D., et al. (2015). A YAP/TAZ-induced feedback mechanism regulates Hippo pathway homeostasis. Genes and Development *29*, 1271–1284.

Müller, G.A., and Engeland, K. (2010). The central role of CDE/CHR promoter elements in the regulation of cell cycle-dependent gene transcription. FEBS Journal *277*, 877–893.

Müller, G.A., Quaas, M., Schümann, M., Krause, E., Padi, M., Fischer, M., Litovchick, L., DeCaprio, J.A., and Engeland, K. (2012). The CHR promoter element controls cell cycle-dependent gene transcription and binds the DREAM and MMB complexes. Nucleic Acids Research *40*, 1561–1578.

Müller, G.A., Wintsche, A., Stangner, K., Prohaska, S.J., Stadler, P.F., and Engeland, K. (2014). The CHR site: Definition and genome-wide identification of a cell cycle transcriptional element. Nucleic Acids Research *42*, 10331-10350A.

Murzina, N. V., Pei, X.Y., Zhang, W., Sparkes, M., Vicente-Garcia, J., Pratap, J.V., McLaughlin, S.H., Ben-Shahar, T.R., Verreault, A., Luisi, B.F., et al. (2008). Structural Basis for the Recognition of Histone H4 by the Histone-Chaperone RbAp46. Structure *16*, 1077–1085.

Musacchio, A. (2015). The Molecular Biology of Spindle Assembly Checkpoint Signaling Dynamics. Current Biology *25*, R1002–R1018.

Muzumdar, M.D., Tasic, B., Miyamichi, K., Li, N., and Luo, L. (2007). A global double-fluorescent cre reporter mouse. Genesis *45*, 593–605.

Naetar, N., Soundarapandian, V., Litovchick, L., Kelsey, L., Sablina, A.A., Bowman-colin, C., Sicinski, P., William, C., Decaprio, J.A., and Livingston, D.M. (2014). PP2A-mediated regulation of RAS signaling in G2 is essential for stable quiescence and normal G1 length. Molecular Cell *54*, 932–945.

Nicolas, E., Ait-Si-Ali, S., and Trouche, D. (2001). The histone deacetylase HDAC3 targets RbAp48 to the retinoblastoma protein. Nucleic Acids Research *29*, 3131–3136.

Olivetti, G., Cigola, E., Maestri, R., Corradi, D., Lagrasta, C., Gambert, S.R., and Anversa, P. (1996). Aging, cardiac hypertrophy and ischemic cardiomyopathy do not affect the proportion of mononucleated and multinucleated myocytes in the human heart. Journal of Molecular and Cellular Cardiology *28*, 1463–1477.

Osterloh, L., von Eyss, B., Schmit, F., Rein, L., Hübner, D., Samans, B., Hauser, S., and Gaubatz, S. (2007). The human synMuv-like protein LIN-9 is required for transcription of G2/M genes and for entry into mitosis. The EMBO Journal *26*, 144–157.

Pan, D. (2010). The hippo signaling pathway in development and cancer. Developmental Cell *19*, 491–505.

Park, H.J., Costa, R.H., Lau, L.F., Tyner, A.L., and Raychaudhuri, P. (2008). Anaphase-Promoting Complex/Cyclosome-Cdh1-Mediated Proteolysis of the Forkhead Box M1 Transcription Factor Is Critical for Regulated Entry into S Phase. Molecular and Cellular Biology *28*, 5162–5171.

Pasumarthi, K.B.S., Nakajima, H., Nakajima, H.O., Soonpaa, M.H., and Field, L.J. (2005). Targeted expression of cyclin D2 results in cardiomyocyte DNA synthesis and infarct regression in transgenic mice. Circulation Research *96*, 110–118.

Pattschull, G., Walz, S., Gründl, M., Schwab, M., Rühl, E., Baluapuri, A., Cindric-Vranesic, A., Kneitz, S., Wolf, E., Ade, C.P., et al. (2019). The Myb-MuvB Complex Is Required for YAP-Dependent Transcription of Mitotic Genes. Cell Reports *27*, 3533–3546.

Plouffe, S.W., Meng, Z., Lin, K.C., Lin, B., Hong, A.W., Chun, J. V., and Guan, K.L. (2016). Characterization of Hippo Pathway Components by Gene Inactivation. Molecular Cell *64*, 993–1008.

Poolman, R.A., and Brooks, G. (1998). Expressions and Activities of Cell Cycle Regulatory Molecules During the Transition from Myocyte Hyperplasia to Hypertrophy. Journal of Molecular and Cellular Cardiology *30*, 2121–2135.

Porrello, E.R., Mahmoud, A.I., Simpson, E., Hill, J.A., Richardson, J.A., Olson, E.N., and Sadek, H.A. (2011). Transient regenerative potential of the neonatal mouse heart. Science *331*, 1078–1080.

Porrello, E.R., Mahmoud, A.I., Simpson, E., Johnson, B.A., Grinsfelder, D., and Canseco, D. (2013). Regulation of neonatal and adult mammalian heart regeneration by the miR-15 family. Proceedings of the National Academy of Sciences *110*, 187–192.

Poss, K.D., Wilson, L.G., and Keating, M.T. (2002). Heart regeneration in zebrafish. Science *298*, 2188–2190.

Quinlan, A.R., and Hall, I.M. (2010). BEDTools: A flexible suite of utilities for comparing genomic features. Bioinformatics *26*, 841–842.

Ramírez, F., Dündar, F., Diehl, S., Grüning, B.A., and Manke, T. (2014). DeepTools: A flexible platform for exploring deep-sequencing data. Nucleic Acids Research *42*, 187–191.

Del Re, D.P., Yang, Y., Nakano, N., Cho, J., Zhai, P., Yamamoto, T., Zhang, N., Yabuta, N., Nojima, H., Pan, D., et al. (2013). Yes-associated protein isoform 1 (Yapl) promotes cardiomyocyte survival and growth to protect against myocardial ischemic injury. Journal of Biological Chemistry *288*, 3977–3988.

Reichert, N., Wurster, S., Ulrich, T., Schmitt, K., Hauser, S., Probst, L., Götz, R., Ceteci, F., Moll, R., Rapp, U., et al. (2010). Lin9, a subunit of the mammalian DREAM complex, is essential for embryonic development, for survival of adult mice, and for tumor suppression. Molecular and Cellular Biology *30*, 2896–2908.

Rosa-Garrido, M., Chapski, D.J., Schmitt, A.D., Kimball, T.H., Karbassi, E., Monte, E., Balderas, E., Pellegrini, M., Shih, T.T., Soehalim, E., et al. (2017). High-resolution mapping of chromatin conformation in cardiac myocytes reveals structural remodeling of the epigenome in heart failure. Circulation *136*, 1613–1625.

Saade, E., Mechold, U., Kulyyassov, A., Vertut, D., Lipinski, M., and Ogryzko, V. (2009). Analysis of interaction partners of H4 histone by a new proteomics approach. Proteomics *9*, 4934–4943.

Sadasivam, S., and DeCaprio, J.A. (2013). The DREAM complex: Master coordinator of cell cycle dependent gene expression. Nature Reviews Cancer *13*, 585–595.

Sadasivam, S., Duan, S., and DeCaprio, J.A. (2012). The MuvB complex sequentially recruits B-Myb and FoxM1 to promote mitotic gene expression. Genes and Development *26*, 474–489.

Sandoval, R., Pilkinton, M., and Colamonici, O.R. (2009). Deletion of the p107/p130-binding domain of Mip130/LIN9 bypasses the rquirement for CDK4 activity for the dissociation of Mip130/LIN9 from p107/p130-E2F4 complex. Experimental Cell Research *315*, 2914–2920.

Schmit, F., Korenjak, M., Mannefeld, M., Schmitt, K., Franke, C., Von Eyss, B., Gagrica, S., Hänel, F., Brehm, A., and Gaubatz, S. (2007). LINC, a human complex that is related to pRB-containing complexes in invertebrates regulates the expression of G2/M genes. Cell Cycle *6*, 1903–1913.

Schmit, F., Cremer, S., and Gaubatz, S. (2009). LIN54 is an essential core subunit of the DREAM/LINC complex that binds to the cdc2 promoter in a sequence-specific manner. FEBS Journal *276*, 5703–5716.

Sdek, P., Zhao, P., Wang, Y., Huang, C.J., Ko, C.Y., Butler, P.C., Weiss, J.N., and MacLellan, W.R. (2011). Rb and p130 control cell cycle gene silencing to maintain the postmitotic phenotype in cardiac myocytes. Journal of Cell Biology *194*, 407–423.

Senyo, S.E., Steinhauser, M.L., Pizzimenti, C.L., Yang, V.K., Cai, L., Wang, M., Wu, T. Di, Guerquin-Kern, J.L., Lechene, C.P., and Lee, R.T. (2013). Mammalian heart renewal by pre-existing cardiomyocytes. Nature *493*, 433–436.

Sherr, C.J., and Roberts, J.M. (1999). CDK inhibitors: Positive and negative regulators of G1-phase progression. Genes and Development *13*, 1501–1512.

Shlyueva, D., Stampfel, G., and Stark, A. (2014). Transcriptional enhancers: From properties to genome-wide predictions. Nature Reviews Genetics *15*, 272–286.

Sloan, C.A., Chan, E.T., Davidson, J.M., Malladi, V.S., Strattan, J.S., Hitz, B.C., Gabdank, I., Narayanan, A.K., Ho, M., Lee, B.T., et al. (2016). ENCODE data at the ENCODE portal. Nucleic Acids Research *44*, D726–D732.

Soonpaa, M.H., Kim, K.K., Pajak, L., Franklin, M., and Field, L.J. (1996). Cardiomyocyte DNA synthesis and binucleation during murine development. American Journal of Physiology - Heart and Circulatory Physiology *271*, 2183–2189.

Stanley, E.G., Biben, C., Elefanty, A., Barnett, L., Koentgen, F., Robb, L., and Harvey, R.P. (2002). Efficient cre-mediated deletion in cardiac progenitor cells conferred by a 3'UTR-ires-Cre allele of the homeobox gene Nkx2-5. International Journal of Developmental Biology *46*, 431–439.

Di Stefano, L., Jensen, M.R., and Helin, K. (2003). E2F7, a novel E2F featuring DP-independent repression of a subset of E2F-regulated genes. EMBO Journal *22*, 6289–6298.

Stein, C., Bardet, A.F., Roma, G., Bergling, S., Clay, I., Ruchti, A., Agarinis, C., Schmelzle, T., Bouwmeester, T., Schübeler, D., et al. (2015). YAP1 Exerts Its Transcriptional Control via TEAD-Mediated Activation of Enhancers. PLoS Genetics *11*, e1005465.

Stopp, S., Gründl, M., Fackler, M., Malkmus, J., Leone, M., Naumann, R., Frantz, S., Wolf, E., Von Eyss, B., Engel, F.B., et al. (2017). Deletion of Gas2l3 in mice leads to specific defects in cardiomyocyte cytokinesis during development. Proceedings of the National Academy of Sciences of the United States of America *114*, 8029–8034.

Subramanian, A., Tamayo, P., Mootha, V.K., Mukherjee, S., Ebert, B.L., Gillette, M.A., Paulovich, A., Pomeroy, S.L., Golub, T.R., Lander, E.S., et al. (2005). Gene set enrichment analysis: A knowledge-based approach for interpreting genome-wide expression profiles. Proceedings of the National Academy of Sciences of the United States of America *102*, 15545–15550.

Sudol, M., Shields, D.C., and Farooq, A. (2012). Structures of YAP protein domains reveal promising targets for development of new cancer drugs. Seminars in Cell and Developmental Biology *23*, 827–833.

Tanaka, Y., Patestos, N.P., Maekawa, T., and Ishii, S. (1999). B-myb is required for inner cell mass formation at an early stage of development. Journal of Biological Chemistry *274*, 28067–28070.

Tane, S., Ikenishi, A., Okayama, H., Iwamoto, N., Nakayama, K.I., and Takeuchi, T. (2014). Biochemical and Biophysical Research Communications of mammalian cardiomyocytes. Biochemical and Biophysical Research Communications *443*, 1105–1109.

Tapon, N., Harvey, K.F., Bell, D.W., Wahrer, D.C.R., Schiripo, T.A., Haber, D.A., and Hariharan, I.K. (2002). salvador promotes both cell cycle exit and apoptosis in Drosophila and is mutated in human cancer cell lines. Cell *110*, 467–478.

Tian, Y., Kolb, R., Hong, J.-H., Carroll, J., Li, D., You, J., Bronson, R., Yaffe, M.B., Zhou, J., and Benjamin, T. (2007). TAZ Promotes PC2 Degradation through a SCFβ-Trcp E3 Ligase Complex. Molecular and Cellular Biology *27*, 6383–6395.

Tschöp, K., Conery, A.R., Litovchick, L., DeCaprio, J.A., Settleman, J., Harlow, E., and Dyson, N. (2011). A kinase shRNA screen links LATS2 and the pRB tumor suppressor. Genes and Development *25*, 814–830.

Tsika, R.W., Ma, L., Kehat, I., Schramm, C., Simmer, G., Morgan, B., Fine, D.M., Hanft, L.M., McDonald, K.S., Molkentin, J.D., et al. (2010). TEAD-1 overexpression in the mouse heart promotes an age-dependent heart dysfunction. Journal of Biological Chemistry *285*, 13721–13735.

Tzahor, E., and Poss, K.D. (2017). Cardiac regeneration strategies: Staying young at heart. Science *356*, 1035–1039.

Uxa, S., Bernhart, S.H., Mages, C.F.S., Fischer, M., Kohler, R., Hoffmann, S., Stadler, P.F., Engeland, K., and Müller, G.A. (2019). DREAM and RB cooperate to induce gene repression and cell-cycle arrest in response to p53 activation. Nucleic Acids Research *47*, 9087–9103.

Uygur, A., and Lee, R.T. (2016). Review Mechanisms of Cardiac Regeneration. Developmental Cell *36*, 362–374.

Vargas, R.E., Duong, V.T., Han, H., Ta, A.P., Chen, Y., Zhao, S., Yang, B., Seo, G., Chuc, K., Oh, S., et al. (2019). Elucidation of WW domain ligand binding specificities in the Hippo pathway reveals STXBP 4 as YAP inhibitor. The EMBO Journal *39*, e102406.

Wang, J., Liu, S., Heallen, T., and Martin, J.F. (2018). The Hippo pathway in the heart: pivotal roles in development, disease, and regeneration. Nature Reviews Cardiology *15*, 672–684.

Weinberg, R.A. (2014). The Biology of Cancer (New York: Garland Science, Taylor & Francis Group, LLC).

Werwein, E., Schmedt, T., Hoffmann, H., Usadel, C., Obermann, N., Singer, J.D., and Klempnauer, K.H. (2012). B-Myb promotes S-phase independently of its sequence-specific DNA binding activity and interacts with polymerase delta-interacting protein 1 (Pdip1). Cell Cycle *11*, 4047–4058.

Werwein, E., Cibis, H., Hess, D., and Klempnauer, K.H. (2019). Activation of the oncogenic transcription factor B-Myb via multisite phosphorylation and prolyl cis/trans isomerization. Nucleic Acids Research *47*, 103–121.

Whyte, W.A., Orlando, D.A., Hnisz, D., Abraham, B.J., Lin, C.Y., Kagey, M.H., Rahl, P.B., Lee, T.I., and Young, R.A. (2013). Master transcription factors and mediator establish super-enhancers at key cell identity genes. Cell *153*, 307–319.

Wiseman, E.F., Chen, X., Han, N., Webber, A., Ji, Z., Sharrocks, A.D., and Ang, Y.S. (2015). Deregulation of the FOXM1 target gene network and its coregulatory partners in oesophageal adenocarcinoma. Molecular Cancer *14*, 69.

Wolter, P., Schmitt, K., Fackler, M., Kremling, H., Probst, L., Hauser, S., Gruss, O.J., and Gaubatz, S. (2012). GAS2L3, a target gene of the DREAM complex, is required for proper cytokinesis and genomic stability. Journal of Cell Science *125*, 2393–2406.

Xiao, G.H., Chernoff, J., and Testa, J.R. (2003). NF2: The Wizardry of Merlin. Genes Chromosomes and Cancer *38*, 389–399.

Xin, M., Kim, Y., Sutherland, L.B., Qi, X., McAnally, J., Schwartz, R.J., Richardson, J.A., Bassel-Duby, R., and Olson, E.N. (2011). Regulation of Insulin-Like Growth Factor Signaling by Yap Governs Cardiomyocyte Proliferation and Embryonic Heart Size. Science Signaling *4*, ra70.

Xin, M., Kim, Y., Sutherland, L.B., Murakami, M., Qi, X., McAnally, J., Porrello, E.R., Mahmoud, A.I., Tan, W., Shelton, J.M., et al. (2013). Hippo pathway effector Yap promotes cardiac regeneration. Proceedings of the National Academy of Sciences *110*, 13839–13844.

Yin, F., Yu, J., Zheng, Y., Chen, Q., Zhang, N., and Pan, D. (2013). Spatial organization of hippo signaling at the plasma membrane mediated by the tumor suppressor merlin/NF2. Cell *154*, 1342–1355.

Yu, F.X., Zhao, B., Panupinthu, N., Jewell, J.L., Lian, I., Wang, L.H., Zhao, J., Yuan, H., Tumaneng, K., Li, H., et al. (2012). Regulation of the Hippo-YAP pathway by G-protein-coupled receptor signaling. Cell *150*, 780–791.

Yu, F.X., Luo, J., Mo, J.S., Liu, G., Kim, Y.C., Meng, Z., Zhao, L., Peyman, G., Ouyang, H., Jiang, W., et al. (2014). Mutant Gq/11 promote uveal melanoma tumorigenesis by activating YAP. Cancer Cell *25*, 822–830.

Yu, J., Zheng, Y., Dong, J., Klusza, S., Deng, W.M., and Pan, D. (2010). Kibra Functions as a Tumor Suppressor Protein that Regulates Hippo Signaling in Conjunction with Merlin and Expanded. Developmental Cell *18*, 288–299.

Yuan, Y., Park, J., Feng, A., Awasthi, P., Wang, Z., Chen, Q., and Iglesias-Bartolome, R. (2020). YAP1/TAZ-TEAD transcriptional networks maintain skin homeostasis by regulating cell proliferation and limiting KLF4 activity. Nature Communications *11*, 1472.

Yue, Q., Wagstaff, L., Yang, X., Weijer, C., and Münsterberg, A. (2008). Wnt3a-mediated chemorepulsion controls movement patterns of cardiac progenitors and requires RhoA function. Development *135*, 1029–1037.

Zaffran, S., Kelly, R.G., Meilhac, S.M., Buckingham, M.E., and Brown, N.A. (2004). Right ventricular myocardium derives from the anterior heart field. Circulation Research *95*, 261–268.

Zanconato, F., Forcato, M., Battilana, G., Azzolin, L., Quaranta, E., Bodega, B., Rosato, A., Bicciato, S., Cordenonsi, M., and Piccolo, S. (2015). Genome-wide association between YAP/TAZ/TEAD and AP-1 at enhancers drives oncogenic growth. Nature Cell Biology *17*, 1218–1227.

Zhang, N., Bai, H., David, K.K., Dong, J., Zheng, Y., Cai, J., Giovannini, M., Liu, P., Anders, R.A., and Pan, D. (2010). The Merlin/NF2 Tumor Suppressor Functions through the YAP Oncoprotein to Regulate Tissue Homeostasis in Mammals. Developmental Cell *19*, 27–38.

Zhang, W., Tyl, M., Ward, R., Sobott, F., Maman, J., Murthy, A.S., Watson, A.A., Fedorov, O., Bowman, A., Owen-Hughes, T., et al. (2013). Structural plasticity of histones H3-H4 facilitates their allosteric exchange between RbAp48 and ASF1. Nature Structural and Molecular Biology *20*, 29–35.

Zhang, W., Gao, Y., Li, P., Shi, Z., Guo, T., Li, F., Han, X., Feng, Y., Zheng, C., Wang, Z., et al. (2014a). VGLL4 functions as a new tumor suppressor in lung cancer by negatively regulating the YAP-TEAD transcriptional complex. Cell Research *24*, 331–343.

Zhang, X., Milton, C.C., Humbert, P.O., and Harvey, K.F. (2009). Transcriptional output of the Salvador/Warts/Hippo pathway is controlled in distinct fashions in Drosophila melanogaster and mammalian cell lines. Cancer Research *69*, 6033–6041.

Zhang, Y., Liu, T., Meyer, C.A., Eeckhoute, J., Johnson, D.S., Bernstein, B.E., Nussbaum, C., Myers, R.M., Brown, M., Li, W., et al. (2008). Model-based analysis of ChIP-Seq (MACS). Genome Biology *9*, R137.

Zhang, Z., Lin, Z., Zhou, Z., Shen, H.C., Yan, S.F., Mayweg, A. V., Xu, Z., Qin, N., Wong, J.C., Zhang, Z., et al. (2014b). Structure-based design and synthesis of potent cyclic peptides inhibiting the YAP-TEAD protein-protein interaction. ACS Medicinal Chemistry Letters *5*, 993–998.

Zhao, B., Wei, X., Li, W., Udan, R.S., Yang, Q., Kim, J., Xie, J., Ikenoue, T., Yu, J., Li, L., et al. (2007). Inactivation of YAP oncoprotein by the Hippo pathway is involved in cell contact inhibition and tissue growth control. Genes and Development *21*, 2747–2761.

Zhao, B., Ye, X., Yu, J., Li, L., Li, W., Li, S., Yu, J., Lin, J.D., Wang, C.Y., Chinnaiyan, A.M., et al. (2008). TEAD mediates YAP-dependent gene induction and growth control. Genes and Development *22*, 1962–1971.

Zhao, B., Li, L., Tumaneng, K., Wang, C.Y., and Guan, K.L. (2010). A coordinated phosphorylation by Lats and CK1 regulates YAP stability through SCFβ-TRCP. Genes and Development *24*, 72–85.

Zhou, D., Conrad, C., Xia, F., Park, J.S., Payer, B., Yin, Y., Lauwers, G.Y., Thasler, W., Lee, J.T., Avruch, J., et al. (2009). Mst1 and Mst2 Maintain Hepatocyte Quiescence and Suppress Hepatocellular Carcinoma Development through Inactivation of the Yap1 Oncogene. Cancer Cell *16*, 425–438.

6. Appendix

6.1 List of Figures

6.2 List of Tables

6.3 Supplementary Figures

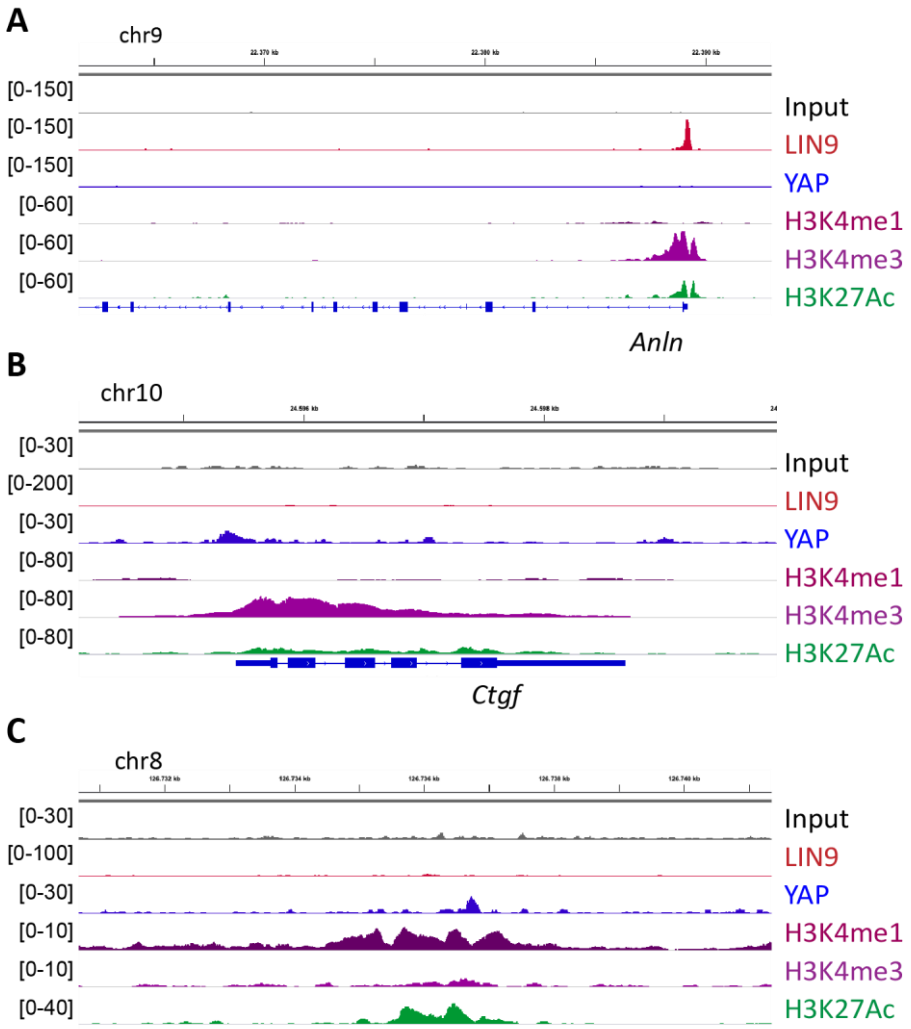

Figure 37: Genome browser tracks of the *Anln* and *Ctgf* genomic loci
(**A**) Genome browser tracks illustrating the binding of LIN9 to the promoter of *Anln.* (**B**) Genome browser tracks illustrating the binding of YAP to the promoter of *Ctgf*. (**C**) Genome browser tracks illustrating of the binding of YAP to an enhancer. ChIP-Seq data of LIN9 and YAP are from E16.5 heart ventricles and histone modifications H3K4me1, H3K4me3 and H3K27Ac in E14.5 heart ventricles are from ENCODE (GSE31039).

6.4 Supervised theses

1. **Hauf, Laura.** Bachelorthesis: *Role of the Myb-MuvB complex in cardiomyocyte proliferation and binucleation process.* Supervisors: **Marco Gründl**, Prof. Dr. Stefan Gaubatz, 07 2017.

2. **Schwab, Melissa.** Research internship: Biomedicine: Supervisors: **Marco Gründl**, Prof. Dr. Stefan Gaubatz, 02 2018.

3. **Werner, Marcela.** Masterthesis: *Wechselwirkung zwischen dem onkogenen Hippo-YAP Signalweg und dem Myb-MuvB Komplex während der Zellzyklusregulation und Differenzierung.* Supervisors: **Marco Gründl**, Prof. Dr. Stefan Gaubatz, 04 2019.

6.5 Abbreviations

4-OHT	4-Hydroxytamoxifen
aa	Amino acids
APS	Ammonium persulfate
bp	base pairs
BSA	Bovine serum albumine
CDK	Cyclin dependent kinase
cDNA	Complementary deoxyribonucleic acid
ChIP	Chromatin immunoprecipitation
ChIP-Seq	Chromatin immunoprecipitation sequencing
Co-IP	Co-immunoprecipitation
Ctrl	Control
ddH_2O	double-distilled water
DEPC	Diethyl pyrocarbonate
DMEM	Dulbecco`s modified eagle medium
DMSO	Dimethyl sulfoxide
DNA	Deoxyribonucleic acid
dNTP	Deoxyribonucleotide triphosphate
Doxy	Doxycycline
DREAM	DP, RB-like, E2F and Multi-vulval class B complex
DTT	Dithiothreitol
ECL	Enhanced chemiluminescence solution
EDTA	Ethylenediaminetetraacetic acid
ESB	Electrophoresis sample buffer
FCS	Fetal calf serum
G0, G1, G2	Gap0/gap1/gap2 phases
gDNA	genomic deoxyribonucleic acid
GFP	Green fluorescent protein
h	Hours
HCl	Hydrochloric acid
HPRT	Hypoxanthine-phosphoribosyl transferase 1
HRP	Horseradish peroxidase
IHC	Immunohistochemistry
kb	Kilobase
kDa	Kilodalton
LB	Luria Bertani
M phase	Mitosis and cytokinesis
min	Minutes
MMB	Myb-MuvB complex
MuvB	Multi-vulval class B
NGS	Next-generation sequencing
OptiMEM	Opti-Minimum essential medium
PAGE	Polyacrylamide gel electrophoresis
PBS	Phosphate buffered saline
PCR	Polymerase chain reaction
PFA	Paraformaldehyde

PI	Propidium idodide
PIC	Protease inhibitor cocktail
PLA	Proximity ligation assay
PMSF	Phenylmethylsulphonyl fluoride
pRB	Retinoblastoma protein
P/S	Penicillin-Streptomycin
PVDF	Polyvinylidene fluoride
PY	Proline-tyrosine
qPCR	Quantitative polymerase chain reaction
RNA	Ribonucleic acid
RNA-seq	Ribonucleic acid-sequencing
RNAi	RNA interference
rpm	Rounds per minute
RT	Room temperature
S phase	Synthesis phase
SDS	Sodium dodecyl sulfate
siRNA	small interfering ribonucleic acid
TBS	Tris-buffered saline
TBS-T	Tris buffered saline-Tween
TEMED	N'N'N'N'-tetramethyl ethylene-diamine
Tris	Tris(hydroxymethyl)aminomethane
UV	Ultraviolet
WB	Western blot
wt	Wild-type

6.7 Publication list and conference contributions

6.7.1 Publications

Gründl M., Walz S., Hauf L., Schwab M., Werner KM., Spahr S., Schulte C., Maric HM., Ade CP., Gaubatz S. (2020): **Interaction of YAP with the Myb-MuvB (MMB) complex defines a transcriptional program to promote the proliferation of cardiomyocytes.** PLoS Genet 16(5): e1008818. https://doi.org/10.1371/journal.pgen.1008818

Pattschull G., Walz S., **Gründl M**., Schwab M., Rühl E., Baluapuri A., Cindric-Vranesic A., Kneitz S., Wolf E., Ade CP., Rosenwald A., von Eyss B., Gaubatz S. (2019): **The Myb-MuvB complex is required for YAP-dependent transcription of mitotic genes.** Cell Reports 27:12, 3533-3546. https://doi.org/10.1016/j.celrep.2019.05.071

Gründl, M., Engel, F. B., & Gaubatz, S. (2017). **GAS2L3: Coordinator of cardiomyocyte cytokinesis?** Cell cycle, 16(20), 1853–1854. https://doi.org/10.1080/15384101.2017.1372546

Stopp, S., **Gründl, M**., Fackler, M., Malkmus, J., Leone, M., Naumann, R., Frantz, S., Wolf, E., von Eyss, B., Engel, F. B., & Gaubatz, S. (2017). **Deletion of Gas2l3 in mice leads to specific defects in cardiomyocyte cytokinesis during development.** Proceedings of the National Academy of Sciences of the United States of America, 114(30), 8029–8034. https://doi.org/10.1073/pnas.1703406114

6.7.2 Conference contributions

06/2019 **Poster at the Cell Cycle Meeting 2019** in Trieste Italy;

Poster: “The Myb-MuvB complex is required for YAP-induced proliferation in postnatal cardiomyocytes” by Marco Gründl, Laura Hauf, Kerstin Marcela Werner and Stefan Gaubatz

10/2018 **Poster at the 13th Eureka International GSLS student Symposium** in Wuerzburg Germany;

Poster: “The Myb-MuvB complex and the Hippo pathway – crosstalk during heart development” by Marco Gründl, Laura Hauf and Stefan Gaubatz

10/2018 **Poster at the 34th Ernst Klenk Symposium** in Cologne Germany

Poster: “The Myb-MuvB complex and the Hippo pathway – crosstalk during heart development” by Marco Gründl, Laura Hauf and Stefan Gaubatz

10/2017 **Poster at the 12th Eureka International GSLS student Symposium** in Wuerzburg Germany;

Poster: “B-MYB-MuvB dependent gene regulation during heart development in mice” by Marco Gründl, Laura Hauf and Stefan Gaubatz

10/2016 **Poster at the 11th Eureka International GSLS student Symposium** in Wuerzburg Germany;

Poster: “MuvB dependent gene regulation during heart development in mice” by Marco Gründl, Sabine Stopp and Stefan Gaubatz

03/2016 **Participation at the 3th Immunotherapy of Cancer Conference** in Munich Germany

6.8 Acknowledgements

Mein besonderer Dank gilt Prof. Dr. Stefan Gaubatz, der es mir ermöglicht hat an diesem spannenden Projekt zu arbeiten und diese Doktorarbeit in seiner Arbeitsgruppe anzufertigen. Ich danke ihm für die ständige Bereitschaft meine Fragen zu beantworten oder Ergebnisse wissenschaftlich zu diskutieren.

An dieser Stelle möchte ich mich gerne bei den Mitgliedern meines Thesis Committees, Prof. Dr. Manfred Gessler und Prof. Dr. Eva Klopocki, für den wissenschaftlichen Input und die professionelle Begleitung während der gesamten Promotionszeit bedanken.

Außerdem danke ich Dr. Elmar Wolf, Dr. Carsten Ade, Dr. Susanne Walz, Dr. Hans Maric, Laura Hauf, Melissa Schwab, Susanne Spahr, Clemens Schulte und Marcela Werner für die gute Zusammenarbeit und die experimentelle Unterstützung an dem Projekt.

Nette Kollegen und ein angenehmes Arbeitsklima sind ein willkommener Ausgleich für einen langen und anstrengender Laboralltag. Dafür möchte ich mich bei allen ehemaligen und derzeitigen Mitgliedern der AG Gaubatz bedanken, insbesondere bei Stefan Gaubatz, Susanne Spahr, Adelgunde Wolpert, Grit Weinstock, Steffen Hanselmann, Camila Fetiva Mora und Dörthe Gertzmann. Außerdem möchte ich den Bachelor- und Masterstudenten danken, die während meiner Doktorarbeit immer wieder für frischen Wind in unserem Labor gesorgt haben. Danke an Magda, Eva, Viktoria, Woojin und Anika.

Ein weiterer großer Rückhalt während meiner Zeit im Labor war meine Familie. Auch wenn ihr nicht immer verstanden habt woran ich eigentlich arbeite, hattet ihr immer ein offenes Ohr für mich. Ich bedanke mich bei meinen Eltern, meinem Bruder und allen Omas und Opas für eure Unterstützung und Geduld. Außerdem möchte ich mich bei meiner Freundin Christina bedanken. Danke für die Unterstützung während dieser Zeit, für den ein oder anderen wissenschaftlichen Rat und das Korrekturlesen dieser Arbeit.

6.9 Affidavit

6.9.1 Affidavit

I hereby confirm that my thesis entitled “Biochemical characterization of the MMB-Hippo crosstalk and its physiological relevance for heart development" is the result of my own work. I did not receive any help or support from commercial consultants. All sources and / or materials applied are listed and specified in the thesis.

Furthermore, I confirm that this thesis has not yet been submitted as part of another examination process neither in identical nor in similar form.

_____

Place, Date Signature

6.9.2 Eidesstattliche Erklärung

Hiermit erkläre ich an Eides statt, die Dissertation „Biochemische Charakterisierung des MMB-Hippo Signalweges und dessen physiologische Rolle in der Herzentwicklung“ eigenständig, d.h. insbesondere selbstständig und ohne Hilfe eines kommerziellen Promotionsberaters, angefertigt und keine anderen als die von mir angegebenen Quellen und Hilfsmittel verwendet zu haben.

Ich erkläre außerdem, dass die Dissertation weder in gleicher noch in ähnlicher Form bereits in einem anderen Prüfungsverfahren vorgelegen hat.

_____

Ort, Datum Unterschrift